Measurements of the Higgs boson produced in association with a vector boson and decaying to a pair of b-quarks with the ATLAS detector

Konie Al Khoury

université
PARIS-SACLAY

Measurements of the Higgs boson produced in association with a vector boson and decaying to a pair of b-quarks with the ATLAS detector

Thèse de doctorat de l'Université Paris-Saclay

École doctorale n° 576, Particules, Hadrons, Énergie, Noyau, Instrumentation, Imagerie, Cosmos et Simulation (PHENIICS)
Spécialité de doctorat: Physique des Particules
Unité de recherche: Université Paris-Saclay, CNRS, IJCLab, 91405, Orsay, France.
Référent: : Faculté des sciences d'Orsay

Thèse présentée et soutenue à Orsay, le 23 Septembre 2020, par

Konie AL KHOURY

Composition du jury:

Marie-Hélène Schune Directrice de recherche, IJCLab, Orsay	Présidente
André David Professeur, CERN	Rapporteur & examinateur
Marco Delmastro Directeur de recherche, LAPP, Annecy	Rapporteur & examinateur
Tim Scanlon Professeur, University College London, UK	Examinateur
William Murray Professeur, University of Warwick, UK	Examinateur
Nicolas Morange Chargé de recherche, IJCLab, Orsay	Directeur de thèse

Thèse de doctorat

NNT: 2020UPASP006

Contents

Introduction

The Standard Model of elementary particles is a theory developed since the 1960's to describe all fundamental particles and their interactions. The discovery of a new particle at the Large Hadron Collider (LHC) in 2012 consistent with the Higgs boson, was a confirmation of the existence of the Higgs field as predicted by this model. This field was introduced to explain the electroweak symmetry breaking mechanism and the masses of the W and Z bosons but can also be extended to describe the origin of mass of all fundamental particles, with the possible exception of neutrinos. A Higgs boson with a mass of 125 GeV was first observed by the ATLAS and CMS experiments at the LHC using data collected during Run-1 from p-p collisions at a center-of-mass energy of 7-8 TeV. After the discovery, the Higgs sector became an active research topic at the LHC to measure the properties of this particle and in particular its coupling to other particles. As all Higgs couplings can be predicted once its mass is known, it is interesting to measure the Higgs boson in different production modes and decay channels since each measurement brings additional constraints to the Standard Model and to physics beyond it.

The first research project described in this thesis concerns the Liquid argon calorimeter (LAr) electronics Phase-II upgrade required for the high luminosity LHC (HL-LHC) project. The HL-LHC will reach a higher instantaneous luminosity of $7.5\times10^{34}\,\mathrm{cm}^{-2}\mathrm{s}^{-1}$ and deliver an integrated luminosity of $3000\,\mathrm{fb}^{-1}$, thereby increasing the amount of collected data needed for precision measurements and to look for rare processes. The HL-LHC program is scheduled to start in 2027 and to operate at least for 10 years. Therefore the ATLAS sub-detectors will undergo several upgrades which will take place during the second long shut down (from 2019 to 2020) and the third long shut down (from 2024 to 2026). To cope with the new challenging environment, the LAr readout electronics will be replaced with new and more adapted electronics during the Phase-II upgrade. In the on-detector electronics, the signal coming from the detectors is amplified, shaped into a bipolar signal and sampled at 40 MHz rate. The signal is then sent to the off-detector electronics for further processing. The first on-detector elements are the signal analog pre-amplifiers. Two upgrade designs are proposed, LAUROC0 and HLC1. These prototypes should fulfill stringent requirements for the HL-LHC: a large dynamic range to measure energies up to 3 TeV, an excellent linearity (at the per-mill level) throughout the whole dynamic range and especially at low energies (the Higgs and W boson masses) for electroweak precision measurements, and an electronic noise lower than the MIP energy deposited by the muons and ideally not worse than the current electronics. The upgraded pre-amplifiers will have a two gain output system, replacing the current three gain system, with a gain ratio value that must fulfill conflicting requirements. The two proposed designs were tested on the same test bench to check if they match the requirements and identify what needs to be improved for the next prototype iterations to finally be able to decide on a single design for the upgrade.

The decay of the Higgs boson to pairs of b-quarks dominates the total Higgs decay width with

a branching fraction of ∼58% and has therefore a particular importance in the combination by driving the uncertainty of the total Higgs boson width. In addition, it allows the direct measurement of the coupling of the Higgs boson to down-type quarks. The most sensitive production mode for this measurement is the production of the Higgs boson alongside a vector boson (W or Z) when the vector boson decays to leptons, because of their very clean signature in the detector which allows to suppress QCD multi-jet background. Three different channels are studied, identified depending on the number of charged leptons in the final state and targeting the following decays: $Z(\to \nu\nu)H(\to b\bar{b})$, $W(\to l\nu)H(\to b\bar{b})$ and $Z(\to ll)H(\to b\bar{b})$, collectively referred to as $VH(H \to b\bar{b})$. The second research project presented in this thesis is the measurement of the $VH(H \to b\bar{b})$ process performed using $139\,\text{fb}^{-1}$ of data collected during Run-2 by the ATLAS detector at a center-of-mass energy of 13 TeV. The measurement is done using different event categories, defined depending on the number of jets in the final state and on the energy of the vector boson. The events are further split into signal regions and background-enriched control regions to better control the dominant backgrounds. Even though the VH production is the most sensitive mode to measure the $H \to b\bar{b}$ decay, the analysis remains complicated due to the large amount of backgrounds (S/B ratio is a few percents) and the complexity to control them, as well as the difficulty of estimating the associated systematic uncertainties. The analysis uses a multivariate method (MVA) to increase the sensitivity by constructing a BDT from different discriminant kinematic variables to have the best separation between the VH signal and the background processes. In addition to measuring the VH signal, the WH and ZH signals are measured independently and differential cross-section measurements are performed. Two cross-check and validation analyses are also considered: the di-jet mass analysis that uses the mass of the Higgs boson as a discriminant variable and the diboson analysis that measures the VZ process which is very similar to the Higgs boson (VH) process and can be measured with a higher sensitivity.

In this thesis my contributions to the ATLAS liquid argon calorimeter Phase-II upgrade and to the $VH(H \to b\bar{b})$ physics analysis are presented. The manuscript is divided as follows:

- Chapter 1 presents an overview of the theoretical context of the Standard Model as well as the Higgs mechanism and the measurements of the Higgs boson. It also presents the motivations for the measurements of the $VH(H \to b\bar{b})$ process.
- Chapter 2 is dedicated to the description of the LHC and to the ATLAS detector used to collect the data analysed in this thesis. This Chapter includes a description of the ATLAS sub-detectors and the different upgrades planned for the HL-LHC project.
- A description of the liquid argon calorimeter readout system and of the pre-amplifier prototypes proposed for the Phase-II upgrade are presented in Chapter 3. This Chapter presents the results of the characterisation study that I conducted to test if the two prototypes comply to the physics requirements and which led to changes in the design of the next iterations.
- A detailed description of the different methods used to reconstruct the physics objects using the signals collected by the different ATLAS sub-detectors is given in Chapter 4.
- Chapter 5 presents an overview of the $VH(H \to b\bar{b})$ analysis. I was a major contributor to the analysis of the 1-lepton channel that specifically targets the WH production. This Chapter describes the selection criteria for events to enter the analysis, including the study I performed to define the categorisation of the events into signal and control regions, harmonised across the three channels (i.e., not limited to the 1-lepton channel).
- The signal and background modelling in the $VH(H \to b\bar{b})$ analysis are discussed in Chapter 6. This is a critical aspect of the analysis, and in particular I worked on two cases which are presented in detail: the estimation of the multi-jet background and the associated uncertainties in the 1-lepton channel, and the estimation of the $t\bar{t}$ background shape

uncertainties using a multi-dimensional reweighting method based on boosted decision trees (BDTs).

- Finally Chapter 7 presents a description of the statistical analysis of data. The results of the $VH(H \to b\bar{b})$ analysis on the Run-2 dataset, to which I have contributed by studying the fit model and the robustness of the fit, are presented in this Chapter.

Chapter 1

The Standard Model of particle physics

The Standard Model (SM) is a theory developed in the early 1970's to describe the fundamental particles, the building blocks of matter in the universe, and their interactions. This model accurately explains the behavior of the elementary particles since the experimental observations have failed to disprove the theoretical predictions. However, it does not answer all physics questions: for example the neutrinos are described as massless particles in this model, but experiments have proven the opposite. Over time, the Standard Model has been tested in many experiments and as of today all the particles it contains have been observed, the first being the electron discovered in 1897 and the latest being the new particle observed by both the ATLAS [1] and CMS [2] experiments at the Large hadron Collider (LHC) which was found to be consistent with the Higgs boson. The Higgs boson is the representation of the Higgs field which is the source of the mass of all subatomic particles. After its discovery in 2012, it became an active research field at the LHC, from measuring its properties, its coupling to other particles and as a tool to explore physics beyond the Standard Model.

This chapter describes the Standard Model, starting with the elementary particles constituting the theory in Section 1.1 and the SM Lagrangian and the Higgs mechanism in Section 1.2. In Section 1.3, the production mechanisms and the decay channels of the Higgs boson at the LHC are described. Section 1.4 is dedicated to the search for the Higgs boson, its discovery and the latest Higgs boson measurements results. In this Chapter, the measurements of its decay to a pair of b-quarks in the vector boson associated production mode is presented as well, which is an introduction to the analysis work presented in this thesis. Section 1.5 describes the limitations of the Standard Model and the open questions in high energy physics. In Section 1.6, the methods to interpret the measurements in the Higgs sector and to test the compatibility of the experimental results with the Standard Model are presented.

1.1 The fundamental particles

The particles in the Standard Model can be categorised into two types: the fermions with half integer spin and the bosons with an integer spin. Fermions are fundamental particles that make up matter and can interact under four fundamental forces: the strong force responsible for keeping the quarks inside hadrons and the neutrons and the protons confined inside the nucleus, the weak force leading to radioactive decays like the β decay and the electromagnetic force that describes the interactions between charged particles. The last of the four forces is gravity which

is negligible at the subatomic scale and is not included in the Standard Model description. The gauge bosons are called force mediators, since the fermions interact by exchanging a boson. The fermions can be either leptons or quarks that carry a color charge. They are divided into three generations, having the same properties (electrical charge, spin, leptonic number and baryonic number) but different masses, where the particles of the first generation have the smallest masses and the particles in the third generation have the largest masses.

There are six types of quarks called flavors having either a positive or a negative electrical charge: +2/3 for up (u), charm (c), and top (t) quarks and -1/3 for down (d), strange (s) and bottom (b) quarks. They have a charge color which can be either red, green or blue (or their anti-colors). The quarks are the only particles in the Standard Model that interact through all the three fundamental interactions. These particles are predicted to not be directly observable due to the color confinement, so quarks through the strong force gather together to form hadrons. These hadrons are composed of valence quarks and a sea of (anti-)quarks and gluons, and can be mesons composed of two valence quark and anti-quark or baryons made of three valence quarks. Observations have indicated the existence of more complex hadrons called tetraquarks and pentaquarks, made of 4 and 5 valence quarks respectively. Table 1.1 summarises the measured properties of quarks.

Generation	Flavor	Electric charge	Mass
First	up	+2/3	$2.2^{+0.5}_{-0.4}$ [MeV]
	down	-1/3	$4.7^{+0.5}_{-0.3}$ [MeV]
Second	charm	+2/3	$1.275^{+0.025}_{-0.035}$ [GeV]
	strange	-1/3	93^{+9}_{-3} [MeV]
Third	top	+2/3	$173.0^{+0.4}_{-0.4}$ [GeV]
	bottom	-1/3	$4.18^{+0.04}_{-0.03}$ [GeV]

Table 1.1 – Summary of the properties of the quarks [3].

For leptons, each of the three generations includes a pair of two leptons, one with a negative charge of -1 and the other a neutrally charged particle called the neutrino (ν). The first generation is formed by the electron (e) and by the electronic neutrino, the second generation is composed by the muon (μ) and the muonic neutrino, while the tau (τ) and the tau neutrino are in the third generation. Since neutrinos do not carry an electric charge they can only interact via the weak interaction whilst the charged leptons interact in addition via the electromagnetic force. Neutrino oscillations [4], which is a phenomenon observed experimentally where a neutrino created initially with a certain leptonic flavor can oscillate and change into another leptonic flavor, prove that the mass of at least neutrinos is non-zero contrary to what the Standard Model predicts. These oscillations occur from a mixing between the neutrino flavor eigenstates and the so called neutrino mass eigenstates, where each flavor eigenstates is the superposition of three mass eigenstates: the neutrinos propagate through space in their mass eigenstates, whereas interact with other particles as flavor eigenstates. Neutrino oscillations allow to measure the squared mass difference and as of today, these mass eigenstates have not been yet measured individually. Properties of the leptons are detailed in Table 1.2.

The carriers of the forces are bosons, known as gauge bosons, and have a spin equal to one. A different type of boson mediates each of the interactions: the photons (γ) are mediators of the electromagnetic force, the $W^{\pm}$ and Z bosons are the force carriers of the weak interaction and finally gluons (g) carry the strong force. A scalar boson is a type of boson with a spin equal to 0. The Higgs boson is the only elementary scalar boson that has been observed experimentally. This boson is the experimental expression of the Higgs mechanism which provides mass to all particles and Section 1.2.2 is dedicated to explain this mechanism. A summary of the main

Generation	Lepton	Electric charge	Mass
First	e	-1	0.51 ± 0.00 [MeV]
	ν_e	0	< 2.2 [eV]
Second	μ	-1	105.66 ± 0.00 [MeV]
	ν_μ	0	< 0.19 [MeV]
Third	τ	-1	1776.86 ± 0.12 [MeV]
	ν_τ	0	< 18.2 [MeV]

Table 1.2 – Summary of the properties of the leptons [3].

properties of the bosons can be found in Table 1.3 .

Interaction	Boson	Spin	Electric charge	Mass
electromagnetic	Photon (γ)	1	0	$< 1\times10^{-18}$ [eV]
Weak	W	1	-1	80.38 ± 0.01 [GeV]
	Z	1	0	91.188 ± 0.002 [GeV]
Strong	g	1	0	0
	Higgs	0	0	125.18 ± 0.16 [GeV]

Table 1.3 – Summary of the properties of the bosons [3].

1.2 Mathematical description of the Standard Model

1.2.1 The Gauge Lagrangian

The Standard Model is a Quantum Field Theory (QFT) that describes the electromagnetic, weak and strong interactions of the particles with a local gauge symmetry $SU(3)_C \otimes SU(2)_L \otimes U(1)_Y$. $SU(3)_C$ is for the strong interaction with C being the color charge. The electroweak (EW) [5] theory describes the combination of the electromagnetic and weak interactions based on the local gauge symmetry $SU(2)_L \otimes U(1)_Y$ where L denoted the isospin and Y the hypercharge. These two quantities are related to the electric charge Q of the fermion as described in the Gell-Mann-Nishijima formula [6, 7], where I_3 is the third component of the isospin, as follows:

$$Q = \frac{Y}{2} + I_3 \tag{1.1}$$

The Lagrangian allows to give a mathematical formulation of the behavior of particles and their interactions. The Lagrangian of a free Dirac fermion can be written as follows:

$$\mathcal{L}_{free} = \bar{\psi}(i\gamma^\mu \partial_\mu - m)\psi \tag{1.2}$$

Where ψ is the Dirac spinor that denotes a fermionic field, γ^μ are the Dirac matrices and m is the mass of the fermion. The first term is the kinematic term and the second is the mass term. The Quantum Electro-Dynamic (QED) Lagrangian representing the interaction between a particle of spin 1/2 and the electromagnetic field should be invariant under a $U(1)$ gauge transformation, a rotation as an example:

$$\psi(x) \rightarrow \psi(x)' = e^{i\alpha(x)}\psi(x) \tag{1.3}$$

With $\alpha(x)$ being an arbitrary real function and x is the 4-dimensional phase-space components. Since the Lagrangian in Equation 1.2 is not invariant under this transformation, a recovering term is needed to restore this invariance, and thus a covariant derivative is introduced:

$$D_\mu = \partial_\mu - ieA_\mu \tag{1.4}$$

A new field of a spin 1 particle comes into play as shown:

$$A_\mu \to A'_\mu = A_\mu + \frac{1}{e}\partial_\mu \alpha(x) \tag{1.5}$$

The complete QED Lagrangian can therefore be written as follows:

$$\mathcal{L}_{QED} = \bar{\psi}(i\gamma^\mu \partial_\mu - m)\psi - \frac{1}{4}F_{\mu\nu}F^{\mu\nu} - eA_\mu \bar{\psi}\gamma^\mu \psi \tag{1.6}$$

where $F_{\mu\nu}F^{\mu\nu}$ is the electromagnetic (EM) field tensor and can be expressed as $\partial_\mu A_\nu - \partial_\nu A_\mu$, e is the electric charge of the fermion and A_μ is the EM field 4-vector. The first additional term to the free fermion Lagrangian represents a free electromagnetic field, while the second term describes the interaction between the EM carrier, the photon, and the fermionic field.

The electromagnetic and weak forces are unified by the electroweak (EW) theory. This gives rise to the EW fields, 3 associated to $SU_L(2)$ symmetry: W^1, W^2, W^3 and one associated to $U_Y(1)$: B. The 4 bosons carriers of the EW interaction, W^+, W^-, Z and γ described in Section 1.1 are expressed as function of these fields as follows:

$$\begin{aligned} W^\pm_\mu &= \frac{1}{\sqrt{2}}(W^1_\mu \mp iW^2_\mu) \\ Z_\mu &= W^3_\mu cos\theta_W - B_\mu sin\theta_W \\ A_\mu &= W^3_\mu sin\theta_W + B_\mu cos\theta_W \end{aligned} \tag{1.7}$$

with θ_W being the Weinberg angle (or the weak mixing angle) establishes the connection between the mass of the W and Z bosons and allows for a mixing between the Z and A fields. It can be expressed as function of g and g' which are the coupling constants of $SU_L(2)$ and $U_Y(1)$ respectively:

$$\cos\theta_W = \frac{g}{\sqrt{g^2 + g^{2'}}};\ \sin\theta_W = \frac{g'}{\sqrt{g^2 + g^{2'}}} \tag{1.8}$$

the electrical charge e can also be written as function as the mixing angle as:

$$e = g\sin\theta_W = g'\cos\theta_W \tag{1.9}$$

Both the leptons and quarks behave similarly under the $SU_L(2)$ and $U_Y(1)$ transformations since the color charge does not operate under these transformations. The particles operating under $SU_L(2)$ are left-handed (L) isospin particles. For leptons, the left-handed electron is put together with the left handed neutrino in a doublet while for the quarks the up and down quarks form together a doublet. The EW Lagrangian describing the interaction between the fermions and the four EW fields can be written as follows:

$$\mathcal{L}_{EW} = i\bar{\psi}_L\gamma^\mu D_\mu \psi_L + i\bar{\psi}_R\gamma^\mu D_\mu \psi_R - \frac{1}{4}W^a_{\mu\nu}W^{\mu\nu}_a - \frac{1}{4}B^a_{\mu\nu}B^{\mu\nu}_a \tag{1.10}$$

The left-handed fermionic field corresponds to the doublets described above, while the right-handed fields correspond to the right-handed up and down singlets in addition to the right-handed singlet electron. The covariant derivative introduced in the EW Lagrangian contains both the W and B fields.

The second part of the gauge theory is Quantum Chromodynamics (QCD) [8]. It is a non-abelian theory that describes the interactions of quarks and gluons based on the local gauge symmetry of $SU(3)_C$. It describes these interactions assuming that each of the quark fields carries a flavor and a color charge. The gauge covariant derivative can be expressed in terms of the coupling constant of $SU(3)$ g_s, the gluon gauge field G_μ and the Gell-Mann matrices λ as follows:

$$D_\mu = \partial_\mu - \frac{1}{2} i g_s \sum_{a=1}^{8} \lambda_a G_\mu^a \tag{1.11}$$

The index a (and later b and c) represents the 8 required colors of the gluon fields and f^{abc} is the structure constant of the $SU(3)$ color group. The QCD Lagrangian can be written as function of $G^a_{\mu\nu} = \partial_\mu G^a_\nu - \partial_\nu G^a_\mu + g_s f^{abc} G^b_\mu G^c_\nu$ which is the needed kinematic term introduced to obtain a gauge invariant gluon field:

$$\mathcal{L}_{QCD} = \bar{\psi}_i (i(\gamma^\mu D_\mu)_{i,j} - m\delta_{i,j})\psi_j - \frac{1}{4} G^a_{\mu\nu} G_a^{\mu\nu} \tag{1.12}$$

The QCD theory has two consequences on the behavior of quarks. The first called the asymptotic freedom, where the strength of the coupling of quarks to gluons g_s, scales with the energy under the renormalisation theory: the quark-gluon coupling decreases as the energy scale of the interaction increases. This means that at low energy, the coupling constant becomes so large and the QCD enters a non-perturbative regime. This has consequences on the simulation of hadronic Monte Carlo processes as presented later in Section 2.2.9. The second consequence is the color confinement because only colorless physical objects can be observed, the reason why elementary quarks cannot be isolated so they gather together to form colorless hadrons.

1.2.2 The Higgs mechanism

The Standard Model theory detailed above describes all bosons as massless particles. Experiments have shown that both the W [9] and Z [10] are not massless particles, unlike the photon and the gluon. To be able to represent these masses in the Lagrangian a mass term cannot be just added as the local gauge symmetry will no longer be conserved. For that reason a theory was developed of spontaneous electroweak symmetry breaking in the 1964 by François Englert and Robert Brout [11] and by Peter Higgs [12] to explain the origin of mass of the electroweak bosons, resulting in the Brout-Englert-Higgs (BEH) mechanism. This mechanism predicts the existence of a new particle called the Higgs boson, which has later been observed in 2012 to confirm the theory.

This theory postulated that the EW symmetry can be broken by introducing a new complex scalar field ϕ, the Higgs boson field. The following Higgs Lagrangian can be added to the gauge Lagrangian described in Section 1.2.1 to describe the electroweak symmetry breaking:

$$\mathcal{L}_{Higgs} = (D^\mu \phi)^\dagger (D_\mu \phi) - V(\phi) \tag{1.13}$$

The Higgs potential $V(\phi)$ is expressed as function of the mass term μ and a real coupling constant

λ as:

$$V(\phi) = \mu^2 \phi^\dagger \phi + \lambda(\phi^\dagger \phi)^2 \tag{1.14}$$

The spontaneous symmetry breaking arises from the vacuum expected value (VEV) of the Higgs field at the minimum of the potential. This value should not be equal to 0 which happens when $\mu^2 > 0$. In the other case when $\mu^2 < 0$, the vacuum expected value can have two values: $v = \pm\sqrt{\frac{\mu^2}{\lambda}}$. The Higgs potential is illustrated in Figure 1.1 in the case of $\mu^2 < 0$.

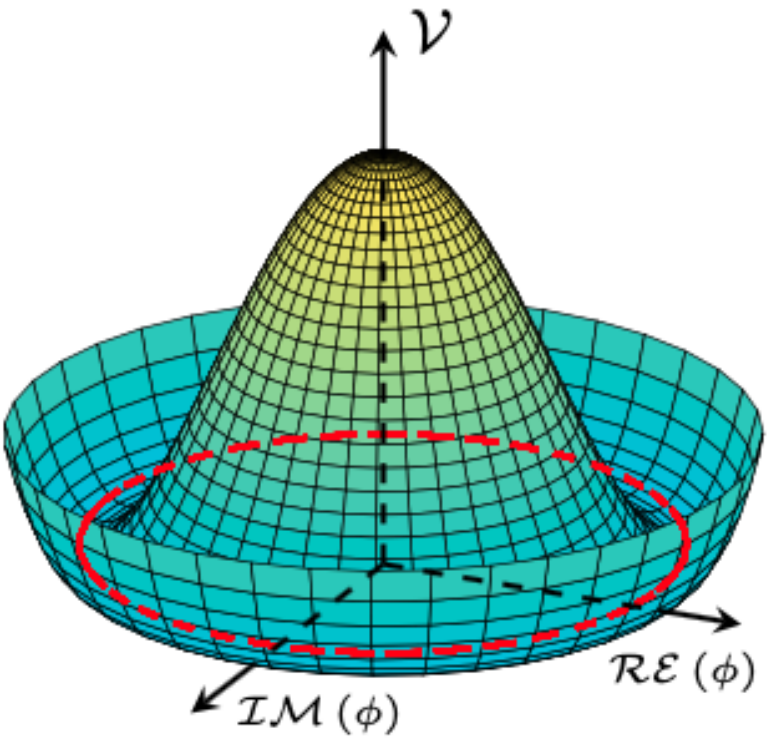

Figure 1.1 – Illustration of the Higgs potential in the SM. The spontaneous symmetry breaking arises from the vacuum value at the minimum of the potential, which occurs for $\phi \neq 0$ along the red line.

The Higgs complex scalar field acting under $SU_L(2)$ transformation can be expressed in terms of a doublet with 4 degrees of freedom. When the symmetry is spontaneously broken, only one degree of freedom remains corresponding to one of the multiple ground states, expressed in terms of the vacuum expected value as shown in the following expression, where $h(x)$ is a real scalar field:

$$\phi_0 = \frac{1}{\sqrt{2}} \begin{pmatrix} 0 \\ v \end{pmatrix} \rightarrow \phi(x) = \frac{1}{\sqrt{2}} \begin{pmatrix} 0 \\ v + h(x) \end{pmatrix} \tag{1.15}$$

The physical masses of the gauge bosons can be expressed using 3 of the degrees of freedom of the scalar field while the remaining one corresponds to the Higgs boson. On the other, since the local QED $U(1)$ gauge symmetry should not be violated, the photon is required to be massless. The masses of the gauge bosons are given as function of the vacuum expected value and as a

function of the $SU(2)$ and $U(1)$ coupling constants as follows:

$$\begin{aligned} m_{W^{\pm}} &= \frac{1}{2}gv, \\ m_Z &= \frac{1}{2}v(g^2 + g'^2)^{\frac{1}{2}} = \frac{m_W}{cos_{\theta_W}}, \\ m_{Higgs} &= v\sqrt{2\lambda} \end{aligned} \tag{1.16}$$

Fermion masses were introduced to the Standard Model as a completely separate term corresponding to the Yukawa term. The Yukawa term represents the coupling between the Higgs field and the fermions represented by the Dirac fields (Yukawa interaction) and is introduced as an additional term while preserving the local symmetry. Fermions acquire their masses from the Higgs field as a consequence of the spontaneous symmetry breaking. The fermion mass is proportional to the coupling constant with the Higgs boson λ_f and the vacuum expected value which is measured to be 246 GeV [13] as follows:

$$m_f = \frac{\lambda_f v}{\sqrt{2}} \tag{1.17}$$

Measuring the mass of the top quark with precision is important, as this value has a direct impact on the Yukawa coupling, and thus on the production rate of Higgs boson in the top quark associated production mode described below.

1.3 The Higgs boson at the LHC

The search for the Higgs boson was conducted with large colliders operating at high energies such as the Large Electon-Positron collider (LEP), the Tevatron and the Large Hadron Collider (LHC). It is at the LHC that this particle was first observed and its mass was measured to be around 125 GeV. At the LHC, proton beams are accelerated at an energy up to 6.5 TeV allowing the quarks and gluons inside the proton to interact together and produce the Higgs boson. Since the mean lifetime of the Higgs boson is of the order of 10^{-22} seconds, it cannot be observed directly inside the detector, the reason why only the resulting decay states can be detected and studied.

1.3.1 Production modes of the Higgs boson

At the LHC, there are four main production modes of the Higgs boson coming from p-p collisions. The cross-section of each of these modes as a function of centre-of-mass for the Higgs boson mass of 125 GeV is shown in Figure 1.3. These mechanisms are:

- **Gluon fusion (ggF)** is the dominant production mechanism at the LHC (85%) due to the high density of gluons inside the high-energy protons. This mode is one order of magnitude larger than the second main production mode. Since gluons do not couple directly to the Higgs boson, this mode occurs through a loop of heavy quarks (mainly top and bottom quarks) since the Higgs-quark coupling strength is proportional to the mass of the quark.
- **Vector boson fusion (VBF)** is the second most important mode (7%). Through this mode two quarks each will radiate a vector boson (W or Z) that will then fuse together to produce the Higgs boson. The final state consists of the Higgs boson alongside two quarks in the forward or backward direction.

- **Vector Boson Associated Production (VH)** also know as Higgs-Strahlung (4%). In this process mainly two quarks interact to produce an off-shell vector boson which then radiates the Higgs boson. The Higgs boson is produced together with either a W or Z boson. Even though it is not the dominant mode of production it is still a very unique mechanism since the vector boson can decay leptonically which makes it easy to trigger on such process.
- **Top quark Associated Production (ttH)** is two orders of magnitude smaller than ggF (1%). Through this mode two gluons each create a pair of top quarks ($t\bar{t}$), two of which then couple to produce the Higgs boson. The final state includes a Higgs boson in addition to two top quarks that produce very busy final states, making the search of the Higgs in this mode difficult. But this mode is of great importance since it allows to measure directly the Higgs coupling to the top quark.

Feynman diagrams illustrative of the highest order processes of each production mechanism are shown in Figure 1.2.

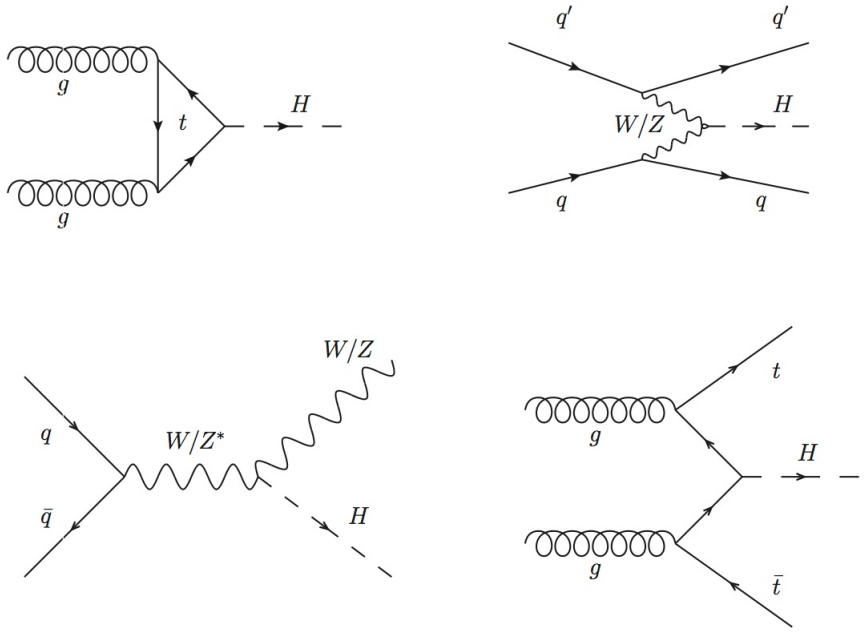

Figure 1.2 – The Feynman diagrams of the four main production modes of the Higgs boson at the LHC: gluon fusion, vector boson fusion, vector boson associate production (Higgs-Strahlung) and the top quark associate production.

1.3.2 Higgs boson decay channels

The Higgs boson has a short lifetime and can decay to a set of lighter particles. Since the Higgs-fermion coupling is directly proportional to the mass of the fermion, it is more likely to decay to heavy fermions. The branching ratio of the different decay channels of the Higgs boson can be found as function as its mass in Figure 1.4. The decay can be to either fermions or bosons:

- The fermionic decay channels give a pair of fermion and anti-fermion. The one with the highest branching ratio is the Higgs decaying to a pair of bottom quarks ($H \to b\bar{b}$) which represents 58% of all decays. Then comes the decay to a pair of taus ($H \to \tau^+\tau^-$) and to a pair of charm quarks ($H \to c\bar{c}$) with branching ratios of 6.3% and 2.9% respectively.

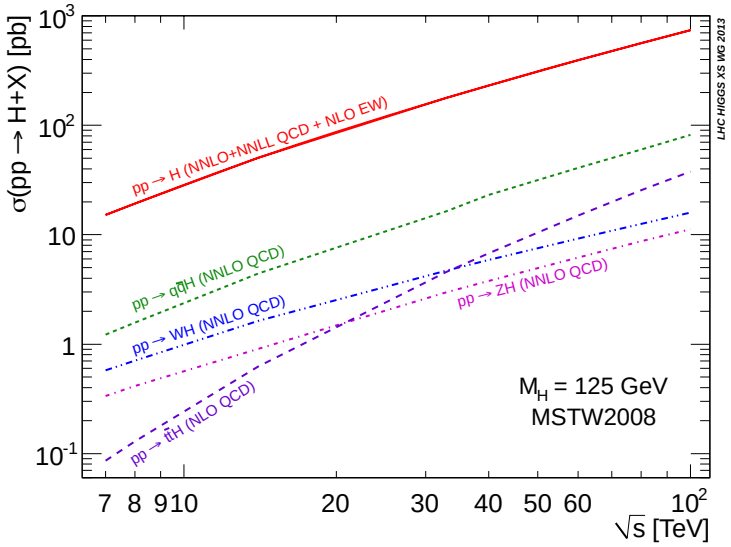

Figure 1.3 – Cross-sections of the different production modes of the SM Higgs boson as a function of centre-of-mass energies ($\sqrt{s}$) for a Higgs boson mass (m_H) of 125 GeV [14].

The branching ratio of the decay to a pair of muons ($H \to \mu\mu$) or to a pair of any of the remaining quarks is small since these particles are very light and represent all together 0.02% of the total decay.

- Another mode of decay is to a pair of bosons. The second largest decay channel is of 21.4% and corresponds to the decay of the Higgs boson to two W bosons ($H \to W^+W^-$), which then decay to leptons or quarks. By the same process it can also decay to Z bosons ($H \to ZZ$) with a branching ratio of 2.6%. The Higgs boson can decay to $\gamma\gamma$ and gg through loops of heavy quarks or bosons, and these two modes have a branching ratios of 0.23% and 8.2% respectively. Last, the decay channel to bosons with the smallest branching ratio (0.15%) is the decay to a Z boson and a photon ($H \to Z\gamma$).

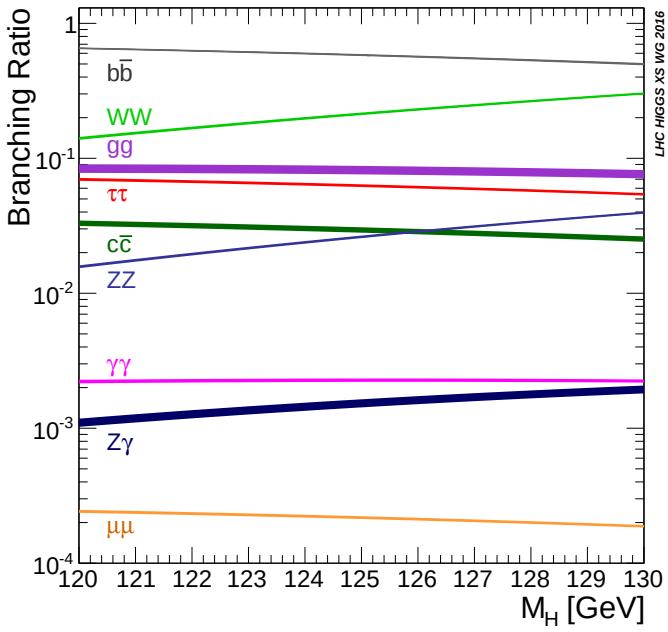

Figure 1.4 – The Branching ratios of the SM Higgs boson decays around 125 GeV [15].

1.4 Higgs boson measurements

The quest for the Standard Model Higgs boson has been a major research topic at particle colliders in the past three decades. Since the mass of the Higgs boson is a free parameter in the Standard Model, the search for this particle was done in different energy ranges up to the TeV energy scale. Prior to the discovery at the LHC, measurements at the LEP and Tevatron colliders allowed to put constraints on the mass of the Higgs boson and provided directions where to search for this particle. The discovery of this particle was a major milestone and the last building block of the Standard Model. Searches have continued to measure its coupling to other particles to test any deviation from Standard Model predictions.

1.4.1 Experimental searches for the Higgs boson before the LHC

The Large Electron-Positron collider, or LEP, was the first collider to put constraints on the mass of the Higgs boson. This e^+-e^- collider operated until 2000 with an energy up to 210 GeV and was installed in the same tunnel as the LHC. The experiments at LEP allowed to put a lower bound for the Higgs mass at 114.4 GeV with 95% confidence level (CL) [16]. The dominant mode of production for such a Higgs boson mass was through the Higgs-Strahlung mode: $e^+e^- \to Z^* \to ZH$. Figure 1.5 shows the LEP limits on the Higgs boson mass.

After the LEP shut down, the search for the Higgs boson continued at the Tevatron. The Tevatron was a p-$\bar{p}$ collider installed in Fermilab that operated until 2011 at a center-of-mass energy of about 2 TeV. The CDF and DØ experiments were able to put limits on the mass of Higgs boson by exploring many decay channels led by $H \to b\bar{b}$ and $H \to WW$. Results using data collected during Run-1 and combined with results from LEP, from W boson and top quark mass measurements allowed to put an upper limit on the mass of the Higgs boson at 193 GeV [17]. Using data collected during Run-2 the upper limit was narrowed to 144 GeV. Considering only the $H \to b\bar{b}$ decay, the first evidence at the Tevatron corresponded to an excess of 2.8 standard deviation (σ) for a Higgs boson mass of 125 GeV [18]. Later, the signal strength, which is ratio of the measured signal yield over the expected signal yield, was measured to be ∼1.6 times the Standard Model predictions in this channel [19]. Furthermore, the mass range between 156 GeV and 177 GeV was excluded at 95% confidence level. Figure 1.6 shows the results at the Tevatron using data collected during Run-2.

1.4.2 Observation in the data of the first Run of the LHC

After the direct measurements from the LEP and Tevatron experiments, results from the first run of the LHC at a center-of-mass of 7 TeV corresponding to an integrated luminosity of 4.6-4.9 fb^{-1} (ATLAS) and 4.6-4.8 fb^{-1} (CMS), have allowed to exclude the existence of the Higgs boson in the following ranges: 111.4-116.6 GeV, 119.4-122.1 GeV and 129.2-541 GeV by ATLAS [21] and 127-600 GeV by CMS [22]. The search continued until the announcement in 2012 of the observation of a new particle corresponding to the Standard Model Higgs boson at the LHC, using data collected from p-p collisions at a center-of-mass energy of $\sqrt{s} = 7$ and 8 TeV, corresponding to an integrated luminosity of 11 fb^{-1} (ATLAS [1]) and 10 fb^{-1} (CMS [2]).

The observation by the ATLAS [1] detector was obtained by combining the 2 most sensitive modes $H \to ZZ \to 4l$ and $H \to \gamma\gamma$ with 3 other channels: $H \to W^+W^- \to e\nu_e\mu\nu_\mu$ and both $H \to \tau^+\tau^-$ and $VH, H \to b\bar{b}$ using only the dataset collected at 7 TeV. Figure 1.7 shows the invariant mass of the $4l$ channel where the four leptons should be a pair of either electrons or muons with opposite electrical charges. The results of the combination allowed to exclude the Higgs mass regions of 111-122 GeV and 131-559 GeV with 95% CL. In addition an excess of

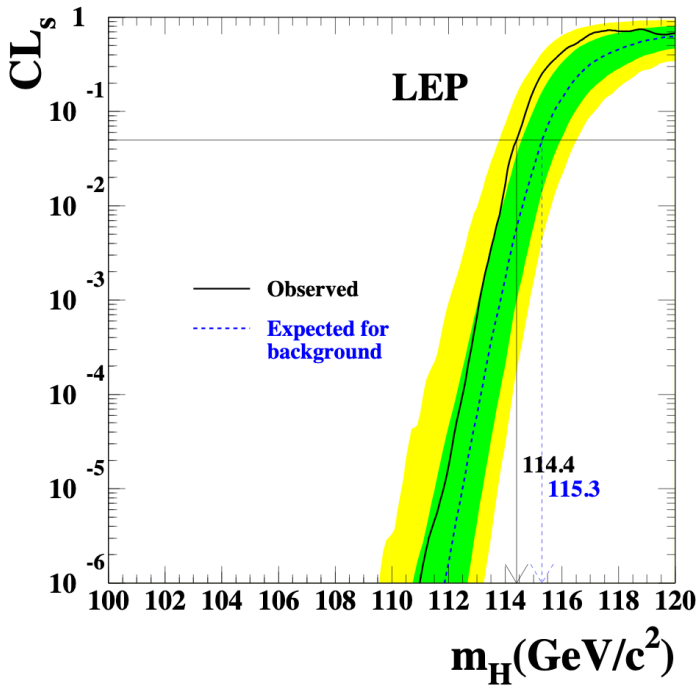

Figure 1.5 – The observed and expected ratio $CL_s = CL_{s+b}/CL_b$ which is the signal confidence level as function of the Higgs of the Higgs boson mass at the LEP [20].

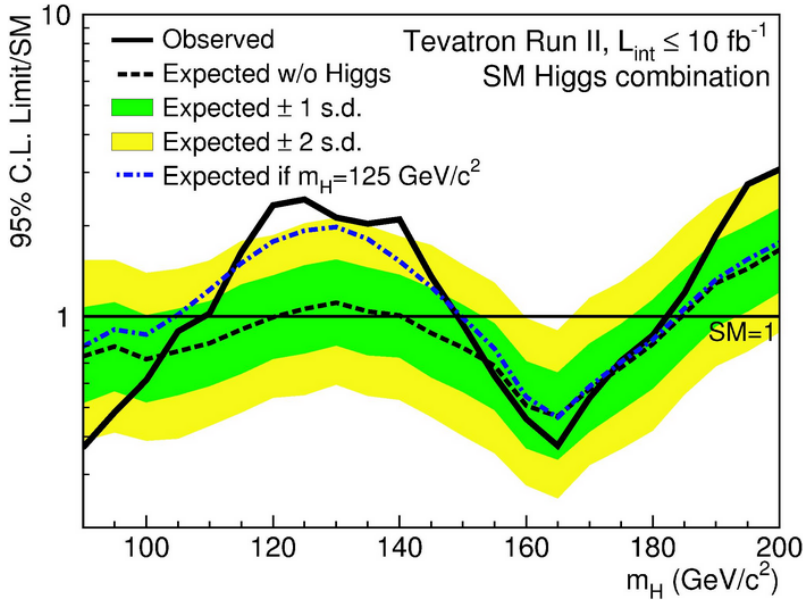

Figure 1.6 – Observed and expected upper limits at 95% CL of the ratio of the cross-section to the standard model cross-section as function of the Higgs boson mass at the Tevatron, using the full luminosity [19].

events over the expected background was observed in the two most sensitive modes, showing the existence of new particle compatible with the Standard Model Higgs boson with a mass of 126.0 ± 0.4 (Stat) $\pm$ 0.4 (Syst) GeV with a significance of 5.9σ, proving the compatibility of the measurement with the Standard Model prediction within uncertainties.

Results from CMS [2] were obtained from combining the same five channels using the full dataset. An excess of signal events over background was observed with a local significance of 5.0σ. A fit in the two most sensitive channels, $\gamma\gamma$ and ZZ, allowed to measure the mass of the new

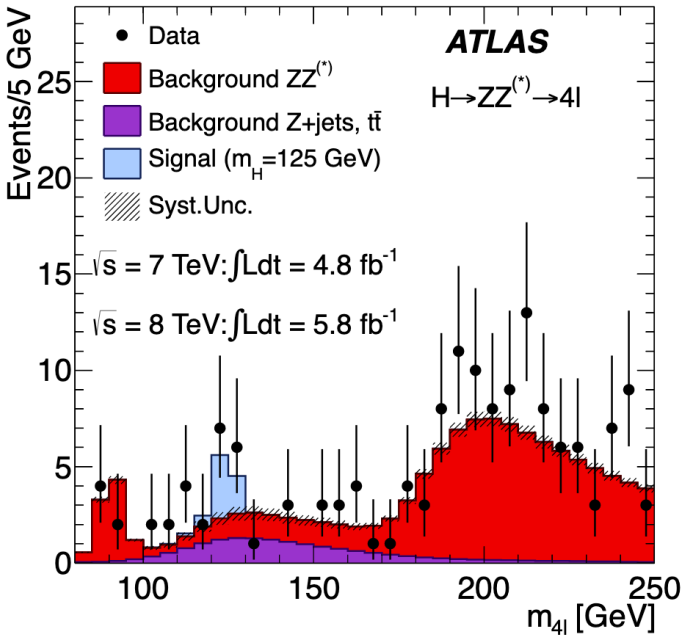

Figure 1.7 – Distribution of the invariant mass of the four leptons candidates. The Higgs boson signal and the background are shown in the mass range 80-250 GeV in the analysis of 10.6 fb^{-1} of ATLAS data at 7 and 8 TeV [1].

discovered particle to be 125.3 ± 0.4 (Stat) ±0.5 (Syst) GeV. Figure 1.8 shows the invariant mass in the diphoton mode.

The Run-1 data for the $H \to \gamma\gamma$ and $H \to ZZ \to 4l$ channels from the ATLAS and CMS experiment were combined to give a more precise measurement of the mass of the Higgs boson, which was found to be $m_H = 125.09 \pm 0.24\,\text{GeV} = 125.09 \pm 0.21\ (\text{Stat}) \pm 0.11\ (\text{Syst})\,\text{GeV}$ [23].

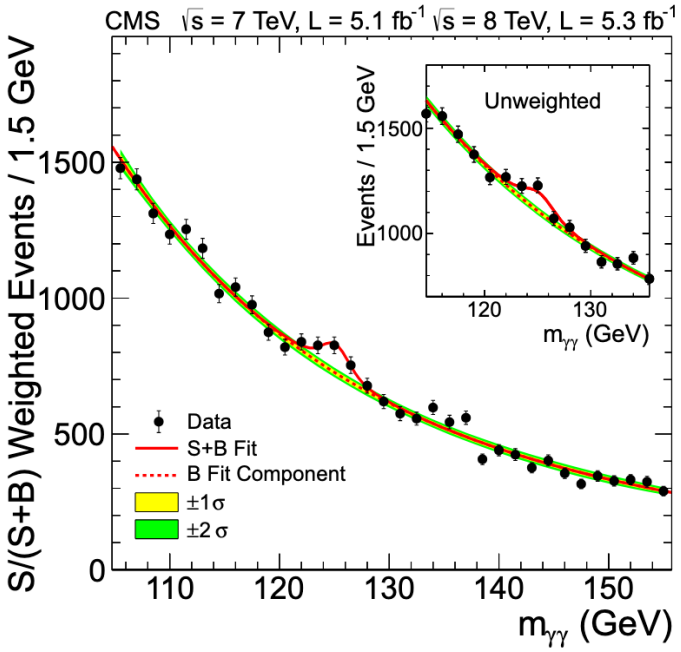

Figure 1.8 – Distribution of the diphoton invariant mass showing the background fit and the signal+background fit around 125 GeV in the analysis of 10.4 fb^{-1} of CMS data at 7 and 8 TeV [2].

1.4.3 Search for the $VH(H \to b\bar{b})$ process

The Standard Model Higgs boson decay into a $b\bar{b}$ pair has the largest branching ratio (0.58). This channel is interesting to study because it allows to directly measure the coupling of the Higgs boson to b-quarks, which is the only coupling to a down-type quark that is accessible at the LHC. Since a large amount of b-jets are produced from p-p collisions this mode is overwhelmed by background events, the reason why the search for this decay in associated production modes is of interest. The gluon fusion mode is the dominant mechanism and is submerged by $gg \to b\bar{b}$ background events by a factor of 10^7. The boosted regime of this mode is a subject of searches at the LHC, corresponding to the production of a boosted Higgs boson in association with a jet with high transverse momentum (p_T) coming from initial state radiation (ISR) [24, 25]. In the VBF mode, the Higgs boson is produced alongside 2 jets, making a total of 4 jets in the final state where 2 jets are produced in the forward direction and the other two in the central part of the detector [26, 27]. In this mode an additional photon can be produced from one of the vector bosons alongside the jets, which can be of use to suppress QCD multi-jet background [28, 29]. The ttH mode is very interesting since not only it allows a direct measurement of the coupling to top quarks but also because the coupling to the top quark is sensitive to effects of physics beyond the Standard Model [30, 31]. This mode is very challenging since it is overwhelmed by $ttbb$ background events and because it is difficult to identify the $b-$jets coming from the Higgs decays from the ones coming from the top quark decays. Finally, the VH mode is the most sensitive mode since the vector boson can decay leptonically leaving a clean signature in the detector which makes it easy to trigger on such events and reject multi-jet background events.

The main contribution to the production of $VH(H \to b\bar{b})$ events comes from $qq \to VH$ process with a smaller contribution from $gg \to ZH$ process ($\sim$10%). The analysis focuses on the vector boson (Z/W) produced in association with the Higgs boson when the Z boson decays to either a pair of charged leptons with opposite charges or a pair of neutrinos, or when the W boson decays to a pair of a lepton and its neutrino. A WH charge asymmetry in p-p collisions is expected because W^+H has a cross-section larger than W^-H in p-p collisions. The cross-sections of these processes and their uncertainties are summarized in Table 1.4.

	σ (fb)	QCD Scale (%)	PDF + α_s (%)
$pp \to W^+(\to l^+\nu)H$	94.26	$^{+0.5}_{-0.7}$	$\pm$1.8
$pp \to W^-(\to l^-\nu)H$	59.83	$^{+0.4}_{-0.7}$	$\pm$2.0
$pp \to Z(\to l^+l^-)H$	29.82 (4.14 from $ggZH$)	$^{+3.8}_{-3.1}$	$\pm$1.6
$pp \to Z(\to \nu\bar{\nu})H$	177.62 (24.57 from $ggZH$)	$^{+3.8}_{-3.1}$	$\pm$1.6

Table 1.4 – WH and ZH cross-sections for each of the leptons generations (where l is either e, μ or τ) and summed over three neutrino generations, with QCD scale and PDF $+\alpha_s$ uncertainties at a center-of-mass energy of 13 TeV and a Higgs mass of 125 GeV [15].

As already discussed in Section 1.4.1, the search for the $VH(H \to b\bar{b})$ process started with the CDF and DØ experiments at the Tevatron. The first evidence at the LHC was obtained using data collected at a center-of-mass energy of 13 TeV corresponding to an integrated luminosity of 36.1 fb^{-1} (ATLAS) and 35.9 fb^{-1} (CMS), where ATLAS [32] observed an excess of events with a significance of 3.5σ (expected 3.0σ) at 125 GeV and measured a signal strength, which is the ratio of the measured signal events to the Standard Model prediction, of $\mu = 1.20 \pm 0.38$. The CMS experiment [33] observed an excess with a significance of 3.3σ (expected 2.8σ) and $\mu = 1.20 \pm 0.40$.

In the summer of 2018, ATLAS [34] and CMS [35] observed the Higgs boson decaying to bottom quarks using data up to 80 fb^{-1} collected during Run-1 and Run-2. The observation was possible by combining $H \to b\bar{b}$ searches targeting the VH, $t\bar{t}H$ and VBF production modes. ATLAS

reported an observed significance of 5.4σ (expected 5.5σ) with $\mu = 1.01 \pm 0.20$ and CMS reported an observed significance of 5.6σ (expected 5.5σ) with $\mu = 1.04 \pm 0.20$ as shown in Figure 1.9. In addition, a combination of the $b\bar{b}$, $4l$ and $\gamma\gamma$ channels using Run-2 data collected by the ATLAS detector yielded the observation of the VH production mode with a significance of 5.3σ (expected 4.8σ) with $\mu = 1.13 \pm 0.24$ as shown in Figure 1.10.

The $VH(H \to b\bar{b})$ analysis presented in this thesis is a follow up analysis, that uses the full dataset collected by the ATLAS detector during Run-2 and improved analysis techniques to make precision measurements in this channel.

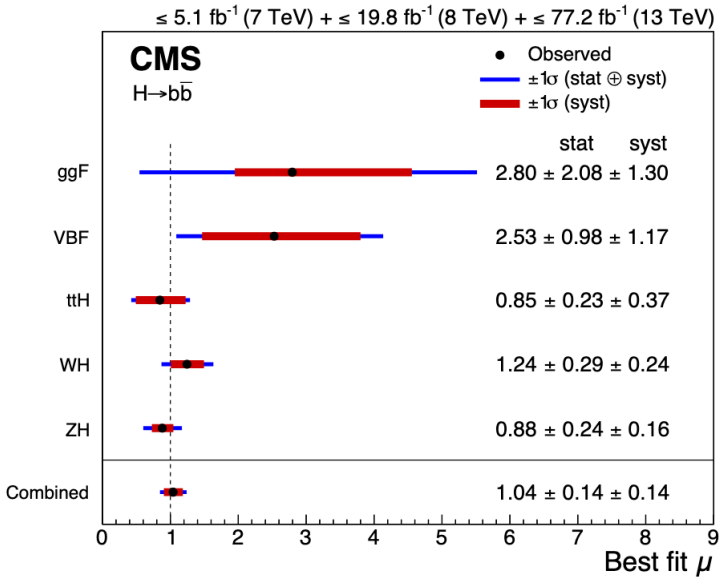

Figure 1.9 – The fitted value of the Higgs boson signal strength in the $H \to b\bar{b}$ decay for the five production modes separately along with their combination for a mass of 125 GeV. All results are extracted from a single fit combining all input analyses with the CMS experiment [35].

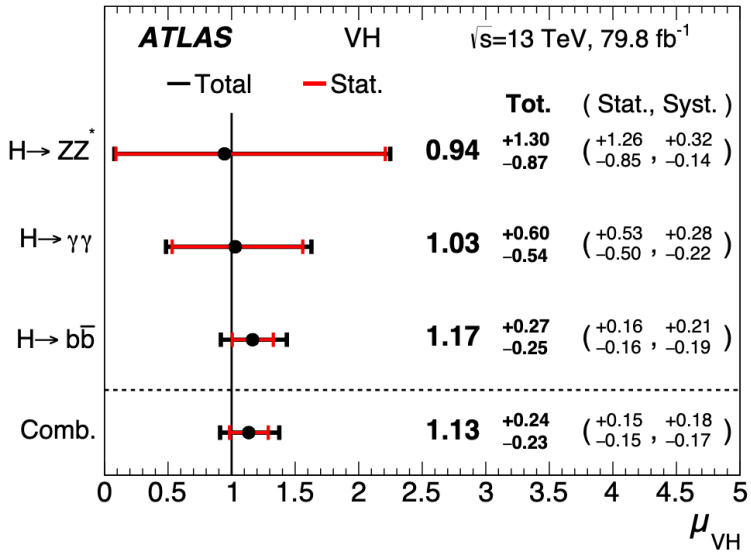

Figure 1.10 – The fitted value of the Higgs boson signal strength in the VH production mode for $H \to b\bar{b}$, $H \to \gamma\gamma$ and $H \to 4l$ decay channels separately and their combination for a mass of 125 GeV. The individual μ values of the three processes are obtained from a simultaneous fit with the ATLAS experiment [34].

1.4.4 State of the art of the Higgs boson measurements

The Higgs boson search at the LHC is led by ATLAS and CMS operating separately. The measurements from different analysis can be combined together and results from the two experiments can also be combined to further improve the measurements. The coupling properties of the Higgs boson to other Standard Model particles can be computed through the different decay channels and production modes. All production modes described in Section 1.3.1 have been observed at the LHC: the ggF was observed by both ATLAS and CMS during Run-1 and the VBF modes observations have been claimed during Run-1 by combining ATLAS and CMS results [36]. The VH mode has been observed during Run-2 by ATLAS [34] and finally the ttH fusion mode was observed after combining different decay channels during Run-2 by CMS [37] and ATLAS [38] separately.

As of today, the decay channels accounting for almost 90% of the Higgs Branching ratio have been observed. The analyses $H \to \gamma\gamma$, $H \to ZZ \to 4l$ and $H \to WW$ played a major role in the Higgs discovery due to the good mass resolution of the $\gamma\gamma$ and $4l$ channels and the good sensitivity. These channels allow to carry out precision measurements of the Higgs mass and differential cross-section measurements. The other channels are also important as the combination improves the understanding of Higgs properties. The analysis targeting $H \to b\bar{b}$ allows to measure the coupling of Higgs to down-type quark and drives the Higgs boson total width. It was first observed by both ATLAS and CMS during Run-2 using 79.8 fb^{-1} after combining different production modes as described in Section 1.4.3. The $H \to c\bar{c}$ analysis is similar to $H \to b\bar{b}$ because both channels have similar background composition but $H \to c\bar{c}$ has a smaller signal over background ratio. This analysis is very challenging due to the difficulty to identify c-quark jets. In addition, this channel has a small cross-section and small signal over background ratio, the reasons why no signal excess has yet been observed. As of today, the best limit of this channel was performed with the CMS detector using 35.9 fb^{-1}, where the limit of the signal strength was found to be 70 times the Standard Model prediction [39]. The $H \to \tau\tau$ channel, one of the leading decay channels, has been observed during Run-1 when combining ATLAS and CMS measurement with a significance of 5.5σ [36]. The $H \to \mu\mu$ decay is very challenging due to the large background contamination and the small branching ratio. An evidence of this decay was set by ATLAS [40] and CMS [41] with a significance 2.0σ of and 3.0σ respectively.

Results from the latest Higgs combination measurements from CMS [42] are shown in Figure 1.11 and from ATLAS [43] in Figure 1.12. The results were found to be consistent with the Standard Model predictions.

1.5 Limitations and beyond the Standard Model

The Standard Model represents a description of the observed subatomic particles. Even though experimental results have confirmed its predictions, it does not provide an explanation to all the phenomenons in the universe. Since this model is incomplete, sevaral theories have been developed to explain these deficiencies. Until today there is no direct experimental evidence of any of these theories, and physics beyond the Standard Model (BSM) remains an active field of research:

- **Matter Anti-matter Asymmetry** Cosmological observations show that the universe is mostly made up of matter. However in the Big Bang theory the universe should be created with an equal amount of matter and anti-matter. The CP (charge conjugal and parity symmetry) violation is responsible for this asymmetry. Even though the CP-violation is allowed in weak interactions, it still does not explain why matter dominates in the universe.

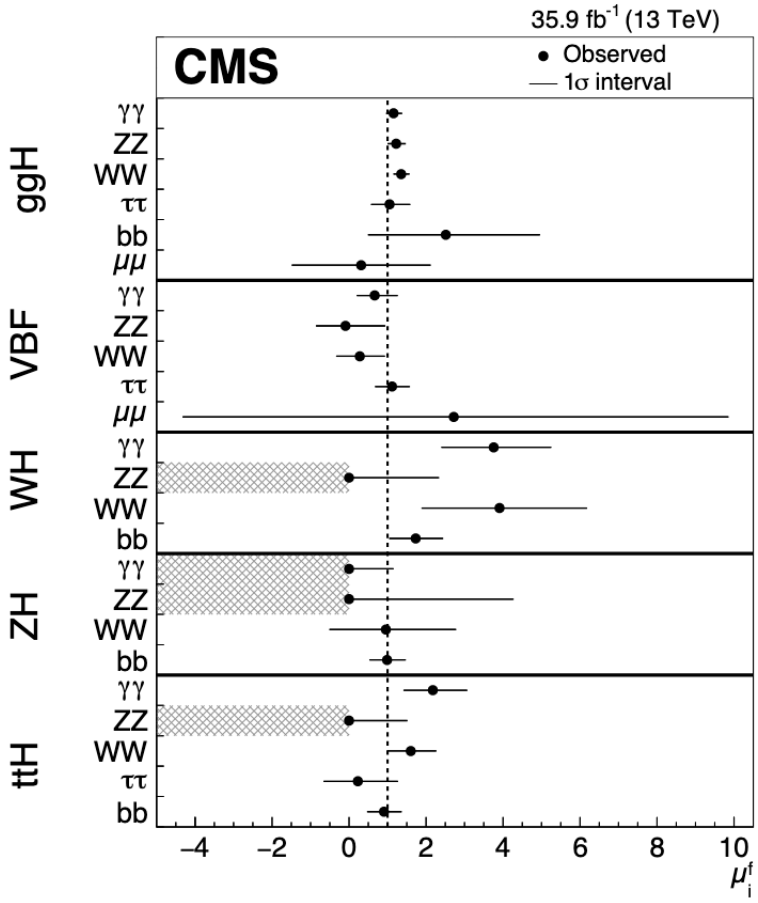

Figure 1.11 – The signal strength for the production modes and the relevant decay channels from a combination of all channels using $35.9\,\mathrm{fb}^{-1}$ with CMS [42].

- **Dark Matter and Dark Energy** Only 5% of the content in the universe is made up of the particles of the Standard Model. Dark matter is supposed to account for 27% of the universe. Unlike other particles of the Standard Model, dark matter does not act via the electromagnetic force, so it does not interact with the light making it impossible to be observed by experimental instruments. Dark matter candidates emerge in theories beyond the Standard Model. The remaining 68% [44] of the universe corresponds to the dark energy which fills the space uniformly and is responsible for the acceleration in the expansion of the universe.
- **The Hierarchy Problem** The hierarchy problem is an important problem with the Standard Model arising from the big difference between the mass of the Higgs boson and the Planck mass. A problem occurs when calculating the Higgs boson mass using QFT where radiative contributions (from loop diagrams) should be taken into consideration. These contributions come from all energy scales up to the energy scale Λ where the Standard Model ceases to be valid. The main problem is that the Higgs boson mass calculated at a large energy scale such as the Planck scale will be much larger than the experimental observation of $m_H = 125\,\mathrm{GeV}$.
- **Gravitation** The Standard Model is a gauge theory with gauge symmetry $SU(3)_C \otimes SU(2)_L \otimes U(1)_Y$ to describe three of the fundamental interactions, whereas gravity is the only fundamental force not included in its description. A dedicated theory, called general relativity, was developed to give an accurate description of the gravitational force. Superstring theory is one example of theories that try to unify the four forces under a single theory.

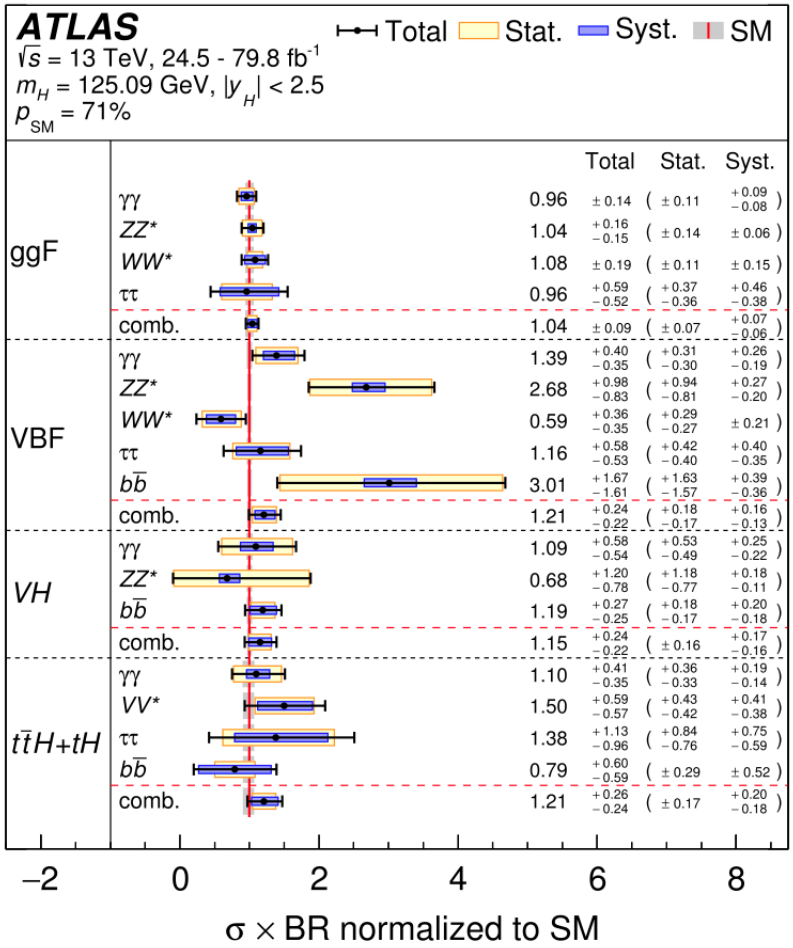

Figure 1.12 – Cross-section times the branching ratio for the production modes and the relevant decay channels normalised to the Standard Model predictions. The results are obtained from a combination of all channels using up to 79.8 fb^{-1} of data with ATLAS [43].

- **Neutrino Masses** Neutrinos in the SM are represented as massless particles. However experimental observations confirmed that neutrinos can oscillate and change their leptonic flavor. These oscillations imply that these particles are not massless. It is possible to add a mass term in the SM while conserving the gauge symmetry, but the question remains if they should be added as Dirac particles (like electrons, muons and taus) where neutrinos and anti-neutrinos are two different particles or as Majorana particles where neutrinos are their own anti-particles.

The studies carried out in the Higgs sector contribute to answering these questions, in particular by the interpretation of the measurements of the Higgs boson for the search of new physics when performing differential measurements and constraining effective field theory (EFT) operators.

1.6 Interpretation of the Higgs boson measurements

1.6.1 Couplings

The Higgs boson measurements constitute a fairly important test to the Standard Model. In addition to the measurement of the mass of this particle and the signal strength, putting constraints on its couplings to different particles allows to compare the compatibility of the results

with the Standard Model or find indications of new physics. The couplings of the Higgs boson to fermions and to bosons are measured in the same way, except that the coupling to fermions is proportional to the mass of the fermion, while the coupling to weak bosons is proportional to the square of the mass. The comparison of the measurements to the Standard Model allows to highlight any deviation since there might be new particles that interact with the Higgs boson. To probe such deviations, the measurements are parametrised as follows:

$$y_i = \kappa_i y_i^{SM} \tag{1.18}$$

κ_i (kappa) is the scaling factor or the coupling modifier [45] introduced to parametrise the deviation of the production or the decay from the Standard Model. Figure 1.13 shows the fermions and weak boson coupling modifiers measured with the ATLAS detector. The κ_i values were found to be very close to unity within uncertainties and therefore consistent with the Standard Model.

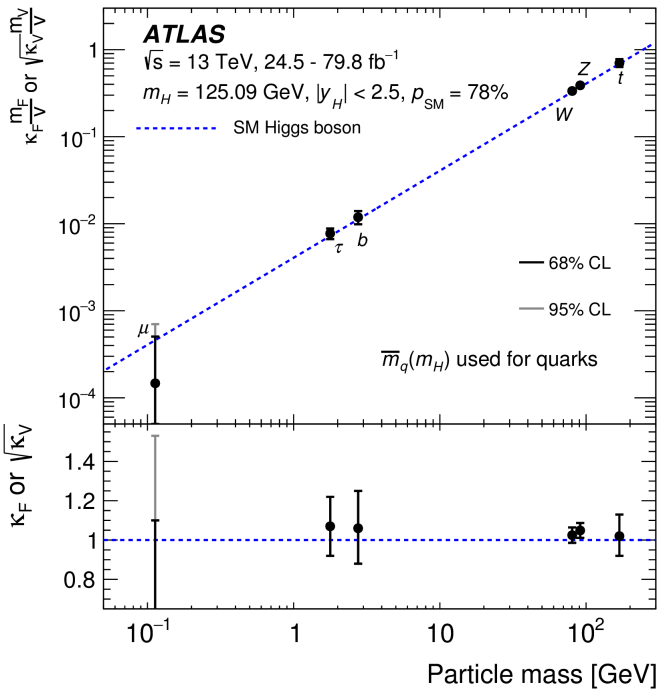

Figure 1.13 – The upper pad shows the reduced coupling modifiers for fermions and bosons as function of their masses. The dotted line corresponds to the SM prediction, the black error bars correspond to 68% CL measurement and the gray line to 95% CL from ATLAS analyses. The lower pad corresponds to the ratio to the SM prediction [46].

1.6.2 Simplified template cross-sections

The simplified template cross-sections (STXS) [47] is a choice of measurement which allows to have various interpretation of the results. When doing STXS measurements, each of the Higgs boson production modes are treated individually after categorising the events into regions defined based on the kinematics of the Higgs boson and the associated final state particles. The primary goal is to provide a fine-grained measurement of the cross-section in these fiducial regions of the phase space to separate the bins with kinematic which are sensitive to physics beyond the Standard Model, and reduce the theoretical uncertainties. The STXS definition is common between ATLAS and CMS making it easy to combine their results. The resulting measurements can be interpreted in the context of the Standard Model or beyond. There are

different definition to the STXS kinematic bins, the most granular ones are shown in Figure 1.14 and are referred to as stage 1.2 binning. For the VH production STXS measurement, a first split is implemented to measure the $qqZH$, $ggZH$ and WH signal processes separately. More splits are introduced depending on the number of jets in the final state and the vector boson transverse momentum.

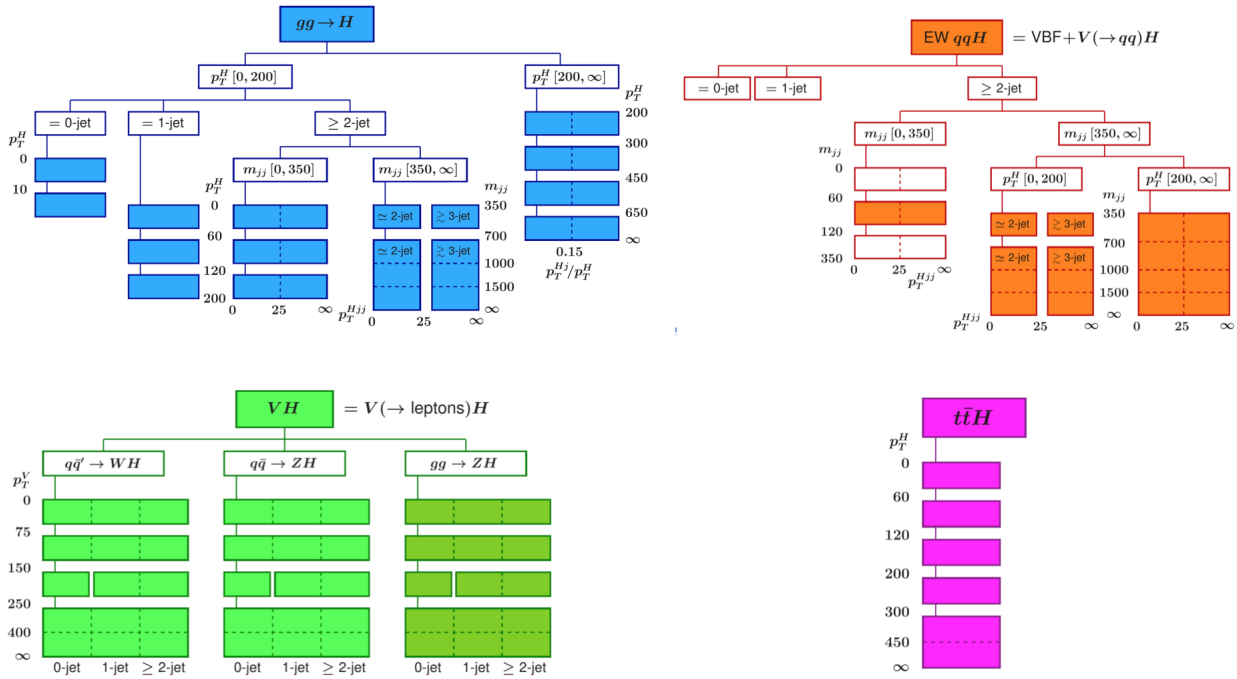

Figure 1.14 – The STXS stage 1.2 binning for each of the Higgs production processes [48]. The dashes lines determine the bins which are used to define to calculate the signal uncertainties.

1.6.3 Effective field theory interpretation

The Standard Model effective field theory (SMEFT) is a model-independent approach to interpret all the Standard Model measurements, including the Higgs boson measurements in terms of constraints to new physics. In this approach, interactions generated at large energy scales can be added to the Standard Model description and expressed through operators of mass dimension equal to 6 compatible with $SU(3) \otimes SU(2) \otimes U(1)$ symmetry [49]. A total of 2499 operators can be added to the lagrangian, but only the ones that affect the Higgs boson measurements are considered, thus reducing the number to 76 operators. Furthermore the number is reduced to 59 operators by excluding CP violating operators. The new physics is considered completely decoupled from the Standard Model, therefore the SMEFT Lagrangian can be written as:

$$\mathcal{L}_{EFT} = \mathcal{L}_{\text{SM}} + \mathcal{L}_{\text{dim=6}} = \mathcal{L}_{\text{SM}} + \frac{c_i}{\Lambda^2} O_i \tag{1.19}$$

Where Λ is the energy scale at which these new interactions appear, O_i are the new operators and c_i are the coupling constants also called Wilson coefficients, where one coupling constant is assigned to each operator.

The STXS measurements can be interpreted within the SMEFT. Since the STXS binning is defined to separate different kinematic regions, the cross-sections can be expressed as function

of the coupling constants [50]. The predicted cross-section in each of the STXS bins can be split as following:

$$\sigma_{EFT} = \sigma_{\text{SM}} + \sigma_{\text{interference}} + \sigma_{\text{BSM}} \tag{1.20}$$

The additional contributions correspond to effects of the processes generated by the new physics and their interferences with the Standard Model. These contributions are considered relative to the Standard Model and expressed as linear and quadratic terms on the EFT parameters:

$$\frac{\sigma_{\text{interference}}}{\sigma_{\text{SM}}} = A_i c_i; \; \frac{\sigma_{\text{BSM}}}{\sigma_{\text{SM}}} = B_{ij} c_i c_j \quad \Rightarrow \frac{\sigma_{\text{EFT}}}{\sigma_{\text{SM}}} = 1 + A_{\text{i}} c_i + B_{ij} c_i c_j \tag{1.21}$$

Where A_i and B_{ij} are numerical parameters obtained using Monte Carlo simulations of the cross-section in each of the STXS bins. Measuring the cross-section parametrised as function of the Wilson coefficients allows to put constraints on the values of the latter and put limits on the deviations from the Standard Model.

The same physical effect can be modelled by different combinations of these operators. Therefore different complete and non-redundant operator bases have been developed offering different advantages when applied to the same process. Thereby the EFT basis choice can depend on the analysis. Instead of measuring the Wilson coefficients separately, the analysis can choose to measure a linear combination of these operators. The Warsaw basis [49] is the most suited to use for comparisons with beyond Standard Model theories interpretations and allows to perform combination measurements of the EFT operators for the precision measurements of the top quark and the Standard Model. This basis is used in the $VH, H \to b\bar{b}$ analysis, with the couplings presented in Table 1.5 to which this channel is sensitive.

Wilson coefficient	Operator	Impact vertex	
		Production	Decay
c_{HWB}	$O_{HWB} = H^\dagger \tau^I H W^I_{\mu\nu} B^{\mu\nu}$	HZZ	
c_{HW}	$O_{HW} = H^\dagger H W^I_{\mu\nu} H W_I^{\mu\nu}$	HZZ,HWW	
c_{Hq3}	$O^{(3)}_{Hq} = (H^\dagger i \overleftrightarrow{D}^I_\mu H)\ (\bar{q}_p \tau^I \gamma^\mu q_r)$	$qqZH$, $qq'WH$	
c_{Hq1}	$O^{(1)}_{Hq} = (H^\dagger i \overleftrightarrow{D}_\mu H)\ (\bar{q}_p \gamma^\mu q_r)$	$qqZH$	
c_{Hu}	$O_{Hu} = (H^\dagger i \overleftrightarrow{D}_\mu H)\ (\bar{u}_p \gamma^\mu u_r)$	$qqZH$	
c_{Hd}	$O_{Hd} = (H^\dagger i \overleftrightarrow{D}_\mu H)\ (\bar{d}_p \gamma^\mu d_r)$	$qqZH$	
c_{dH}	$O_{dH} = (H^\dagger H)(\bar{q} d H)$		Hbb

Table 1.5 – The Wilson coefficients to which the $VH, H \to b\bar{b}$ mode is sensitive, at leading order, and the corresponding SMEFT operators. The operators impacting the $ggZH$ production are still under study and are not considered since $ggZH$ is produced through a loop of heavy quarks which means that it is not at leading order.

Chapter 2

The Large Hadron Collider and the ATLAS experiment

In this Chapter are presented the Large Hadron Collider in Section 2.1 and the ATLAS [51] experiment in Section 2.2. The HL-LHC [52] program as well as the upgrades needed for the LHC machine and for the ATLAS detector to be able to cope with the increase in luminosity are presented in Section 2.3. Finally, Section 2.2.9 is dedicated for the Monte Carlo simulations which a key element in most analyses to investigate the data collected by the detector.

2.1 The Large Hadron Collider

The Large Hadron Collider (LHC) is the highest energy particle collider in the world. Situated at the border between France and Switzerland, this circular collider is designed mainly to collide proton beams in a ring of 27 km circumference. For about a month every year, heavy-ion collisions are recorded instead for studies such as that of quark–gluon plasma. Four main experiments with complex detectors are placed around the interaction points, each having a dedicated research program. The LHC project was approved by the CERN Council in 1994, and the construction started in 2000 in the same tunnel used previously for the LEP. The LHC acceleration chain consists of a succession of machines that accelerate the particles to increase gradually their energy.

2.1.1 The acceleration chain

The proton beams are first created from hydrogen gas ionisation using an electric field to extract the electrons and only keep the protons. The beams then travel through an acceleration chain where at each step the particle beam is accelerated before injecting it into the next accelerator to finally enter in the LHC ring as show in Figure 2.1. The first acceleration step is the linear accelerator 2 (Linac 2) which is 30 m long and used to raise the energy of the particles up to 50 MeV. Linac 2 is replaced by the Linac 4 accelerator for Run-3, to increase the energy by up to 160 MeV. The beams are then injected to the Proton Synchrotron Booster (PSB), which is a circular accelerator of four superimposed synchrotron rings of 157 m circumference to accelerate the beams to an energy of 1.4 GeV. After the PSB, the particles arrive in the 628 m circumference Proton Synchrotron (PS) and their energy is increased to 25 GeV. The PS also prepares the LHC beam structure, where the particles are arranged in bunches separated by 25 ns. The particles are then injected into the Super Proton Synchrotron (SPS) which is the last step before the LHC.

The SPS which was used previously as the first p-$\bar{p}$ collider in the 80's, is a circular accelerator with 7 km circumference placed at 40 m underground, that brings the energy of the particles up to 450 GeV. The SPS then injects two beams into the LHC in opposite directions. It provides at the same time beams to the NA61/SHINE, NA64 and COMPASS experiments situated in the SPS North Area.

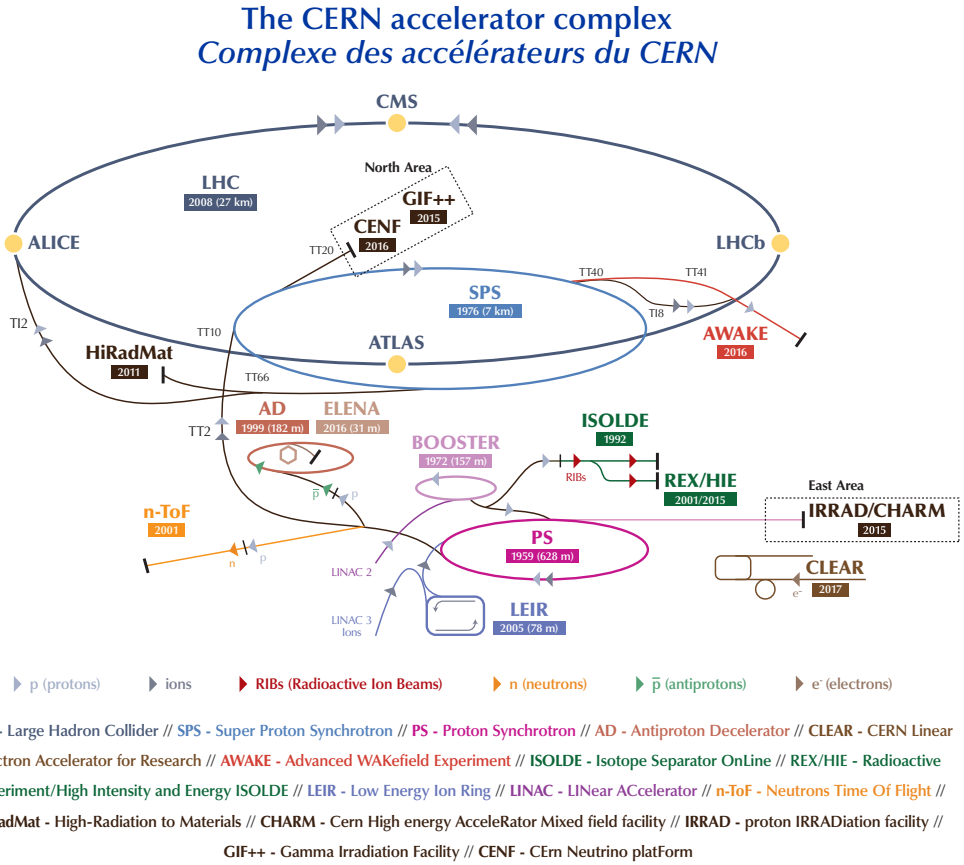

Figure 2.1 – The LHC acceleration system [53] for both the proton and lead beams.

Protons entering the LHC are organised in 2808 bunches per injection, of 1.15×10^{11} protons per bunch separated by 25 ns. In each beam, the bunches are gathered together into bunch trains to make a total of 3.2×10^{14} protons per beam. The proton beams in the LHC are accelerated up to an energy up to 13 TeV. Due to the high proton density in each bunch, many p-p interactions occur per bunch crossing.

The beams circulate in the LHC in opposite directions and in two different beam pipes under vacuum. The LHC accelerator includes several parts necessary to maintain the protons on their circular orbit and to accelerate them to the desired energy. The acceleration is provided by the 8 radio frequency (RF) cavities per beam, placed in cryomodules to operate in a super-conductive state, at a rate of 400 MHz. These cavities allow to increase the energy of the beam per turn to be able to increase the energy from 450 GeV to 6.5 TeV over a period of 20 minutes. Besides, 1232 Superconducting dipoles magnets of 15 m each are installed and operating at a temperature of 1.9 K. These dipoles create a magnetic field of up to 8.3 T responsible for keeping the particles in their trajectory. In addition, 392 Superconducting quadrupole magnets operating at 4.5 T are used to focus the beams.

The expected lifetime of the beam inside the LHC is approximately 15 hours. Experiments can start collecting data during stable beams (beams are aligned, squeezed, focused and directed to collide head-to-head) when the beams reach the expected energy, after which the intensity of

the beams decreases with time due to the collisions. When the beam intensity is too low, the beams are directed out of the ring and the LHC prepares for the injection of new beams.

2.1.2 Luminosity and pile-up

For experimental searches and measurements, collecting a large number of events is important, as the statistical uncertainties are dominant in analyses looking for rare processes. The number of events produced per second for a certain process is given by:

$$N_{event} = \mathcal{L} \times \sigma_{process} \tag{2.1}$$

Where $\sigma_{process}$ is the cross-section of the process and $\mathcal{L}$ is the instantaneous luminosity. The instantaneous luminosity is one of the most important parameters of an accelerator. It is related to the number of collisions that can be produced in the effective surface area per second, and therefore its unit is $\mathrm{cm}^{-2}\mathrm{s}^{-1}$. Figure 2.2 shows the peak luminosity reached per fill during 2018 where the peak luminosity was able to reach more than $2{\times}10^{34}$ $\mathrm{cm}^{-2}\mathrm{s}^{-1}$. The instantaneous luminosity can be computed from the beam parameters presented in Table 2.1 as:

$$\mathcal{L} = \frac{n_1 n_2 N_b f}{4\pi\sigma_x\sigma_y} F \tag{2.2}$$

Having a larger luminosity allows to increase the number of events produced per second, which can be crucial for the processes with small cross-sections. The instantaneous luminosity is not constant and decreases over time due to the degradation of the number of particles per bunch from interactions. The integrated luminosity corresponds to the integral of luminosity over time. It describes the amount of produced data and is expressed as $\int \mathcal{L}dt$. The full Run-2 integrated luminosity is illustrated in Figure 2.3 and corresponds to $156\,\mathrm{fb}^{-1}$ delivered by the LHC. Since the cross-section of the inelastic collisions is very large, dozens of p-p interactions occur in each bunch crossing. These events are referred to as pile-up events. The pile-up affects the reconstruction of the objects resulting from the interaction and degrades their performance. The loss of efficiency and resolution, depending on the case, have an impact in the analysis.

The average number of interactions per bunch crossing, or pile-up, is proportional to the luminosity and is calculated as:

$$\mu = \frac{\mathcal{L}\ \sigma_{inel}}{N_b\ f} \tag{2.3}$$

The σ_{inel} refers to the cross-section of the p-p inelastic interactions and is roughly 75 mb for a center-of-mass energy of 13 TeV. When the luminosity increases μ increases as well (for a constant N_b). For this reason, the number of interactions per bunch crossing is different for each data taking period during Run-2 as shown in Figure 2.4.

2.1.3 Experiments

Four experiments are build along the LHC ring at the four beam collision points:

- **ATLAS** (A Toroidal LHC Apparatus [51]) is a general purpose experiment. It is dedicated for a wide physics program, mainly focusing on the study of the Standard Model, precision measurements of electroweak interactions, the measurement of the Higgs boson properties, and the search for physics beyond the Standard Model.

Parameter	Description	Value
n_1, n_2	number of particles per bunch	1.15×10^{11} protons
N_b	Number of bunches per beam	2808 bunches
f	Revolution frequency	11.25 kHz
σ_x, σ_y	Bunch size	16.7×10^{-4} cm
F	Geometric factor for the angle at which the beams collide	0.84

Table 2.1 – The LHC beam nominal parameters for p-p collisions [54]. These parameters evolved during Run-2 to increase the instantaneous luminosity.

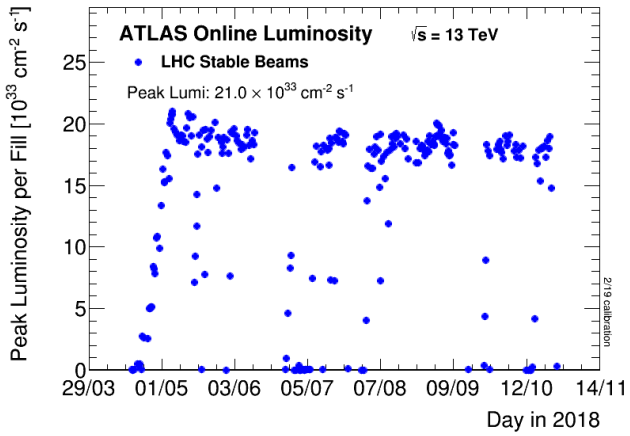

Figure 2.2 – The peak instantaneous luminosity delivered to the ATLAS detector as a function of time during 2018.

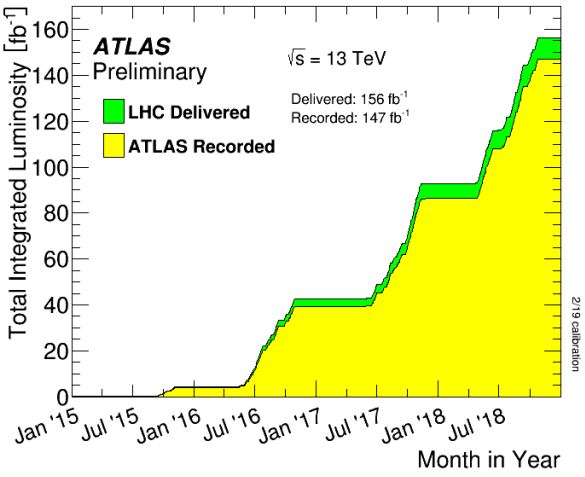

(a)

Figure 2.3 – The integrated luminosity versus time delivered to ATLAS (green) and recorded by ATLAS (yellow) from 2015 to 2018.

- **CMS** (Compact Muon Solenoid [55]) is also a general purpose detector, where both ATLAS and CMS have the same physics program. The two detectors are built with a different design and using different technologies. Having ATLAS and CMS as two similar but independent experiments allows to cross-check the measurements.
- **LHCb** (Large Hadron Collider Beauty [56]) is a detector dedicated for flavor physics. It consists of several sub-detectors, in the forward direction only, spanning on a distance

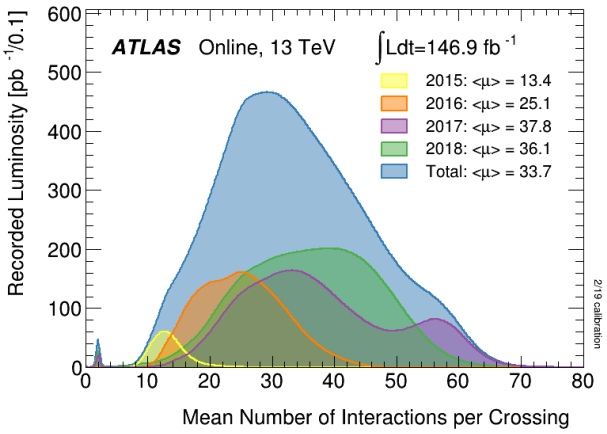

(a)

Figure 2.4 – The mean number of interactions per bunch crossing for the 2015-2018 data recorded by the ATLAS detector.

of 20 meters. The first sub-detector is very close to the collision point to be able detect short lived heavy flavor hadrons. The studies in the LHCb experiment focus on precision measurements of CP violation and B-physics.

- **ALICE** (A Large Ion Collider Experiment [57]) is dedicated for the study of heavy ion collisions to investigate the quark-gluon plasma which is a state of matter at extreme energy densities. These collisions produce three order of magnitude more outgoing particles than in p-p collisions, so the detector is designed to detect all these particles.

2.2 The ATLAS detector

The ATLAS detector is the largest by volume of the four detectors at the LHC, with a cylindrical shape 46 m long, 25 m wide and a weight of 7000 tonnes. The detector is composed of different sub-detectors wrapped in layers around the collision point in the forward and backward directions, and is installed in the cavern at 100 m underground. The detector was designed and optimised to deal with the high interaction rate and the radiation doses of the LHC. The ATLAS sub-detectors are illustrated in Figure 2.5 and are divided into three parts:

- **The inner detector** used to reconstruct the trajectory and the momentum of charged particles using the curvature of their trajectory in the magnetic field. It is composed of high granularity sub-systems needed to handle the high particle fluxes and identify the primary vertices to remove overlapping events and identify pile-up jets.
- **The calorimeters** are used to absorb the particles as they pass through the detector. They use a combination of active and absorber materials to measure the energy of the particles. There are two types of calorimeters: the electromagnetic and the hadronic calorimeters.
- **The muon spectrometer** is dedicated to identify the muons, since they deposit only the minimum ionising particles (MIP) energy in the calorimeters. It is composed of layers of tracking chambers and is complementary to the inner tracker for the muon reconstruction.

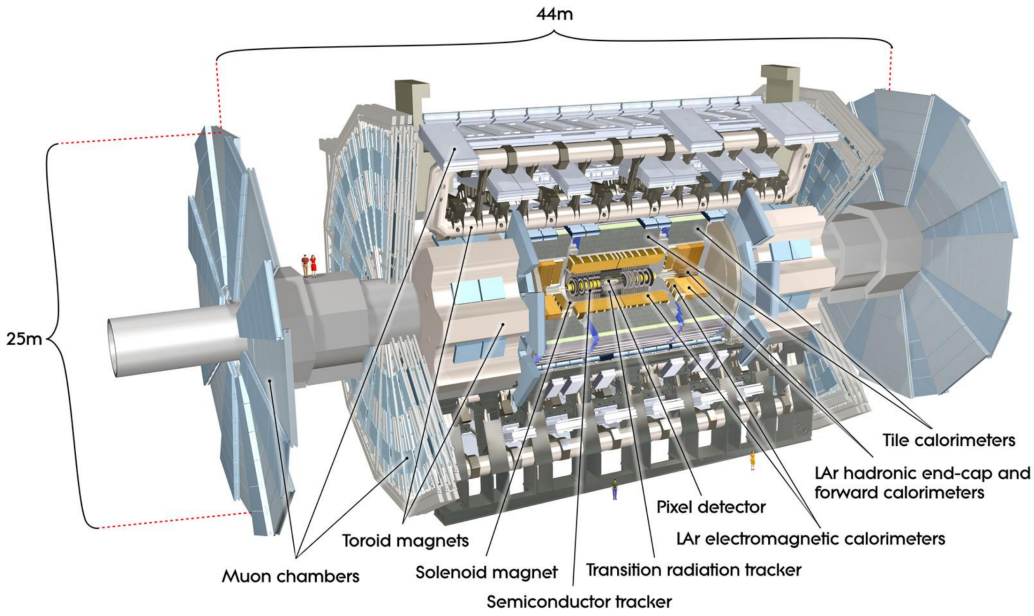

Figure 2.5 – Picture of the ATLAS detector showing all the sub-detectors.

2.2.1 The coordinate system

In the ATLAS coordinate system, the origin is defined as the interaction point and the z-axis corresponds to the counter-clockwise beam direction. The x-y plane is the transverse plane to the beam direction, where the x-axis points towards the center of the LHC and the y-axis points up. The transverse momentum and energy as well as the missing transverse energy are defined in the x-y transverse plane.

Due to the cylindrical geometry of the detector, the cylindrical coordinates θ, ϕ and z are used. The angle θ is the radial coordinate defined with respect to the beam axis, and the azimuth angle ϕ is measured in the transverse plane with respect to the x-axis. the polar angle θ is expressed in term of pseudo-rapidity as:

$$\eta = -\ln\left(\tan\frac{\theta}{2}\right) \tag{2.4}$$

The pseudo-rapidity $\eta = 0$ corresponds to the transverse plane at the center of the detector. The barrel and end-caps parts of the ATLAS detector are defined depending on η: $|\eta| < 1.4$ defines the barrel and $|\eta| > 1.4$ the end-caps. This definition of the pseudo-rapidity is chosen to be equal for the rapidity for relativistic particles, which is defined as function of the energy and the longitudinal momentum:

$$y = \frac{1}{2}\ \ln\left(\frac{E\ +\ p_z}{E\ -\ p_z}\right) \tag{2.5}$$

The angular distance in this coordinate system can be defined as :

$$\Delta R = \sqrt{\Delta\eta^2 + \Delta\phi^2} \tag{2.6}$$

2.2.2 Inner detector

The inner detector [58] (ID) is the most central part of the ATLAS detector, designed to provide an excellent precision on the reconstruction of tracks, created by the charged particles coming from the collisions. It is installed a few centimeters away from the collision point in a cylindrical envelope of 3.5 m length and a radius of 1.15 m, immersed in the magnetic field provided by a superconducting solenoid. It is a highly granular detector operating within a pseudo-rapidity range of $|\eta|$ <2.5 and with a full coverage in ϕ.

The ID is formed of three sub-detectors as shown in Figure 2.6: the silicon pixel detector which is the most inner part, then comes the SemiConductor Tracker (SCT) and finally the Transition Radiation Tracker (TRT). It is made up of several layers which are used to reconstruct the tracks of the charged particles from the hits they leave in each layer. The ID design resolution as function of the transverse momentum p_T of the particles is given by:

$$\frac{\sigma_{p_T}}{p_T} = 0.05\%\ p_T \ \oplus\ 1\% \tag{2.7}$$

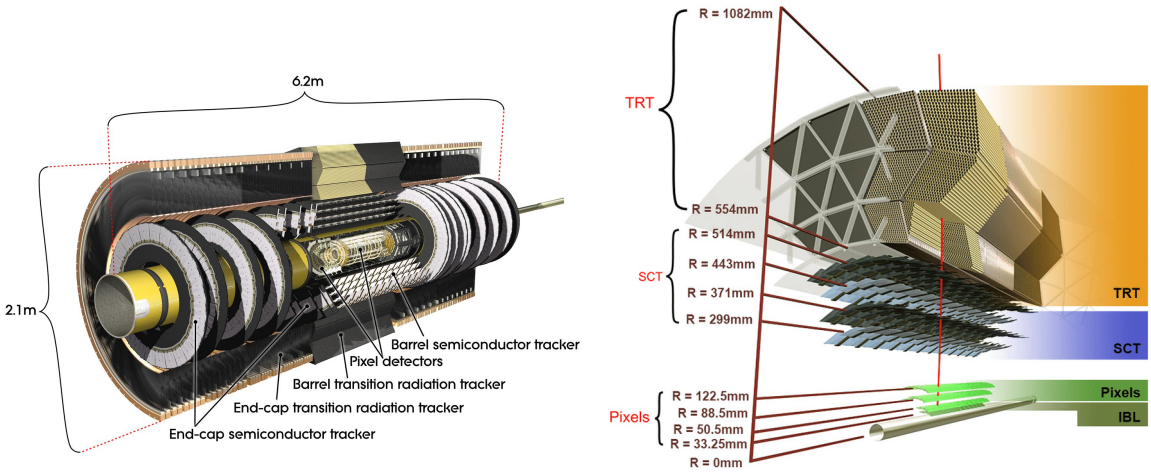

Figure 2.6 – The ATLAS inner detector.

Pixel detector

The pixel detector is designed to achieve an excellent primary and secondary vertex reconstruction. It consists of pixel layers arranged in cylinders around the beam pipe in the barrel, and in disks perpendicular to the beam in the end-caps to cover the $|\eta| \leq 2.5$ region. the pixel detector is consisted of three layers, placed at 50.5, 88.5 and 122.5 mm away from the beam, which provides a high granularity and a good resolution. The detector layers are composed of 1744 silicon pixel modules of 50 μm × 400 μm dimensions in R-ϕ and z with 46080 readout channels per module.

The Insertable B-Layer (IBL) is an additional pixel layer inserted between the beam pipe and the innermost layer at 33.25 mm away from beam. It was installed between Run-1 and Run-2 during the first shutdown of the LHC. The inclusion of IBL was necessary to compensate for the radiation damages caused during Run-1, and to also improve the spatial resolution. It consequently provided a better reconstruction of B-hadrons coming from secondary vertices, which lead to an improvement in the b-tagging algorithm performance.

The silicon pixels are made of a semiconductor pn junction. When passing the detector, the particles create pairs of electron-hole along their trajectory when interacting with the materials.

The electrons and the holes then drift towards the cathode and the anode respectively and produce an electric current which is then collected as signal by the readout electronics.

Semiconductor Tracker

The Semi Conductor Tracker is a silicon microstrip tracker with the same technology as the pixel detector, but using 4088 microstrip modules instead of pixels. It has also a similar design of four strip layers placed at a distance of 299, 371, 443 and 514 mm from the beam in the barrel to cover particles with $|\eta|$ <1 and of strip modules arranged on three disks in the end-caps covering up to $|\eta|$ <2.5. Each layer consists of two-sided modules comprised of strips with a width of 80 μm and a length of 64 mm, providing a resolution of 17 μm in R-ϕ and 580 μm in z.

Transition Radiation Tracker

The Transition Radiation Tracker is the outer-most part of the ID with an acceptance range of $|\eta|$ <2.1. It consists of straws of 4 mm diameter providing information only in the R-ϕ plane with a precision of 130 μm per straw. In the barrel, 50000 straws each of 144 cm long are placed parallel to the beam, while 250000 straws are used in both end-caps each of 39 cm long and placed in wheels perpendicular to the beam.

The straws are filled with a gas mixture of 70% Xe, 27% CO_2 and 3%O_2. During Run-2, some of the straws had gas leaks, so several modules were filled with argon instead of xenon because it is less expensive while keeping a good efficiency for photons from transition radiation. When the particle pass through the gas it interacts with it and ionises it, resulting in the emission of electrons. Due to the high voltage applied, these electrons then drift towards the anode wires placed at the center of each straw tube. This drift will result in the creation of an electric current which is then collected by the readout electronics.

Even though the TRT does not provide the best spatial resolution per hit, however it provides an average of 35 hits per track. Due to this large number of hits, the TRT offers a good pattern recognition accuracy and momentum measurement. It also provides good electron identification based the detection of photons, emitted from the transition radiation (TR) process. A particle at the interface of two mediums of different indices can emit TR photons. The probability of emitting TR photons is greater for electrons at a given p_T than for light hadrons such as a pion for example. The xenon in the gas mixture has a high probability to detect the TR photons, while the argon has a much lower TR probability but a similar tracking efficiency as xenon.

2.2.3 Calorimeters

The ATLAS calorimeter system installed around the ID detector, is designed to measure the energy of particles. It consists of a number of sampling detectors covering the pseudo-rapidity range $|\eta|$ <4.9 and providing a full coverage in ϕ. It is composed of two types of sub-detectors: the electromagnetic calorimeter to measure the electrons and the photons and the hadronic calorimeter for the measurement of jets from hadrons. The calorimeters are designed from an alternation of layers of active and passive materials, where the passive part is used to create a shower from the incident particles and the active part for the detection of the energy of the particles deposited through ionisation. In the electromagnetic calorimeters the radiation length (X_0) is one characteristic of the material, corresponding to the mean length that the particle needs to travel to reduce its energy by a factor of 1/e. The calorimeter was designed to be at least 24 X_0 deep which ensures that the electromagnetic showers, on average and up to a certain energy, will be contained in the electromagnetic calorimeter. Similarly the hadronic calorimeter is at least 8 nuclear interaction lengths (λ) deep to prevent most of the hadronic cascades from

reaching to the muon spectrometer.

The calorimeter system is composed of different calorimeters technology: the Liquid Argon technology (LAr) used for the electromagnetic calorimeter in the barrel (EMB) and the two end-caps (EMEC), for the hadronic calorimeter in the end-caps (HEC) and for the forward calorimeter (FCal). While as the steel/plastic scintillator sampling is used in the barrel and the extended barrel of the hadronic calorimeter. A cut-away view of the calorimeters is shown in Figure 2.7.

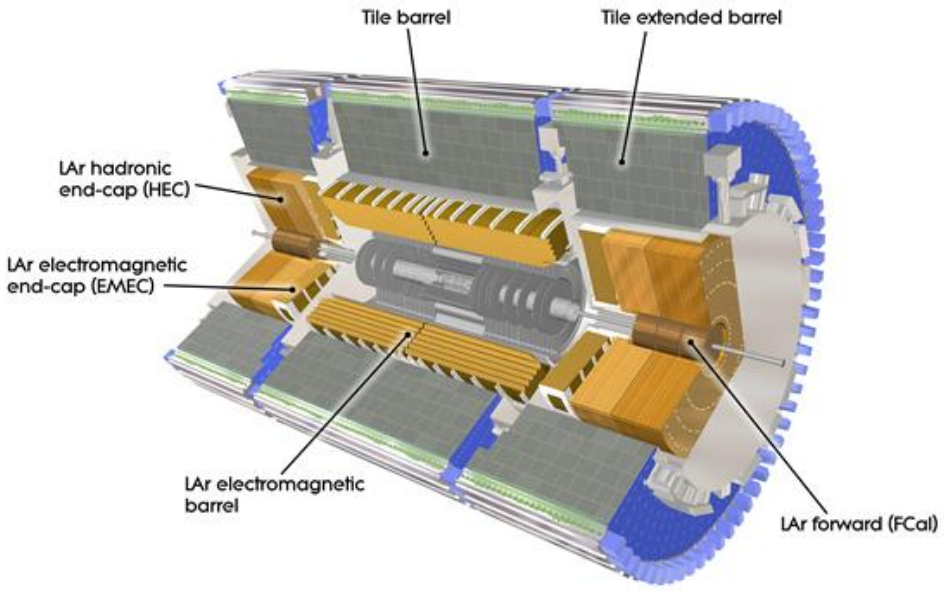

Figure 2.7 – Cut-away view of the ATLAS calorimeter system.

The energy resolution of the calorimeters as function of the energy of the particles is expressed as the quadratic sum of three terms:

$$\frac{\sigma_E}{E} = \frac{a}{\sqrt{E}} \oplus \frac{b}{E} \oplus c \tag{2.8}$$

The first term on the left is the stochastic term, corresponding to the fluctuations of the shower development when using sampling calorimeters. The second term is the noise term, for the pile-up noise and noise coming from the electronic readout chain. And finally the constant term which does not depend on the energy of the particle and becomes dominant at high energies, the reason why this term should be kept at a level less than a percent. This last term corresponds to the calorimeter design and geometry, channels intercalibration and energy lost in dead material.

Electromagnetic calorimeters

The electromagnetic calorimeters are designed to identify and measure the electrons and photons. They are lead/liquid-Argon [59] (LAr) detectors with accordion shaped copper-kapton electrodes placed between lead absorber plates as shown in Figure 2.8. The electrons and photons passing through the detector form an electromagnetic cascade and continue until they reach a threshold of energy. This shower is produced in the passive material since it has a more dense material (smaller X_0) before reaching the active material where they ionise the liquid argon and create free electrons. These electrons then drift towards the electrodes in the high voltage fields, which creates the signal. The accordion geometry enables a full coverage in ϕ without azimuthal cracks.

The calorimeters consist of the barrel that is placed from either sides of the collision point and covers particles with $|\eta| < 1.475$, and of the two end-caps to cover $1.375 < |\eta| < 3.2$. The barrel is made up of two half-barrels placed in the same cryostat where on both sides are placed two wheels corresponding to the end-cap calorimeter. These wheels consist of two co-axial wheels, where the outer wheel covers the $1.375 < |\eta| < 2.5$ and the inner wheel covers the $2.5 < |\eta| < 3.2$ region.

The calorimeters present a longitudinal segmentation providing a good measurement of the electromagnetic shower direction. In the barrel and the outer wheel, the calorimeter has three layers in depth (the front, the middle and the back layers as shown in Figure 2.9) with different cell granularities for particle identification, while the inner wheel has two layers. An additional thin layer using the same LAr technology, called the pre-sampler, is placed in front of the other layers and covers the $|\eta| < 1.8$ region. The pre-sampler allows to estimate the energy lost in the upstream material (magnet cryostat, ID, ...).

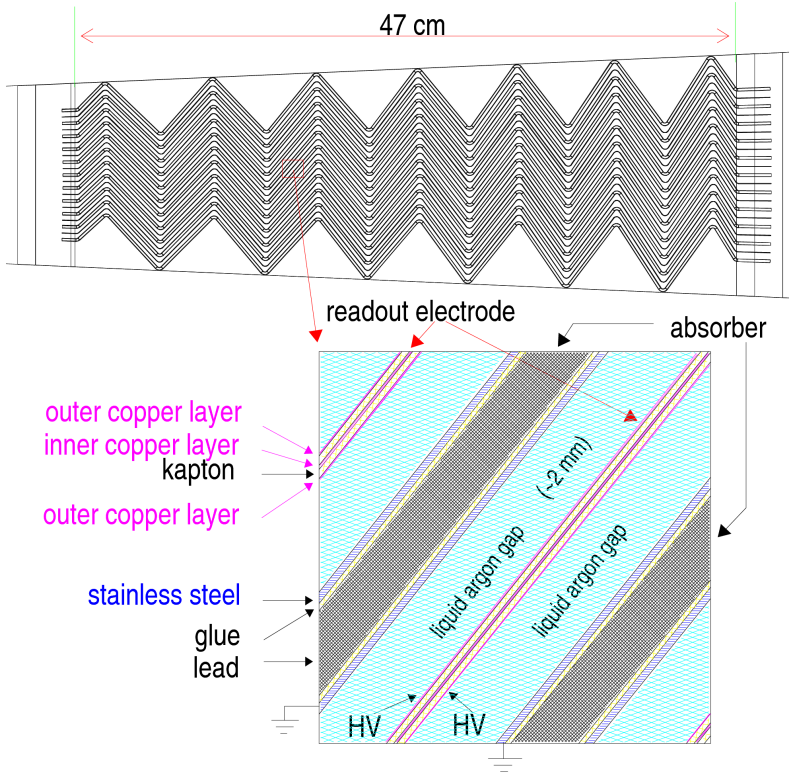

Figure 2.8 – Sketch showing the LAr electromagnetic calorimeter sampling.

The calorimeter provides a typical energy resolution for electrons of:

$$\frac{\sigma_E}{E} = \frac{10\%\,[\sqrt{\text{GeV}}]}{\sqrt{E}} \oplus \frac{170\,[\text{MeV}]}{E} \oplus 0.7\% \tag{2.9}$$

A more detailed description of the LAr calorimeter readout electronics and their performance, in addition to the upgraded electronics to fulfill the demanding conditions when the LHC will be operating at high luminosity are presented in Chapter 3.

Hadronic calorimeters

The hadronic calorimeter (HCAL) is a sampling calorimeter designed to measure the energy deposited by hadrons and their position inside the detector. The hadronic shower is created when the particle interacts via both the electromagnetic and the strong interactions. A strong

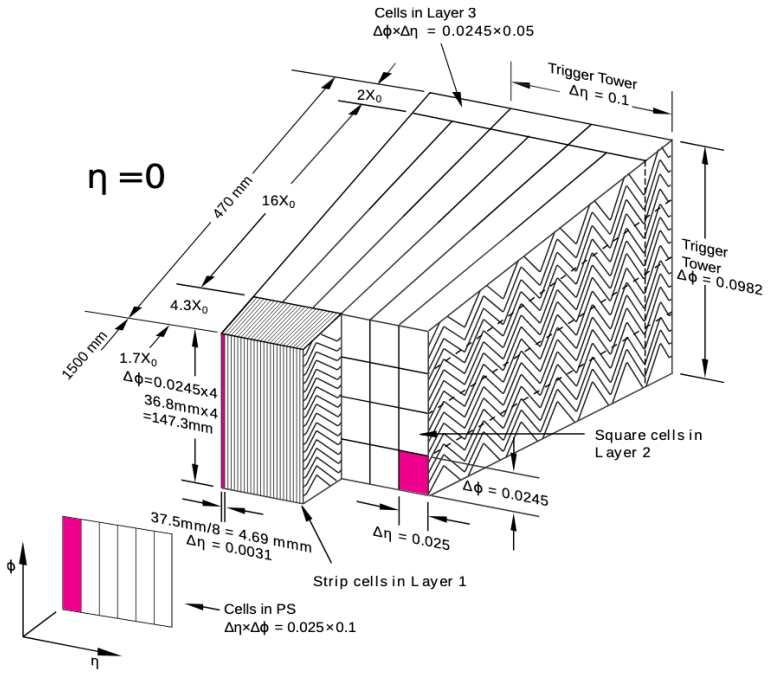

Figure 2.9 – Sketch of electromagnetic barrel calorimeter showing the different layers and their granularity in η and ϕ.

interaction of a single hadron with the detector material can lead to the production of many secondary showers. The HCAL is placed outside the EMCAL to cover the range up to $|\eta| < 4.9$ and is composed of three different parts: the Tile calorimeter (TileCal), the LAr hadronic end-cap calorimeter (HEC) and the LAr forward calorimeter (FCal).

The TileCal [60] is a sampling calorimeter constructed of steel as the absorber and plastic scintillator tiles as the active material. It includes two central long barrels (LBA, LBC) of 2.82 m long each covering the $|\eta| < 1.0$ region and two extended barrels (EBA, EBC) with a length of 2.91 m and a coverage of $0.8 < |\eta| < 1.7$. They are divided into 64 modules each covering an azimuthal angle of $\Delta\phi = 0.1$. The scintillating tiles are perpendicular to the beam pipe and staggered along the R-axis in depth as shown in Figure 2.10.

The HEC is placed behind the EMEC and is contained in the same cryostat together with the EMEC wheels and the FCal as shown in Figure 2.11. It is a copper/LAr calorimeter providing a coverage of particles in the region $1.5 < |\eta| < 3.2$. It consists of two wheels, each made up of four longitudinal layers of copper plates with 32 modules. The HEC together with the TileCal, provide a good measurement of hadrons and the missing energy, with an energy resolution for jets of:

$$\frac{\sigma_E}{E} = \frac{50\%}{\sqrt{E}} \oplus 3\% \tag{2.10}$$

Finally, the FCal located in the $3.1 < |\eta| < 4.9$ region is designed to increase the coverage of the ATLAS calorimeter system and to work in a challenging environment of high radiation doses and high particle fluxes. It is made of three modules, where the closest one to interaction point is the FCal1, optimised for electromagnetic interactions and uses copper as absorber. The other two layers are the FCal2 and FCal3 that use tungsten as absorber material for the measurement

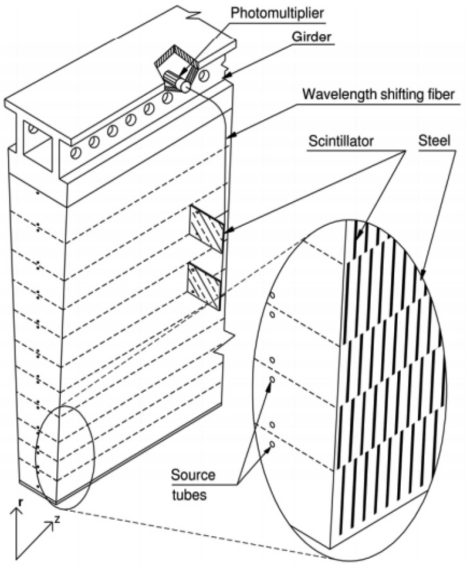

Figure 2.10 – Sketch of Tile calorimeter showing the steel/scintillating tiles sampling and the readout chain.

of hadronic particles. The energy resolution provided by the FCal is [61]:

$$\frac{\sigma_E}{E} = \frac{100\%}{\sqrt{E}} \oplus 10\% \tag{2.11}$$

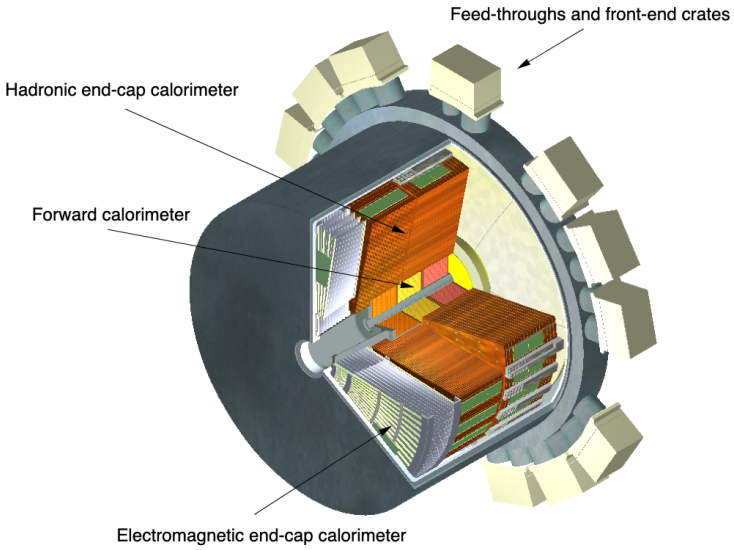

Figure 2.11 – Cut-away view of the end-cap cryostat showing the positions of the three end-cap calorimeters.

2.2.4 Muon spectrometer

Muons are the only particles, besides neutrinos, that can pass through the ID and the calorimeter system without being absorbed. A dedicated system is installed in the outer most part of the ATLAS detector to identify them and measure their momentum with a $|\eta| < 2.7$ coverage, working independently from the ID. This is achieved through a strong magnetic field generated

by the large air-core toroid in the barrel and two air-core toroids in the end-cap allowing to deflect the muons trajectories when passing the detector. The muon spectrometer [62] (MS) consists of two different types of detectors as shown in the cut-away view of the muon spectrometer in Figure 2.14.

The first type corresponds to the tracking chambers that give a precise measurement in the η coordinate. They include the monitored drift tubes (MDT) installed in the barrel and the end-caps and the cathode-strip chambers (CSC) installed only in the end-caps which allow to improve the measurement of the muon tracks and momentum. The resistive-plate chambers (RPC) installed in the barrel and the thin-gap chambers (TGC) in the end-caps are the second type of detectors constituting the muon trigger chambers. The trigger chambers provide a measurement in both the η and ϕ coordinates. The MS is designed to provide a momentum resolution of $\frac{\sigma_{p_T}}{p_T} = 3\%$ for p_T around 100 GeV and 10% at 1 TeV. At low energy, a better muon energy resolution can be achieved by combining the measurement in the MS with the momentum information from the ID.

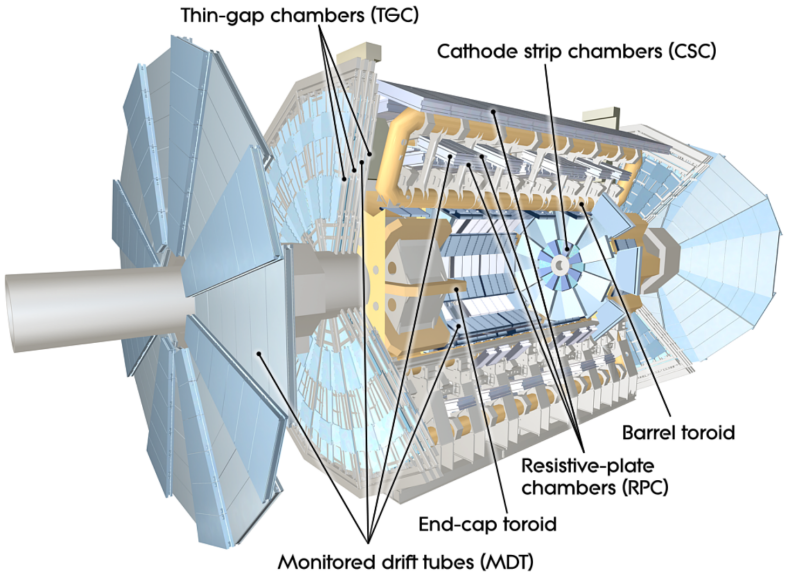

Figure 2.12 – Sketch of muon spectrometer system.

2.2.5 Magnet system

The magnet system [63] is an essential part of the ATLAS detector and is a complex system because of its large volume. It allows to measure the momentum of charged particles from their deviation in the magnetic field. The system is composed of the power system, controls, cryogenics and the refrigeration plant, in addition to four superconducting magnets, with an overall dimension of 26 m long and 20 m diameter. The first magnet is the central solenoid, of 5.3 m long and 2.4 m diameter, that generates an axial magnetic field of 2 T to the inner detector. It is surrounded by three air-core toroid magnets as shown in Figure 2.13, which are the barrel toroid and two end-cap toroids. They are composed of 8 separate coils providing the muon spectrometer with an azimuthal magnetic field of 3.9 T and 4.1 T by the barrel and end-cap toroids respectively. The barrel toroid has a length of 25.3 m and a diameter of 20.1 m diameter while the end-cap toroids have a 5.0 m length and 10.7 m diameter.

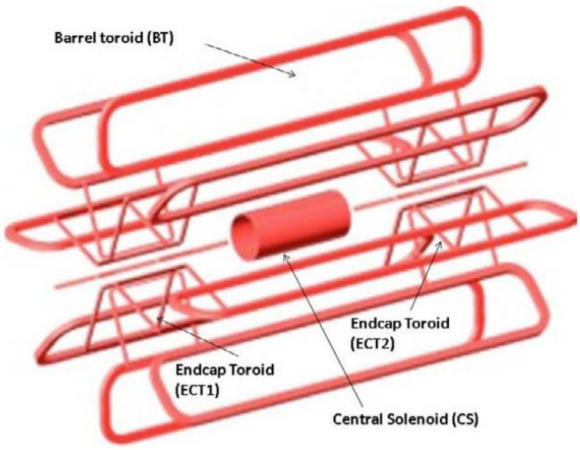

Figure 2.13 – View of the ATLAS magnetic system.

2.2.6 Trigger system

The ATLAS detector was designed for a bunch spacing scheme of 25 ns corresponding to a bunch crossing rate of 40 MHz. The event rate has to be reduced in order to be able to store all the events, the reason why a trigger system is implemented to reduce the rate down to 1 kHz to record only events with potential physics interest. The trigger system operates online, and is used to select and record events of interest using a two-stage system [64] applying different selection criteria: the level-1 (L1) and the high-level trigger (HLT) as shown in Figure 2.14.

The L1 is a hardware-based system that reduces the rate down to 100 kHz with a decision latency of less than 2.5 μs. It uses information from the calorimeters and the muon system, and applies selection cuts on quantities such as the energy deposited in the calorimeter or the transverse momentum for muons, or from topological requirements such as angular distances and the invariant masses of the particles. The L1 also identifies a region-of-interest (RoI) that are forwarded with full detector granularity. To reduce the collection rate even more, the events accepted by the L1 are then transmitted to the HLT trigger.

The HLT is a software-based system that uses a combination of trigger algorithms within a processing time of ∼200 ms. During the first long shut down, the two-level HLT system was merged into one event processing system. The HLT analyses the RoI information by running sophisticated selection algorithm and using information from the whole detector. The data flow is therefore reduced down to 1 kHz rate to meet the storage capabilities. A prescaled selection can be applied to only keep a certain amount of events accepted by the HTL trigger to reduce furthermore the event rate. The triggers used later in this thesis in the $VH, H \to b\bar{b}$ analysis are un-prescaled triggers.

2.2.7 Luminosity monitor

The ATLAS experiment has a luminosity monitoring detector LUCID-2 [65] (LUminosity Cherenkov Integrating Detector) consisting of an array of 40 Cherenkov detectors, each with a length of 50 cm long. This detector is an upgraded version of the previous LUCID-1 which operated until 2013, and is placed around the beam pipe on both sides of the interaction point. It consists of photomultiplier tubes to detect the Cherenkov light produced by the particles when interacting with the gas inside the detector, thus offering an intrinsically fast response. The main purpose of LUCID-2 is to monitor and precisely measure the luminosity delivered by the LHC to ATLAS.

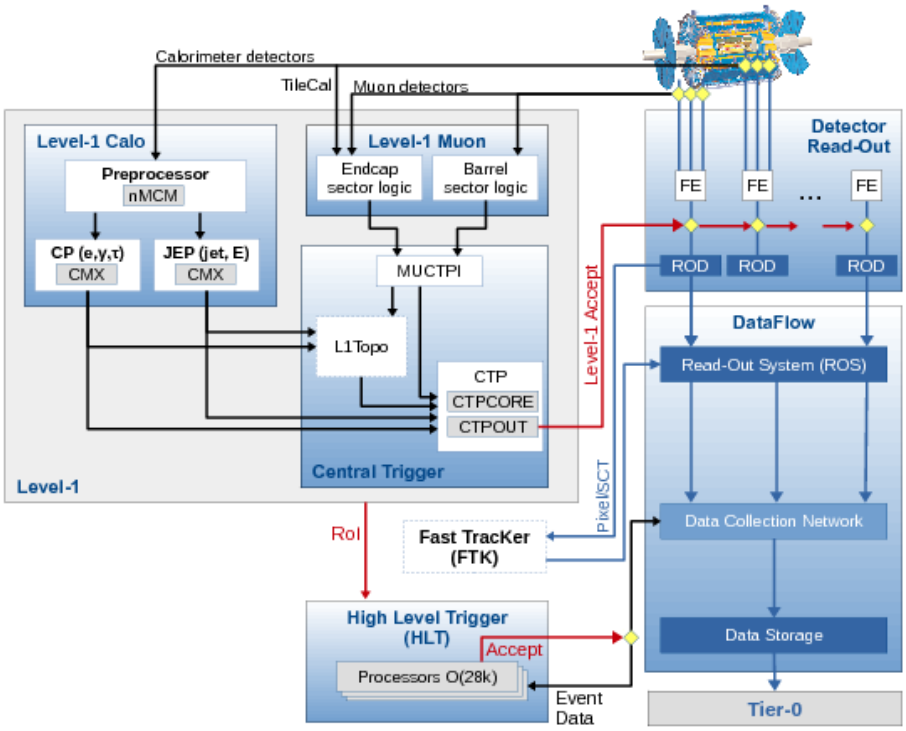

Figure 2.14 – The ATLAS trigger and data acquisition system used during Run-2.

2.2.8 ATLAS Run-1 and Run-2

The first events coming from p-p collisions were first recorded by ATLAS in 2009. Since then, the center-of-mass energy as well as the instantaneous luminosity increased throughout the years. Run-1 corresponds to the period of data taking from 2009 to 2012, during which data was collected at a center-of-mass energy of 7 and 8 TeV corresponding to 26.4 fb^{-1} recorded by ATLAS. After 2012, the LHC entered a period of long shutdown (LS1) where the ATLAS detectors underwent upgrades and improvements to be able to handle the increase in the LHC performance. The LHC activities resumed in 2015 and continued until 2018 which is the period referred to as Run-2. During this period, the center-of-mass energy was increased to 13 TeV and ATLAS was able to record an integrated luminosity of 147 fb^{-1}. Since the end of 2018, the LHC is in the second long shutdown (LS2), and ATLAS is undergoing several upgrades in preparation for Run-3.

2.2.9 Monte Carlo and events simulation

Monte Carlo generators are used to simulate p-p collisions at the LHC with a high level of precision. Event simulation is used to predict and estimate the signal and background composition of the data collected by the detector, and is used in analyses to compare the agreement of the Monte Carlo prediction with the data. In addition, the simulated events are used for analysis optimisation studies and background modelling systematics estimation as well as for detector effect corrections.

Monte Carlo generators describe a complex final state of the interactions, as shown in Figure 2.15, and are built around different models of hard scattering, parton shower (PS), hadronisation and underlying event (UE). Monte Carlo generators simulate the collision, the interaction of partons and the particles resulting from their interaction. The Monte Carlo events are passed through a simulation of the ATLAS detector using GEANT 4, which simulates the interactions of particles

in the materials to create realistic detector signals.

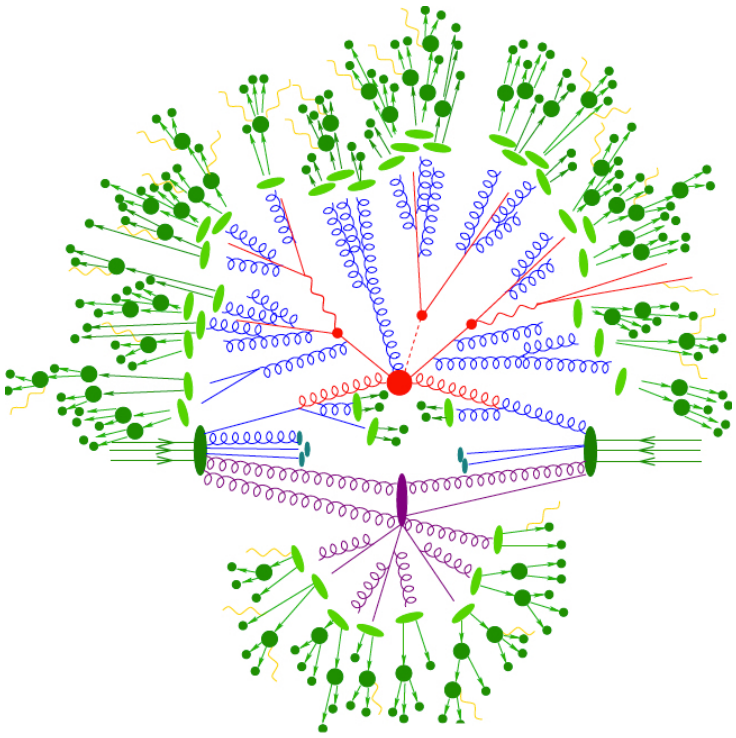

Figure 2.15 – Schematic view of the interactions from a single p-p collision [66]. The red lines correspond to the hard scattering process, the blue to the parton shower and ISR/FSR, the green to the hadronisation and the purple to the underlying event.

Hard scattering

The matrix element (ME) corresponds to the hard scattering generation of the processes of interest. It is computed from Feynman diagrams at a given order in perturbation theory (depending on the generator and the process considered). The ME, when computed beyond the first few orders of perturbation theory, requires a considerable effort and time.

Since the protons are composite particles made up of quarks and gluons, the parton distribution functions (PDFs) are a key component to be able to compute the hard process. The PDFs correspond to the probability of a parton to carry a fraction x of the proton's momentum. The calculation of the cross-section of the hard scattering consists of integrating the matrix element-squared, expressed as function of the PDFs over the phase space of the process of interest.

Parton shower

The parton shower corresponds to the radiative QCD corrections, added to simulate a real emission of partons before hadronisation. The partons produced through the hard process are emitted with a large momentum, which leads to them loosing their energy through QCD radiations in the form of gluon emissions. The gluon will then produce a pair of quarks, which will also emit a gluon and so on. This is referred to as the QCD cascade or the tree structure. This process ends when the partons have a low energy for any QCD emission and thus proceed to the hadronisation. The QCD radiation at each emission stage is expressed in terms of the Sudakov form factor which is the probability of a parton to not emit a parton within a certain interval of time. There are two types of showering: the final state showers (FSR), that develop from the outgoing partons of the hard process and the initial state showers (ISR) that develop from the incoming partons. In the FSR, the parton follows the process described where it keeps

splitting until it reaches a certain energy in the so-called forward evolution. On the other hand when the correction is ISR, the process is initiated with a higher energy than that of the colliding partons, and is added by fixing the final state partons and going backwards to model the initial partons in the so-called backward evolution. These corrections are calculated using perturbation theory. This implies that a very large number of processes must be generated, so to reduce the computational time only the leading processes in each order are taken into account.

Hadronisation

The hadronisation is the step at which the partons in the final state are transformed into hadrons. The partons generated by the hard scattering and the parton shower are colorful objects that cannot be observed as objects by the detector. At the end of the parton showering, since the QCD running constant g_s increases at low energies, the perturbation theory becomes invalid and the process enters a non-perturbative phase. Therefore, the gluons and quarks gather together to form hadrons which can be observed in the final state. The hadronisation simulation is performed using one of the two models: the Lund string model or the cluster model. In the string model, the potential of the pair of quark and anti-quark created through a gluon increases linearly as they move apart and creates further gluons. In this model each gluon field is considered as a line, that form all together one string. The cluster model is based on the QCD pre-confinement property [67], in which the partons bind into clusters during parton showering depending on their color charge, and then break down into final state hadrons.

Underlying event

The underlying event correspond to the particles coming from the p-p collision and not associated to the hard process, in addition to events from FSR and ISR radiation from the hard scattering. The UE is associated to all the simulated events and has low energy, so it will not create additional hard processes, but rather create hadrons with low energy.

ATLAS simulation and software

After the simulation of particles produced from the interaction point, the next step consists on simulating the ATLAS detector response to the particles passing through it. The simulation of the ATLAS detector is a major challenge given the complexity of the detector, and is provided by the GEANT 4 toolkit [68]. The GEANT 4 design provides a detailed description of the geometry of all the sub-detectors, the physics processes (electromagnetic, hadronic and optical) over a wide range of energy and the energy deposited by the particles when they interact with the material. The tracks in the detector are digitised by simulating the same readout electronics as the sub-detectors to convert the electric signal in the detector to a digitised signal. Due to the details in the characterisation, this simulation is very CPU intensive. It can be reduced by using a fast-simulation (AF2) [69] with a parametrised calorimeter response of single particles. The GEANT 4 design has been upgraded to include in its description all the detector upgrades and improvements. The events are then reconstructed, using the same ATLAS software as the one used to reconstruct data events. At this step, the digitised signals collected by the detector are converted into physical objects using the ATHENA framework based on the Gaudi framework [70].

2.3 High luminosity LHC and ATLAS upgrades

The LHC machine is expected to operate until 2037 and to push the limits of its research programs. The High Luminosity LHC project [52] (HL-LHC) is a physics program taking place

after Run-3 and scheduled to start operation in 2027. The project aims to increase the center-of-mass energy to 14 TeV and achieve an instantaneous luminosity higher than the current Run-2 design of $7.5\times10^{34}\,\mathrm{cm}^{-2}\mathrm{s}^{-1}$, and deliver an integrated luminosity of $3000\,\mathrm{fb}^{-1}$ over the LHC operation period. This implies tuning the beam parameters: increase the number of protons per bunches to 2.2×10^{11} protons, reduce the number of bunches per beam to 2748 bunches and reduce the bunch sizes to 8.2×10^{-4} cm. For the LHC to achieve the expected performance, many improvements are required including the replacement of four of the superconducting magnets with shorter magnets of 11-12 T freeing space to add collimators, use new technologies for the beams injection and collimation systems and update several modules of the LHC to be resistant to the high radiation doses. The LHC machine will therefore undergo several upgrades, taking place over the first, the second and the third LHC long shutdowns as shown in Figure 2.16. First, the consolidation of the electrical splices between the superconducting magnets took place during LS1, which allowed to improve the center-of-mass energy up to 13 TeV. During LS2, the injector chain is being upgraded to increase the number of proton in the bunches, which improves the intensity and brightness of the beam and later during LS2, the main installations for the HL-LHC will take place.

ATLAS detector upgrades are necessary to cope with the HL-LHC configuration and to maintain its performance. They correspond to the Phase-I and Phase-II upgrades which will take place during the LS2 and LS3 respectively. In Phase-I, the new muon small wheels [71] (NSW) are being installed to replace the inner most part of muon system in the end-caps by eight layers of small-strip TGC (sTGC) and Micro-Mesh Gaseous Structures (Micromegas) to cope with the high radiation and pile-up rate and to cover up to $|\eta|$ <4.0. The NSW provides a higher granularity for a better momentum reconstruction and reduces the reconstruction of fake muons which therefore reduces the trigger rate. In addition, the LAr L1 trigger upgrades are taking place aiming to provide a better resolution and granularity, which will improve the rejection of the jets for the electromagnetic triggers.

The majority of the ATLAS upgrades will take place during Phase-II. Due to the radiation damage, the current ID will be replaced by the Inner Tracker (ITK) [72, 73] to improve the performance. The ITK detector will be made of layers of silicon modules with a fine granularity and a better handling of the pile-up and a high radiation resistance. In addition, the LAr readout electronics will be replaced because of their aging, in addition to coping with the increase of the radiation doses and with the new trigger configuration. Similarly, the Tile calorimeter readout electronics will be updated to cope with the increase in luminosity. Finally, the trigger system architecture will be changed to handle the increase in the particle fluxes. The updated level-0 trigger will take information from the calorimeters and from the muon trigger and then send the accepted events to the level-1 trigger. The level-1 benefits from the improved granularity of the calorimeters to match the cell to tracks in the muon spectrometer and uses pattern recognition to match the information in all the sub-detectors before passing the accepted events to the HLT.

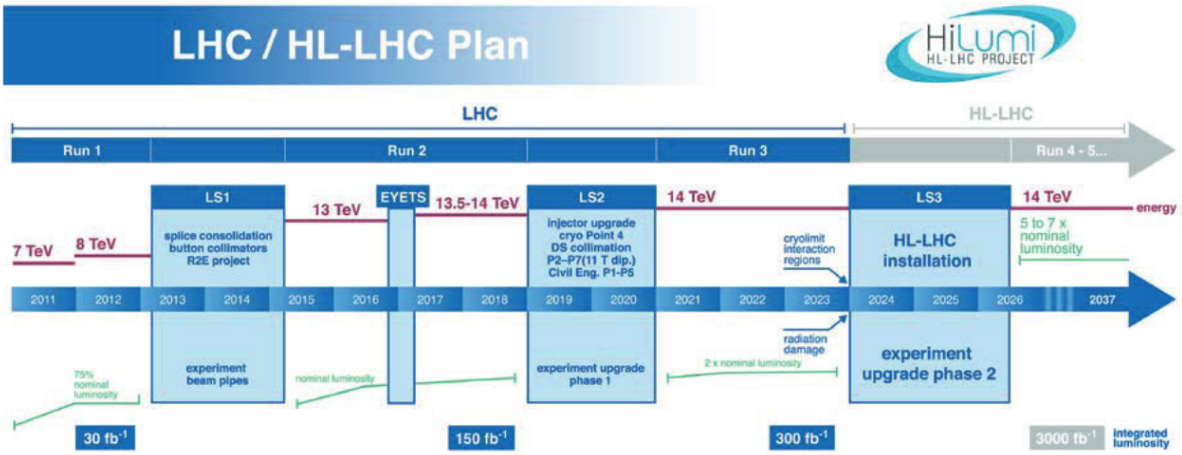

Figure 2.16 – The LHC plan for upgrades aiming for HL-LHC as of 2017 [52].

Chapter 3

Characterisation of the LAr pre-amplifiers for the HL-LHC

The liquid argon (LAr) calorimeters readout electronics will be replaced during the Phase-II upgrade for the operation of the High luminosity LHC. In the LAr front-end electronics, the pre-amplifiers handle the first stage of the signal processing which consists on amplifying and shaping the signal. Two ASIC designs matching the requirements, LAUROC0 and HLC1, have been proposed to substitute the current pre-amplifiers and shapers. In this Chapter, the liquid argon readout electronics system is presented in Section 3.1, the Phase-I upgrade in Section 3.2 and the Phase-II upgrade for the HL-LHC program in Section 3.3. Section 3.4 is dedicated for the study of the specification of the gains of the pre-amplifiers. The new LAUROC0 and HLC1 ASICs are presented in Section 3.5. The test bench used for the characterisation of the new front-end chips is presented in Section 3.6 and the results in Section 3.7. Finally, Section 3.8 is dedicated for the next pre-amplifier/shaper ASIC iterations.

3.1 The LAr readout electronics system

Incident particles coming inside the detector create showers and ionise the liquid argon to induce signal current. Due to the high voltage applied between the absorber material and the electrodes, the electrons and ions drift towards the electrodes which are made with copper layers and Kapton. The signals are collected in the form of a triangular shaped pulse of 450 ns in the electromagnetic barrel (EMB) corresponding to the drift gap of 2.1 mm, with the amplitude proportional to the energy deposited by the incident particle. The drift gap size is different and varies in the end-caps as well as the HEC and the FCal because of their geometry. The LAr readout electronics are designed to collect and record these energies and then convert them into digitised signals to be used for offline processing. The LAr readout electronics system covers a large dynamic range of energies from the minimum ionising particles (MIP) of around 50 MeV up to an energy of 5 TeV, with a good energy resolution (a constant term of 0.4% in a single cell and 0.7% over the whole calorimeter). The LAr system is composed of the on-detector and off-detector signal processing systems as shown in Figure 3.1 and has been operating since the beginning of Run-1.

The on-detector electronics correspond to the Front-End (FE) electronics which were initially designed to operate up to 10 years. They are mounted directly on the LAr cryostats, in the gap between the barrel and endcap calorimeters and on the outer face of the end-cap cryostats. They are housed in 58 crates, in both the barrel and the end-caps, for noise optimisation, each

containing: the Front-End Boards, the readout Tower Builder Boards (TBBs) to perform the final level of analog summation and to transmit the trigger tower signals to the Level-1 trigger, the Calibration Boards to inject current with a precisely known amplitude and shape to simulate energy deposits in the calorimeters, and the Controller Boards used to receive and distribute the control and monitoring signal from the various FE boards.

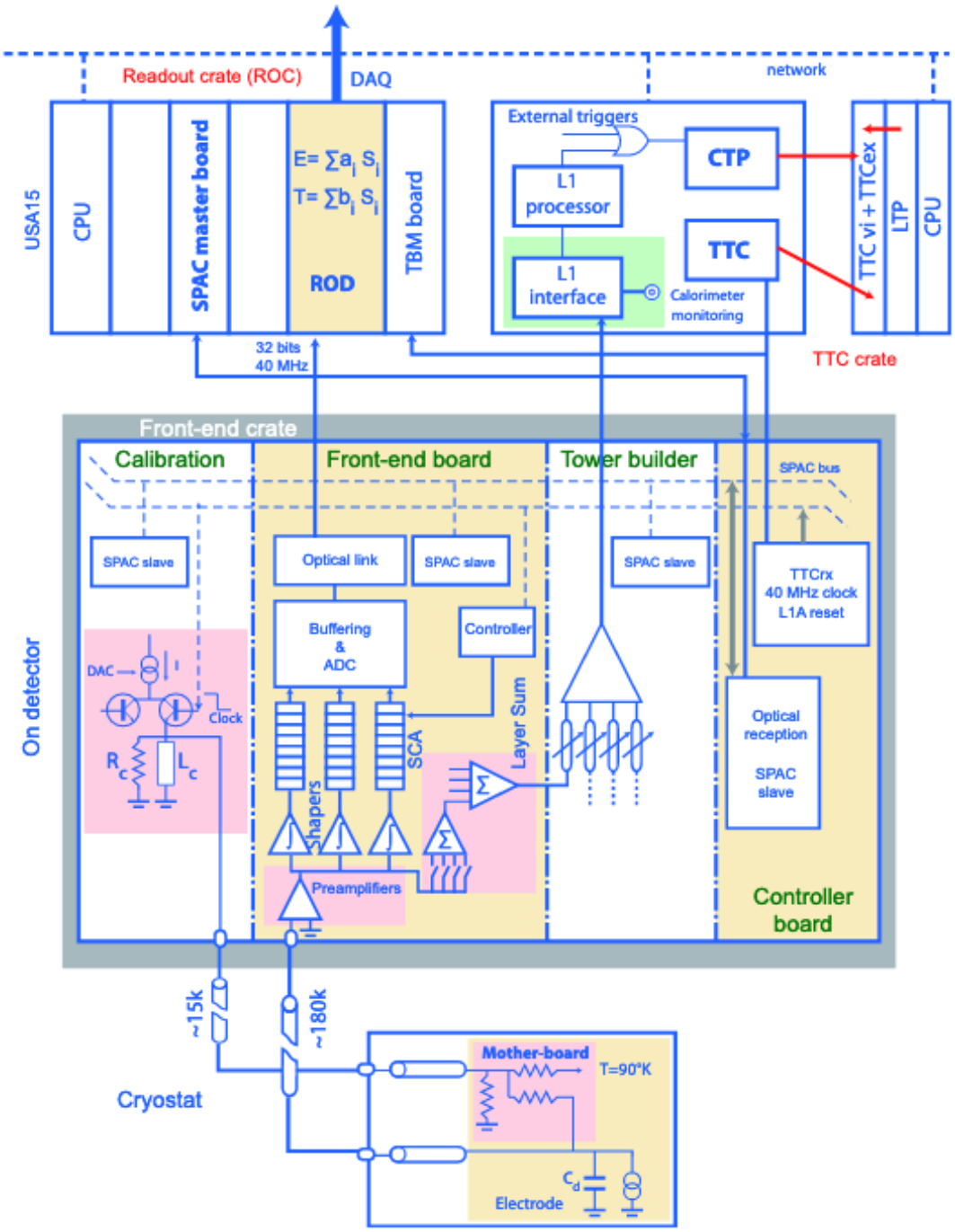

Figure 3.1 – Sketch showing the LAr readout electronics architecture. The bottom is a depiction of the LAr calorimeter equivalent circuit. The middle corresponds to the FE electronics. The top corresponds to the off-detector electronics.

The Front-End Boards (FEBs) are the main element of the FE. On the FEBs, the signal coming from the detector is amplified above the electronic noise level and then split into three overlapping linear gain scales (high, medium and low gains) each covering different energy ranges with gain ratios of about 10. Furthermore, shaping is applied to convert the triangular shaped signal into

a bipolar signal using a CR-$(RC)^2$ filter upon signals accepted by the L1 trigger. The signal is sampled at the LHC bunch crossing frequency of 40 MHz by creating signal samples separated by 25 ns as shown in Figure 3.2. Finally, the signals are digitised using Analog-to-Digital Converter (ADC) to create 4 (5) samples per event during Run-2 (Run-1).

These events are formatted and then transmitted using optical output links to the back-end (BE) off-detector readout electronics. On the BE electronics, the Readout Driver (ROD) are responsible for digital filtering, formatting, and monitoring of the calorimeter signals. They allow to compute the energy, the time and the quality of the digitised samples sent by the FEBs.

Analog sums are performed on the analog signal in neighbouring cells in one layer on each FEB to create trigger towers with a granularity of 0.1×0.1 in $\Delta\eta \times \Delta\phi$, which are then sent to the TBB (or the Tower Driver Board (TDB) for cells in the HEC or the FCal). Afterwards, the TBB performs signal processing before sending the signal to the L1 calorimeter trigger.

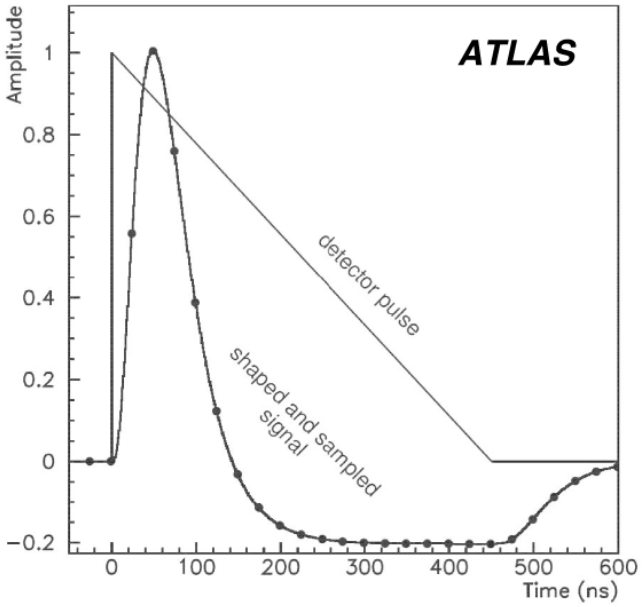

Figure 3.2 – Shape of the LAr calorimeter triangular pulse from the detector and the signal pulse after shaping and sampling. The dots on the bipolar signal illustrate the digital samples separated by 25 ns.

3.2 LAr readout electronics Phase-I upgrades

The Phase-I upgrade towards the HL-LHC configuration concerns the calorimeter Level-1 trigger system and the readout electronics will remain unchanged. The aim of this upgrade is to provide higher-granularity, higher-resolution and longitudinal shower information to the trigger processors. The new trigger configuration replaces the Trigger Tower concept based on the sum of energy deposited in the longitudinal calorimeter layers in cells of dimensions 0.1×0.1 in $\Delta\eta \times \Delta\phi$. The new configuration computes the calorimeter information using a finer granularity scheme which is based on the Super Cells configuration. Figure 3.3 shows the increase in the trigger granularity.

This upgrade provides a finer segmentation in cells of dimensions 0.025×0.1 in $\Delta\eta \times \Delta\phi$ in the region of $|\eta| \leq 2.5$, in addition to providing information in each of the four calorimeter layers. The new trigger configuration improves the trigger energy resolution and therefore provides sharper trigger turn-on curves. In addition, the smaller quantisation scale allows to make selections based on the shower shape and thus to have a better rejection of hadrons.

The new LAr Trigger Digitizer Boards (LTDB) will digitise the super cell signals and will send them off-detector to the LAr Digital Processing System (LDPS) that will handle the processing. These boards are installed during the Phase-I upgrade and will not change for the Phase-II upgrade.

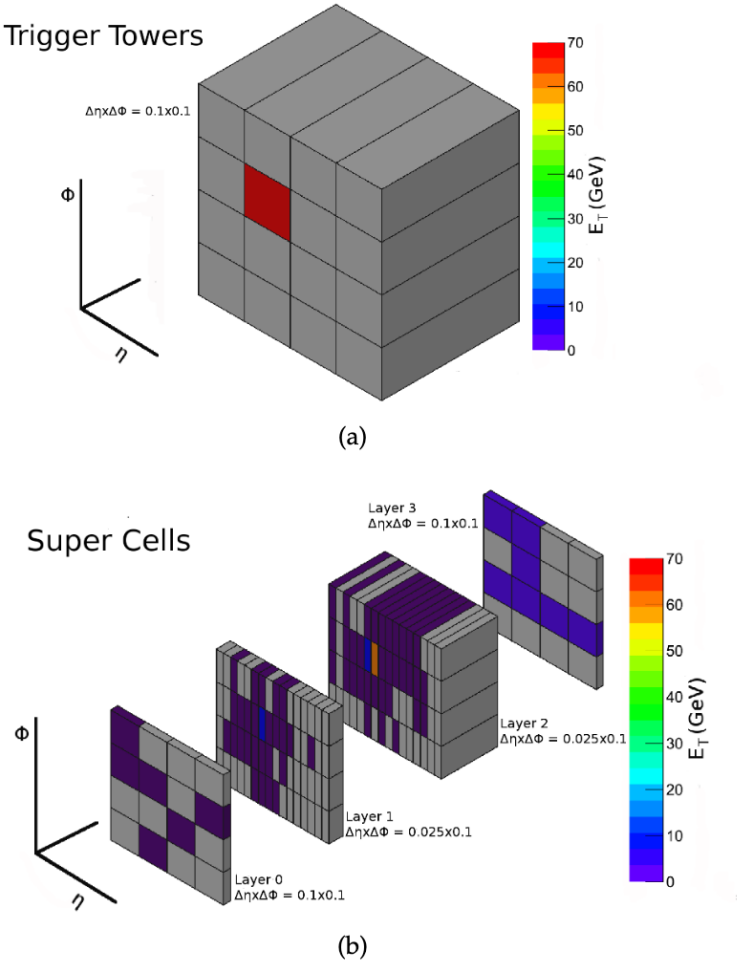

Figure 3.3 – Illustration of the energy deposited by an electron in the existing trigger electronics (a) and in the super cells configuration (b).

3.3 LAr readout electronics Phase-II upgrades

3.3.1 Requirements for the HL-LHC

The second phase of the LAr readout upgrades aims at preserving the performance of the readout system with the increased pile-up level (up to 200 interactions per bunch crossing) and data taking rate, in addition to coping with the Phase-II upgraded trigger and data acquisition system which is incompatible with the current electronics. Therefore the existing LAr readout electronics will be completely replaced during LS3. Moreover, the current front-end electronics were designed to operate for 10 years under the current LHC conditions, so they would not handle the increase of radiation doses and would reach the limit of their radiation resistance before the end of the HL-LHC operation.

The requirements of the new electronics [74] have been studied from the expected physics performance at the HL-LHC. Therefore the new design will have a two gain output: the high and

low gains, which allows to remove a limitation of the current system of three gains as presented later in Section 3.4.2. Two different line-adapted pre-amplifiers are used in different parts of the detector: the 25Ω pre-amplifiers are used in the middle and the back layer cells and the 50Ω pre-amplifiers used in the pre-sampler (PS) and the front layer. Since energies up to 5 TeV are expected to be measured, new electronics should also have a wide dynamic range and cover signal up to 10 mA and 2 mA in the middle/back and front/PS cells respectively. These requirements on the dynamic ranges are defined from the study using high energy jets and electrons coming from high mass Z' resonance decays with energies up to 5 TeV. To be able to perform electroweak precision measurements (determining the Higgs boson and the W boson masses), a good linearity better than the percent is required throughout the whole dynamic range and especially at low energies (up to 10% of the dynamic range). Even though a high level of pile-up is expected with the increase in luminosity, the electronic noise should be low enough to measure the MIP deposited by the muon in the calorimeters and ideally similar to the current electronics.

3.3.2 Architecture of the Phase-II readout electronics

The Phase-II implementation is shown in Figure 3.4. During the Phase-II upgrade the FEBs will be replaced with the next generation FEB2 that will be placed in the same position in the FE crates on the LAr cryostat. The FEB2 will include a new front-end analogue ASIC which contains a pre-amplifier and a shaper. Two 14 bits ADCs are used to digitise both of the two gain outputs of the pre-amplifiers. The signals are then sent at 40 MHz rate to the off-detector electronics, where the new LAr Signal Processor (LASP) acquisition card will do the processing, which is currently carried out in the RODs. Finally, the Calibration Boards and the Controller Boards will also be replaced to conclude the LAr phase-II upgrade.

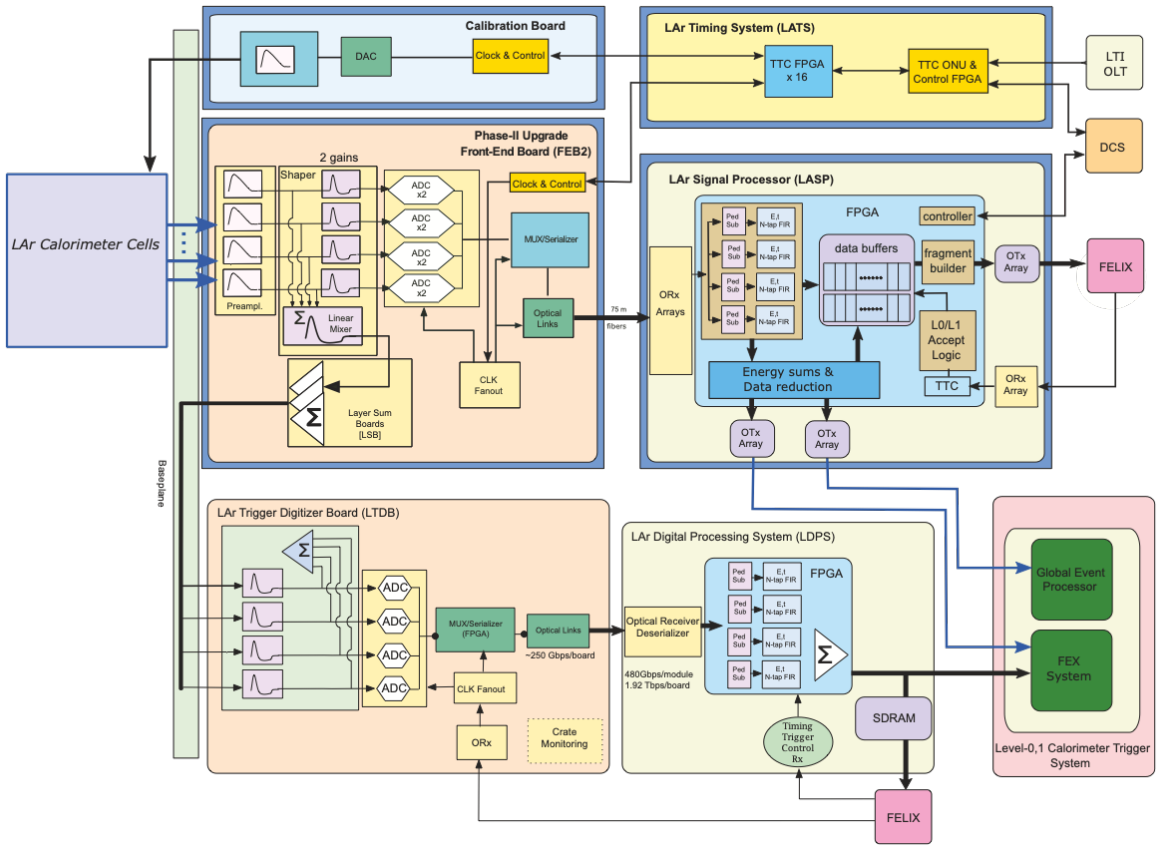

Figure 3.4 – Sketch of the LAr calorimeter readout architecture for the Phase-II upgrade.

3.4 Specification of the ratios between the low and high gain outputs

3.4.1 Quantisation effect

The pre-amplifier/shaper ASICs have been developed to be used on the new FEBs using a 14-bit range ADC with 12-bit resolution. Each ADC digitises one gain output and sends the digitised signals to the back-end electronics. The gain quantisation noise is taken of the order of the ADC Least Significant Bit (LSB). On the low gain (LG), this represents a larger noise value. Gain switching happens when the high gain (HG) reaches the maximum of its dynamic range. An increase of the total noise in the high energy cell due to the larger quantisation noise when switching gains should be avoided. A simulation study has been performed to test if the HG and the LG meet the requirement of having a quantisation noise significantly lower than the intrinsic LAr resolution at the gain switching energy.

The digitisation is performed assuming an ADC with a noise of half an LSB. The calorimeter bipolar pulse requires having one fourth of the dynamic range reserved for the negative lobe of the signal. Therefore the absence of a signal corresponds to an ADC code of $\frac{1}{4} \times 2^{14}$. Figure 3.5 shows the comparison of the LAr intrinsic resolution in a single cell approximated by $\frac{10\%}{\sqrt{E}} + 0.2\%$, to the quantisation noise with a typical gain ratio (ratio of the HG over LG) of 23 for the middle layer and 19 for the front layer, which are also used in the LAUROC0 pre-amplifier prototype presented in the next Section. A representative cell was taken for each of the middle/front and endcap/barrel to do the comparison.

The quantisation noise is better than the LAr resolution through out the dynamic range. At the gain switching point, occurring at the highest energy digitised in the HG of around 30 GeV in the front layer and 120 GeV in the middle layer, the digitisation noise is an order of magnitude lower than the LAr resolution. This satisfies the digitisation scheme requirements, necessary to not degrade the total resolution and shows that the gain ratio can be set to other values around 20-25 without compromising this result.

3.4.2 $H \to \gamma\gamma$ decay simulation in LAr cells

The gain intercalibration is a source of uncertainty with a high impact on the measurement of the mass of the Higgs boson in the diphoton channel [75, 76]. With the current three gains system, the electrons coming from $Z \to ee$ decay that are used to calibrate the energy scale and have most of their cells in the high gain, while many of the photons from $H \to \gamma\gamma$ decay have their highest energy cell in the medium gain. The gain switching should be arranged such that, which the new two gain system, all the photons coming from $H \to \gamma\gamma$ decays land in the HG cells, similarly to the electrons coming from $Z \to ee$ decays. This requirement would remove any gain intercalibration systematic from the Higgs mass measurement.

The study was conducted using 80k events from a $H \to \gamma\gamma$ simulation when the Higgs boson is produced in the gluon-gluon fusion mode. The events were generated using Powheg [77] generator using the PDF4LHC NLO PDF set [78] and interfaced with Pythia8 [79]. The maximum current deposited in each of the LAr cells is computed for each photon after using the correct μA/GeV conversion value for each of the front and middle cells, determined from the real LAr cells. The photons have a cell in the LG if the energy in the cell's energy is larger than the maximum of HG dynamic range. The results are presented in Figure 3.6, assuming gain ratios of 23 (19) for the middle (front) layer, which also shows the gain switching energy assuming that it happens at 90% of maximum of the high gain dynamic range, and not at 100% as a safety margin.

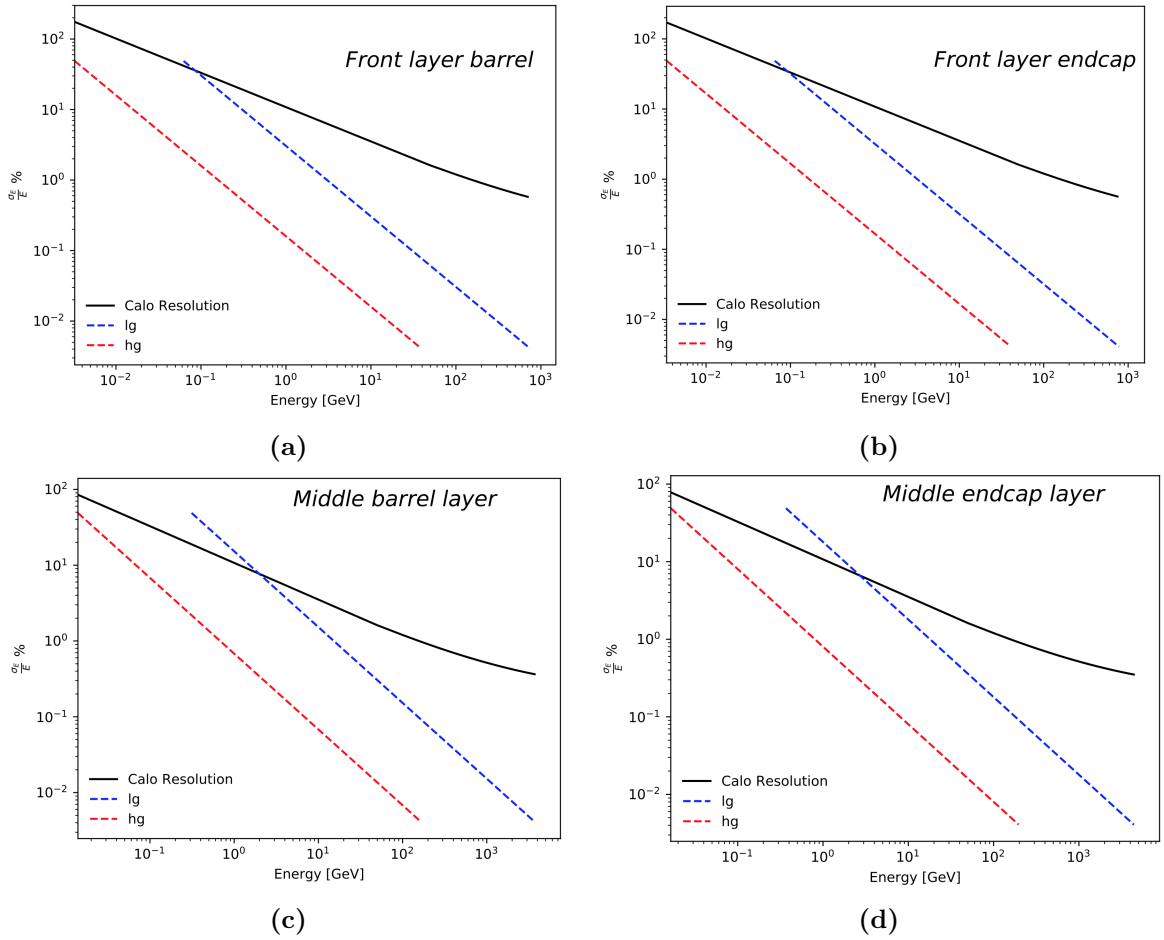

Figure 3.5 – The estimated quantization noise and the intrinsic calorimeter resolution as function of energy in the LAr EM front layer in the barrel in (a) in the end-cap in (b) in the LAr middle layer in the barrel in (c) in the end-cap in (d).

The starting values for the gain ratio are good values, where only 1.1% of the photons have one middle layer cell in the LG and 1.8% have one front LG cells. Therefore, the vast majority of the $H \rightarrow \gamma\gamma$ events will not be affected by the gain intercalibration systematic. Most of the photons with LG cells are photons in the end-caps ($\eta > 1.4$) as shown in Figure 3.7 ,which anyway contribute less to the mass measurement of the Higgs boson mass as their resolution is worse than the central barrel ones.

Different gain ratio values of 15, 20, 25 and 30 were investigated using the same $H \rightarrow \gamma\gamma$ simulated samples for the front and middle layer cells. This is done to estimate the amount of photons having LG cells for each gain ratio and thus decide on the most optimal gain ratio. Table 3.1 shows that the tested gain values are all fine and that even when increasing the gain ratio up to 30, the fraction of photons with one cell in the LG remains reasonable. A given ASIC design can implement any gain ratio between 18 and 28 without impacting significantly the performance.

3.5 The LAUROC0 and HLC1 pre-amplifier prototypes

Two ASIC prototypes are developed, one using 65 nm and the other 130 nm CMOS technology. The ASIC design should match the stringent specifications: an integrated linearity at the per mille level over 10% of the full dynamic range and an equivalent noise current similar to

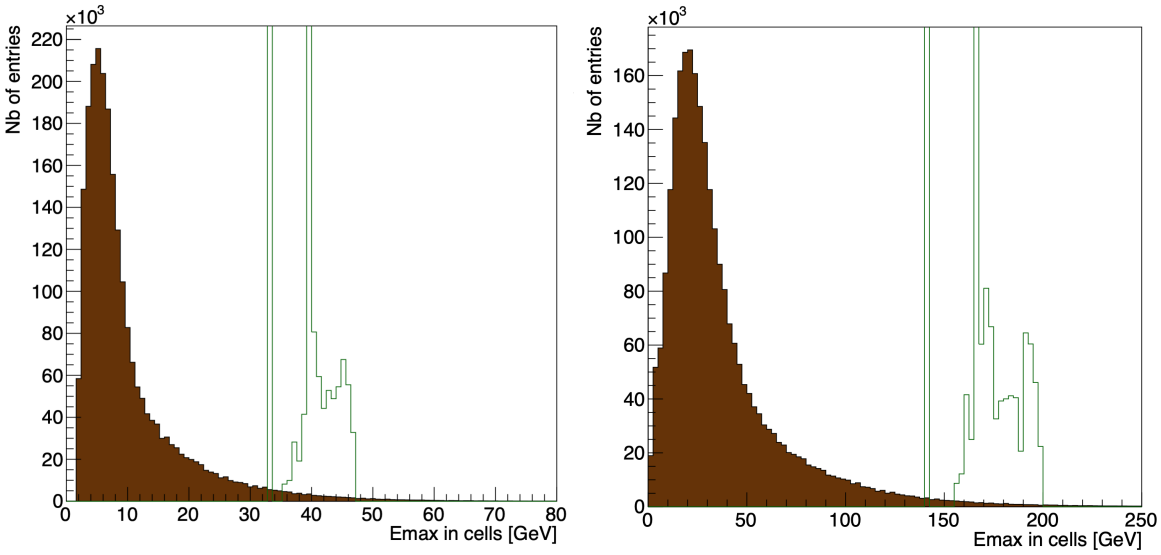

(a) **(b)**

Figure 3.6 – The maximum energy of the cells represented in the brown histogram of photons coming from the Higgs decay in the front layer (a) and the middle layer (b). The green histograms correspond to the energy at which the gain switching occurs. The gain switching energies are shown in a histogram because they depend on the η.

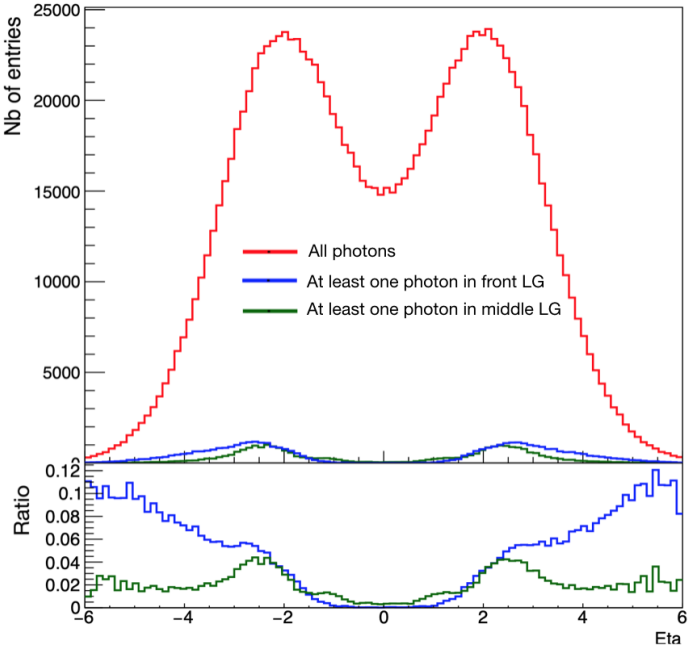

Figure 3.7 – The pseudo-rapidity distribution showing the fraction of photons with cells in front LG and middle LG. The lower panel shows the ratio with respect to all the photons.

the current electronics of 150 nA and 46 nA for the 25Ω and 50Ω pre-amplifiers respectively. Two different prototype designs have been proposed: the Liquid Argon Upgrade Readout Chip (LAUROC0) which is designed by teams at IJCLab and OMEGA-Centre de Microélectronique and the HLC1 chip designed by a team at Brookhaven National Laboratory (BNL). The final decision will be made based on the design that has the best performance.

Both prototypes have a pre-amplifier to amplify the signal coming from the detector into two different gain outputs, the low gain (LG) and the high gain (HG). A CR -$(RC)^2$ filter is imple-

Gain ratio	Front layer	Middle layer
Current design	1.8%	1.1%
15	0.7%	0.2%
20	2.1%	0.7%
25	4.2%	1.6%
30	6.5%	3.0%

Table 3.1 – The fraction of photons having LG cells in the front and middle layer.

mented in the HLC1 design to create a the bipolar shaped signal as shown in Figure 3.2, with a peaking time constant around 15 ns. The signals are then digitised through 14-bit ADCs at a 40 MHz rate. Both designs have two different types of line-adapted pre-amplifiers (25Ω and 50Ω) with different dynamic ranges, to be used in different part of the calorimeters. The 25Ω channels are used for the cells in the middle and back layers in addition to the FCAL cells and the 50Ω channels are used for the pre-sampler and the front layer cells.

LAUROC0 design

The LAUROC0 ASIC is designed in 130 nm CMOS technology and was received in October 2016. The prototype includes eight different single-ended line-adapted pre-amplifiers to accommodate the maximal input currents, with different transistor sizes and different dynamic ranges. Five of these pre-amplifiers are dedicated 25Ω channels and two are dedicated 50Ω channels. The last channel can be used as either a 25Ω or 50Ω and was implemented to compare its performance with the other dedicated channels, to decide if the next iterations will only include channels with configurable terminations. Since this design does not include an integrated shaper, an external CR-$(RC)^2$ shaper is applied with $\tau = 15$ ns to create a signal with a typical rise time of 45 ns for a calorimeter cell of 1.5 nF capacitance. The schematic of the LAUROC0 design is shown in Figure 3.8.

One specificity of the LAUROC0 design is that the HG is made on the same pre-amplifier as the LG. Therefore, when the HG output saturates at high energies, it affects the linearity of the LG output. In order to not disturb the LG, a tunable switch discriminator was implemented to cut the HG output when it is triggered above a certain energy threshold. This discriminator is controlled by a voltage threshold on the LG output.

The pre-amplifiers feature a tunable input impedance (Z_{in}) to match the cable and mitigate the signal reflections by adjusting the following capacitor ratio:

$$Z_{in} = \frac{R_0 + Z_{inSCB}}{1 + |G|} \tag{3.1}$$

Where the voltage amplifier G is made using capacitors from the ratio -C_1/C_2 with C_1 value being fixed to 30 pF. The Z_{inSCB} is a low input impedance of a Super Common Base (SCB) amplifier and R_0 is the input transistor with a fixed value. The R_0 resistance defines the maximal pre-amplifier input current while a tunable R_f resistance is implemented to control the LG dynamic range. The parameters for each of the 25Ω and 50Ω pre-amplifiers are presented in Table 3.2.

Channel	Z_{in}	C_2	R_0	R_f
PA 25Ω A	Adjustable	coded on 7-bits	100Ω	1kΩ or 2kΩ
PA 25Ω B	Adjustable	coded on 7-bits	100Ω	1kΩ or 2kΩ
PA 25Ω C	Adjustable	coded on 7-bits	100Ω	1kΩ or 2kΩ
PA 25Ω D	Adjustable	coded on 7-bits	100Ω	1kΩ or 2kΩ
PA 25Ω E	Fixed	coded on 7-bits	100Ω	1kΩ or 2kΩ
PA 50Ω A	Fixed	coded on 7-bits	500Ω	10kΩ or 20kΩ
PA 50Ω B	Adjustable	coded on 7-bits	500Ω	10kΩ or 20kΩ
PA 25_50Ω	Adjustable	coded on 9-bits	same as 25Ω or 50Ω PAs	

Table 3.2 – Characteristics of the different LAUROC0 input channels. The letters are used to distinguish between the dedicated 25Ω and 50Ω channels. The adjustable channel is noted as 25_50.

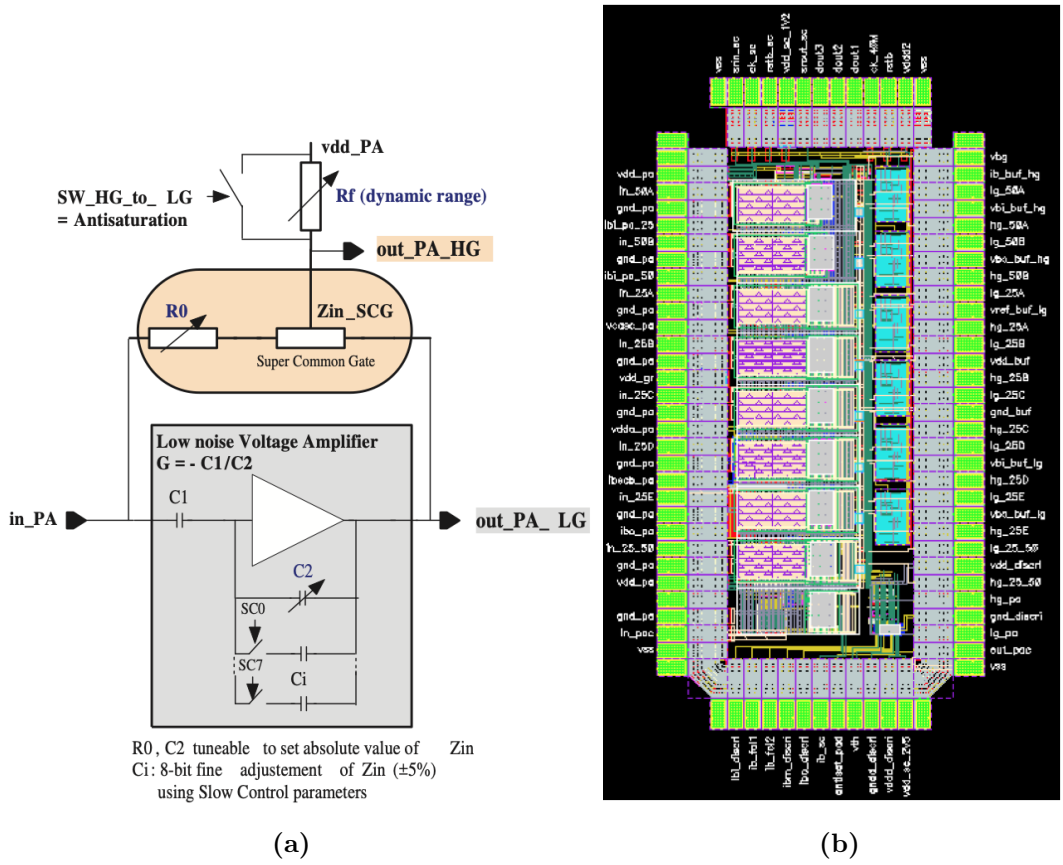

(a) **(b)**

Figure 3.8 – Sketch of the LAUROC0 pre-amplifier in (a) and the Layout of the LAUROC0 ASIC in (b) [74].

HLC1 design

The HLC1 is a design developed in the 65 nm CMOS process from TSMC which includes a pre-amplifier and a shaper and was received in July 2017. The design is packaged in a 128-pin LQFP package with 14 mm × 14 mm dimensions and is presented in Figure 3.9. The HLC1 contains eight identical fully differential pre-amplifiers with passive feedback to optimise the noise performance. These pre-amplifiers are configurable to be used as either 25Ω or 50Ω terminations. Contrary to the LAUROC0, the pre-amplifier delivers a LG output then makes an amplified copy to give the HG, thus allowing to read out simultaneously both gains to have a good coverage of

the dynamic range. The ASIC includes also a trigger summing output, of either four or eight output channels.

The peaking time can be adjusted in the integrated shaper over 2-bits from 30 ns to 50 ns. This allows to optimise the detector response and deal with the different pile-up rates in the calorimeters. The input impedance is configurable directly over 3-bits with a step of 0.65Ω for the 25Ω channel and 1.20Ω for the 50Ω channel.

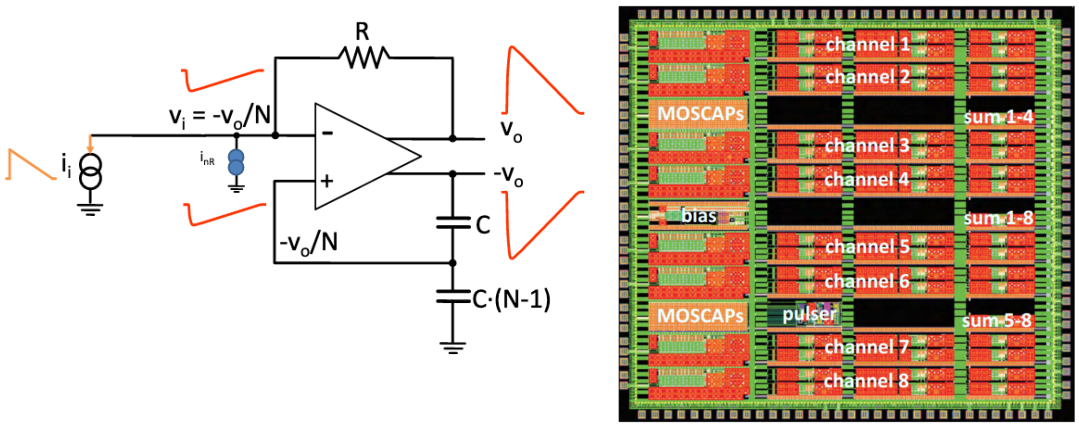

(a) (b)

Figure 3.9 – Sketch of the fully differential pre-amplifier design implemented in HLC1 in (a) and the Layout of the HLC1 ASIC in (b) [74].

3.6 Experimental setup to conduct measurements

Both architectures are tested using the same test bench to be able to evaluate them in a consistent manner. The same test stand is built in both IJCLab and BNL to test the performance of the analog front-end designs and cross-check the measurements. The test stand consists of: the toy calorimeter board, the two different Device Under Test (DUT) boards to house the ASIC prototypes obeying the requirements for the test stand, the front-end test board (FETB) and the digital readout board (ZC706). The setup also includes 25Ω and 50Ω Axon cables to be used for the corresponding channel. Figure 3.10 shows the measurement setup at IJCLab with the LAUROC0 test board.

Toy calorimeter board

The toy calorimeter is essential for the test stand, and is used to emulate the signal current coming from calorimeters to the front-end readout electronics. The toy calorimeter is connected at the input of the front-end ASIC to convert the input signal voltage into a signal current, injected using either the pulse injector in the FETB or using the integrated generator in the HLC1 board. The toy calorimeters, having eight separate outputs, are built with different injector resistance R_{inj} of 1kΩ/3kΩ and different capacitance of 1.5 nF/330 pF to be able to mimic the signal coming from the (middle and back)/(front and pre-sampler) LAr cells and reach the whole dynamic range with a reasonable voltage.

Front-end test board

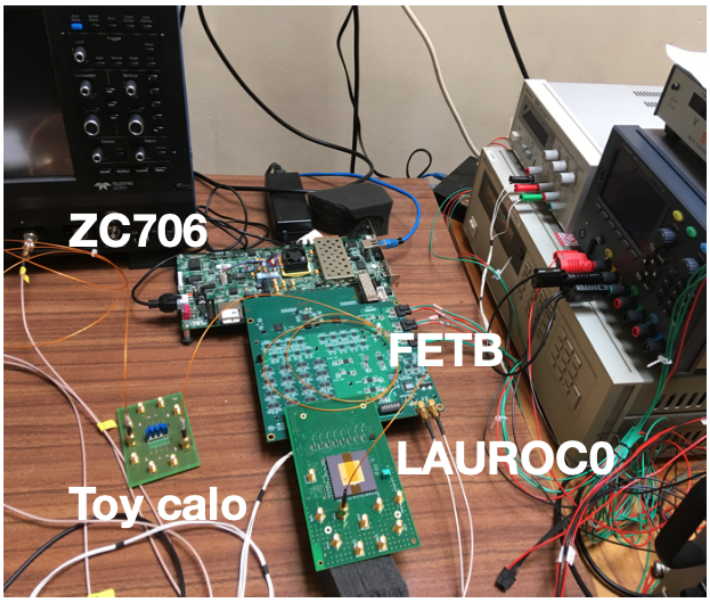

Figure 3.10 – Picture of the test bench with the LAUROC0 test board.

The FETB has an ADC driver circuit of 32 ADC channels to shape and digitise the analog signals coming from the front-end ASIC board. Half the ADCs are reconfigured to digitise single-ended inputs signals from the ASICS and the other half are used to digitise differential signals. Since the LAUROC0 does not include a built-in shaper, a CR-$(RC)^2$ filter is implemented at the input of the ADC driver to be used when the LAUROC0 is connected.

The FETB has an integrated calibration circuit (similar to the one in the ATLAS detector), with adjustable amplitude that can reach up to 5 V with a linearity of ∼0.1%, to inject a typical LAr pulse in the toy calorimeter.

Digital readout board

The Xilinx ZC706 evaluation board is used for the data acquisition of the digitised signals sent out from the FETB. The board sends the data in the right format to a computer to be able to store them to analyse them offline. The ZC706 board has a flexible configuration to control the front-end test stand and make it adaptable to the two different ASIC chips.

3.7 ASICs performance

The tests conducted on the ASICs to characterise their performance compared to the main requirements include: the integral nonlinearity (INL) through the dynamic range, the equivalent noise current (ENI) level and finally the cross-talk rate between the channels. Since the choice of the input impedance has an impact on the output gains, the input impedance is first tuned before conducting the tests. The results of the tests allow to identify what works according to the specifications in the ASICs, and what to improve for the next iteration of the prototypes.

3.7.1 Input impedance tuning

LAUROC0

The tuning was performed on the 25_50 input channel, configured once as a 25 Ω channel and once as a 50 Ω channel. The input impedance measurement was computed by fixing the value of the control parameter C_2 and measuring the voltage at the input channel for a know current injected following:

$$I_{inj} = \frac{V_{pulser}}{R_{inj} + Z_{in}} = \frac{V_{measured}}{Z_{in}} \tag{3.2}$$

A square wave generator is used to inject the current into the toy calorimeter to measure the DC input impedance. The C_2 capacitor, coded over 9-bits, is tunable within a range of 31.5 fF to ∼16 pF with a step of 31.5 fF. The measurement at the input of the channel is done using an oscilloscope, and is repeated for different C_2 configurations, in order to find the configuration for which the Z_{in} value matches that of the input channel. The results are shown in Figure 3.11.

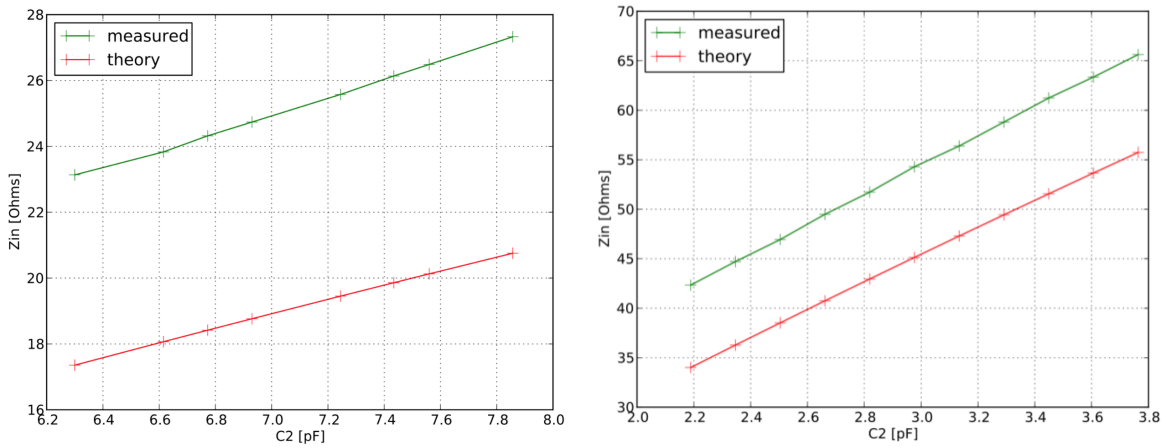

(a) **(b)**

Figure 3.11 – The measured Z_{in} values as function of C_2 in green for the 25_50 channel tuned as a 25 Ω channel in (a) and 50 Ω channel in (b). The expected values from simulation are shown by the red line.

The most adapted C_2 values were found to be 7.2 pF for the 25 Ω channel and 2.8 pF for the 50 Ω channel. A 5 Ω difference is observed between the measured Z_{in} values and expected values calculated using Equation 3.1. This difference may be due a the Least Significant Bit (LSB) capacitor true value of 160 fF instead of 125 fF for the 25 Ω channel and 40 fF instead of 31.5 fF for the 50 Ω dedicated channel and 25_50 channel. This difference in LSB values can come from variations in the manufacturing process, but has no impact since the input impedance can be tuned over a large enough range to achieve the required value. The uniformity between the pre-amplifier should be tested to see if it is necessary to make adaptations to each one of them.

HLC1

Similarly to the LAUROC0 case, the HLC1 input impedance is tuned by configuring the board to all the possible values and measuring the voltage at the input of chip. The input termination is trimmable and is 3-bit coded, corresponding to a Z_{in}range of 24.4 Ω - 28.9 Ω with a step

of 0.65Ω and a range of 47.6 Ω - 56.0 Ω with a step of 1.20Ω for the 25 Ω and 50 Ω channels respectively.

The measured Z_{in} values as function of the possible configurations are presented in Figure 3.12. The most adapted configurations were found to be config-0 in for the 25 Ω and config-2 for the 50 Ω channel and were chosen for the following measurements. These configurations are marginal and it is better to have a larger tuning range for the next iteration.

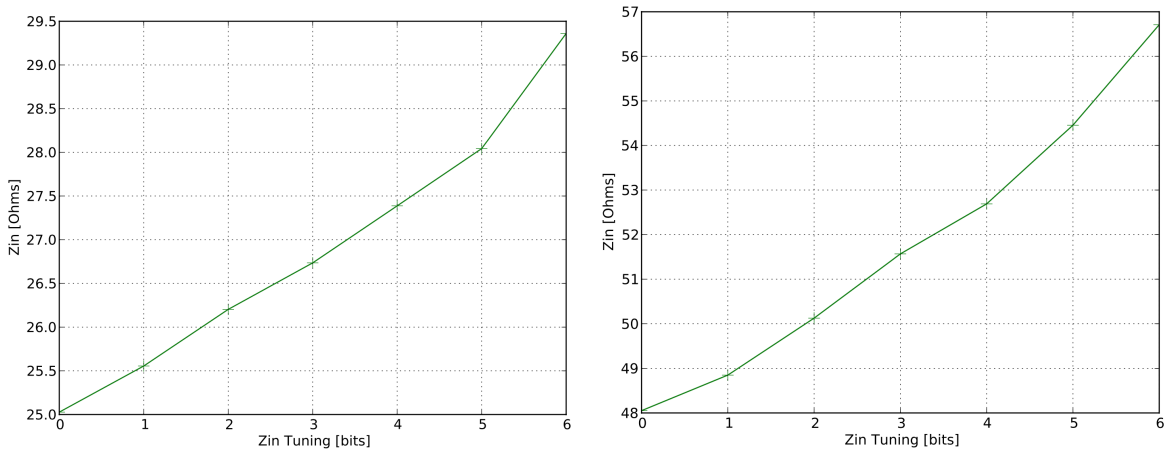

(a) (b)

Figure 3.12 – The measured Z_{in} values as function of C_2 as function of the different configurations for the 25 Ω channel in (a) and the 50 Ω channel in (b).

3.7.2 Linearity measurement

LAUROC0

The linearity is measured by injecting a known signal current at the input of the toy calorimeter until the outputs are saturated. For each current value the output of the digital readout board is evaluated, where the peak of the pulse is measured to obtain the signal amplitude. This allows to calculate the integral non-linearity (INL) of the pre-amplifiers, computed from the maximum deviation of the measured amplitude with respect to a linear-fit to these amplitudes.

For each current value, the amplitudes of the LG and HG outputs pulses are computed from the difference between the maximum of the pulse and the ramps of the pulse. The results of the linearity measurement for the 25_50 configured as 25Ω channel for both the LG and the HG outputs are presented in Figure 3.13. The dynamic range shows an INL, defined with respect to 7 mA which is a value expected to be in the dynamic range, of 0.15% for the LG up to 7 mA and 1% beyond this value and an INL defined with respect to 0.5 mA of 0.15% for the HG up to 0.5 mA, with a gain ratio of 23 between the two gains. The results of the linearity measurement indicate that the LG dynamic range meets the specifications and reaches up to 10 mA with an INL of 1% which is acceptable.

As mentioned previously, the saturation of the LAUROC0 HG output affects the linearity of the LG output and therefore a discriminator is implemented to reduce this effect. It is essential to quantify the effect of the discriminator on the linearity of the LG output, in particular around the threshold value when the HG is cut to make sure that the LG is not affected. The discriminator switch is controlled by a voltage threshold (Vth) which is coded over 10-bits.

For the characterisation of the discriminator, the gain and linearity are computed for different

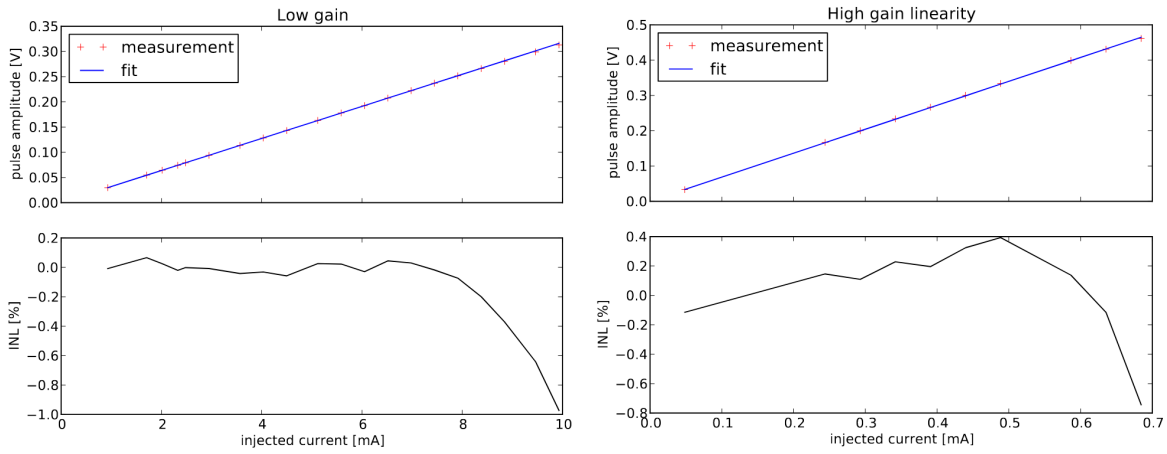

(a) **(b)**

Figure 3.13 – LAUROC0 linearity measurement of the 25_50 output configured as 25Ω channel for the LG output in (a) and the HG output in (b). The upper panel shows the pulse amplitude as function of the input current and the lower panel shows the integral of non-linearity.

Vth values. The linearity is measured after configuring the LAUROC0 to a certain Vth value, and injecting into the toy calorimeter a current value from within the expected dynamic range.

The HG output for the 25Ω A channel was measured for two different Vth DAC values of 1000 and 4000. For these values, the discriminator is enabled at values beyond the maximum of the dynamic range. In addition, the linearity was measured for a Vth value of 630 for which the HG is switched around 0.3 mA and for a value of 700 for which the HG is switched around 0.8 mA. The results of the different measurements are shown in Figure 3.14. A linear fit was performed up to the value of 0.8 mA at which the HG saturates (or is cut) to compute the gain. Small variations of the gain were observed for the different Vth configurations with unclear origins. The INL is very similar between the 4 configurations and shows that the HG saturates around 0.8 mA, after which the INL becomes larger than the per mille level. This implies that a good Vth value is 700, to cut the HG just when it starts to saturate.

When compared to the 25_50 channel, the 25Ω A channel shows an equivalent performance for the linearity, the gain as well as for the dynamic range.

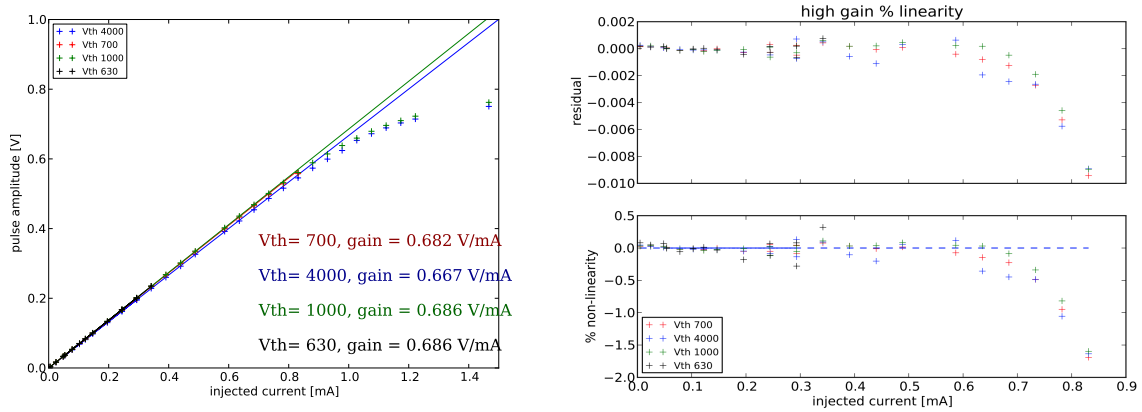

(a) **(b)**

Figure 3.14 – The pulse amplitude as function of the injected current for the different Vth configurations in (a) and corresponding integral of non-linearity in (b).

The effect of the discriminator on the LG linearity is quantified by comparing the LG output with Vth = 700 to a configuration where the discriminator is alway enabled (Vth = 80), to prevent any saturation of the high gain output. Figure 3.15a shows the LG pulse shape of the 25_50 channel configured as 25Ω for the two cases for an input current just above the discriminator threshold. It shows that there is a difference between the two pulses around the maximum of the peak. In addition glitches are seen in the tail of the pulse taken with Vth = 700.

The local INL is computed in Figure 3.15b and shows that for Vth = 700, the discriminator has a small effect at the 1% level on the LG output. Optimal Filtering (OF) [80] algorithm is applied to the LG output to check its impact on the linearity, by calculating the amplitude of the pulse from a fit of five samples around the maximum of the pulse peak. This simple version of the OF does not take into account the noise auto-correlations, but allows to improve the reconstruction of the pulse amplitude by reducing the distortion of the pulse. No change was observed with OF, thus proving that the discriminator has a small but visible impact on the LG. This effect was suppressed in the next ASIC iteration since the OMEGA team opted for a more traditional design with a HG output which is a copy of the LG output followed by an additional amplifier, similarly to the current HLC1 design.

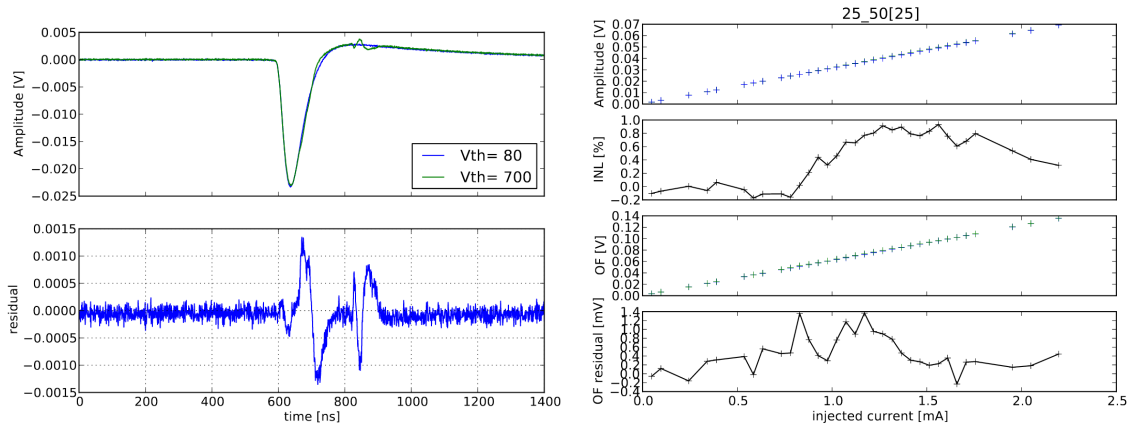

(a) **(b)**

Figure 3.15 – Figure (a) showing in the upper panel the two LG pulse shapes taken with different Vth configuration and the difference (in mV) between the two shapes in the lower panel. Figure (b) shows the amplitude of the pulses as function of the current in the first panel, the INL with Vth configured to 700 in the second panel, the amplitude of the pulses using optimal filtering in the third panel and the residual of the two pulses after optimal filtering in the last panel.

The 50Ω linearity measurement is presented in Figure 3.16 for both the LG and HG outputs. The 2 mA dynamic range is unreachable by the LG, as the output saturated beyond 1.4 mA where the INL is more than 1% and reaches ∼8% at 2 mA. The INL defined with respect to 1.1 mA is 0.25% up to ∼1 mA for the LG output and less than the per mille level for the HG through the whole dynamic range with a gain ratio of 19 between the two gains. The 50Ω channel does not meet the specifications of 2 mA of dynamic range. That was fixed in the next iteration.

HLC1

The HLC1 linearity measurement was performed using the same method and setup as LAUROC0. Since the peaking time is adjustable to modify the gain outputs, the board was configured with the configuration giving the highest gain. Figures 3.17 and 3.18 shows the results for the 25Ω and 50Ω channels. The HLC1 matches the requirements as the 25Ω LG dynamic range was able to reach 9 mA with an INL defined with respect to 8 mA better than 0.5% and an INL of

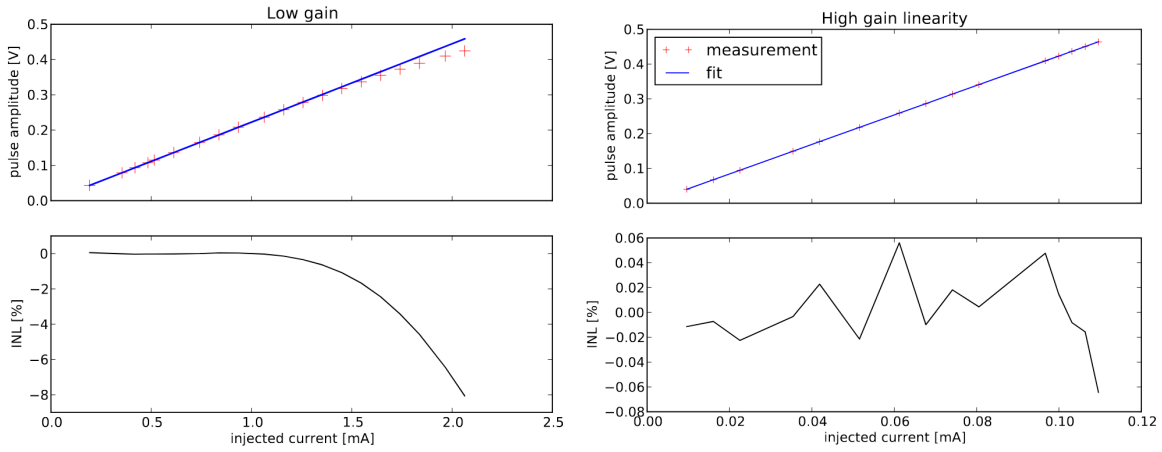

(a) **(b)**

Figure 3.16 – LAUROC0 linearity measurement of the 25_50 output configured as 50Ω channel for the LG output in (a) and the HG output in (b). The upper panel shows the pulse amplitude as function of the input current and the lower panel shows the integral of non-linearity.

0.15% in the whole HG range. The 50Ω channel shows an INL defined with respect to 1.7 mA better than 0.3% up to 80% of the LG output dynamic range and better 0.2% for the HG in the whole dynamic range.

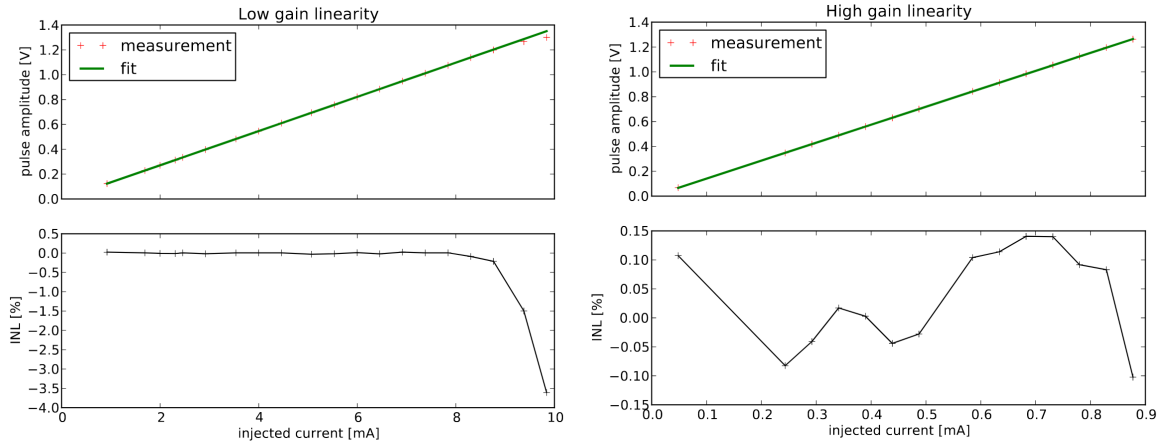

(a) **(b)**

Figure 3.17 – HLC1 linearity measurement of the 25Ω channel for the LG output in (a) and the HG output in (b). The upper panel shows the pulse amplitude as function of the input current and the lower panel shows the integral of non-linearity.

3.7.3 Noise measurement

The noise measurement for the LAUROC0 and HLC1 is conducted to compare to the current noise of the electronics of 150 nA and 45 nA for the 25Ω and 50Ω respectively, by using the same configurations as for the linearity measurement. The noise voltage is first measured from the root mean square (rms) of the HG output taken with the pre-amplifier switched on and off without any injected signal. The rms values are then substracted quadratically and divided by the gain obtained from the linearity measurement. The equivalent noise current (ENI) of the LAUROC 25ΩA and 50ΩB channels were measured to compare their performance to the 25_50Ω channel.

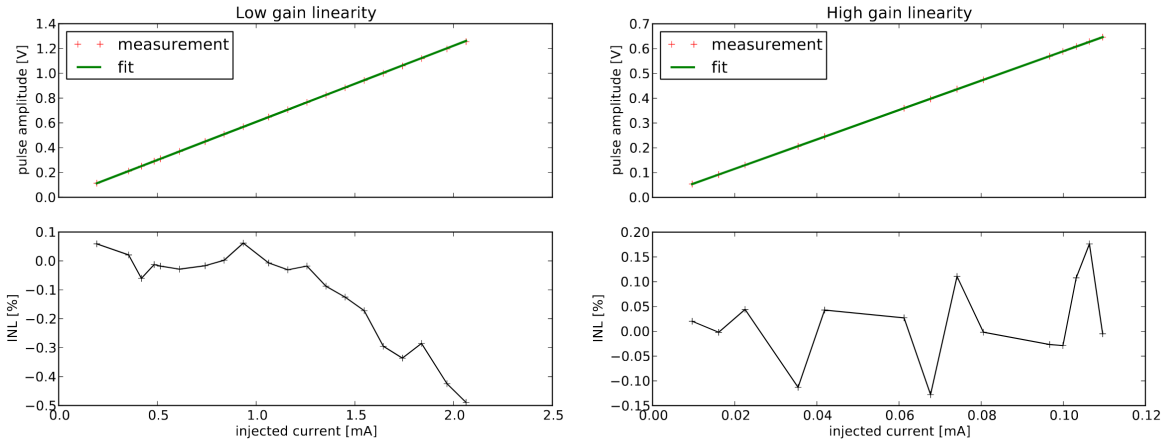

(a) **(b)**

Figure 3.18 – HLC1 linearity measurement of the 50Ω channel for the LG output in (a) and the HG output in (b). The upper panel shows the pulse amplitude as function of the input current and the lower panel shows the integral of non-linearity.

Channel	Peaking time (ns)	Gain (mV/mA)	V_{rms} (mV)	ENI (nA)	Expected ENI (nA)	MIP (nA)
LAUROC0, 25ΩA	45	682	0.223	327	150	350
LAUROC0, 50ΩB	40	4280	0.312	73	46	120
LAUROC0, 25_50Ω[25]	45	678	0.201	295	150	350
LAUROC0, 25_50Ω[50]	40	4241	0.352	83	46	120
HLC1, 25Ω	67	1446	0.424	293	150	350
HLC1, 50Ω	60	5932	0.573	97	46	120

Table 3.3 – The equivalent noise current results for the LAUROC0 and HLC1 channels compared to the expected values and to the MIP energies deposited by muons.

The measured ENI are presented in Table 3.3 and were found to be around 300 nA for the LAUROC0 25Ω channels and around 80 nA for the 50Ω channels. The ENI level measured on the 25A and 25_50 configured to 25Ω and the 50B and 25_50 configured to 50Ω channels is similar. The measured ENI was found to be a factor two larger than the expected noise from simulation. Part of the difference with simulation was found to be coming from using an inappropriate input transistor model. Knowing this, the next iteration was improved to reduce the noise.

The HLC1 ENI was measured to be around 300 nA and around 100 nA for the 25Ω and 50Ω channels respectively which are also higher than the expected noise from simulation of the design, and should be lowered in the next iteration. This is due to some of the noise sources which were not taken into account when simulating the expected noise of the chip.

The HLC1 peaking time is adjustable and affects both the gain and the ENI measurement. The measurements presented here were taken for the highest peaking time configurations of 67 ns and 60 ns for the 25Ω and 50Ω channels respectively, which give the lowest ENI. Hence, the comparison of the HLC1 ENI to the LAUROC0 ENI is not fair as the LAUROC0 peaking time is 45 ns and 40 ns for the 25Ω and 50Ω channels respectively. Therefore, the noise was re-measured after adjusting the HLC1 peaking time to the closest value to that of LAUROC0, where the LAUROC0 ENI was found similar to that of the HLC1 on the 25Ω channel and better on the 50Ω channel [81].

3.7.4 Cross-talk evaluation

To comply to the specification, the cross-talk level between the channels should be 0.5%. The cross-talk has been tested by injecting a signal current into one of the inputs channels and reading on the ADC of the FETB the output of all the other channels. For the LAUROC0, the test was performed by injecting the signal into either the 25ΩA or the 50ΩB channel and measuring their output and that of the other channels to compare the amplitude of the output signals. The cross-talk between the channels was found to be low, where the the highest level of cross-talk was measured to be 0.6% [81]. For the HLC1, the same method is used to test two neighboring channels. The cross-talk was found to be higher than LAUROC0 with a maximum level of 2.6% [81]. The cross-talk level for HLC1 is too high and needs to be improved.

3.8 Next iterations of the pre-amplifier/shaper ASICs

The LAUROC0 measurements highlight the aspects of the ASIC satisfying the requirements and the improvements needed for the next iteration. The LAUROC1 prototype was received in February 2019 and designed with 4 front-end analogue 25_50 channels. These 4 channels correspond to one channel with an architecture similar to that of the LAUROC0 prototype and three channels with the new architecture. The three new channels use one LG pre-amplifier followed by one CR-$(RC)^2$ LG shaper and by one CR-$(RC)^2$ HG shaper to get the HG output. This allows to remove the LAUROC0 discriminant and therefore eliminate the pulse glitches which were related to it. The characterisation tests of the LAUROC1 ASIC showed that the input impedance tuning works well within the expected range and that the linearity is excellent over the whole dynamic range for the 25Ω channel and up to 80% of the 50Ω channel dynamic range. In the LAUROC1 iteration, the 2 mA dynamic range is reachable by the 50Ω channel. In regards to the noise measurement, the new design provides a noise level lower than LAUROC0 of ∼250 nA for the 25Ω, channel but is still 20% higher than the expected value. This was found to be due to one noise source that is missing from the simulation tools. The latest version of the ASIC, the LAUROC2 board, was received in 2019 with a full functionality design similar to LAUROC1 but with two additional features: a trigger sum output to sum the output of the four channels and a radiation hard, triplicated slow control I2C connection for the slow control of the chip.

The ATLAS LAr Calorimeter Front-End (ALFE) is an upgraded prototype of HLC1. It is designed by the BNL group, with a fully differential architecture to achieve a lower noise. The ALFE0 test chip was built with two channels of 25Ω configuration only. The results of the analogue measurements showed an excellent linearity of INL less than 0.2% and a pre-amplifier noise of 150 nA which is similar to that of the existing electronics. The test bench measurements of ALFE0 showed good results, and ALFE1 has been submitted with full functionality and 4 channels. the new ALFE1 design is lacking the trigger summing output and the radiation hard I2C configuration.

The tests of the new ASIC prototypes will continue to verify if they match the specifications, and a single design will be selected at the preliminary Design Review later in 2020, to continue the development towards the production of the final chip that will be installed in LS3.

Chapter 4

Reconstruction of physics objects with ATLAS

In this Chapter are presented the different procedures used to identify, reconstruct and measure the properties of the physics objects from the signals deposited in the different detectors of ATLAS. Only objects used in the $VH(H \to b\bar{b})$ analysis presented in this thesis are described.

4.1 Tracks and vertices

The tracks of charged particles are reconstructed using information from the ID detector. The clusters in the pixel and SCT detectors and the drift circles in the TRT are transformed into three dimensional measurements referred to as hits. Track candidates are selected using pattern recognition algorithm [82] to match the tracks to the corresponding hits. First, track seeds are defined from three hits, starting from the the SCT and pixel detectors. The track seeds which are found, are then extrapolated to the TRT to collect the matching TRT hits and combine the measurements. Then a combinatorial Kalman filter [83] is used to build the track candidates from the seeds. If more than one seed in the same layer is compatible to the track, the filter creates several track candidates per seed. To determine which track candidates correspond to real tracks and to distinguish between fake and real tracks, a track score is defined from the number of clusters assigned to that track.

Since many interactions occur in a single bunch crossing, a set of selections is applied to reduce furthermore the amount of fake tracks. Tracks are removed if they occur in the $\eta \geq 2.5$ region or if they have more than two holes (intersection of the reconstructed track with the detector layers with no matched hits) or less than seven hits in the SCT and pixel detectors. They are also removed if they more than one hole in the pixel detector, more than one shared cluster on the same layer or a transverse momentum less than 400 MeV [84]. Additional selections on the impact parameters d_0 and z_0, representing the transverse and longitudinal impact parameters with respect the beam axis, are also implemented. Finally, a fitting algorithm is applied to the combination of selected tracks using all the ID information from the detector, to construct the trajectory and the momentum of charged particles with a high precision.

The primary vertex, corresponding to the interaction point where the particles were emitted, are built from the reconstructed tracks. Among the large number of candidate vertices produced, the primary vertex is designated as having the largest sum of the track transverse momentum squared. The position of the vertex is selected from a fitting algorithm, and tracks which are incompatible with the vertex are removed from the event. These removed tracks can be used in

the determination of another vertex. Reconstructing the primary vertex of the hard scattering is essential, as it allows to reconstruct the full kinematics of the event.

4.2 Electrons

4.2.1 Cluster and track reconstruction

The reconstruction of electrons starts by building clusters of cells, called topological clusters (topo-clusters), from the energy deposited in the electromagnetic calorimeter. The clusters are then matched to reconstructed tracks in the ID detector. These topo-clusters are built using a sliding-window algorithm with fixed sizes [85] to identify cluster candidates. The first step consists of forming proto-clusters from the calorimeter cells having the cell significance $|\zeta_{cell}^{EM}| \geq 4$, following:

$$\zeta_{cell}^{EM} = \frac{E_{cell}^{EM}}{\sigma_{noise,cell}^{EM}} \tag{4.1}$$

Where E_{cell}^{EM} and $\sigma_{noise,cell}^{EM}$ are the energy and the noise (including the electronic and pile-up noise) in each of the EM cells. The pre-sampler and the first layer cells are not included in this process to suppress the formation of noise clusters. The neighbouring cells are merged together when passing the significance requirement of $|\zeta_{cell}^{EM}| \geq 2$. If two clusters share the same cell, the two clusters are merged. The final step consists of adding the neighbouring cells with $|\zeta_{cell}^{EM}| \geq 0$ to the cluster.

The second stage of the reconstruction consists of matching the clusters to the ID tracks. This is done in two steps: the track pattern reconstruction and the track fit. First, the standard pattern reconstruction [86] is performed using a pion hypothesis for energy loss when interacting with the material volume in addition to a modified algorithm, based on a Kalman filter-smoother formalism [83] to account for possible bremsstrahlung energy loss. Another pattern recognition is performed using electron hypothesis if the track seed in the silicon detectors is matched to one of the EM cluster in the region of interest and if the track seed with $p_T > 1\,\text{GeV}$ cannot be extrapolated to match at least 7 hits in to the full tracker. In the second step of the track candidate reconstruction, the track is fitted with a global χ^2 fitter [87].

The matching of the candidate tracks to the clusters is then performed using the distance between them in η and ϕ. The tracks are considered loosely matched if the tracks can be extrapolated to the second layer of the EM calorimeter and if the tracks have $|\eta_{track} - \eta_{cluster}| < 0.05$ and $-0.10 < q \times (\phi_{track} - \phi_{cluster}) < 0.05$, where q is the charge of the reconstructed track. If multiple tracks are matched to one cluster, first the tracks with hits in the pixel detector are selected, then the tracks with hits in only the SCT and not in the pixel detector. The track selection takes also into account the distance in ΔR between the cluster and the track.

After Run-1, a new algorithm was developed for the reconstruction of the electrons using super-clusters [88] with dynamic size clusters istead of fixed size clusters. It allows to account for the low energy photons emerging from bremsstrahlung radiation when the electron is crossing the detector material. The algorithm iterates over the clusters starting from the one with highest p_T and proceeds in two stages: building the seed cluster candidate and identifying satellite cluster candidate. First, the electron seed cluster candidate is identified when having an energy more than 1 GeV matched to a track with at least 4 hits in the silicon detectors. Then electron satellite clusters are selected around the seed cluster in a window of 0.125×0.3 in $\Delta\eta \times \Delta\phi$ having ≥ 1 matched track to the cluster candidate. Finally, the satellite clusters passing the selection are added to the cluster candidates to form the supercluster.

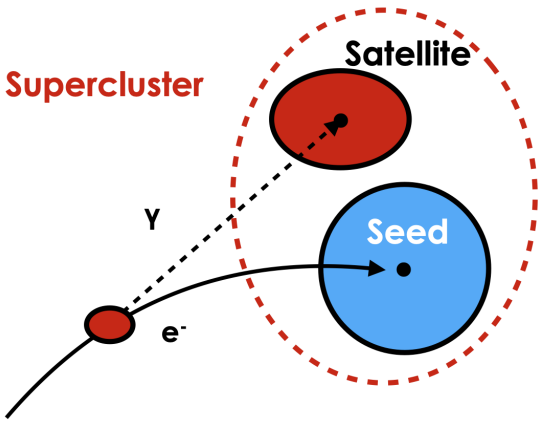

Figure 4.1 – Diagram of a supercluster showing an electron seed cluster and a photon satellite cluster.

4.2.2 Identification and calibration

The reconstruction of electron objects requires having at least one loose-track which is matched to a cluster with a tighter selection in $\Delta\eta$ and $\Delta\phi$. The track and the charge of the electron are reconstructed from the η and ϕ information from the ID while the energy of the electron is calculated using the measurement from the calorimeter. An electron identification algorithm is used to distinguish between real electrons and background objects as well as electrons coming from heavy flavor jet decays or photon conversions ($\gamma \to ee$).

The electron identification is done using a likelihood identification, that uses the signal and background probability density functions (PDFs) and a set of parameters such as the longitudinal and transverse shapes of the shower in addition to using information from the tracker. This method allows to define three working points, the loose, the medium and the tight, with different background rejection efficiencies as presented in Figure 4.2. The identification efficiency depend on the electron transverse energy, and for the loose working point which is used in the $VH, H \to b\bar{b}$ analysis, the efficiency varies between 82% and 95% as shown in Figure 4.2. Efficiency scale factors are derived from the comparison between data and both Z and J/ψ Monte Carlo samples as a function of the transverse energy and the pseudo-rapidity of the electrons. Good agreement between data and Monte Carlo was observed, with precision of the scale factor of few percents at low E_T= 4.5 GeV and decrease to better than 1% at high E_T [85].

The calibration of the electron energy measurement is computed in different steps. The first step consists of using a multivariate regression algorithm to minimise the impact of the material in front of the calorimeter. Then, the relative energy scales in the different EM calorimeter layers are adjusted and the non-uniform geometry of the detector is corrected. Finally, a correction of the overall energy scale is applied using electrons coming from the Z boson decay. At this last step, a correction is applied to the simulated samples to account for the difference between data and the Monte Carlo simulation using scale factors close to 1 and measured with uncertainties less than the percent. The results of the calibration are checked using electrons from the J/ψ decay. The associated systematic uncertainties depend on the transverse momentum of the electron: between 0.03% and 0.2% for electrons with p_T of 45 GeV and between 0.3% and 0.8% for electrons with p_T around 10 GeV [89] for electrons in the region $|\eta| < 2.5$. These uncertainties have a negligible impact in the $VH, H \to b\bar{b}$ analysis.

4.2.3 Isolation

To further improve the discrimination between the signal-electrons and the backgrounds, electrons are required to fulfill isolation requirements. For this purpose, two isolation variables have

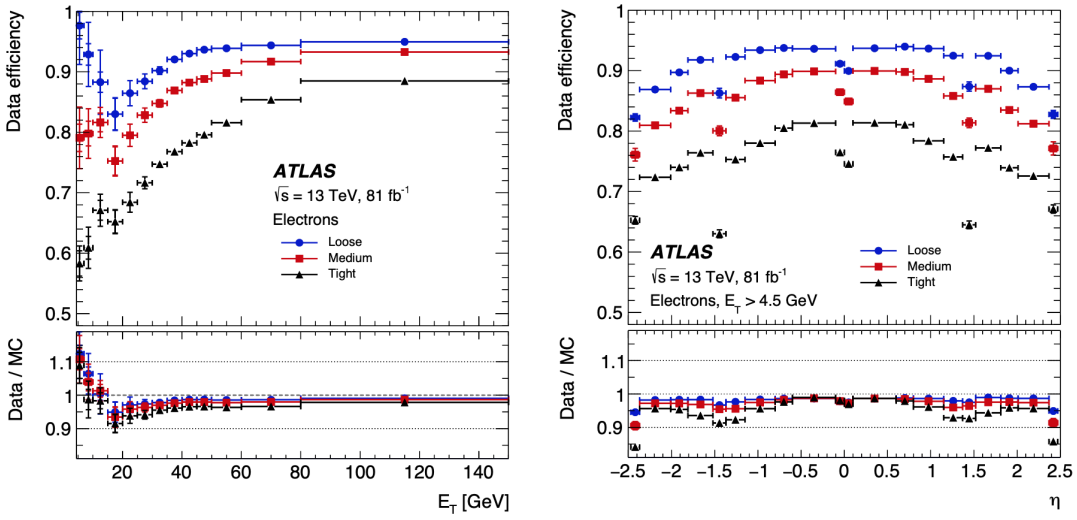

(a) (b)

Figure 4.2 – The electron identification efficiency using data events from $Z \to ee$ decay [85] as a function of the transverse energy (a) and the pseudo-rapidity (b) for the three working points.

been defined: the calorimetric isolation energy ($E_T^{cone0.2}$) and the track isolation ($p_T^{varcone0.2}$), later referred to as topoEtCone20 and PtCone20 respectively. The $E_T^{cone0.2}$ is defined as the sum of the transverse energy of the topological clusters with positive energy, within a cone of $\Delta R = 0.2$, centered around the electron cluster barycenter. The $p_T^{varcone0.2}$ is defined as the sum of the transverse momenta of all tracks passing the quality requirements. These tracks are constructed within a cone of $\Delta R = \min(0.2, 10\text{ GeV}/E_T)$ centered around the electron track-candidate and originating from the primary vertex. The different electron isolation working points are summarised in Table 4.1 and their efficiencies as a function of the energy spectrum and the pseudo-rapidity are shown in Figure 4.3.

Working point	Calorimeter isolation	Track isolation
Gradient	Efficiency $= 0.1143 \times p_T + 92.14\%$	Efficiency $= 0.1143 \times p_T + 92.14\%$
Loose	Cut: $E_T^{cone0.2}/p_T < 0.20$	Cut: $p_T^{varcone0.2}/p_T < 0.15$
Tight	Cut: $E_T^{cone0.2}/p_T < 0.06$	Cut: $p_T^{varcone0.2}/p_T < 0.06$
FixedCutHighPtCaloOnly	Cut: $E_T^{cone0.2} < \max(0.015 \times p_T\ , 3.5\,\text{GeV})$	-

Table 4.1 – The electron isolation working points [85], and the corresponding calorimeter and track isolation cuts.

4.3 Muons

4.3.1 Reconstruction

The muon reconstruction is performed by using information from both the ID and the MS. In the ID the muon tracks are reconstructed using the same procedure as for any other charged particle. The combined ID-MS information can be achieved through several algorithms using information not only from the ID and the MS, but also from the calorimeters. Depending on which sub-detector information is included in the reconstruction, four different type of muons are defined:

- **Combined (CB) muons:** are reconstructed from both the ID and all the MS sub-

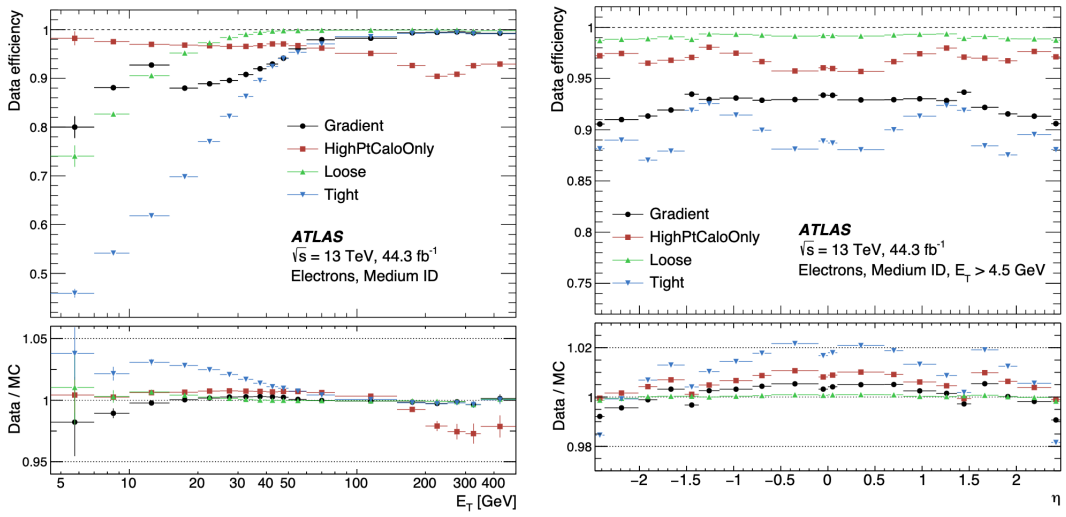

(a) **(b)**

Figure 4.3 – The efficiency of the different electron isolation working points for the $Z \to ee$ decay as a function of the electron E_T in (a) and the pseudo-rapidity in (b) [85].

detectors. A global fit is performed using all hits in both the ID and MS track to form a combined track. During the fit, hits from the MS can be added or removed to the track to improve the fit quality. Most of the muons are reconstructed first in the MS and then extrapolated to match the ID track. But another approach can be used to match the tracks in the ID to that in the MS.

- **Segment-tagged (ST) muons:** a muon track is accepted if the track in the ID can be matched to at least one segment in the MDT or the CSC chambers. The ST muons are defined when they cross only one layer of the MS due to either a low MS acceptance or to their low energy.
- **Calorimeter-tagged (CT) muons:** a muon track is identified if the ID track is matched to an energy deposit in the calorimeter cells compatible with the MIP energy. The CT muons are reconstructed in the η <0.1 region, even if they have the lowest purity, to recover the loss in acceptance in the region where the MS have low coverage.
- **Extrapolated (ME) muons:** the muon track is reconstructed using only information from the MS, with a loose requirement to be extrapolated to the interaction point. To be able to reconstruct the muon track, the muon is required to pass though at least two layers of MS or three in the forward region. This type of muons is reconstructed in the $2.5 < |\eta| < 2.7$ region, allowing to extend the tracking acceptance.

4.3.2 Identification

Four selection working points are defined: loose, medium, tight and High-p_T muons. These selections are based on several kinematic variables allowing to suppress the background in addition to non-prompt muons. The loose identification uses all four type muons, is intended to maximise the reconstruction efficiency while providing good-quality muon tracks and is specifically optimised for the $H \to 4l$ analysis. On the other hand, the medium selection is designed to reduce the muon reconstruction and calibration uncertainties using only CB and MS muons. The tight selection criteria uses only CB muons with hits in at least two of the MS sub-detectors and satisfying the medium requirements. In addition the tight muons should satisfying requirements of χ^2 of the combined track fit and the selection of the ρ' and q/p significance, where ρ' is defined as the absolute value of the difference the p_T measurements in the ID and MS

divided by the p_T of the combined track and q/p significance as the absolute difference between the ratio of the charge and momentum of the muons measured in the ID and MS divided by the sum in quadrature of the corresponding uncertainties. The tight selection is optimised to maximise the purity of muons with a small loss in efficiency. Finally the High-p_T muons can only be CB muons passing the medium selection and having at least three hits in three of the MS sub-detectors, in addition to vetoing specific regions of the MS with bad quality alignment. This High-p_T selection is optimised for analyses looking for the W' and Z' boson resonances by improving the muon p_T resolution in regimes above 100 GeV. The muon and background selection efficiencies, for each working point, are summarised in table 4.2.

The calibration of the muon momentum is computed only from CB muons satisfying the medium selection using samples of $Z \to \mu\mu$ and $J/\psi \to \mu\mu$. The scale factors were found to be close to 1 with momentum scale uncertainties that depend on the pseudo-rapidity and rage from 0.05% to 0.2%. These uncertainties have no major impact on the $VH, H \to b\bar{b}$ analysis.

	$4\,\text{GeV} < p_T < 20\,\text{GeV}$		$20\,\text{GeV} < p_T < 100\,\text{GeV}$	
Selection	ϵ_μ^{MC} [%]	$\epsilon_{hadrons}^{MC}$ [%]	ϵ_μ^{MC} [%]	$\epsilon_{hadrons}^{MC}$[%]
Loose	96.7	0.53	98.1	0.76
Medium	95.5	0.38	96.1	0.17
Tight	89.9	0.19	91.8	0.11
High-pT	78.1	0.26	80.4	0.13

Table 4.2 – Muon and background efficiencies of the muon selection working points [90].

4.3.3 Isolation

Muon isolation selections are applied to suppress the background, similarly to the electrons. These selections are defined from the isolation variables $E_T^{cone0.2}$ and $p_T^{varcone0.2}$ in addition to the track isolation $p_T^{varcone0.3}$ constructed within a cone of $\Delta R = \min(0.3, 10\text{ GeV}/E_T)$ around the muon candidate. The muon isolation working point efficiencies are presented in Table 4.3 and Figure 4.4.

Working point	Calorimeter isolation	Track isolation
Gradient	Efficiency $= 0.1143 \times p_T + 92.14\%$	Efficiency $= 0.1143 \times p_T + 92.14\%$
GradientLoose	Efficiency $= 0.057 \times p_T + 95.57\%$	Efficiency $= 0.057 \times p_T + 95.57\%$
FixedCutLoose	Cut: $E_T^{cone0.2}/p_T < 0.30$	Cut: $p_T^{varcone0.3}/p_T < 0.15$
LooseTrackOnly	-	Efficiency = 99%
Tight	Cut: $E_T^{cone0.2}/p_T < 0.06$	Cut: $p_T^{varcone0.3}/p_T < 0.06$
FixedCutHighPtTrackOnly	-	Cut: $p_T^{varcone0.2} < 1.25\,\text{GeV}$

Table 4.3 – The muon isolation working points and the corresponding calorimeter and track isolation cuts.

4.4 Jets

4.4.1 Reconstruction

The jet reconstruction starts first from the topo-clusters similarly to electrons as described in Section 4.2.1, constructed using calorimeter cells at either the electromagnetic scale or after

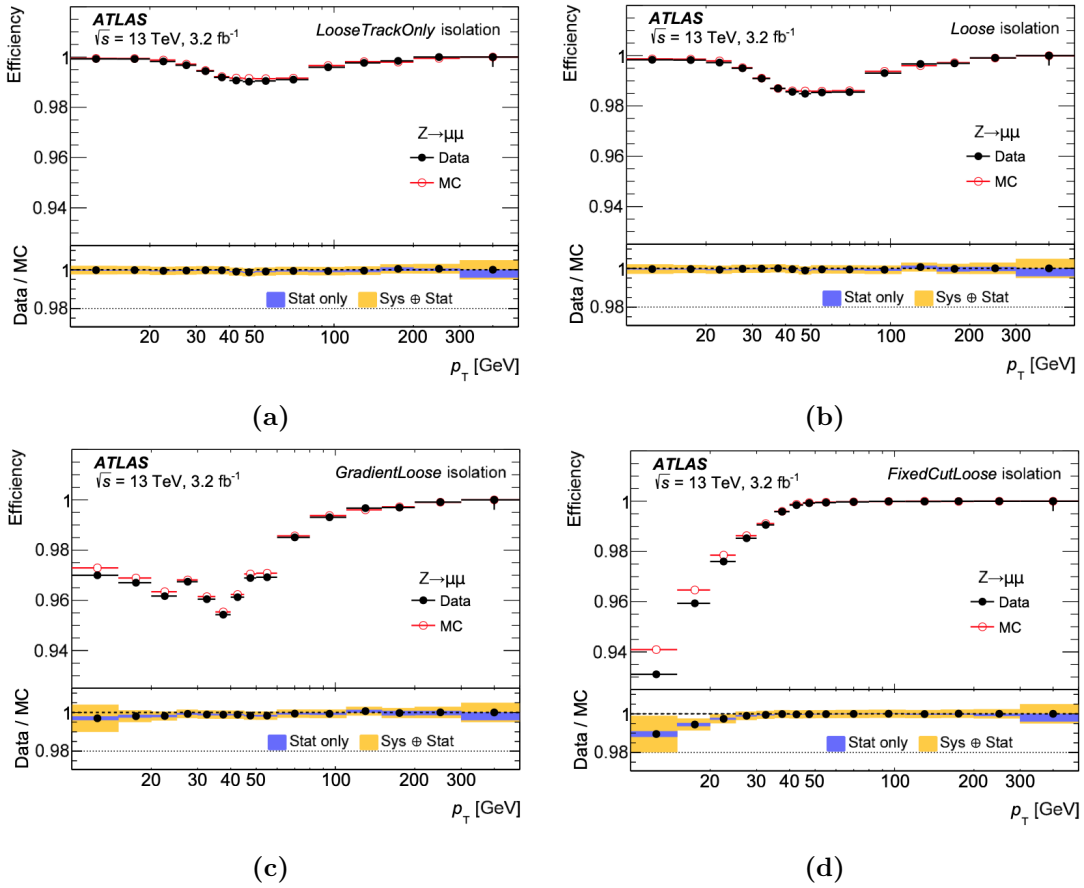

Figure 4.4 – The muon isolation efficiency using data and MC events from $Z \to \mu\mu$ decay [90] as a function of the transverse momentum for the LooseTrackOnly, Loose, GradientLoose and FixedCutLoose working point.

local cluster reweighting to account for the difference between electromagnetic and hadronic interactions. An anti-k_t algorithm [91] based on information from these topo-clusters is then used for the jet reconstruction by clustering the topo-clusters. This algorithm passes through all the topo-clusters, calculating at each one of them the following distance:

$$d_{ij} = min\left(\frac{1}{k_{T,i}^2}, \frac{1}{k_{T,j}^2}\right)\frac{\Delta R_{ij}^2}{R} \tag{4.2}$$

$$d_{iB} = \frac{1}{k_{T,i}^2} \tag{4.3}$$

Where $k_{T,i}^2$ is the transverse momentum of the cluster i and R is a fixed parameter relative to the jet radius. The jet radius parameter used in the ATLAS analyses should be $R \geq 0.4$ and is fixed to 0.4 in the $VH, H \to bb$ analysis study presented in this thesis. ΔR_{ij}^2 is the distance between the two cluster i and j defined using the rapidity and the azimuthal angle as: $\Delta R_{ij}^2 = (\eta_i - \eta_j)^2 + (\phi_i - \phi_j)^2$.

The d_{ij} is computed as the distance between the cluster i and j while d_{iB} is the distance between the cluster i and the beam. The first step of the clustering process corresponds to calculating the two distances d_{ij} and d_{iB} for each cluster. The two values are then compared to find the smallest distance. If d_{ij} was found to be the smallest, then the four momentum of the i and j clusters are combined. In the other case, the cluster i is considered as a jet and is removed from

the sequence. The algorithm continues this procedure until all the clusters are identified as jets.

4.4.2 Calibration

The jets energy calibration is needed to account for several effect such as: the pile-up background, features of the detector and the non-homogeneous detector response, the jet reconstruction algorithm and the difference in the energy scale between the data and the Monte Carlo simulated events. These effects are corrected using jet energy scale (JES) and the jet energy resolution (JER) corrections. The calibration procedure consists of five sequential steps [92].

The first correction is the jet origin correction, where topo-cluster have their directions (in η and ϕ) pointing to the center of the ATLAS detector. The direction can be modified to originate from the hard-scattering primary vertex of the event. This results in a change in the topo-cluster four momenta but does not affect the jet energy since the energy of the topo-clusters is unchanged. The second correction is the pile-up correction, which allows to subtract the pile-up contribution from the event in the jet active areas. The next step is the jet calibration which is obtained from Monte Carlo events and applied to both data and Monte Carlo simulated events. It consists of matching the reconstructed jet to the truth jet and computing the difference between their energies. The fourth step is the global sequential calibration that corrects the fluctuations of the jet in the hadronic shower using the tracking and the topo-cluster information. The last correction corresponds to the residual in situ energy calibration from the difference between data and Monte Carlo events calibrated using Z+jet, γ+jet and multi-jet data.

The jet calibration associated systematic uncertainties are driven by the precision on the in situ measurements and vary from 1% to 3% depending on the transverse momentum of the jet.

4.4.3 Pile-up suppression

In a single bunch crossing many QCD interactions occur, in addition to the hard scattering interaction, and create particles with low energy that may create in-time pile-up jets. Moreover, out-of-time pile-up corresponds to the energy deposited from previous and following bunch crossings in the calorimeters. The jet vertex tagger (JVT) [93] and the jet cleaning are two algorithms used to reduce the pile-up contamination and reduce the fake jets coming from beam backgrounds and noise bursts in the electromagnetic calorimeter respectively.

The jet cleaning uses a set of selection based on three variables: the timing of the pulses in the liquid argon calorimeter which allows to reduce the noise in the calorimeter, the calorimeter information corresponding to the fraction of the jet energy deposited in the electromagnetic calorimeter with respect to the jet total energy and the track information relative to the ratio of the scalar sum of p_T of tracks emerging from the primary vertex to the jet p_T. The combination of these three selections allows to define two jet cleaning selections: the loose selection with more than 99.5% efficiency for jets with $p_T > 20\,\text{GeV}$ and the tight selection with an efficiency of 95% (99.5%) for jets with p_T >20 GeV (p_T >100 GeV). Jets not passing these selections are discarded from the events.

The JVT is a multivariate selection based on the tracking information and optimised as function of the number of reconstructed primary vertices in the event. The JVT output distribution ranges from 0 to 1, allowing to define different JVT selection cuts with different pile-up rejection efficiencies. The JVT distribution of both the pile-up and the hard scattering jets is shown in Figure 4.5. The majority of pile-up events are suppressed when selecting events with JVT > 0.59 corresponding to the hard scattering jets efficiency of 92%.

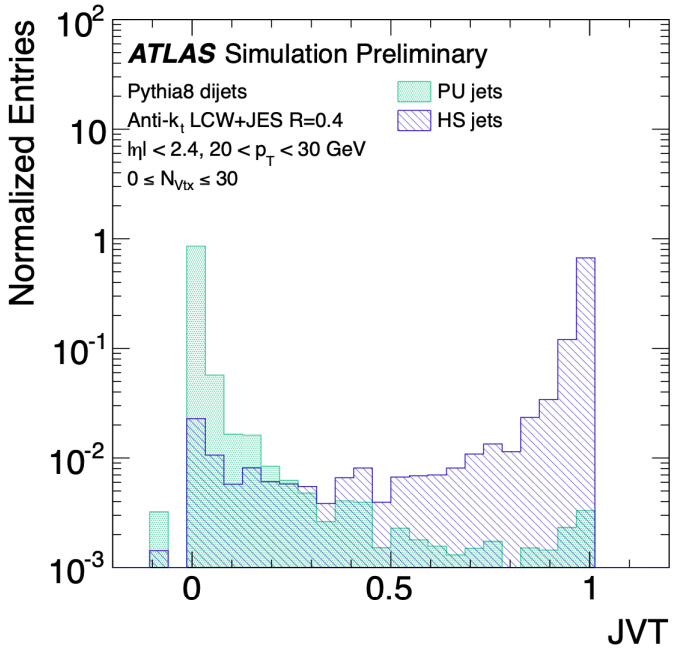

Figure 4.5 – The JVT distribution for pile-up and hard scattering jets with $20 < p_T < 30$ GeV [93].

4.4.4 *b*-jet tagging

The MV2c10 b-tagging algorithm is used for the identification of b-jets from c- and light (jets originating from u-, d- or s- quarks or gluons) jets based on the properties of b-hadrons. It is a combination of several algorithms that use as a basis the long life time of b-hadrons compared to other hadrons, their mass and their momentum to provide the best separation. The first algorithm is based on the impact parameter information of the tracks of the jet using transverse information (IP2D) and using both the transverse and longitudinal information (IP3D). The second algorithm uses the secondary vertex information (SV) and the last algorithm (JetFitter) attempts to reconstruct the full b-hadron decay chain. The information coming from these algorithms is used as inputs to a multivariate algorithm, a boosted decision tree (BDT) that is trained using combination of $t\bar{t}$ events with at least one lepton coming from the W boson decay and Z' events decaying to hadrons since the p_T distribution of the $t\bar{t}$ sample is steeply falling at 250 GeV, to separate b- from c- and light jets. This algorithm gives a final discriminant (MV2c10 output) which is a value between -1 and 1 [94]. Several working points are defined based on their average efficiency on b-jets as shown in Table 4.4. The choice of the working point will have an impact in the analysis and the medium 70% working point is chosen in the $VH, H \to bb$ analysis, corresponding to a cut at 0.83 of the MV2c10 discriminant, allowing to have a rejection rate of about 9 for c-jets and 300 for light jets. The c- and light jets rejections as function of the b-tagging efficiency are presented in Figure 4.6. Scale factors are derived from a calibration performed with $t\bar{t}$ events for the b- and c-jets calibration and the using negative tag technique [95] with Z+jets events for the light jets calibration. These scale factors are then applied to correct the Monte Carlo predictions to match the data depending on the p_T and η of the jets [96].

The efficiency of the b-tagging to identify jets coming from b-hadrons is measured by comparing data collected by the ATLAS detector to di-leptonic $t\bar{t}$ simulated events. The data to Monte Carlo comparisons showed that the data and simulation are in good agreement withing uncertainties and therefore resulted in scale factors close to unity with uncertainties depending on the transverse momentum of the jet and ranging from 2% to 12% for a 70% b-jet tagging working point [97]. The $VH(H \to b\bar{b})$ analysis is sensitive to b-tagging, thus these uncertainties have a

Working point	Selection cut	c-jet rejection	τ-jet	light-jets rejection
60%	0.94	23	140	1200
70%	0.83	8.9	36	300
80%	0.64	4.9	15	110
85%	0.11	2.7	6.1	25

Table 4.4 – Working points selection and rejection of the MV2c10 b-tagging algorithm from the $t\bar{t}$ sample used in the training [96]. The highlighted 70% working point is used in the $VH(H \to b\bar{b})$ analysis.

significant impact in the analysis.

The continuous MV2c10 distribution can be divided into five bins defined from the edges of the four working points in the Table 4.4. This binned distribution corresponds to the pseudo-continuous operating points. The b-tagging efficiency of each operating point corresponds to the integral of the b-tagging probability in that range. Using pseudo-continuous b-tagging allows to assign to each jet a probability of being a b-, c- or light jet instead of just considering the jet as either tagged or not. Therefore it can be used as a powerful discriminating variable in multivariate analyses.

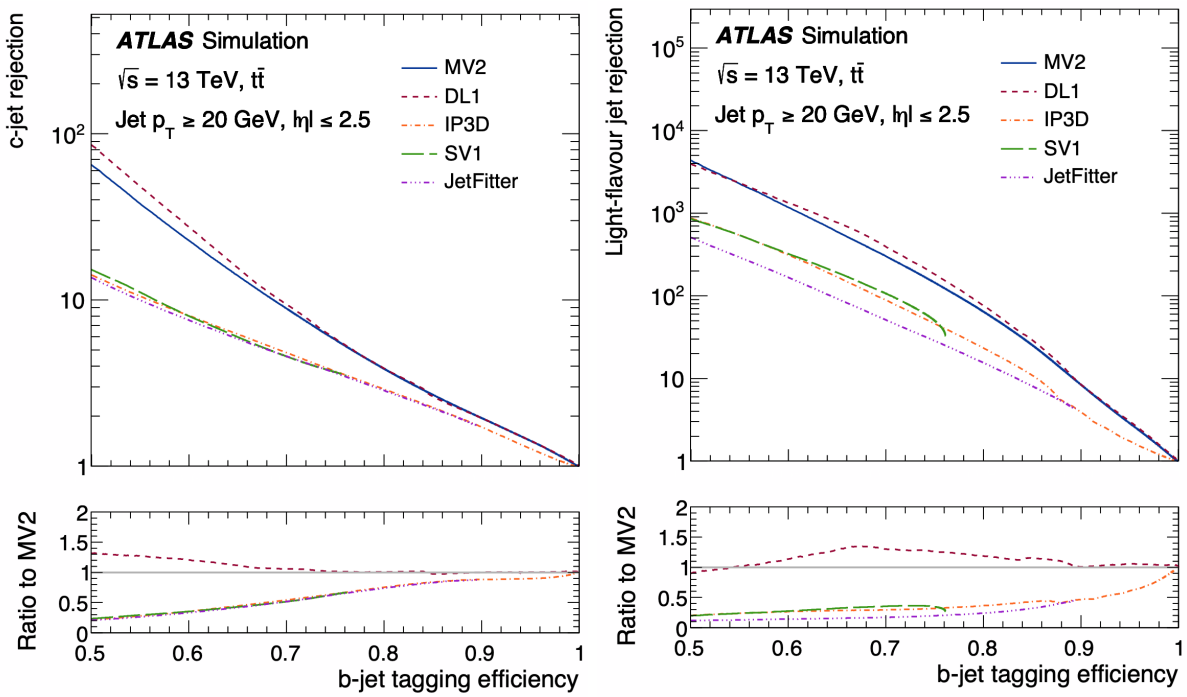

Figure 4.6 – The c-jet (a) and light jet (b) rejections as a function of the the b-tagging efficiency using $t\bar{t}$ events for different tagging algorithms: MV2c10, DL1, IP3D, SV1 and JetFitter [96].

4.5 Taus

The tau lepton is a particle with a short life-time, decaying before it reaches the ATLAS detector. The $VH(H \to b\bar{b})$ analysis has a τ veto to discard the events with the vector boson decaying to τ. The taus decay either leptonically following $\tau \to l\nu_l\nu_\tau$ where l is either an electron or a muon, or hadronically following $\tau \to \nu_\tau$ hadrons. The leptonic decays are included in the $VH(H \to b\bar{b})$ analysis in the lepton and muon channels. 65% of the taus decay hadronically and produce

either a charged pion (72%) or three charged pions (22%). These taus are reffered to as τ_{had}. The τ_{had} candidates are reconstructed using anti-k_t jets having $p_T > 10\,\text{GeV}$ and $|\eta| < 2.5\,\text{GeV}$ and tau candidates in the $1.37 < |\eta| < 1.52$ region are discarded [98]. The tau vertex is used to define 1 or 3 tracks associated to the τ_{had} using clusters collected around the jet in a ΔR =0.2 cone and with $p_T > 1\,\text{GeV}$. Wider tracks of $0.2 < \Delta R < 0.4$ are used to define the tau candidate isolation. The final step consists on applying a tau identification algorithm using the Boosted Decision Tree (BDT) method to identify and remove τ-like objects coming from quark or gluon initiated jets. This algorithm allows to define three working points, loose, medium and tight with efficiencies of 0.6, 0.55 and 0.45 when the τ_{had} is matched to 1 track and 0.5, 0.4 and 0.3 when the τ_{had} is matched to 3 tracks [98].

4.6 Overlap removal

To remove any ambiguity for any of the objects to be reconstructed more than once, an overlap removal procedure is applied:

- If an electron and a muon share the same ID track, the electron is removed, and the energy of the electron deposited in the calorimeter is substracted from the event.
- A tau lepton is removed if it overlaps with a light lepton (electron or muon) following: $\Delta R(\tau_{had}, l) < 0.2$.
- A jet with $\Delta R(jet, e) < 0.2$ of an electron is removed to reduce the effect of tracks reconstructed both as a jet and an electron. The non-prompt electrons from hadronic showers can be suppressed by removing the electron if $\Delta R(jet, e) < 0.4$.
- A jet is removed if it is withing $\Delta R(jet, \mu) < 0.2$ of a muon to reduce the amount of jets created from a muon bremsstrahlung. Similarly to electrons, non-prompt muons are suppressed if $\Delta R(jet, \mu) < 0.4$ by removing the jet only if it has 2 tracks and removing the muon otherwise.
- A jet is removed if it is withing $\Delta R(jet, \tau_{had}) < 0.2$ of a tau.

4.7 Missing transverse energy

The missing transverse energy (E_T^{miss}) corresponds to the transverse energy of the particles which are not reconstructed inside the detector. The E_T^{miss} can be an indication of the presence of the neutrinos or weakly interacting particles from theories beyond the Standard Model. It can be constructed from the transverse momentum $p_{x(y)}$ of the fully reconstructed and calibrated particles (e, γ, τ, μ and jets) known as hard objects and from reconstructed particle tracks matched to a primary vertex known as soft signals. Following the momentum conservation, the sum of the transverse momentum of the particles produced in a collision should be equal to zero. To avoid any double counting, the reconstructed particles used to compute the E_T^{miss} should not share the same detector signal. The missing transverse energy is calculated as the negative sum of the transverse momentum of the reconstructed particles following [99]:

$$E_{x(y)}^{miss} = -\Big(\sum_{i \in hard\,objects} p_{x(y),i} + \sum_{j \in soft\,signals} p_{x(y),j}\Big) \tag{4.4}$$

The vector $\mathbf{E_T^{miss}}$ can be computed following:

$$\mathbf{E_T^{miss}} = (E_x^{miss}, E_y^{miss}) \tag{4.5}$$

The vector $\mathbf{E_T^{miss}}$ allows to compute the amplitude of the E_T^{miss} as:

$$E_T^{miss} = |\mathbf{E_T^{miss}}| = \sqrt{(E_x^{miss})^2 + (E_y^{miss})^2} \tag{4.6}$$

Since the E_T^{miss} is reconstructed using the electrons, muons, photons, jets and the taus, the E_T^{miss} measurement is affected by the reconstruction and calibration of these particles. Therefore these effects are taken into account when calculating the E_T^{miss} associated uncertainties. The track-based soft term contributes as well (small effect of a few GeV) to the E_T^{miss} uncertainties, where this systematic uncertainty is estimated from data to Monte Carlo comparisons. An additional definition of the missing transverse energy is used in the $VH(H \to b\bar{b})$ analysis referred to as $E_{T,trk}^{miss}$, which is constructed only from the ID tracks and used as a good discriminant to reduce multi-jet background.

Chapter 5

Introduction to the $VH(H \to b\bar{b})$ Analysis

The search in the $VH(H \to b\bar{b})$ channel looks for candidate events coming from the Higgs boson decaying to 2 b-jets and the vector boson when it decays to 0-, 1- or 2-charged leptons to explore the following channels: $Z \to \nu\bar{\nu}$, $W \to l\nu$ and $Z \to l\bar{l}$, where l can be either an electron or a muon. The analysis does not consider the hadronic decays of the vector boson or its decay to taus, since the sensitivity would be much lower. Figure 5.1 shows representative Feynman diagrams of the 3 channels of interest at tree-level.

The $H \to b\bar{b}$ mode is the latest observed decay mode and is of particular importance since it drives the total decay width of the Higgs boson. That being said, it is a challenging mode to study because of the low signal to background events ratio. This Chapter presents an overview of the VHbb analysis, dedicated to the measurement of the Standard Model Higgs boson using full Run-2 data. The dataset and the Monte Carlo samples used in the analysis are first presented in Section 5.1. Events used in the analysis are required to pass specific selection criteria, thereby the object and event selections are detailed in Sections 5.2 and 5.3. The events in the final state are required to have exactly two b-tagged jets and a hybrid tagging approach is chosen for the analysis which is presented in Section 5.4. To maximize the sensitivity to this decay channel, a multivariate analysis using boosted decision trees is adopted as presented in Section 5.5, with two validation analyses to cross check the results: the diboson (VZ, Z$\to b\bar{b}$) and the di-jet mass analyses as presented in Section 5.6. Events are also categorised into signal and control regions to better control the dominant backgrounds. The last Section 5.7 contains studies that allowed to define the analysis categorisation and the tests that were conducted leading to the final analysis regions.

In Chapter 6 are presented the systematic uncertainties of the analysis, and the statistical analysis based on the binned profile likelihood on signal and control regions to extract the results on the analysis in Chapter 7.

5.1 Data and simulated events

Data events used in this analysis were collected from p-p collisions during Run-2 from 2015 to 2018 at a center-of-mass energy of 13 TeV corresponding to an integrated luminosity of 139 fb^{-1} [100]. To ensure the good quality of the recorded data events and that all the ATLAS detector was operating well, these events are required to pass a filter requirement given by

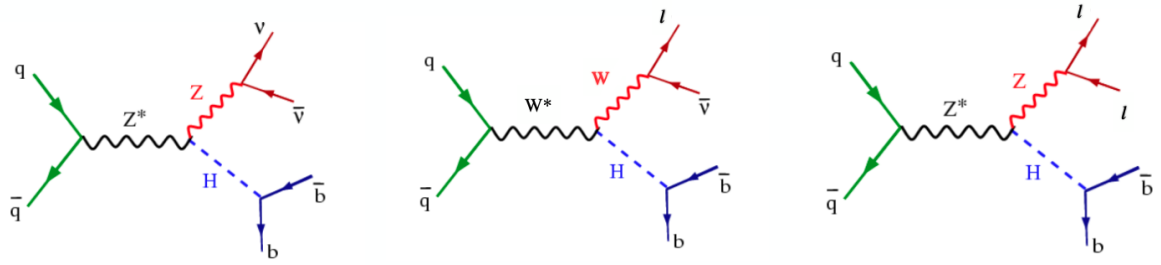

Figure 5.1 – Feynman diagrams of the $VH \to b\bar{b}$ process in the three leptonic decay channels.

the Good Run List (GRL) [101] which has a high efficiency of 95.6%.

An accurate description of the collected data is needed by simulating the expected shape of the signal and background using Monte Carlo generators. These generators are used to describe all signal and background processes, except the multi-jet background in the 1-lepton channel and top events in the 2-lepton channel which are estimated using data-driven methods. Various state of the art Monte Carlo generators are used for the events simulation, sometimes with filters in order to enhance the statistics in the background samples. After generating the events, they are passed through the GEANT4 [102] simulation, used to simulate the passage of particles inside the ATLAS detector and their interactions with the materials. The simulated events are then reconstructed using the same reconstruction algorithms as for the collected data to create physics objects. Each of the produced samples include the pile-up effect and the events are weighted so that the distribution of the number of interactions per bunch crossing matches the one of the data. The signal samples are normalised to the best theoretical prediction of the cross-section for a Higgs boson mass $m_H = 125\,\text{GeV}$.

5.1.1 Signal processes

The $pp \to VH$ signal events are induced by quark interactions at leading order ($qq \to VH$) with a contribution at next-to-leading order to the ZH signal from gluon interactions ($gg \to ZH$) through loops of heavy quarks as shown in Figure 5.2. The quark induced signal samples are modeled using the Powheg MiNLO [103, 104] generator at next-to-leading order accuracy and using Pythia8 [79] for showering with AZNLO [105] tuning. They use the NNPDF 3.0 PDF set [106]. The gluon induced simulated events are created using the Powheg generator at leading order and Pythia8 with AZNLO tuning and NNPDF 3.0. A summary of the different Monte Carlo generators used for the signal samples is presented in Table 5.1.

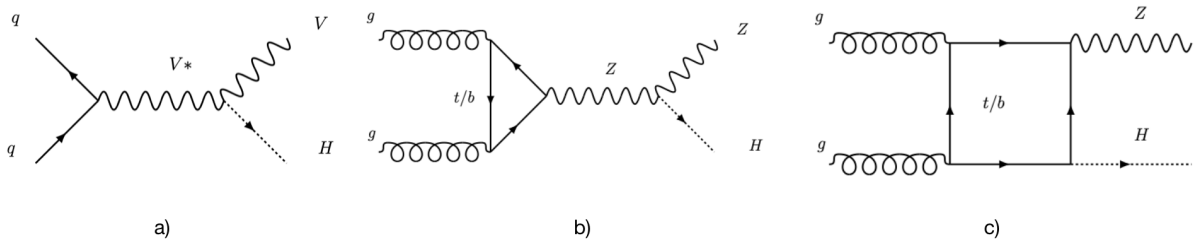

Figure 5.2 – Feynman diagrams at leading order showing the VH signal processes coming from a quarks interaction a) and from gluon interactions b) and c).

Process	Generator	σ [fb]	N_{events} [$\times 10^6$]
$qq \to ZH \to \nu\nu$	Powheg MiNLO + Pythia8 (NNPDF3)	153.05	7.3
$qq \to WH \to l^+\nu$	Powheg MiNLO + Pythia8 (NNPDF3)	282.78	14.6
$qq \to WH \to l^-\nu$	Powheg MiNLO + Pythia8 (NNPDF3)	179.49	7.3
$qq \to ZH \to ll$	Powheg MiNLO + Pythia8 (NNPDF3)	77.04	11
$gg \to ZH \to \nu\nu$	Powheg + Pythia8 (NNPDF3)	24.57	1.5
$gg \to ZH \to ll$	Powheg + Pythia8 (NNPDF3)	12.42	2.25

Table 5.1 – The signal samples generated using state-of-the-art generators, where $l = e$, μ or τ. The cross sections are used to normalise the different processes (for a branching ratio Br($H \to b\bar{b}$) of 0.582), following the LHC Higgs Cross Section Working Group recommendations [15].

5.1.2 Background processes

The dominant background processes in the analysis are: diboson (WW, WZ and ZZ) in the three channels, top (single top quark or top pair ($t\bar{t}$)) mainly in the 0- an 1-lepton channels, W+jets in the 0- and 1-lepton channels and Z+jets mainly in the 0- and 2-lepton channels. Some of the Feynman diagrams of the backgrounds are shown in Figures 5.3 and 5.4.

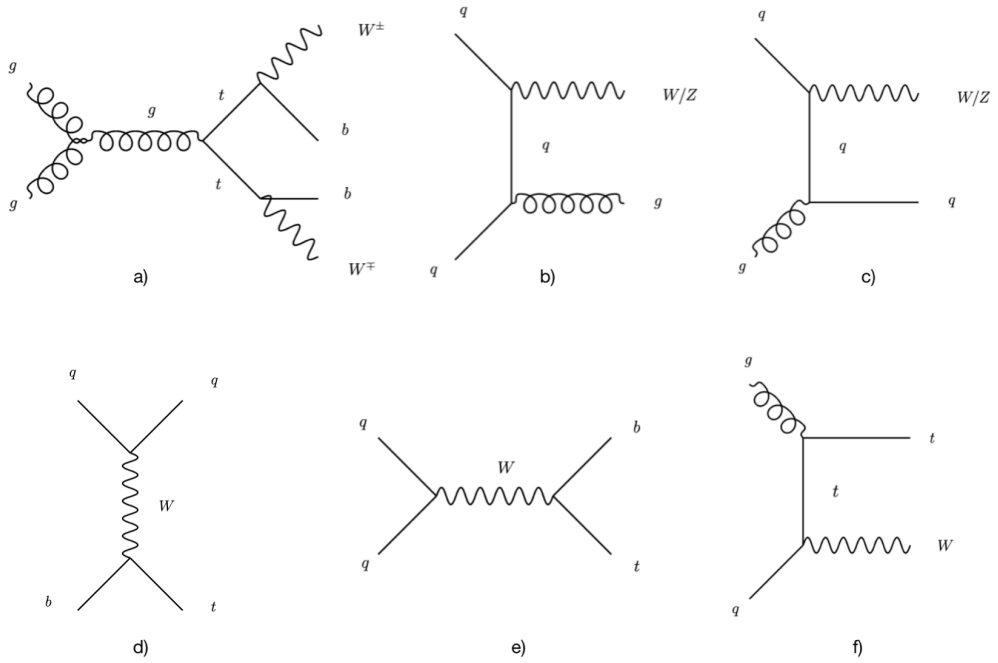

Figure 5.3 – Feynman diagrams at leading order showing the background processes for $t\bar{t}$ in a), V+jets in b) and c) and single top in d), e) and f).

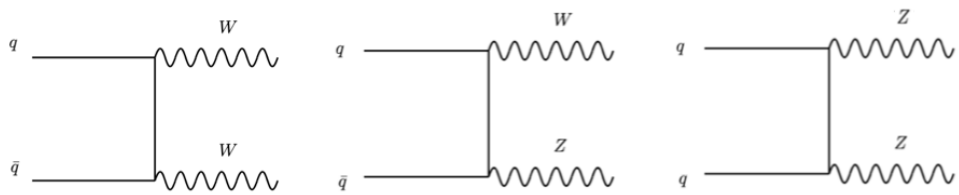

Figure 5.4 – Example of Feynman diagrams showing the diboson background processes.

The main contribution to the diboson background events comes from quark induced interactions $qq \to VV$. The simulated events consist of one vector boson that decays leptonically and the other boson decays hadronically. These samples are simulated using the Sherpa 2.2.1 [66] generator interfaced with NNPDF 3.0 NNLO PDFs. In addition, a small contribution to the diboson samples coming from the loop induced process $gg \to VV$ is modeled using the same generator. Each boson in the pair is considered to have zero-width when computing the matrix element to generate the events. Filtered samples are necessary to increase the statistics of VZ, $Z \to b\bar{b}$ samples where the Z boson in the VZ processes is forced to decay to $b\bar{b}$.

The $t\bar{t}$ background events are created mostly from gluon interactions, where each of the top quarks decays into a b-quark and a W boson. These events are generated using Powheg [107] for the hard scattering using NNPDF 3.0 PDFs and Pythia8 with A14 [108] tune using NNPDF 2.3 PDFs for parton showering. The $t\bar{t}$ samples use p_T^V and E_T^{miss} filters to increase the statistics in high p_T^V regime. In addition, two different $t\bar{t}$ samples are generated. In the first one, at least one of the two W boson coming from the top quarks is forced to decay leptonically and these events are referred to as the non-all-hadronic $t\bar{t}$ samples. In the second samples, the two W bosons coming from the decay of the top quark decay to leptons, and these events are referred to as di-leptonic $t\bar{t}$ samples. Before merging the two samples, the di-lepton events in the non-all-hadronic sample are vetoes in order to avoid double counting.

Single top background events are generated using the Powheg generator with NNPDF 3.0 PDFs interfaced with Pythia8 using NNPDF 2.3 PDFs for parton showering. This process is simulated separately for the 3 production channels: s-channel, t-channel and Wt-channel.

The V+jets background corresponds to the production of a vector boson in association with jets. These events are generated using Sherpa 2.2.1 with a dedicated parton shower tune by the Sherpa authors for W and Z bosons decays. A filter was used to enhance the statistics in the analysis to split the events based on the maximum between p_T^V and the scalar sum of the p_T of jets and charged leptons (H_T) for $W \to l\nu$ and $Z \to ll$, or on p_T^V for $Z \to \nu\nu$ as filtering on p_T is shown to be more effective due to the trigger requirements in the 0-lepton channel. In addition, events are split depending on the flavor of the jets with dedicated filters to increase the contribution of heavy flavored jets: events with at least 1 b-hadron, events with at least 1 c-hadron and no b-hadron and events with no b-hadrons or c-hadrons. The simulated V+jets events in the analysis are split depending on truth flavor label (b, c or light) of the two Higgs boson candidate jets, as they represent events in different corners of the W+jets phase space. This allows to split the V+jets events into 12 different categories: Zbb, Wbb, Zbc, Wbc, Zbl, Wbl, Zcc, Wcc, Zcl, Wcl, Zl and Wl.

The Monte Carlo generators used in the analysis to estimate the background contributions are summarized in Table 5.2.

5.2 Objects selection

The identification and reconstruction of all objects are described in Chapter 4. Moreover, jets, leptons and the MET in the analysis are required to pass a series of selection cuts. In this Section, the specific selections in each of the 3 analysis channels are presented.

5.2.1 Triggers

Since millions of events coming from p-p interactions are produced every second inside the detector, trigger requirements are necessary to keep only events with potential physical interest. These triggers depend on the channel and on the period of data taking (denoted with letters

Process	Generator	$\sigma\times$ BR [pb]	N_{events} [$\times 10^6$]
Diboson			
$qq \to WW \to qql\nu$	Sherpa 2.2.1	112.6 × 0.439	88
$qq \to WZ \to l\nu qq$ (with $Z \to b\bar{b}$ extension)	Sherpa 2.2.1	50.3 × 0.227	55 (23)
$qq \to WZ \to qq\nu\nu$	Sherpa 2.2.1	50.3 × 0.135	22
$qq \to WZ \to qqll$	Sherpa 2.2.1	50.3 × 0.0683	41
$qq \to ZZ \to qqll$ (with $Z \to b\bar{b}$ extension)	Sherpa 2.2.1	15.57 × 0.140	19 (15)
$qq \to ZZ \to qq\nu\nu$ (with $Z \to b\bar{b}$ extension)	Sherpa 2.2.1	15.57 × 0.280	19 (19)
$gg \to WW \to qql\nu$	Sherpa 2.2.1	4.8 × 0.439	2.8
$gg \to ZZ \to qqll$ or $qq\nu\nu$	Sherpa 2.2.1	1.57 × 0.420	18
$t\bar{t}$			
non-full-had (with E_T^{miss}/p_T^V extension)	Powheg + Pythia8	831.76 × 0.543	470 (171)
di-leptonic	Powheg + Pythia8	831.76 × 0.105	145
Single top			
s-channel	Powheg + Pythia8	10.32 × 0.326	16
t-channel	Powheg + Pythia8	216.96 × 0.326	39
Wt-channel (with di-lepton extension)	Powheg + Pythia8	71.7 × 1	88 (57)
V+jets			
$Z \to \nu\nu$	Sherpa 2.2.1	56280 × 0.200	450
$W \to l\nu$	Sherpa 2.2.1	183600 × 0.326	1280
$Z/\gamma^* \to ll$, with m_{ll} >40 GeV	Sherpa 2.2.1	61940 × 0.101	490

Table 5.2 – The different Monte Carlo generators used to generate different background processes.

for the 2016 collection periods: A, D3, D4, ...). Events are recorded only if they pass at least one of the possible triggers. In the 0-lepton channel, an un-prescaled E_T^{miss} trigger is used with a threshold depending on the data taking period. In the 1-lepton channel, the final state corresponds to at least two jets in addition to one lepton (electron or muon) and missing energy (E_T^{miss} or MET) corresponding to the neutrino. In the muon sub-channel, the un-prescaled single muon trigger is used for events with $p_T^V < 150\,\text{GeV}$, whereas the E_T^{miss} trigger is used for events with $p_T^V > 150\,\text{GeV}$ since the muons are not taken into account when reconstructing the E_T^{miss} at the level-1 trigger (LVL1) and the hight-level trigger (HLT). Therefore the E_T^{miss} trigger is used because it is equivalent to a p_T^W trigger for $W \to \mu\nu$ events. On the other hand, an un-prescaled single electron trigger is used in the electron sub-channel. In the 2-lepton channel, at least one of the two leptons in the final state is required to pass either the single electron or the single muon trigger. Only 3 muon triggers are considered while 7 electron triggers are considered depending on the data taking period. All the triggers used in the analysis are listed in Tables 5.3, 5.4 and 5.5 with the corresponding year, threshold and description.

5.2.2 Leptons

The charged leptons present in the 1-lepton and the 2-lepton channels final states should pass loose identification and isolation selection criteria, required to reduce fake-leptons. Different requirements are set on the electrons and muons based on the calorimeter and the track information. Three different lepton selections are defined: VH-loose, ZH-signal and WH-signal, where the WH-signal selection is required to be tighter than the VH-Loose selection to reduce multi-jet QCD background contamination in the 1-lepton channel. These selections are used to determine the number of isolated leptons in the final state and therefore define the leptonic channel for each event.

For electrons, to be able to keep the majority of signal electrons, the VH-loose, ZH-Signal and

Trigger Name	Period	Threshold (GeV)	Description
HLT_xe70_L1XE50	2015	70 GeV	Seeded using the level L1_XE50 or L1_XE55 LAr and Tile calorimeter triggers, calibrated at the EM scale, with a threshold of 50(55) GeV and using to reconstruct the E_T^{miss} at the HLT, either the *mht* (missing H_T) algorithm or $pufit$ algorithm (where the E_T^{miss} is calculated as the negative of the sum of the transverse momentum vector of all the calorimeter topological clusters corrected for pile-up).
HLT_xe90_mht_L1XE50	2016 (A-D3)	90 GeV	
HLT_xe110_mht_L1XE50	2016 ($\geq$ D4)	110 GeV	
HLT_xe110_pufit_L1XE55	2017	110 GeV	
HLT_xe110_pufit_xe70_L1XE50	2018	110 GeV	

Table 5.3 – MET triggers used during the 2015-2018 data collection period.

Trigger Name	Period	Threshold (GeV)	Description
HLT_e24_lhmedium_L1EM20VH	2015	24 GeV	Seeded using L1EM20VH level 1 trigger calibrated at the EM scale with a threshold of 20 GeV, and require medium ID quality.
HLT_e60_lhmedium	2015	60 GeV	Seeded using L1EM20VH level 1 trigger calibrated at the EM scale with a threshold of 20 GeV, and require medium ID quality.
HLT_e120_lhloose	2015	120 GeV	Seeded using L1EM20VH level 1 trigger calibrated at the EM scale with a threshold of 20 GeV, and require loose ID quality.
HLT_e26_lhtight_nod0_ivarloose	2016 – 2018	26 GeV	Tight likelihood ID required, and variable loose isolation required
HLT_e60_lhmedium(_nod0)	2016 – 2018	60 GeV	Medium ID likelihood required
HLT_e140_lhloose(_nod0)	2016 – 2018	140 GeV	Loose ID likelihood required
HLT_e300_etcut	2018	300 GeV	No ID requirements.

Table 5.4 – Single Electron triggers used during the 2015-2018 data collection period.

Trigger Name	Period	Threshold (GeV)	Description
HLT_mu20_iloose_L1MU15	2015	20 GeV	Seeded using L1MU15 level 1 trigger with a threshold of 15 GeV, and requiring loose isolation requirements.
HLT_mu50	2015 – 2018	60 GeV	No isolation requirements.
HLT_mu26_ivarmedium	2016 – 2018	26 GeV	Variable cone medium isolation requirements

Table 5.5 – Single muon triggers used during the 2015-2018 data collection period.

WH-Signal selections require applying a Loose track isolation (FCLoose) to reject hadrons or non-isolated electrons from heavy flavor decays, using track information with an efficiency depending on p_T of the electron. For the WH-Signal selection, an additional tight FixedCutHighPtCaloOnly isolation is applied to suppress non-prompt electrons. In order to reduce tracks from pile-up, cuts on the track-to-vertex associated parameters $|\sigma_{d_0}/d_0| < 5$ (where σ_{d_0} is the estimated uncertainty on d_0) and $|\Delta z_0 \sin\theta| < 0.5\,\text{mm}$ are applied. These additional cuts remove events at the edge of the phase space, allowing to select events coming from the primary vertex and have a better rejection of background events. To pass the selection, electrons are required to have $|\eta| < 2.47$ and $p_T > 7\,\text{GeV}$ for the VH-Loose and $p_T > 27\,\text{GeV}$ for both the ZH-Signal and WH-Signal criteria satisfying the trigger threshold requirements. Table 5.6 shows in detail the electron selection criteria.

Electron Selection	p_{T}	η	ID	Isolation
VH-Loose	>7 GeV	$\|\eta\| < 2.47$	Loose quality	FCLoose
ZH-Signal	>27 GeV	$\|\eta\| < 2.47$	Loose quality	FCLoose
WH-Signal	>27 GeV	$\|\eta\| < 2.47$	Tight quality	FCLoose and FixedCutHighPtCaloOnly

Table 5.6 – Summary of the electron selections.

As for electrons, the VH-loose selection for muons intends to maximize the efficiency for signal muons. The FixedCutLoose isolation is applied using track information with 99% signal efficiency and an additional FixedCutHighPtTrackOnly isolation is used for the WH-Signal selection. Additional cuts on $|\sigma_{d_0}/d_0| < 3$ and $|\Delta z_0 \sin\theta| < 0.5\,\mathrm{mm}$ are applied to suppress tracks from pile-up. For the VH-Loose criteria, the jet should have $p_{\mathrm{T}} > 7$ GeV and $|\eta| < 2.7$, while for ZH-Signal they are required to have $p_{\mathrm{T}} > 27\,\mathrm{GeV}$ and $|\eta| < 2.5$. For the WH-Signal criteria, the muons are required to have $|\eta| < 2.5$, but the p_{T} selection depends on the p_T^V regime to satisfy the trigger requirements: $p_{\mathrm{T}} > 27$ GeV for $p_T^V < 150\,\mathrm{GeV}$ and $p_{\mathrm{T}} > 25\,\mathrm{GeV}$ for $p_T^V > 150\,\mathrm{GeV}$. Table 5.7 summarises the isolation selection for muons.

Muon Selection	p_{T}	η	ID	Isolation
VH-Loose	>7 GeV	$\|\eta\| < 2.7$	Loose quality	FixedCutLoose
ZH-Signal	>27 GeV	$\|\eta\| < 2.5$	Loose quality	FixedCutLoose
WH-Signal	>27 GeV and $p_T^V < 150\,\mathrm{GeV}$	$\|\eta\| < 2.5$	Medium quality	FixedCutLoose and FixedCutHighPtTrackOnly
WH-Signal	>25 GeV and $p_T^V > 150\,\mathrm{GeV}$	$\|\eta\| < 2.5$	Medium quality	FixedCutLoose and FixedCutHighPtTrackOnly

Table 5.7 – Summary of the muon selections.

5.2.3 Jets

Jets are classified as either *signal* or *forward* jets depending on their pseudo-rapidity. *Signal* jets should have a $p_T > 20\,\mathrm{GeV}$ and $|\eta| < 2.5$. These jets should meet a quality criteria known as jet cleaning needed to remove jets from beam background and jets in regions where the calorimeter clusters where very noisy and might have faked a jet. A good suppression of pile-up jets can be achieved using an additional requirement on the jet vertex tagger [93] (JVT), that uses informations based on the primary vertex of the interaction: JVT >0.59 for jets with $p_T < 120\,\mathrm{GeV}$ and $|\eta| < 2.5$. On the other hand, *forward* jets are required to have $p_T > 30\,\mathrm{GeV}$ and $2.5 \leq |\eta| < 4.5$. The full set of selections is listed in Table 5.8. The two jets eligible to reconstruct the Higgs boson candidate in the analysis should be *signal* jets and should pass b-tagging requirements that will be discussed later.

Jet Category	Selection Requirements
Signal Jets	jet cleaning $p_{\mathrm{T}} > 20\,\mathrm{GeV}$ $\|\eta\| < 2.5$ JVT >0.59 if $p_{\mathrm{T}} < 120\,\mathrm{GeV}$ and $\|\eta\| < 2.5$
Forward Jets	jet cleaning $p_{\mathrm{T}} > 30\,\mathrm{GeV}$ $2.5 \leq \|\eta\| < 4.5$

Table 5.8 – Summary of the jets selection requirements.

The resolution of the Higgs boson mass reconstructed using the 2 b-tagged jets candidates can be

improved by applying different b-jet energy corrections. The corrections applied in the analysis are the muon-in-jet correction, PtReco correction and the kinematic likelihood fit.

- **Muon-in-jet** is the first correction applied to b-tagged jets. The jet energy is constructed only from the topo-clusters inside the calorimeter. Around 20% of the b-hadron decays produce muons which deposit only few GeV in the calorimeter, and hence contribute only a little to the reconstructed energy of the b-jets. The jet's energy is corrected for muons with small $\Delta R(jet, muon)$, by using the 4-vector information from the muon spectrometer and the tracker after subtracting the energy loss in the calorimeter, and adding it to the 4-vector of the jet.
- **PtReco correction** allows to compensate the difference between the reconstructed and the truth jets especially at low p_T. This correction is needed to account for the additional undetected neutrino energies produced from b-hadron decays. This correction is applied through a scale factor depending on the presence of an electron or a muon within the jet radius. These scale factors are taken from the ratio between the p_T of the reconstructed jet after applying muon-in-jet correction to the truth jet.
- **Kinematic fit** This correction is only applied in the 2-lepton channel to replace the PtReco correction for events with 2- or 3-jet. Since leptons have better resolution than jets, the $Z \to ll$ decay is used to improve the resolution of the di-jet mass. This is possible by performing a kinematic likelihood fit to the final state $l^+l^-b\bar{b}$ and balancing the momentum of each of the elements in the transverse plane for each event. Knowing the p_T of the Z boson allows to improve the measurement of the p_T of the jets and therefore improve the di-jet invariant mass.

  A comparison of the default energy calibration, muon-in-jet, PtReco and kinematic fit corrections is found in Figure 5.5

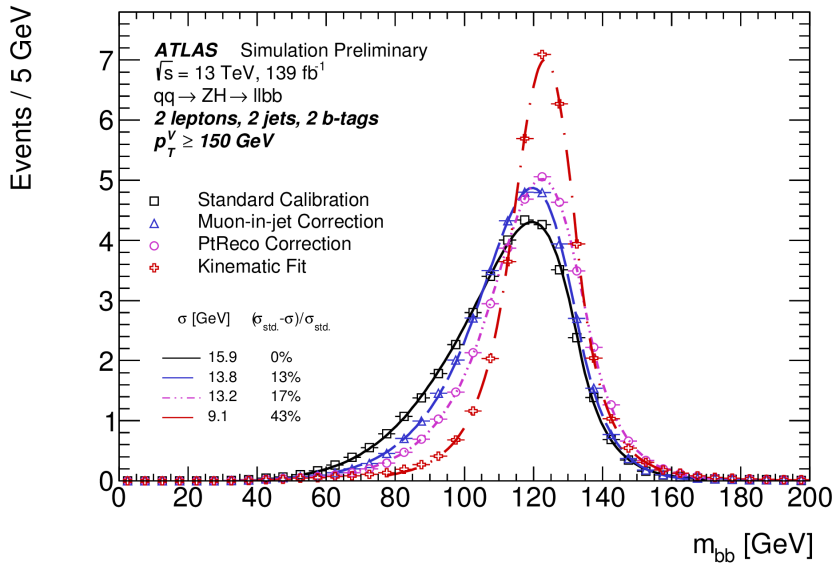

Figure 5.5 – Simulated mass resolution of the di-jet system using $ZH \to llb\bar{b}$ signal events in the 2 jet, $p_T^V > 150\,\text{GeV}$ region showing the default energy calibration and the different energy corrections.

5.3 Events selection

Both data and Monte Carlo events used in the analysis should pass trigger and lepton isolation selections and pass a set of events selection optimised in each of the analysis channels, required

to further suppress background events and increase the signal sensitivity. These selections are optimised separately in each of the 3 channels since each channel has a different background composition. The specific cuts in each of the channels are detailed below and a summary can be found in Table 5.9.

5.3.1 0-lepton channel specific selections

In the 0-lepton channel, the transverse momentum of the Z boson is identified as the missing transverse energy. Due to the trigger requirements, the trigger efficiency is low for events with $E_T^{miss} < 150\,\text{GeV}$, therefore these events are discarded. Additional requirements are applied to the scalar sum of the p_T of the jets in the final state (S_T), to keep only events with $S_T > 120\,\text{GeV}$ in the 2-jet category and $S_T > 150\,\text{GeV}$ in the 3-jet category.

Anti-QCD cuts are necessary in this channel to reduce the multi-jet background. These multi-jet events mainly come from jet energy mis-measurements, therefore the E_T^{miss} tends to be aligned with one of the selected jets. The cuts are defined from the azimuthal angles Φ between the leading selected jet $jet1$, the sub-leading selected jet $jet2$, the Higgs boson candidate h and the missing energy. These cuts allow to reduce the multi-jet contribution to less than 1% of the total background:

- $|\Delta\Phi(E_T^{miss}, E_{T,trk}^{miss})| < 90^\circ$, where $E_{T,trk}^{miss}$ is the track-based missing transverse energy
- $|\Delta\Phi(jet1, jet2)| < 140^\circ$
- $|\Delta\Phi(E_T^{miss}, h)| > 120^\circ$
- $\min[|\Delta\Phi(E_T^{miss}, \text{selected jets})|] > 20^\circ$ for 2-jet events
- $\min[|\Delta\Phi(E_T^{miss}, \text{selected jets})|] > 30^\circ$ for 3-jet events

5.3.2 1-lepton channel specific selections

In this channel the E_T^{miss} trigger or the single lepton trigger is used depending on the lepton flavor (e or μ) and on the p_T^V regime. Events should have one WH-signal lepton, and events with additional VH-loose lepton are dismissed. The W boson is reconstructed in the transverse plane as the sum of the lepton and the missing energy. Only events with $p_T^V > 150\,\text{GeV}$ are selected, similarly to the 0-lepton channel. This p_T^V selection obeys the triggers threshold requirements and allows to reduce the multi-jet background contamination in this channel. Further requirements are set in the electron sub-channel on the missing energy to reduce the multi-jet background: $E_T^{miss} > 30\,\text{GeV}$.

Even though the $75\,\text{GeV} < p_T^V < 150\,\text{GeV}$ region is not currently included in the analysis, there is an effort to include this region in the next round of the analysis, allowing to increase the sensitivity and to improve the WH channel measurement. In this region an additional cut is needed to reduce the multi-jet contribution: the transverse mass is required to satisfy $m_T^W > 20\,\text{GeV}$.

5.3.3 2-lepton channel specific selections

In the 2-lepton channel, events in the final state must contain exactly two VH-loose leptons where at least one of them should be a ZH-signal lepton. The two leptons in the final state should be either a pair of electrons or a pair of muons. In the muon sub-channel, the two leptons are required to be of opposite charges, but this constraint is not required in the electron sub-channel due to possible charge misidentification. The pair of leptons is used to reconstruct

the Z boson. Due to the excellent resolution resolution on the lepton energy and direction measurements, a tight cut on the di-lepton invariant mass allows to eliminate a large fraction of background events: $81\,\text{GeV} < m_{ll} < 101\,\text{GeV}$.

Common Selections	
Jets	≥ 2 signal jets
b-jets	2 b-tagged signal jets
Leading b-tagged-jet p_T	> 45 GeV
0- Lepton	
Jets	≥ 4 selected jets veto
Trigger	lowest un-prescaled E_T^{miss} triggers
Leptons	0 VH-loose lepton
E_T^{miss}	$> 150\,\text{GeV}$
S_T	$> 120\,\text{GeV}$ (2 jets), > 150 (3 jets)
$\lvert\Delta\Phi(E_T^{miss}, E_{T,trk}^{miss})\rvert$	$< 90^\circ$
$\lvert\Delta\Phi(jet1, jet2)\rvert$	$< 140^\circ$
$\lvert\Delta\Phi(E_T^{miss}, h)\rvert$	$> 120^\circ$
$min[\lvert\Delta\Phi(E_T^{miss}, jets)\rvert]$	$> 20^\circ$ (30°) for 2 (3) jet events
p_T^V	$> 150\,\text{GeV}$
1- Lepton	
Jets	≥ 4 selected jets veto
Trigger	e channel: un-prescaled single electron triggers
	μ channel: lowest un-prescaled E_T^{miss} triggers
Leptons	1 WH-signal lepton
	VH-loose lepton veto
E_T^{miss}	$> 30\,\text{GeV}$ (e channel)
m_T^W	$> 20\,\text{GeV}$ ($75\,\text{GeV} < p_T^V < 150\,\text{GeV}$)
p_T^V	$> 75\,\text{GeV}$
2- Lepton	
Trigger	un-prescaled single lepton triggers
Leptons	2 VH-loose lepton
	$\geq$ZH-signal lepton
	Same flavor, opposite-charge for $\mu\mu$
m_{ll}	$81 < m_{ll} < 101\,\text{GeV}$
p_T^V	$> 75\,\text{GeV}$

Table 5.9 – Summary of the channel-specific event selection in the 0-, 1- and 2-lepton channels.

5.3.4 Common selections

Events in analysis are selected if they have exactly two b-tagged signal jets. The first cut applied across the three channels concerns the leading b-tagged jet which is required to have a transverse momentum greater than 45 GeV. Events are split depending on the number of jets into a 2-jet category or a 3-jet category (or $\geq$ 3-jet in the 2-lepton channel only), and are then split into regions based on the reconstructed transverse momentum of the vector boson (p_T^V or E_T^{miss} in the 0-lepton channel): $75\,\text{GeV} < p_T^V < 150\,\text{GeV}$ in the 2-lepton channel only, $150\,\text{GeV} < p_T^V < 250\,\text{GeV}$ and $p_T^V > 250\,\text{GeV}$ in 0-, 1- and 2-lepton channels.

5.4 Tagging strategy

The aim of the analysis is to select signal events with 2 b-jets in the final state. Therefore, b-tagging is needed to distinguish b-jets from c- and light jets. Due to the high rejection rate and the lack of statistics in some of the Monte Carlo samples, the analysis adopted a method called hybrid truth tagging when using simulated events.

5.4.1 Truth tagging

The b-tagging algorithm described in Section 4.4.4, uses a fixed cut which discards the c- and light jets at 70% working point. This increases the statistical fluctuations in the shapes of the Monte Carlo samples and therefore will affect the background modelling. A solution is to use a truth tagging approach where no events are discarded, so all events pass the 2 b- tagged jets requirements by construction. All events are kept and a weight is assigned to these events corresponding to the probability of them being tagged.

The tagged jets are chosen randomly from all the possible permutations of the signal jets and the truth tagging weight is assigned accordingly. The total truth tagging weight of each event corresponds to the sum of all the possible permutations. It is constructed from the product of the b-tagging efficiency (ε) of the tagged jets and product of the complement of the b-tagging efficiency (1 - ε) of the non tagged jets. The ε is an efficiency binned as function of two variables: p_T and η of the jet, and has a fine binning which does not introduce any bias on the efficiency observed on the Monte Carlo samples. For example, the truth tagging weight of an event with 3 jets is:

$$w_{tot} = \varepsilon_1\varepsilon_2(1-\varepsilon_3) + \varepsilon_1(1-\varepsilon_2)\varepsilon_3 + (1-\varepsilon_1)\varepsilon_2\varepsilon_3 \tag{5.1}$$

The probability of randomly selecting jet-2 and jet-3 to be tagged corresponds to the ratio of the single contribution to all the possible permutations:

$$P_{23} = \frac{(1-\varepsilon_1)\varepsilon_2\varepsilon_3}{w_{tot}} \tag{5.2}$$

This probability corresponds to the rate at which this specific selection will be chosen. Since the b-tagging efficiency is higher for b-jets than for other jets, the c- and light jets contribution will be suppressed.

The simulated MV2c10 scores of the selected jets do not all fall in the b-tagging requirements of the analysis. Since the MV2c10 scores are used as input information for the training of the analysis BDT (see Section 5.5), the MV2c10 values are re-assigned to the jets, depending on the choice of the combination to reflect the b-tagging efficiency of each jet: the b-tagging scores for the b-tagged jets will be above the working point and below for the untagged jets. The truth tagging weights are assigned to each event to reflect the new MV2c10 distribution.

5.4.2 Hybrid truth tagging

Another approach, called hybrid truth tagging, is used by the VHbb analysis that consists on using a fixed cut at 70% working point (called direct tagging) to select b-jets and using truth tagging to the other flavors based on the truth flavor labels. When an event contains both b- and non b-jets, direct tagging is first applied only to b- jets and then truth tagging is applied to the remaining jets. Let's take as an example a 3-jet event with two b-jets both above 70%

working point and one c-jet. In this case, first direct tagging is applied on the two b-jets. If one of the two b-jets did not match 70% working point requirement, this one will not be selected and the c-jet will be tagged using truth tagging. In the case where the event contains one b-jet above 70% working point and two c-jets, direct tagging will be applied to the b-jet and one of the c-jets will be randomly tagged using truth tagging.

The b-tagging weight assigned to each event will be therefore a combination of both approaches. It is calculated following Equation 5.1 by taking the efficiency of the directly tagged jets as 1. Similarly to the description in Section 5.4.1, a MV2c10 score is assigned to truth tagged jets.

5.5 Multivariate analysis

Multivariate analyses (MVA) are widely used in high energy physics as a method to distinguish signal from background events. A MVA classification technique called boosted decision trees (BDTs) is used in the VHbb analysis. This algorithm uses simple cuts on the input variables to classify an event as being more signal-like or background-like. It maximises the separation between signal and background events using one discriminant constructed from input variables. In this Section a description of the BDTs, their usage within the analysis, the input variables and details on the training are presented.

5.5.1 Boosted decision trees

The BDTs are a collection of decision trees trained on known Monte Carlo signal and background events to exploit the correlations between all input variables. Each one of these trees defines a series of cuts on the input variables to discriminate between the signal and the background inputs. They are trained on the same set of inputs and each tree is able to learn different patterns and optimise the classification cuts. The algorithm is qualified as "boosted" since the training of each tree depends on the training of the previous one which allows to increase the discrimination power of the ensemble of trees. This method allows to combine all the trees into one powerful classifier. Each tree is composed of nodes, at which each of the events is tested using cuts. Then a decision is made for the event to fall into one of the classification leaves or to pass into the next node. The output of the BDT, called a BDT score, is a value between -1 (the event is 100% background-like) and 1 (the event is 100% signal-like) to determine the purity of the classification of each event after evaluation. Figure 5.6 shows an illustration of the different steps for a decision tree starting from the root node to the leaf classification. In the VHbb analysis, the BDT is trained using a set of discriminant variables as inputs by taking the Monte Carlo signal samples described in Section 5.1.1 as signal inputs and all the background samples (diboson, V+jets and top) described in Section 5.1.2 as background inputs.

5.5.2 Training setup and parameters

Truth tagging was chosen to increase the Monte Carlo statistics in both the signal and background samples as having enough statistics in the training inputs is crucial. This is necessary to avoid over-training of the BDTs where it might be picking up some statistical fluctuation instead of a real physics feature. Another way to mitigate over-training is by using a k-folding technique which serves as a cross-validation as well. The k-folding procedure is done by splitting the inputs into several categories depending on the event number, which is a unique tag assigned to each Monte Carlo generated event. The VHbb analysis uses 2-folds for training, where events are split into even and odd categories (folds) each used for the training of the BDT and used afterwards for the evaluation of the other fold. Table 5.10 shows the events used for the training

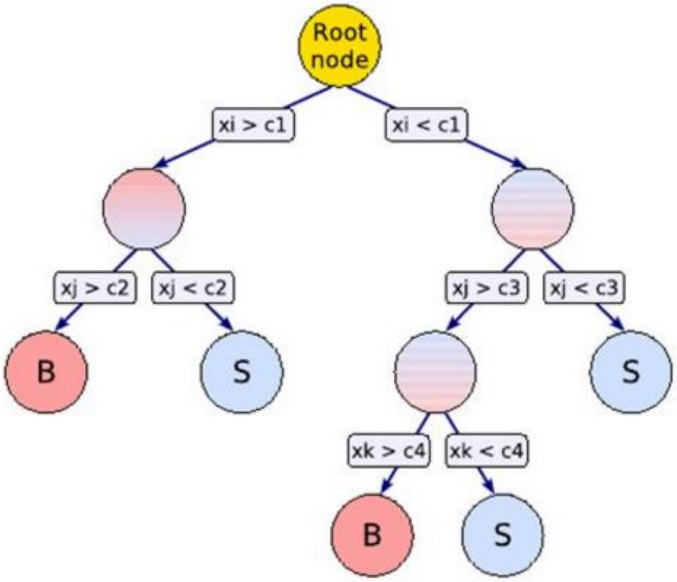

Figure 5.6 – Sketch of a decision tree, showing the leaves and the nodes with the decision cuts. The blue leaf indicate a signal-like event while red indicated a background-like leaf.

and evaluation of each of the 2-folds. This 2-folds method is also used to check if the BDTs are over-trained, as the performance is expected to be the same when using either of the two folds for the evaluation.

	BDT-1	BDT-2
Training	fold-1	fold-2
Evaluation	fold-2	fold-1
Over-training test	fold-1	fold-2

Table 5.10 – The 2-folds used for the BDT training.

Gradient boosting algorithm is used for the training of the BDT. This algorithm consists on building decision trees iteratively to optimise the final classifier. The performance of the BDT can be enhanced by tuning the hyperparameters such as the number of trees used in the training, the depth of the trees or the number of nodes, the learning rate related to the weight assigned to each event by the tree to increase its performance, the Gini index or the minimum number of events at each node. Pruning methods can be implemented to interrupt the classification if the decision was made before reaching the last node, but none was used here for the training. The hyperparameters used in the training are listed in Table 5.11, and were tuned to avoid any over-training.

For the diboson validation analysis described in Section 5.6.1, the training is done by taking the diboson samples as signal inputs and VH, V+jets and top samples as background inputs. The diboson training was performed using the same setup as the VH training.

5.5.3 Input variables

All events passing the event selection described in Section 5.3 are used in the training. The events in the training are split depending on the jet multiplicity and depending on the p_T^V category, where events with p_T^V below 150 GeV are treated separately in the 2-lepton channel. A dedicated training is performed in each of the 3 channels. The choice of variables for the

Training Setting	Value	Definition
BoostType	gradient boosting	Boost procedure
Shrinkage	0.5	Learning rate
SeparationType	Gini index	Node separation gain
PruneMethod	No Pruning	Pruning method
NTrees	200 (600 for 1-lepton VH)	Number of trees
MaxDepth	4 (2 for 1-lepton diboson)	Maximum tree depth
nCuts	100	Number of equally spaced cuts tested per variable per node
nEventsMin	5%	Minimum number of events in a node (% of total events)

Table 5.11 – The hyperparameters used in the training.

training has been optimised separately in each channel. The variables used in each channel are summarized in Table 5.12.

To calculate the mass of the top quark (m_{top}) and the difference in rapidity between the W boson and the Higgs boson candidate ($\Delta Y(W,H)$), the 4-momentum of the neutrino is reconstructed using the missing transverse energy and a W boson mass constraint.

Variable	Description	0-lepton	1-lepton	2-lepton
m_{jj}	Invariant mass of two Higgs boson candidate jets	✓	✓	✓
$\Delta R(jet_1, jet_2)$	Distance between the two Higgs boson candidate jets	✓	✓	✓
p_T^{jet1}	Transverse momentum of the leading b-tagged jet	✓	✓	✓
p_T^{jet2}	Transverse momentum of the sub-leading b-tagged jet	✓	✓	✓
p_T^V	Transverse momentum of the vector boson	✓	✓	✓
$E_{\text{T}}^{\text{miss}}$	Missing transverse energy	$\equiv p_T^V$	✓	
$\Delta\phi(V,H)$	Distance in ϕ between the vector boson and the Higgs boson candidate	✓	✓	✓
binned MV2c10(jet_1)	MV2c10 binned distribution of the leading jet	✓	✓	
binned MV2c10(jet_2)	MV2c10 binned distribution of the sub-leading jet	✓	✓	
$\lvert\Delta\eta(jet_1, jet_2)\rvert$	Distance in η between the two Higgs boson candidate jets	✓		
M_{eff}	Scalar sum of E_T^{miss} and selected jets	✓		
track based soft $E_{\text{T}}^{\text{miss}}$ term	Vectorial sum of the transverse momentum of all tracks not reconstructed in the event	✓		
$\min(\Delta\phi(l, jet))$	Distance in ϕ between the lepton and the closest b-tagged jet		✓	
m_T^W	Transverse mass of the W boson		✓	
$\Delta Y(W,H)$	Difference in rapidity between the W boson and the Higgs boson candidate		✓	
m_{top}	Mass of the top quark decaying leptonically		✓	
$E_{\text{T}}^{\text{miss}}$ significance	Quasi-significance of E_T^{miss} defined as $E_T^{miss}/\sqrt{S_T}$			✓
$\Delta\eta(V,H)$	Difference in η between the vector boson and the Higgs boson candidate			✓
m_{ll}	Invariant mass of the dilepton			✓
$\cos\theta(l^-, Z)$	Angle between the negatively charged lepton and the Z boson flight direction in the Z boson rest frame			✓
	Only in 3-jet events			
$p_T^{\text{jet}_3}$	Transverse momentum of the leading un-tagged jet	✓	✓	✓
m_{jjj}	Invariant mass of the two tagged jets and the leading un-tagged jet	✓	✓	✓

Table 5.12 – Variables used for the BDT training.

5.5.4 BDT transformation

The BDT is evaluated for each event and the output (denoted as mva) is stored in a 500 bins histogram, where the left most bins are populated by background events and the right bins mostly by signal events. The BDT distribution is rebinned to reduce the number of bins in the binned profile likelihood used to extract the analysis result, and at the same time keep the analysis sensitivity close to the maximum value. Different rebinning algorithms have been developed during Run-1 [109] and one of these algorithms is used in this analysis. The BDT binning is defined by applying a transformation based on the following quantity, to create bins of different sizes:

$$Z = z_s \frac{n_s}{N_s} + z_b \frac{n_b}{N_b} \tag{5.3}$$

- $\boldsymbol{N_s}$ **and** $\boldsymbol{N_b}$ are the total number of events in the of signal and background histograms respectively.

- n_s **and** n_b are the number of signal and background events within a certain interval of bins of the histogram.
- z_s **and** z_b are parameters used to tune this algorithm.

The BDT transformation is done by starting with the last bin on the right of the distribution before rebinning and then adding the bins one by one by going to the left of the distribution. The Z function is calculated at each iteration and the bins are merged together into one single bin until Z >1 and the Monte Carlo simulated events statistical uncertainty is less than 20%. The same procedure is iterated until all bins from the original distribution are used.

In this method, z_s and z_b influence the number of bins in the final distribution, as $N_{bins} \leq z_s + z_b$. Note that z_s is required to be larger than z_b to achieve a finer binning at high BDT values, which helps to preserve the sensitivity. The results of the algorithm is that the bin on the right has a fraction of $1/z_s$ of signal events and that of the left has a fraction of $1/z_b$ of background events.

The final BDT distributions have 8 bins in the p_T^V >250 GeV region (corresponding to $z_s = 5$ and $z_b = 3$) and 15 bins in all other regions (corresponding to $z_s = 10$ and $z_b = 5$). Figure 5.7 shows the difference between the BDT distribution after transformation and the BDT distribution after merging each 25 bins together to create an histogram with 20 bins of equal size in the 1-lepton channel. The optimised binning allows to increase the sensitivity like in the 1-lepton channel where the expected stat-only significance after applying the BDT transformation is 5.97σ compared to a significance of 5.64σ when using 25 equal size bins.

5.6 Cross-check analyses

5.6.1 Diboson Analysis

The diboson process $VZ(Z \to b\bar{b})$ is one of the main backgrounds in this analysis. However it offers a good validation of the Higgs boson analysis because both analyses have identical background composition (except that the signal of one analysis is a background in the other), similar kinematics and the same physics objects in the final state. The main kinematic differences between the diboson and the Higgs boson processes are obviously the m_{bb} distribution, but also the p_T^V spectrum which is harder for the VH process. The diboson analysis uses the same event selection as the Higgs boson analysis. The measurement is done using the BDT as a final discriminant where the BDT training is performed using diboson as signal. The same systematic uncertainties are used for both analysis and the same fit regions are adopted.

The BDT output is also rebinned using the same transformation but different tuning parameters. Since the diboson samples (VZ) have lower statistics than the VH samples, the final distributions contain fewer bins than the VH BDT distribution. The final VZ BDT distributions count 5 bins in the p_T^V >250 GeV region (corresponding to $z_s = 3$ and $z_b = 2$) and 10 bins in all other regions (corresponding to $z_s = 5$ and $z_b = 5$). Figure 5.8 shows the BDT_{VZ} distributions after BDT transformation for the 1-lepton, 2-jet signal regions.

5.6.2 Di-jet mass analysis

In the di-jet mass analysis, the BDT discriminant is replaced by the invariant mass of the jets forming the Higgs boson candidate (m_{bb}). No additional cuts or selection are needed and the analysis selection and strategy are similar to that of MVA and the diboson analyses. Figure 5.9 shows the m_{bb} distributions in the 1-lepton channel, 2-jet category.

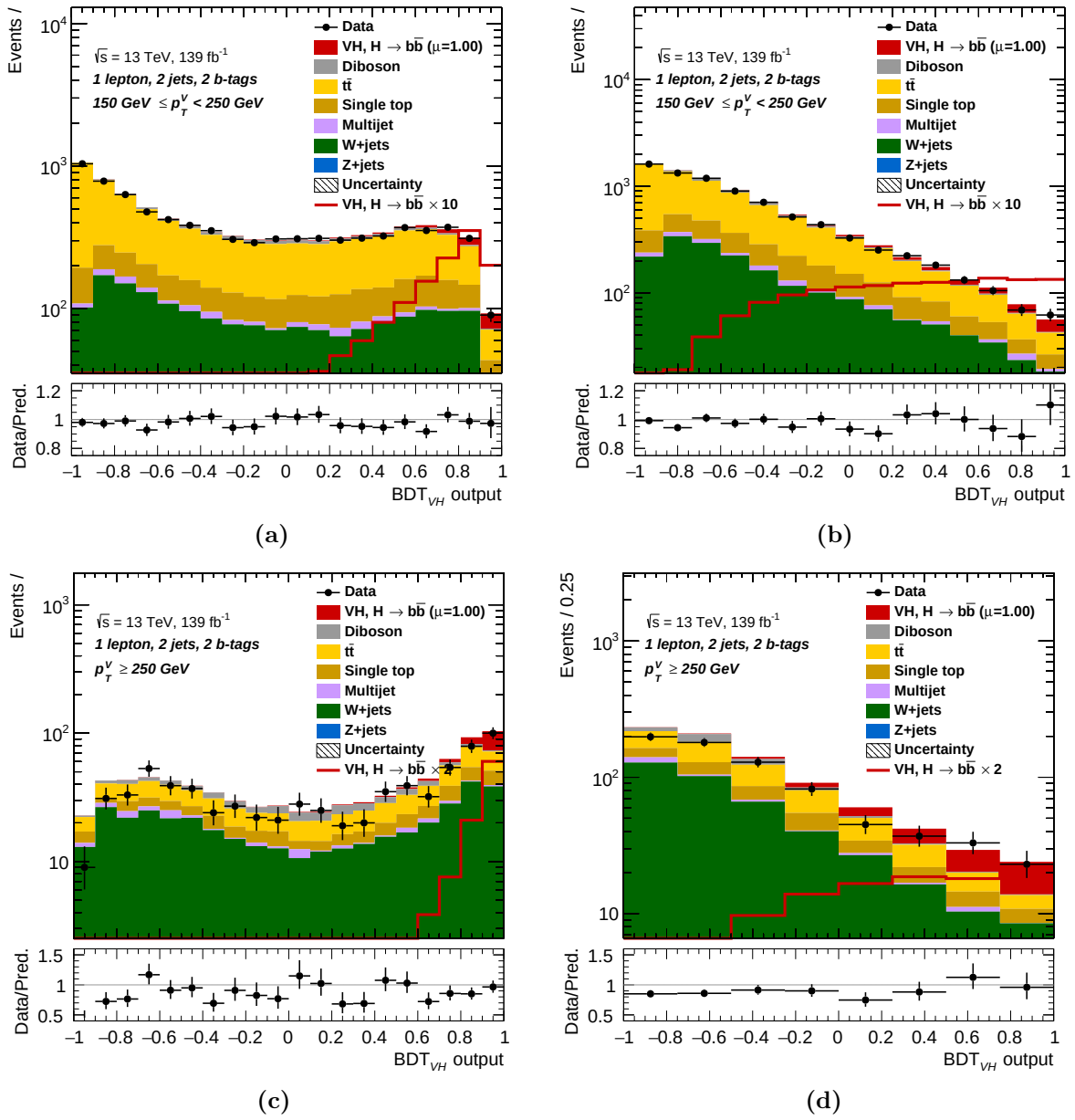

Figure 5.7 – BDT distribution in the 1-lepton channel, 2-jet category, with two different binning algorithms: an unoptimised binning with equal bin sizes on the left in 150 GeV $< p_T^V <$ 250 GeV (a) and $p_T^V >$ 250 GeV (c) signal regions, and after the BDT transformation with dynamic bin sizes on the right in 150 GeV $< p_T^V <$ 250 GeV (b) and $p_T^V >$ 250 GeV (d) signal regions.

5.7 Events categorisation

In order to improve the sensitivity of the analysis, the events are categorised into signal regions or control regions enriched in targeted backgrounds with low signal acceptances. These control regions are distinct from the signal region to better control the dominant background processes and constrain their dedicated modelling systematic uncertainties. The constraints obtained from these control regions are extrapolated towards the signal regions and across the three lepton channels. The events categorisation was chosen and optimised in the 1-lepton channel, since it is dominated by both W+jets and $t\bar{t}$ backgrounds which allows to define dedicated control regions for these two backgrounds. The same signal and control regions are defined in the 0- and 2-lepton channel.

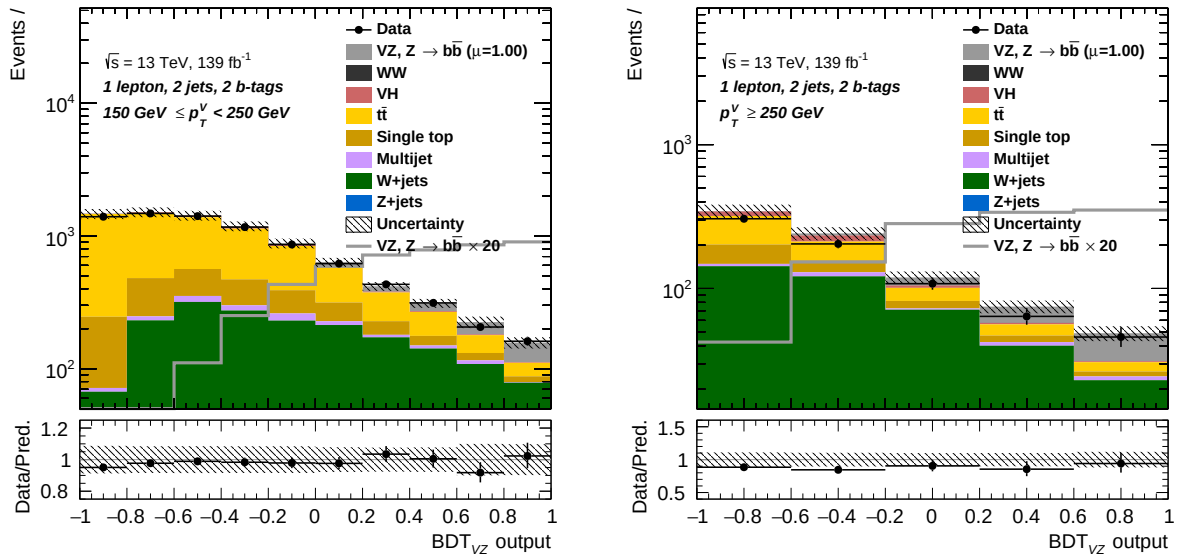

(a) (b)

Figure 5.8 – MVA VZ distribution in the 1-lepton channel, 2-jet category, after the BDT transformation in 150 GeV $< p_T^V <$ 250 GeV (a) and $p_T^V >$ 250 GeV (b) signal regions.

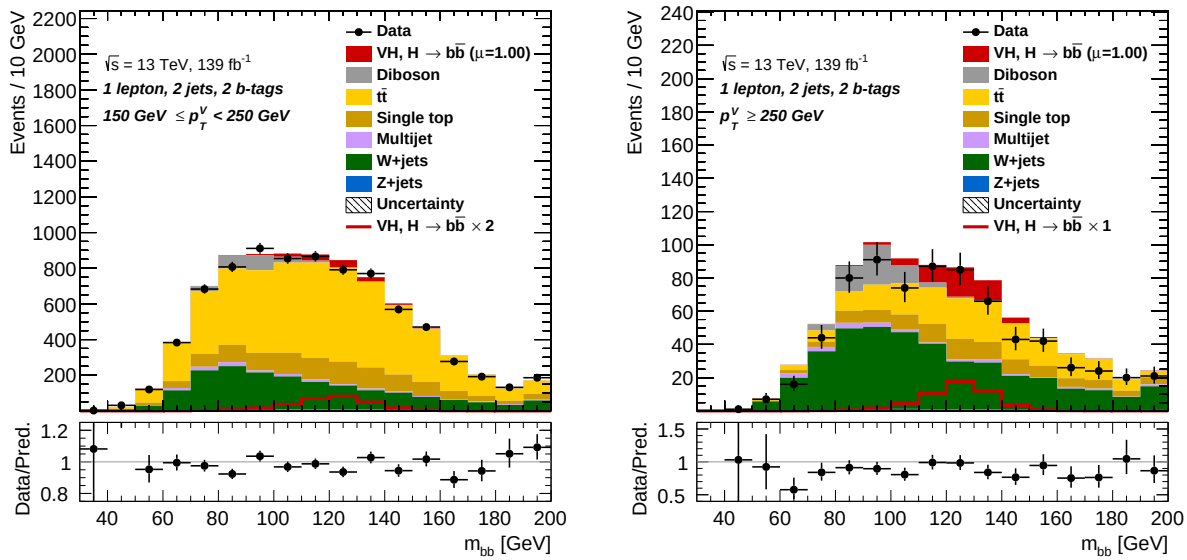

(a) (b)

Figure 5.9 – The di-jet mass distribution in the 1-lepton channel, 2-jet category, 150 GeV $< p_T^V <$ 250 GeV (a) and $p_T^V >$ 250 GeV (b) signal regions.

5.7.1 Defining regions in the 1-lepton channel

The analysis regions are chosen in a way to have large signal and diboson acceptances in the signal regions. In order to not degrade the sensitivity, especially in the di-jet mass fit, these regions are defined using cuts on the angular separation between the two Higgs boson candidate jets (ΔR_{bb}). It is a good discriminant between the signal, the W+jets events which are abundant at low ΔR_{bb} and the $t\bar{t}$ events which are abundant at high ΔR_{bb} as shown in Figure 5.10. Since ΔR_{bb} depends on the p_T^V, the jets are more collimated at high p_T^V. In addition, since the events are already categorised into p_T^V regions and to be able to create unified cuts across channels and regions, the cuts should also depend on the p_T^V. Thereby, the signal and control regions are

defined using continuous cuts of ΔR_{bb} as function of the p_T^V.

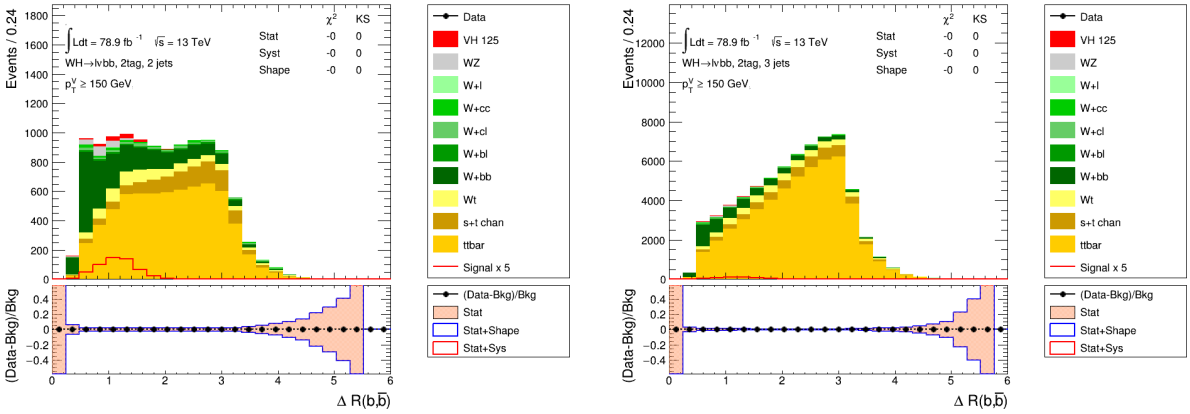

Figure 5.10 – The ΔR_{bb} distribution in the 1-lepton inclusive phase space in the 2-jet (a) and 3-jet (b) region.

The control regions are chosen using continuous cuts taken from the signal distribution in the $\Delta R(b,b)$-p_T^V plane using $80\,\text{fb}^{-1}$ dataset. Only $80\,\text{fb}^{-1}$ of the Run-2 dataset was used because at this stage of the study the $139\,\text{fb}^{-1}$ were not yet available. Table 5.13 shows the signal and background yields in the full phase space. In order to make the signal contribution negligible in the control regions, a lower and an upper cuts are defined by contouring the signal distributions in this plane. This allows to create two control regions: the high and the low ΔR control regions.

process	2-jet	3-jet
signal	109.3 ± 0.2	105.9 ± 0.2
WZ	166.5 ± 4.4	294.1 ± 6.1
Wl	12.6 ± 11.6	70.6 ± 15.4
Wcc	139.4 ± 15.6	375.3 ± 23.5
Wcl	160.8 ± 18.1	310.0 ± 22.7
Wbl	137.3 ± 6.1	311.9 ± 9.4
Wbc	267.7 ± 7.5	550.2 ± 10.7
Wbb	1943.0 ± 17.8	4396.4 ± 28.2
single top Wt	769.1 ± 14.2	3872.9 ± 31.8
single top t	882.8 ± 17.4	4442.3 ± 37.0
single top s	301.4 ± 3.0	424.4 ± 3.6
ttbar	6658.0 ± 42.9	51823.6 ± 119.8

Table 5.13 – Signal and background yields for $80\,\text{fb}^{-1}$ in the 1-lepton channel.

5.7.1.1 Cuts optimisation

The lower and upper cuts were optimised separately for the 2- and 3-jet categories. They were chosen as a compromise to keep the majority of signal events inside the signal region and create control regions highly pure in W+jets and $t\bar{t}$ events. A simple approach is to define the analysis regions using cuts on the quantile of the signal distributions. When choosing the cuts, it is important to keep as much diboson background as possible in the signal region, which is needed for the diboson validation analysis.

The choice of the cuts is very important to improve the signal purity in the signal region and at the same time create background enriched control regions to have a better control of the

modelling systematic uncertainties. Several cuts have been tested to evaluate their impact on the sensitivity. Table 5.14 summaries the tested upper and lower cuts and the signal and background efficiencies for each configuration. For the upper cut, a tighter cut allows to put more $t\bar{t}$ events in the high ΔR control region. For the lower cut, using the signal quantiles deteriorates the diboson acceptances in the signal region, therefore quantiles from diboson distribution were tested.

Cuts	2-jet	3-jet
VH signal		
lower cut at 5% WH - upper cut at 95% WH	89.9%	89.5%
lower cut at 5% WH - upper cut at 90% WH	85.0%	84.7%
lower cut at 10% WZ - upper cut at 95% WH	94.1%	92.0%
lower cut at 10% WZ - upper cut at 90% WH	89.2%	87.2%
lower cut at 10% WZ - upper cut at 85% WH	84.3%	82.3%
Diboson		
lower cut at 5% WH - upper cut at 95% WH	51.1%	68.8%
lower cut at 5% WH - upper cut at 90% WH	50.3%	63.9%
lower cut at 10% WZ - upper cut at 95% WH	86.1%	78.2%
lower cut at 10% WZ - upper cut at 90% WH	85.3%	73.3%
lower cut at 10% WZ - upper cut at 85% WH	84.7%	70.1%
$t\bar{t}$		
lower cut at 5% WH - upper cut at 95% WH	32.5%	40.2%
lower cut at 5% WH - upper cut at 90% WH	26.5%	28.2%
lower cut at 10% WZ - upper cut at 95% WH	36.5%	41.7%
lower cut at 10% WZ - upper cut at 90% WH	30.5%	29.8%
lower cut at 10% WZ - upper cut at 85% WH	26.9%	24.3%
W+bb		
lower cut at 5% WH - upper cut at 95% WH	31.3%	49.1%
lower cut at 5% WH - upper cut at 90% WH	27.3%	41.4%
lower cut at 10% WZ - upper cut at 95% WH	44.0%	53.7%
lower cut at 10% WZ - upper cut at 90% WH	40.0%	48.3%
lower cut at 10% WZ - upper cut at 85% WH	37.3%	43.9%

Table 5.14 – Cuts efficiencies in the signal region.

The lower cut was chosen at 10% of the diboson since it preserves the diboson efficiency without affecting the signal. It also allows to have a dedicated low ΔR control region enriched in W+jets events. For these reasons, this cut was adopted in both the 2- and 3-jet category. The high ΔR control region is designed to control top ($t\bar{t}$ and single top) events, and is chosen at 95% of the signal for 2-jet events and at 85% for 3-jet events. The upper cut is tighter in the 3-jet category to remove more $t\bar{t}$ events away from the signal region given its low signal over background ratio. Table 5.15 summarises the cut used to categorise the events and Figure 5.11 shows these cuts in the $\Delta R(b,b)$-p_T^V plane for the signal, diboson, Wbb and $t\bar{t}$ samples. Figures 5.12, 5.13 and 5.14 show the m_{bb} and the p_T^V distributions to illustrate how the different processes are distributed between the signal region, high and low ΔR control regions. Only W+jets, $t\bar{t}$ and diboson samples are shown since Z+jets and multi-jet backgrounds have a small contribution in the 1-lepton channel irrelevant for this study.

5.7.1.2 Impact on the signal measurement

This new categorisation aims at affecting only minimally the statistical-only sensitivity of the analysis, as the control regions are very depleted in signal events. The BDT distributions in

Category	Cut
high ΔR control region	
2-jet	$\Delta R > 0.87 + e^{1.38-0.00795\times p_T^V}$
3-jet	$\Delta R > 0.76 + e^{1.33-0.0073\times p_T^V}$
low ΔR control region	
2-jet	$\Delta R < 0.40 + e^{0.788-0.01023\times p_T^V}$
3-jet	$\Delta R < 0.42 + e^{0.268-0.00809\times p_T^V}$

Table 5.15 – Cuts defining the high ΔR and low ΔR control regions as function of p_T^V(GeV). Events in these regions are removed from the signal region, such that the three regions are fully orthogonal.

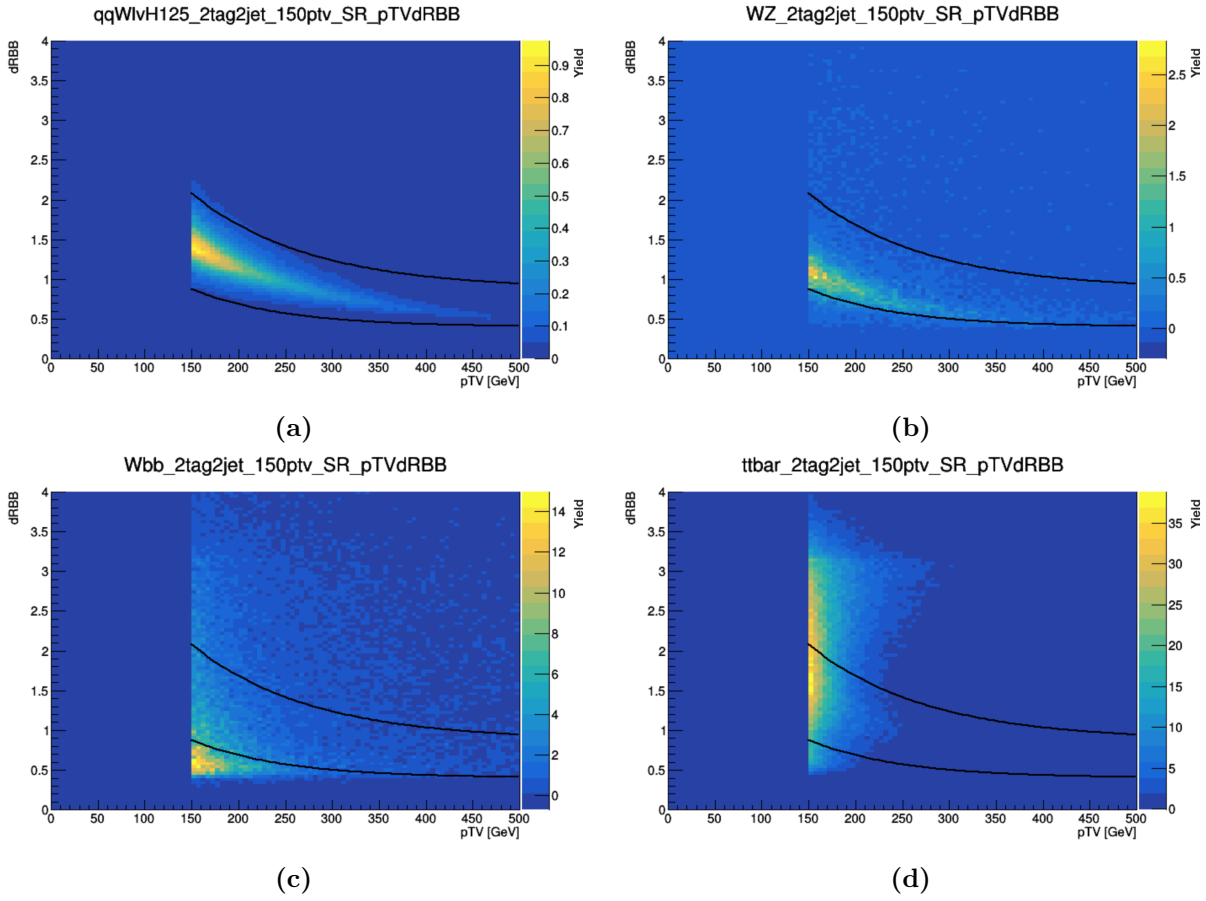

Figure 5.11 – The distribution of the ΔR between the two selected jets as function of p_T^V in the 2-tag 2-jet for signal (a), diboson (b), Wbb (c) and $t\bar{t}$ (d) samples. The black lines demonstrate the upper and lower continuous cuts used to categorize the events into the signal and control regions.

Figure 5.15 showing the events before and after categorisation, proving that the amount of signal events in the high BDT bins in the signal region did not change. Conversely, the events falling in the control regions are background-like and very far from the high sensitivity BDT bins. This change in events categorisation can be quantified by calculating the stat-only significance following [110]:

$$significance = \sqrt{\sum_{i=0}^{N_{bins}} 2 \times ((n_{s_i} + n_{b_i}) \times \ln(1 + \frac{n_{s_i}}{n_{b_i}}) - n_{s_i})} \tag{5.4}$$

- $\boldsymbol{n_{s_i}}$, $\boldsymbol{n_{b_i}}$ are the number of signal and background events in bin i

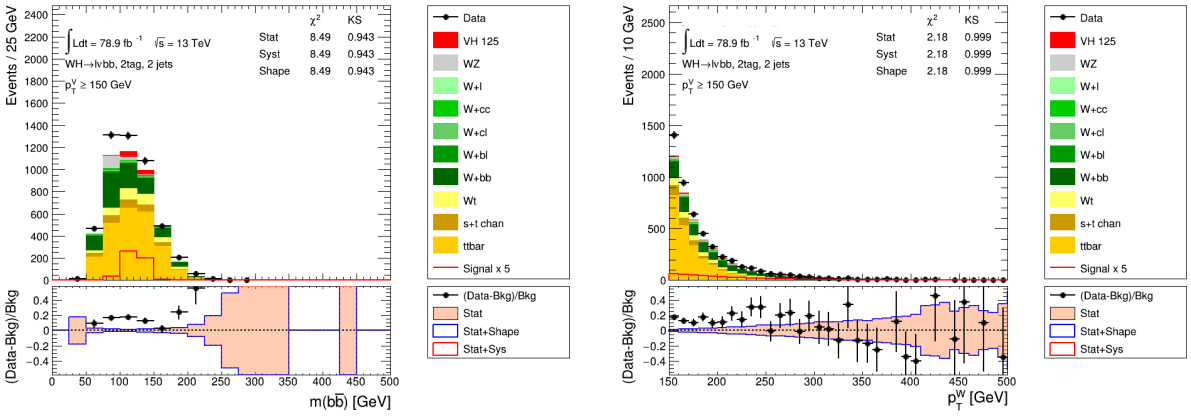

(a) **(b)**

Figure 5.12 – The m_{bb} and p_T^V distribution in the 1-lepton signal region, 2-jet $p_T^V > 150\,\text{GeV}$ category. No scale factors were applied in these distributions.

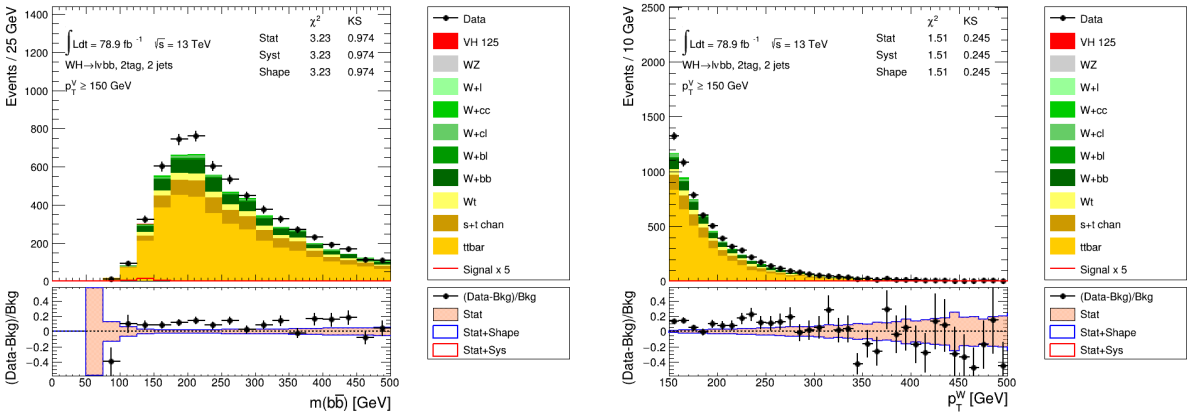

(a) **(b)**

Figure 5.13 – The m_{bb} and p_T^V distribution in the 1-lepton high ΔR control region, 2-jet $p_T^V > 150\,\text{GeV}$ category. No scale factors were applied in these distributions.

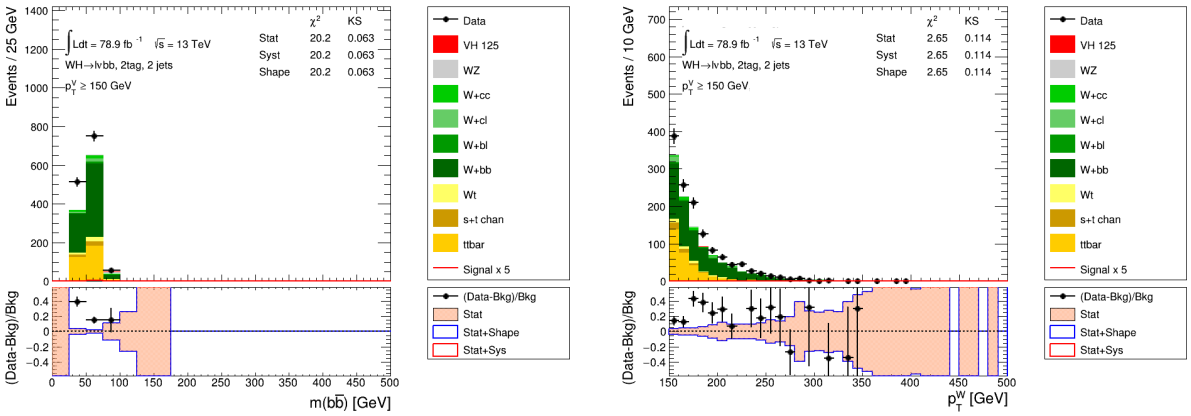

(a) **(b)**

Figure 5.14 – The m_{bb} and p_T^V distribution in the 1-lepton low ΔR control region, 2-jet $p_T^V > 150\,\text{GeV}$ category. No scale factors were applied in these distributions.

The measured sensitivity, as shown in Table 5.16, does not change for the 2-jet events, but decreases by 2% in the 3-jet category due the tighter cut used to define the high ΔR control

region. This loss seems acceptable given the small impact on the total significance (<1%) and the expected gain in control of the $t\bar{t}$ background.

Categorisation	2-jet	3-jet	Total
Full phase space	3.35	1.90	3.86
SR only	3.34	1.87	3.83

Table 5.16 – The stat-only significance in the MVA analysis using $80\,\text{fb}^{-1}$ in the 2-jet, 3-jet categories and their combination.

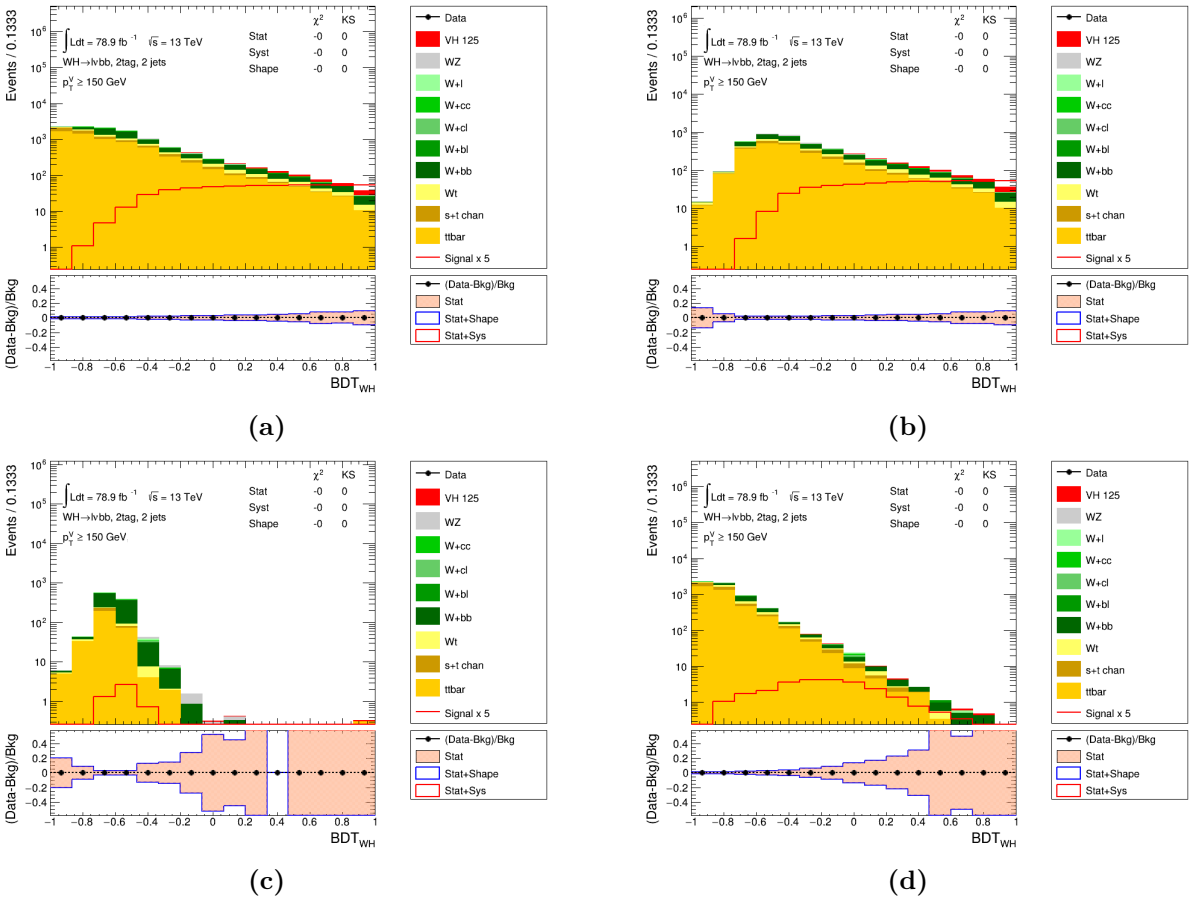

Figure 5.15 – The BDT distribution after transformation in the 1-lepton full phase-space in the 2-jet category (a). The same events are categorised in the signal region in (b), low ΔR control region in (c) and the high ΔR control region in (d). These distributions illustrate the background composition in each region, therefore the data is not shown.

5.7.2 Events categorisation in the 0-lepton channel

The 0-lepton channel is mainly dominated by Z+jets events, but also contains a significant amount of top and W+jets events. This channel is more complicated since it contains three main backgrounds. The same control regions are defined as the 1-lepton channel using the same cuts to obtain regions with different proportions, with more W+jets events at low ΔR and more $t\bar{t}$ at large ΔR. These cuts allow to remove the majority of Z+jets events from the signal region and distribute them in both the low and the high Δ R control regions. Figure 5.16 shows signal $\Delta R(b,b)$-p_T^V plane with the categorisation cuts and the similarity between the 0- and 1-lepton signal quantiles.

Figures 5.17, 5.18 and 5.19 show the m_{bb} and the p_T^V distributions to illustrate how the different processes are distributed between the signal region, high and low control regions.

The implementation of the control regions have a small impact on the stat-only significance, similarly to the 1-lepton channel. As shown in Table 5.17, the measured sensitivity decreases by 1% for 2-jet events and by 2% for 3-jet events.

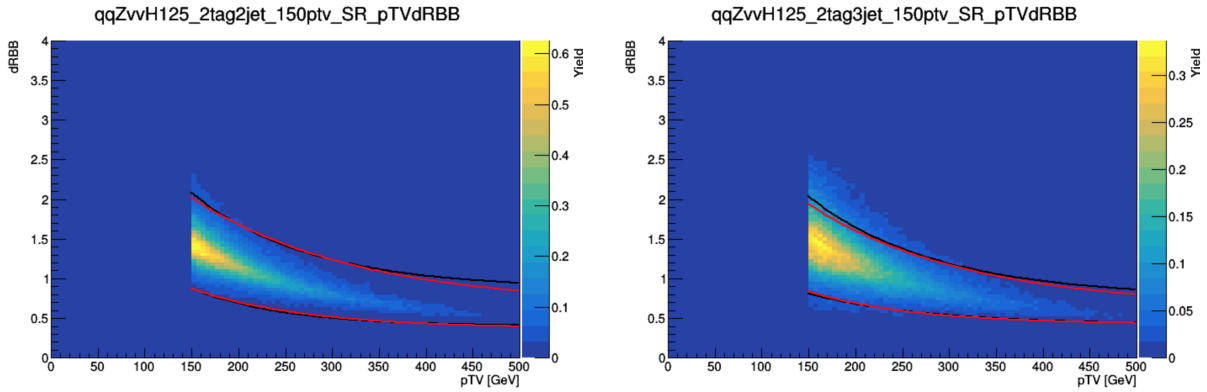

(a) **(b)**

Figure 5.16 – Signal distribution of ΔR between the two selected jets as function of p_T^V in the 2-tag 2-jet (a) and 2-tag 3-jet (b) categories. The black lines demonstrate the upper and lower continuous cuts derived from the 1-lepton distributions while the red lines demonstrate the upper and lower continuous cuts derived from the 0-lepton distributions.

Categorisation	2-jet	3-jet	Total
Full phase space	5.06	3.26	6.02
SR only	5.00	3.18	5.93

Table 5.17 – The stat-only significance in the MVA analysis in the 0-lepton 2-jet, 3-jet categories and their combination using 139 fb^{-1} dataset.

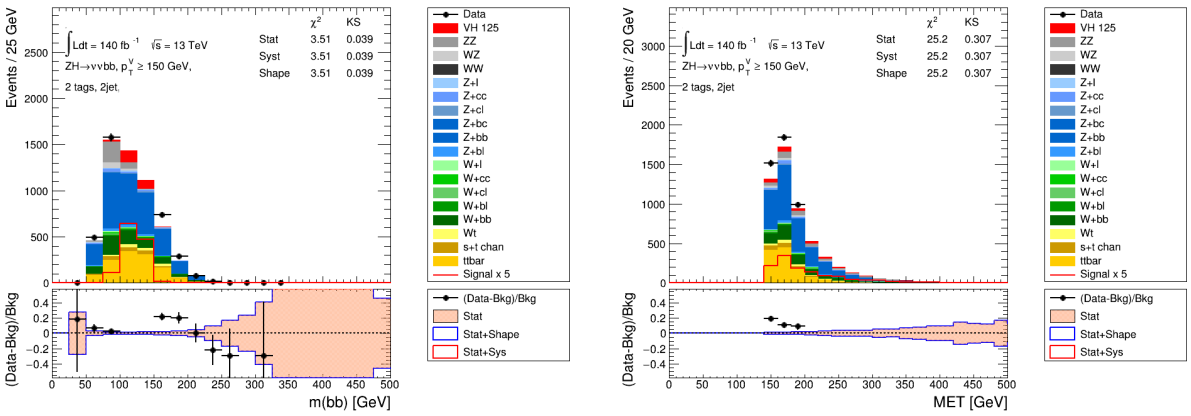

(a) **(b)**

Figure 5.17 – The m_{bb} and p_T^V distribution in the 0-lepton signal region, 2-jet $p_T^V > 150$ GeV category using 139 fb^{-1}. No scale factors were applied in these distributions. At this stage of the analysis, the signal region is blinded around the Higgs boson mass window.

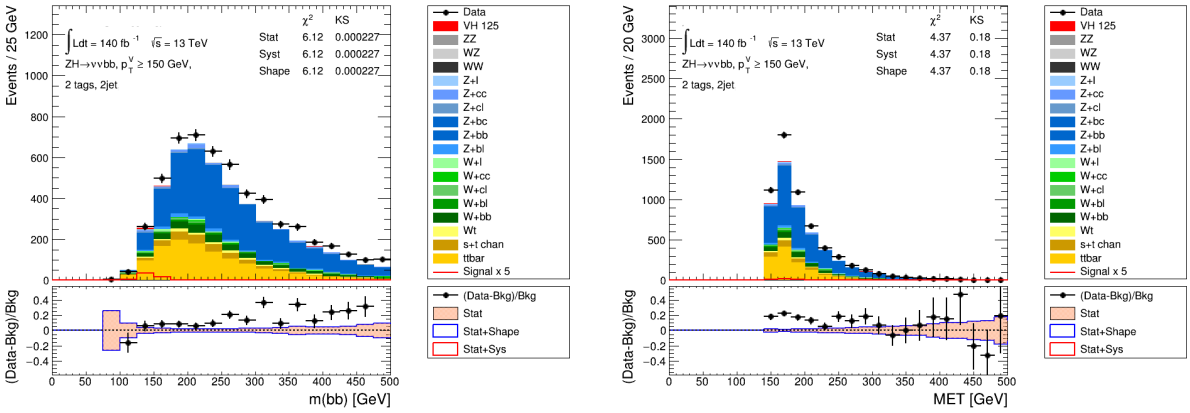

(a) **(b)**

Figure 5.18 – The m_{bb} and p_T^V distribution in the 0-lepton high ΔR control region, 2-jet $p_T^V > 150\,\text{GeV}$ category using $139\,\text{fb}^{-1}$. No scale factors were applied in these distributions.

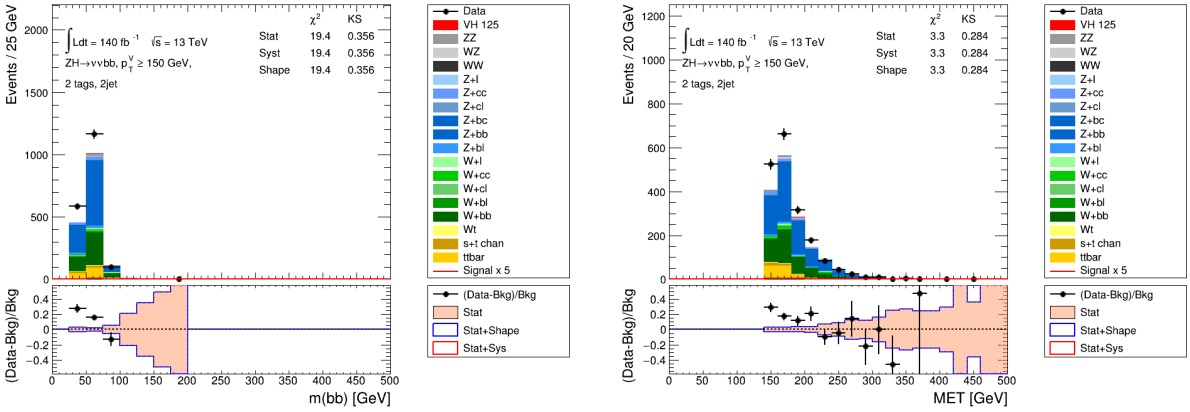

(a) **(b)**

Figure 5.19 – The m_{bb} and p_T^V distribution in the 0-lepton low ΔR control region, 2-jet $p_T^V > 150\,\text{GeV}$ category using $139\,\text{fb}^{-1}$. No scale factors were applied in these distributions.

5.7.3 Events categorisation in the 2-lepton channel

In the 2-lepton channel the only dominant background is Z+jets. The same control regions can still be beneficial in this channel not only to harmonize the categorisation across the 3 channels but also to control this dominant background. In this channel, the cuts derived from the signal distribution are different from the cuts in the two other channels, because in the 0- and 1-lepton channels events should have exactly 3-jet, whereas in the 2-lepton channels events with 3-jet or more are merged into one category (3p-jet). As shown in Figure 5.20, the upper cut in the 3p-jet distribution is tight and corresponds to a selection at 80% of the 2-lepton signal distribution. This tighter cut allows to reduce furthermore the Z+jets contamination in the signal region.

Figures 5.21, 5.22 and 5.23 show the m_{bb} and the p_T^V distributions to illustrate how the different processes are distributed between the signal region, high and low control regions.

As shown in Table 5.18, the new analysis categorisation has no impact on the 2-jet category (decrease by less than 1%). On the other hand, the sensitivity decreased by more than 4% due to tight high ΔR cut in the 3p-jet region. This cut in the 3p-jet category might not be optimal, but it was decided to be kept for the harmonisation between the three channels.

Categorisation	2-jet	3p-jet	Total
Full phase space	4.12	3.72	5.55
SR only	4.09	3.56	5.42

Table 5.18 – The stat-only significance in the MVA analysis in the 2-lepton 2-jet, 3p-jet categories and their combination using 139 fb^{-1} dataset.

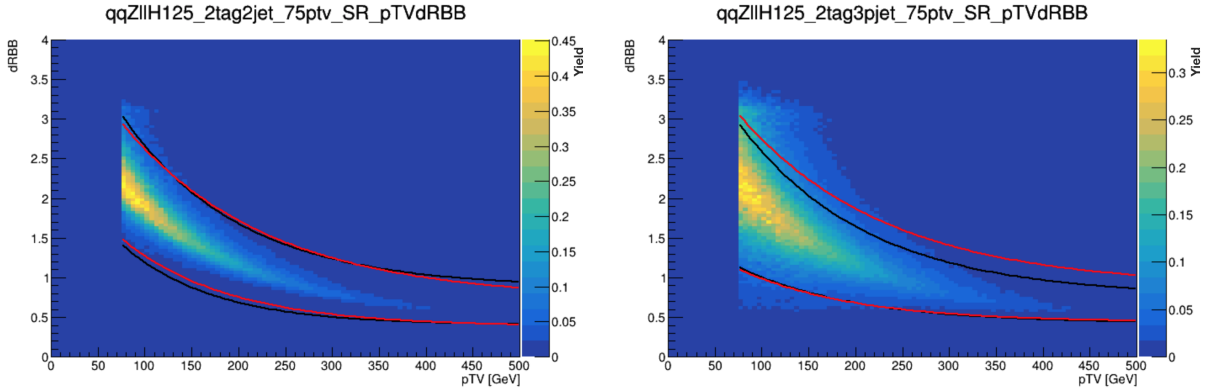

(a) **(b)**

Figure 5.20 – Signal distribution of ΔR between the two selected jets as function of p_T^V in the 2-tag 2-jet (a) and 2-tag 3p-jet (b) categories. The black lines demonstrate the upper and lower continuous cuts derived from the 1-lepton distributions while the red lines demonstrate the upper and lower continuous cuts derived from the 2-lepton distributions.

5.7.4 Analysis Regions

The final analysis includes a total of 14 signal regions, for each of them a low and a high ΔR control regions are associated. Depending on the analysis, the BDT_{VH}, m_{bb} or the BDT_{VZ} distribution in the signal region is used in the binned likelihood fit to measure the signal. A complete description of the likelihood fit and the statistical test can be found in Chapter 7. After combining the three lepton channels, the measured stat-only significance decreased by 2% and 6% in the MVA Higgs boson analysis and diboson analysis respectively and increased by 5% in the di-jet mass analysis with respect to the analysis using the full phase space for the signal regions, as shown in Table 5.19. The loss of stat-only sensitivity in the signal region is reasonable with respect to using the MVA in the inclusive phase space, given that the control regions will allow to better control the systematic uncertainties.

	BDT_{VH}	m_{bb}	BDT_{VZ}
Full phase space	10.15	6.89	21.59
SR only	9.99	7.28	20.40

Table 5.19 – The stat-only significance in the MVA, di-jet mass and diboson analyses after combining the three lepton channels.

The advantage of creating control regions is to constrain the normalisation of the main backgrounds. This can be achieved by combining the three channels and by using the yields in these regions in the fit. Furthermore a better constraint of W+jets, $t\bar{t}$ and single top modelling systematic uncertainties can be achieved by dividing the events through p_T^V categories. Having these categories brings more control to the backgrounds since systematics uncertainties are associated to the p_T^V distribution in the analysis, in addition to the fact that the distribution of p_T^V

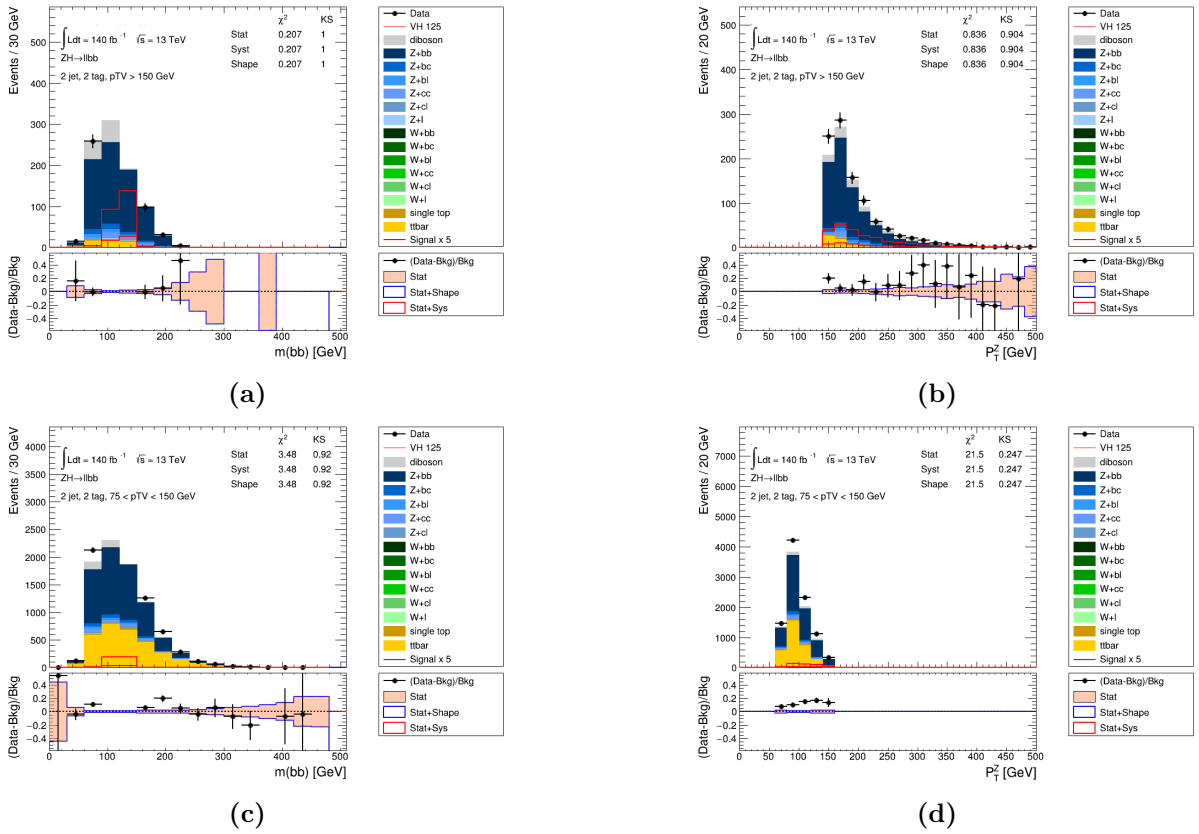

Figure 5.21 – The m_{bb} and p_T^V distribution in the 2-lepton signal region, 2-jet $p_T^V > 150\,\text{GeV}$ category using $139\,\text{fb}^{-1}$. The top quark production Monte Carlo samples are included in these plots. No scale factors were applied in these distributions. At this stage of the analysis, the signal region is blinded around the Higgs boson mass window.

is different between the the main backgrounds. Since the background modelling uncertainties have a large impact in the analysis, the systematic uncertainties were evaluated with the new categorisation.

The systematic model can be tested with the new categorisation by fitting the Monte Carlo samples, called the Asimov dataset, in all the regions simultaneously and in the three channels. In the Asimov fit the signal strength $\hat{\mu}$ is equal to the standard model prediction ($\hat{\mu} = 1$) and the nuisance parameters are set to their best estimated values of 0. The pulls of the nuisance parameters are by construction fitted to zero, however the uncertainties are an indication of how these nuisance parameters will behave within the data fit.

The first systematic model test consisted on fitting the BDT_{VH} distributions in the signal regions and the yields in the control regions. The control regions allow to better control $t\bar{t}$ and Z+jets and W+jets systematic uncertainties as the Figure 5.24 shows, where the nuisance parameters are more constrained in a fit including the control regions compared to a fit without these control regions. Another advantage of having this categorisation would be the harmonisation between the three analyses, and how simple it is to fit the yields in the control region and choose one discriminant (BDT_{VH}, m_{bb} or the BDT_{VZ}) to fit in the signal region. It can be seen in Figure 5.25 where the nuisance parameters are similarly constrained in the three fits. In the previous VHbb analysis using $80\,\text{fb}^{-1}$ [34], where the cross-check di-jet mass analysis had specific fixed ΔR_{bb} cuts, the background modelling fit was different than that of the MVA analysis, which is no longer the case with the common categorisation.

Another fit model was tested, in which either the m_{bb} or the p_T^V distributions were fitted in

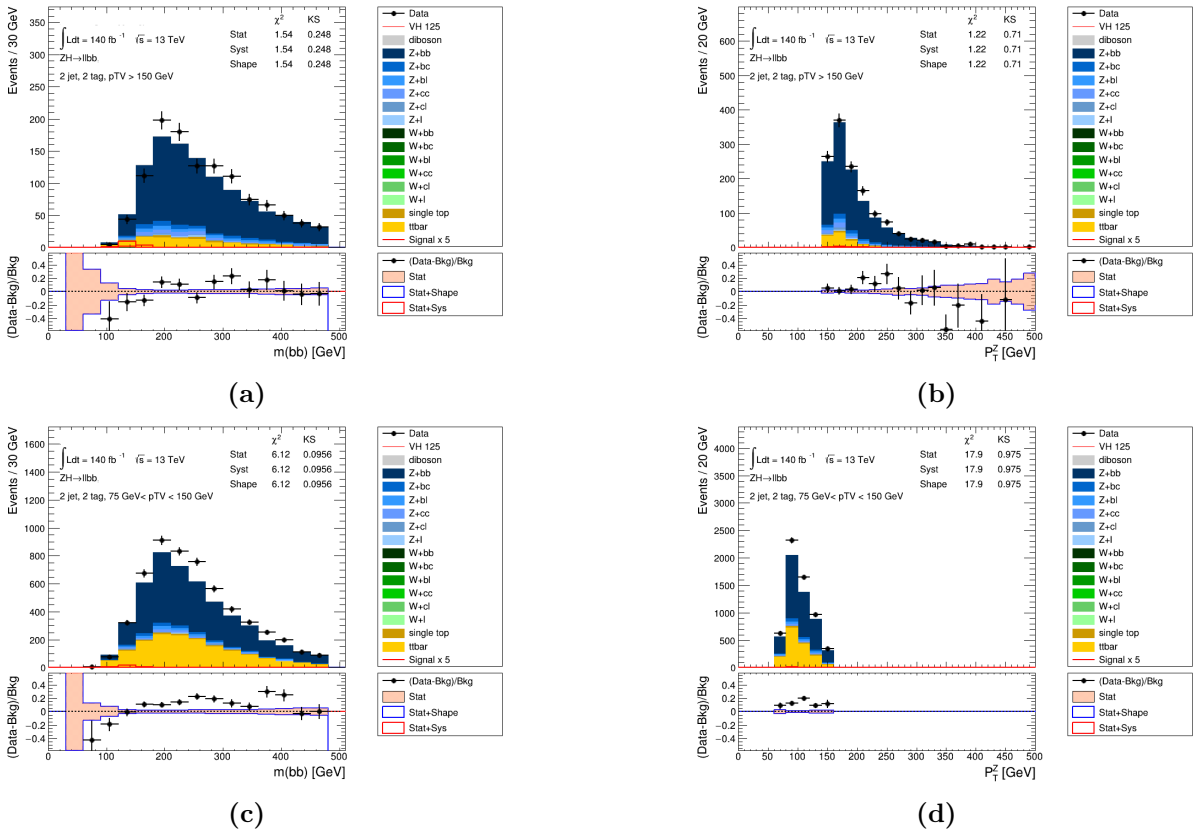

Figure 5.22 – The m_{bb} and p_T^V distribution in the 2-lepton high ΔR control region, 2-jet $p_T^V > 150\,\text{GeV}$ category using $139\,\text{fb}^{-1}$. The top quark production Monte Carlo samples are included in these plots. No scale factors were applied in these distributions.

the control regions instead of just using the yields. This allows to check if having the yields in the control regions is enough, or if the shape of the backgrounds also provide additional constraints on the background contributions in the fit. Figure 5.26 illustrates the VH MVA fit comparison between the three fit configurations, and shows that some nuisance parameters are more constrained when fitting m_{bb} or p_T^V. When the m_{bb} shape is fitted in the control regions, the m_{bb} distribution has many bins in particular in the tail of the distribution which explains why three of the W+jet and Z+jets shape uncertainties are more constrained than in the other fits. The evaluation of the impact of the modelling and experimental systematic uncertainties on the signal measurement can be shown in Table 5.20. As it is seen, the effect of the systematic uncertainties does not change when the p_T^V shape is used. On the other hand, when using the m_{bb} shape, the impact of the modelling systematic uncertainties slightly increases and the impact of the experimental systematic uncertainties such as the b-tagging uncertainties decreases, which is not expected to happen, proving that this fit model is too aggressive and that a more conservative model should be chosen. Since the two distributions do not bring additional improvement to the modelling systematic uncertainties, there is no reason to use them in the control regions.

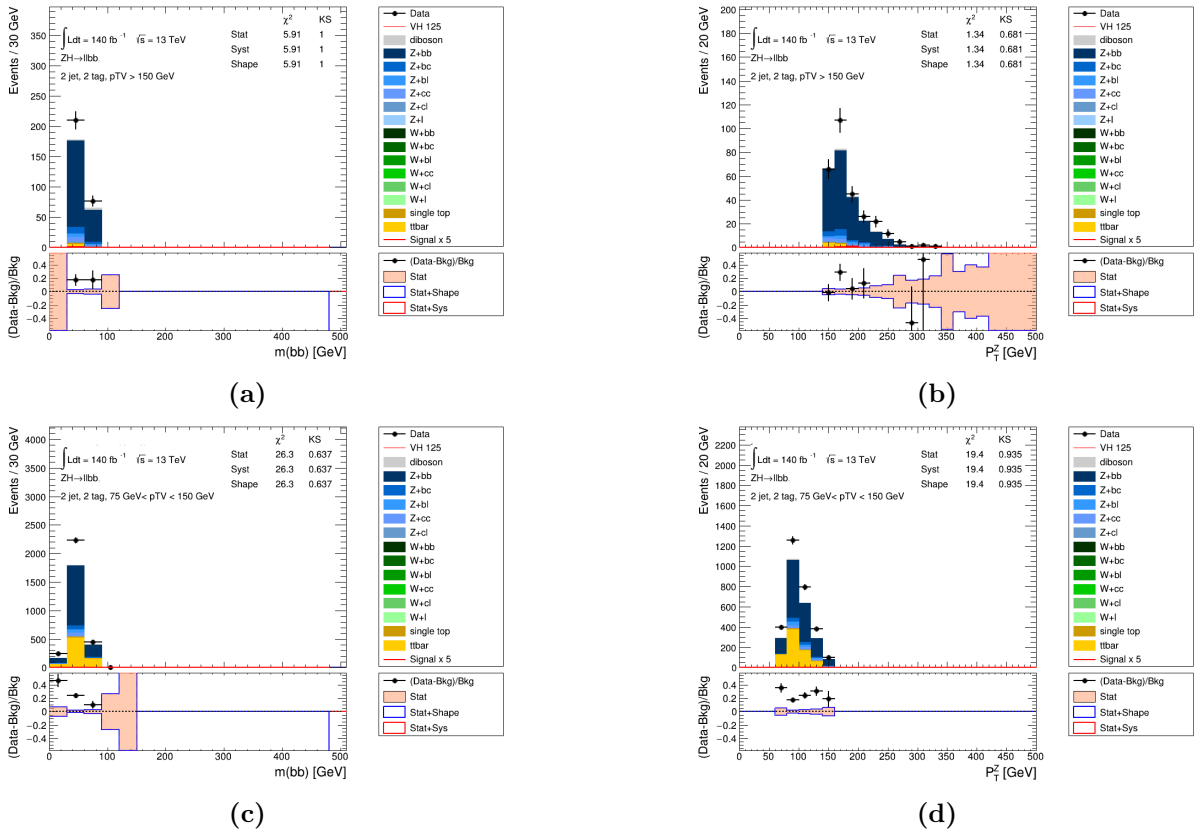

Figure 5.23 – The m_{bb} and p_T^V distribution in the 2-lepton low ΔR control region, 2-jet $p_T^V > 150\,\text{GeV}$ category using $139\,\text{fb}^{-1}$. The top quark production Monte Carlo samples are included in these plots. No scale factors were applied in these distributions.

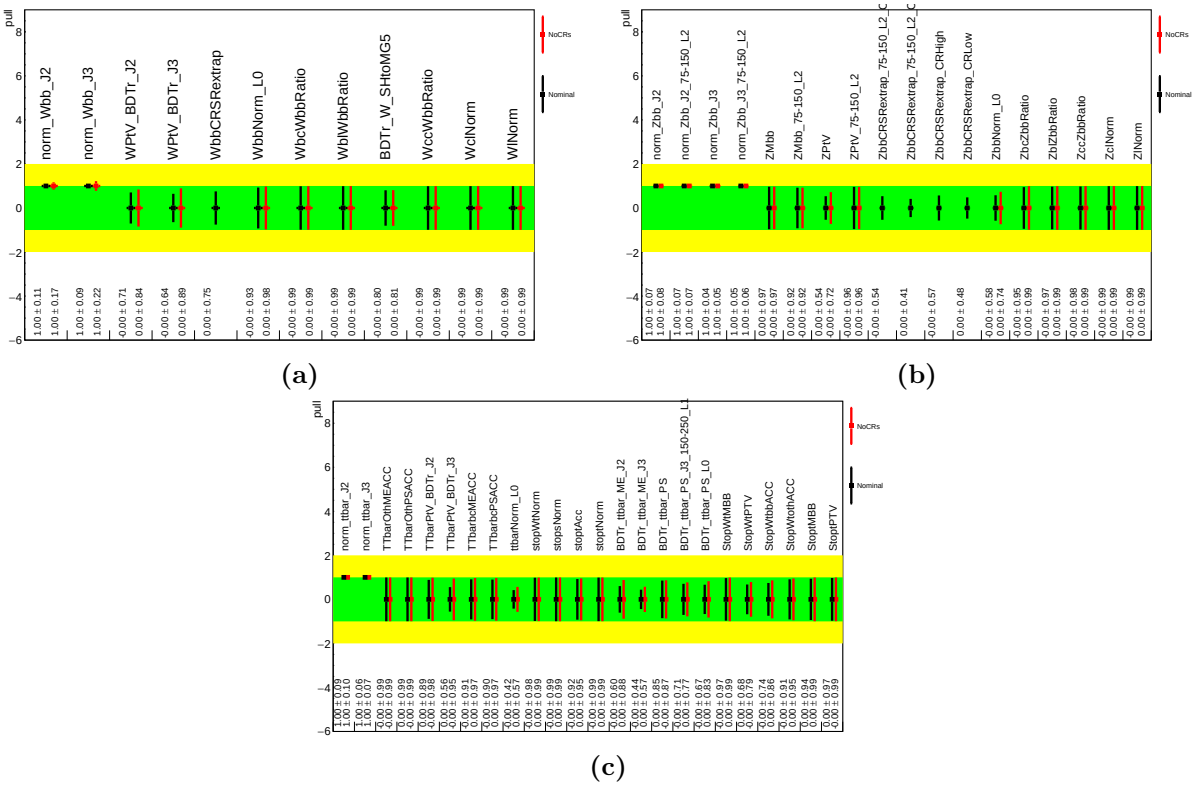

Figure 5.24 – Comparison of the nuisance parameters in the nominal fit in black and the fit without the control regions in red of W+jets NPs in (a), Z+jets NPs in (b) and top NPs in (c).

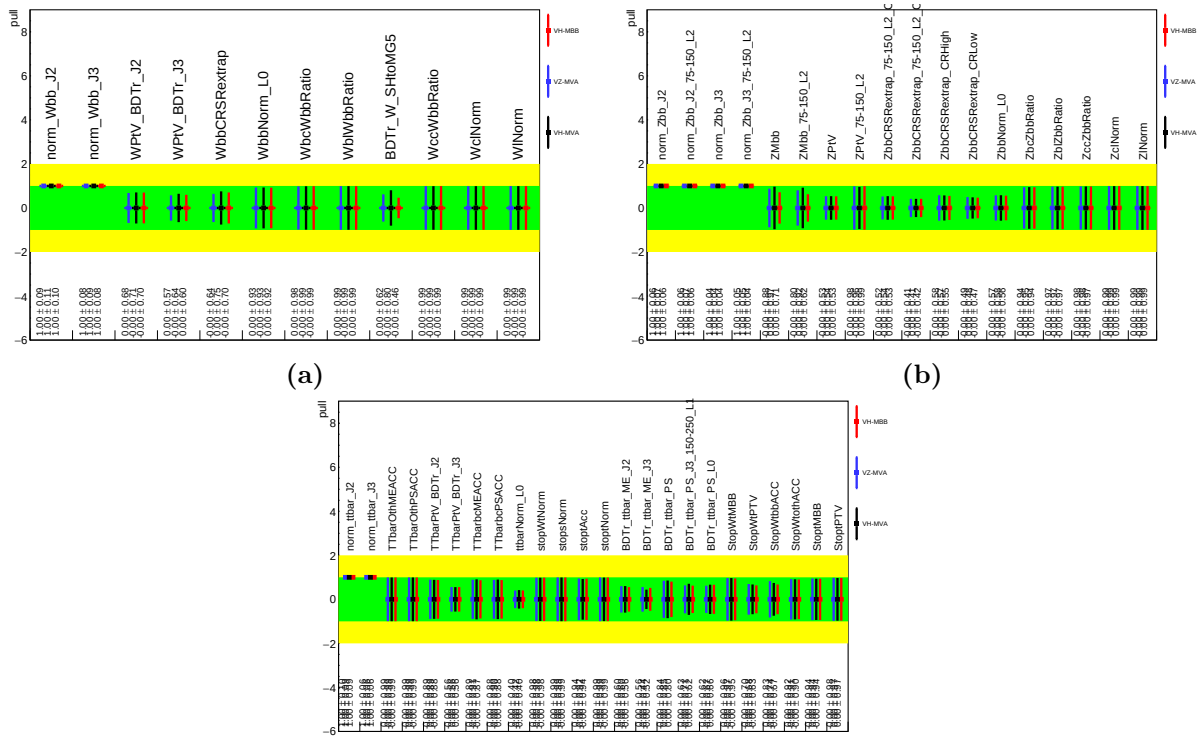

Figure 5.25 – Comparison of the nuisance parameters in the VH MVA fit in black, VH m_{bb} fit in red and the diboson fit in blue of W+jets NPs in (a), Z+jets NPs in (b) and top NPs in (c).

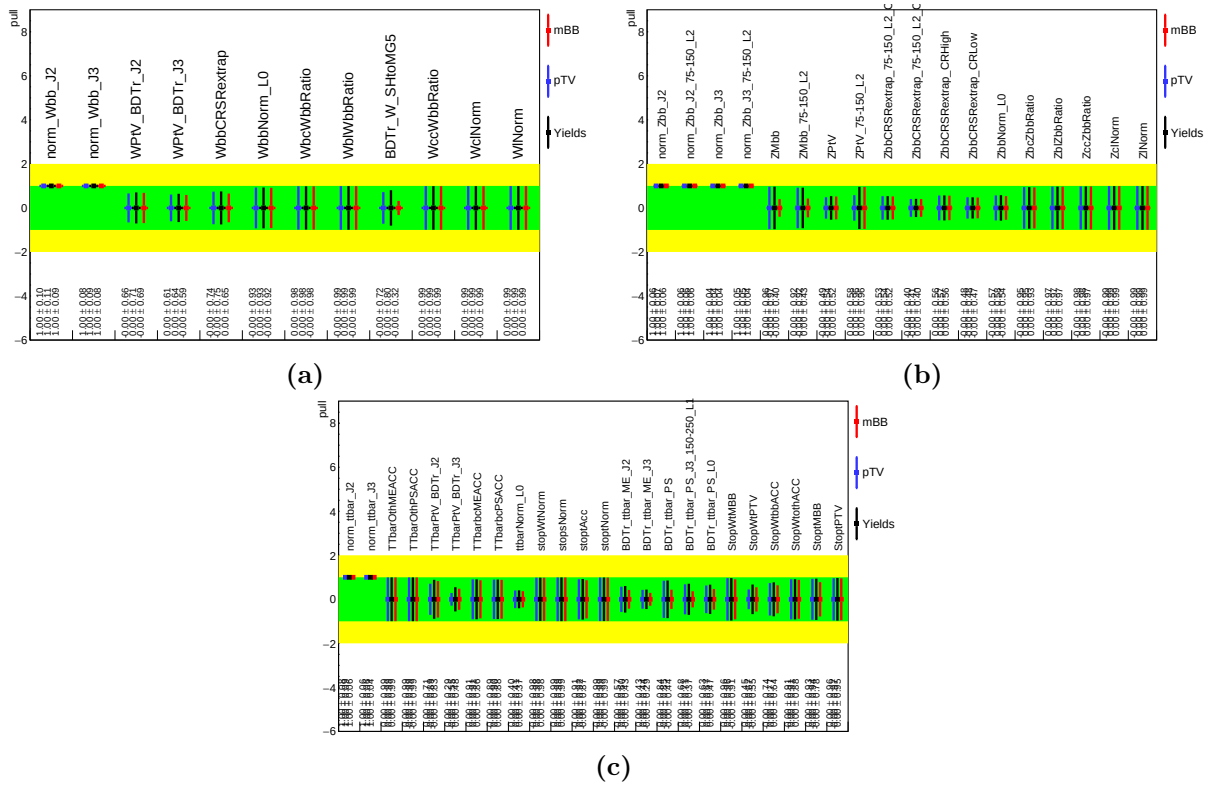

Figure 5.26 – Comparison of the nuisance parameters in the VH MVA fit when fitting the yields in black, m_{bb} in red or p_T^V in blue in the control regions, of W+jets NPs in (a), Z+jets NPs in (b) and top NPs in (c).

POI SigXsecOverSM	Central Value 1	Central Value 1	Central Value 1
Set of nuisance	Yields	p_T^V	m_{bb}
Total	±0.179	±0.178	±0.167
DataStat	±0.116	±0.116	±0.115
FullSyst	±0.137	±0.135	±0.121
Data stat only	±0.108	±0.108	±0.107
Top-emu CR stat	±0.016	±0.017	±0.018
Floating normalizations	±0.036	±0.035	±0.033
Modelling: VH	±0.051	±0.050	±0.048
Modelling: Background	±0.068	±0.067	±0.070
Multi Jet	±0.006	±0.006	±0.007
Modelling: single top	±0.022	±0.022	±0.030
Modelling: ttbar	±0.020	±0.020	±0.023
Modelling: W+jets	±0.037	±0.036	±0.022
Modelling: Z+jets	±0.032	±0.032	±0.030
Modelling: Diboson	±0.039	±0.038	±0.040
MC stat	±0.029	±0.030	±0.029
Experimental Syst	±0.076	±0.076	±0.062
Detector: lepton	±0.004	±0.007	±0.005
Detector: MET	±0.014	±0.015	±0.017
Detector: JET	±0.045	±0.044	±0.032
Detector: FTAG (b-jet)	±0.045	±0.044	±0.023
Detector: FTAG (c-jet)	±0.036	±0.036	±0.034
Detector: FTAG (l-jet)	±0.011	±0.010	±0.008
Detector: FTAG (extrap)	±0.000	±0.000	±0.000
Detector: PU	±0.005	±0.006	±0.010
Lumi	±0.016	±0.015	±0.016

Table 5.20 – Breakdown of systematic uncertainties contributions to the signal strength uncertainty in the VH MVA fit when fitting in the control regions the yields (left), the p_T^V distribution (middle) and the m_{bb} distribution (right).

5.8 Systematic uncertainties

The experimental and modelling uncertainties are two main sources of uncertainties in the analysis. The experimental uncertainties are required to account for the reconstruction of all physics objects, luminosity and pile-up, whereas the modelling uncertainties are assigned to the simulation of the signal and background events in addition to the data-driven multi-jet estimation in the 1-lepton and the top background estimation in the 2-lepton channel. The modelling uncertainties of simulated background also cover the impact of the Monte Carlo statistics on the signal measurement. All sources of uncertainties are propagated to the final discriminant to be used in the fit as nuisance parameters.

5.8.1 Experimental uncertainties

The experimental uncertainties cover the reconstruction and identification of the leptons, E_T^{miss} and the jets, the accuracy of the luminosity measurement by the ATLAS detector, the identification of pile-up jets, trigger efficiency and the b-tagging efficiency.

- **Luminosity:** The luminosity uncertainties corresponding to the 2015-2016, 2017 and 2018 datasets are $0.8\,\text{fb}^{-1}$, $1.0\,\text{fb}^{-1}$ and $1.2\,\text{fb}^{-1}$ respectively [100]. The integrated luminosity collected by the ATLAS detector during the full Run-2 is $139 \pm 2.4\,\text{fb}^{-1}$.
- **Pile-up:** To account for pileup mis-modelling, the Monte Carlo events are weighted so that the Monte Carlo average number of interactions per bunch crossing (μ) distribution matches that of the data after scaling it by a factor of 1/1.03. The pile-up reweighting uncertainty is then estimated by changing the scaling to 1/1.0 or to 1/1.18 to get the up and down variations respectively.
- **Trigger:** Introduced for both the E_T^{miss} and the single lepton triggers to account for the difference between data and the Monte Carlo simulation, to correct it using trigger scale factors. These scale factors are applied by taking into account the impact of the statistical error of the samples used when deriving these scale factors and are derived by taking the $\pm 1\sigma$ variation of the Monte Carlo to data ratio. Two additional sources of variation are applied only to the E_T^{miss} triggers: the difference in scale factors when using the $t\bar{t}$ process to derive the scale factors instead of the W ($\rightarrow \mu\nu$)+jets and the uncertainty describing the dependency of the efficiency of the triggers on S_T, which is taken into account by parameterising the scale factors as a function of S_T.
- **JET:** the uncertainties affecting the jet reconstruction are those affecting the jet energy resolution (JER) and jet energy energy scale (JES). These systematic uncertainties have a large impact in the analysis and they include the following sources of uncertainties: the eta inter-calibration, the high-p_T jets, the pile-up, the flavor response and the flavor composition. The JER uncertainties are introduced as a single source of uncertainty from data to Monte Carlo comparisons, while JES are broken down into 23 sources of uncertainty in the final fit.
- **Leptons:** These uncertainties come from the reconstruction and identification of both electrons and muons, in addition to the calibration of the energy scale and resolution. These systematic uncertainties have a very small impact in the analysis.
- $\boldsymbol{E_T^{miss}}$**:** Since the lepton and jets are used in the reconstruction of the missing energy, their systematic uncertainties are also propagated to the E_T^{miss} calculation in the 0- and 1-lepton channels. Additional uncertainties related to calibration and resolution of the tracks used to reconstruct the $E_{T,trk}^{miss}$ are also considered.

- **Flavor tagging:** These uncertainties correspond to the b-tagging scale factors systematic uncertainties applied to the b- ,c- and light jets separately. Since these scale factors are derived from a data to Monte Carlo comparison using $t\bar{t}$ samples, the calculation of these scale factors are impacted by the Monte Carlo generator modelling uncertainties and the experimental uncertainties such as the jets calibration. Using an eigenvector decomposition, the uncertainties are reduced to 45 components for b-jets, 20 for c-jets and 20 for light jets. Additional uncertainties for the b-tagging efficiency of the extrapolation to high-p_T jets and for the b-tagging efficiency uncertainty on tau jets are also included.

5.8.2 Modelling uncertainties

Systematic uncertainties cover the choice of the Monte Carlo generator to be used in the analysis and its tuning, and how it affects the estimation of the backgrounds. The systematic uncertainties are assigned to both the signal and the background estimations to cover all sources of shape and normalisation variations. Shape uncertainties can be quantified by comparing the kinematic distributions of the nominal generator to different generators. For a single process, several sources of uncertainties are usually considered, each having a different impact on the shape and normalisations. More details can be found in the following Chapter, which is dedicated to the modelling uncertainties in the VHbb analysis. The limited statistics of the Monte Carlo samples is also a source of uncertainties, which is specifically taken into account.

Chapter 6

Signal and Background Modelling

The dominant background processes in the VHbb analysis are simulated using Monte Carlo generators. On the other hand, data-driven techniques are used to model the multi-jet background in the 1-lepton and the top backgrounds in the 2-lepton channels. A good understanding of the systematic uncertainties, assigned to the predicted shape and normalisation is required because they have a large impact in the analysis. This Chapter describes the signal and background modelling and their dedicated systematic uncertainties. Section 6.1.1 is dedicated to the data-driven template fit method used to estimate the multi-jet background, as well as their associated uncertainties. The method to derive the data-driven top background is presented in Section 6.1.2, the Monte Carlo normalisation as well as the acceptance uncertainties in the VHbb analysis are presented in Sections 6.2.1 and 6.2.2. Section 6.2.3 contains a detailed description of the shape systematic uncertainties, and a presentation of a new method developed to determine the shape uncertainties using boosted decision trees.

6.1 Data-driven background estimations

6.1.1 Multi-jet estimation in the 1-lepton channel

The multi-jet background arises from semi-leptonic decays of heavy flavor jets inside the detector called fake leptons, from converted photons ($\gamma \rightarrow ee$) coming from decays of neutral pions or from hadrons which are mis-identified as electrons. However, in the 0-lepton channel the multi-jet events mainly come from the jet energy mis-measurement. In this channel, the contribution of the multi-jet events is significantly reduced after the events selection. This is mainly due to the anti-QCD cuts described in Section 5.3. Therefore the multi-jet background has a negligible impact in this channel. The multi-jet contribution in the 2-lepton channel was also found to be negligible since the selected events are required to have two isolated leptons in the final state. On the other hand, the multi-jet has a non-negligible contribution in the 1-lepton channel and represents a few percent of the total background. Monte Carlo generators cannot be used for the modelling due to the difficulties to accurately reproduce fake leptons and due to small statistics in the samples after event selection. Therefore a data-driven approach was chosen to model this background.

As described in Section 5.2.2, loose lepton isolation criteria are used in the electron and muon sub-channels to reduce the multi-jet contamination. In addition to the loose selection, a WH-tight selection is applied with a tight isolation cut in the 1-lepton channel to further reduce this background. This selection is based on fixed cuts applied on the track information for muons

(PtCone20) and the calorimeter information for electrons (topoEtCone20).

6.1.1.1 The template fit method

In this method, the multi-jet template in the signal region is obtained from the multi-jet template in the control region, which will be then correctly normalised. This shape obtained from the control region is extrapolated to the analysis phase space where a template fit to the data events is performed. This allows to set the normalisation of the multi-jet background and all the electroweak backgrounds modelled by simulation. The shape is obtained in the multi-jet control region defined from events passing the analysis selection but passing the inverted tight isolation cuts. Table 6.1 summarises the cuts used to define the isolated region (the main analysis phase space) and the inverted isolation region used to derive the multi-jet shape.

	Isolated Region	Inverted Isolation Region
Electron	FCLoose topoEtCone20 $<$ max(0.015 p_T^l,3.5) GeV	FCLoose topoEtCone20 $>$ max(0.015 p_T^l,3.5) GeV
Muon	FixedCutLoose PtCone20 $<$ 1.25 GeV	FixedCutLoose PtCone20 $>$ 1.25 GeV PtCone20 $<$4 GeV

Table 6.1 – Summary of the differences in lepton isolation between the isolated and the inverted isolation regions used for the template method. The muon tighter upper cut in the inverted isolation region allows to improve the multi-jet template at low p_T, as the poorly isolated muons change the kinematics of the event.

Since the source of multi-jet is different between the muons and the electrons, the multi-jet events in the two sub-channels are estimated independently. Events are split furthermore into categories depending on the jet multiplicity in the final state. The two p_T^V regions 150 GeV $< p_T^V <$ 250 GeV and $p_T^V >$ 250 GeV are merged together into one region $p_T^V >$ 150 GeV. The multi-jet background was also estimated in the 75 GeV $< p_T^V <$ 150 GeV region, making a total of eight different regions in which the template fit will be performed.

The template fit is performed on a variable providing a good separation power between the multi-jet and the electroweak backgrounds. The transverse mass of the W boson (m_T^W) fulfills these requirements, as the multi-jet is abundant at low m_T^W, and is thus chosen to perform the fit. However, the m_T^W does not provide any discrimination between W+jets and top events. Therefore a W+heavy flavors dedicated control region is defined (denoted WhfCR), which is more pure in W+jets than the low ΔR control region in the main analysis. This control region is separated from the signal region (denoted WhfSR) using cuts on the mass of the top quark decaying leptonically (m_{top}) and on the m_{bb} as shown in Table 6.2. This means that for each template fit, the events are split into two regions: WhfSR and WhfCR.

	WhfSR	WhfCR
Cuts	$m_{top} <$ 225 GeV or $m_{b\bar{b}} >$ 75 GeV	$m_{top} >$ 225 GeV and $m_{b\bar{b}} <$ 75 GeV

Table 6.2 – Cuts applied to define the W+heavy flavors control region.

In order to reduce the impact of the statistical fluctuations in the fit, the events used to derived the multi-jet template are required to have exactly 1 b-tagged jet instead of having two $b-$tagged

jets. The multi-jet events are obtained after subtraction of all the background simulated events from data. Figure 6.1 show the m_T^W in the 1-tag WhfSR inverted isolation region where the differences between the data and the simulated backgrounds provide the multi-jet templates. The same distribution in the W+heavy flavors control region is shown in Figure 6.2. The m_T^W distribution in the 1-tag inverted isolation, 75 GeV$< p_T^V <$150 GeV region in WhfSR and WhfCR are presented in Figures 6.3 and 6.4 respectively.

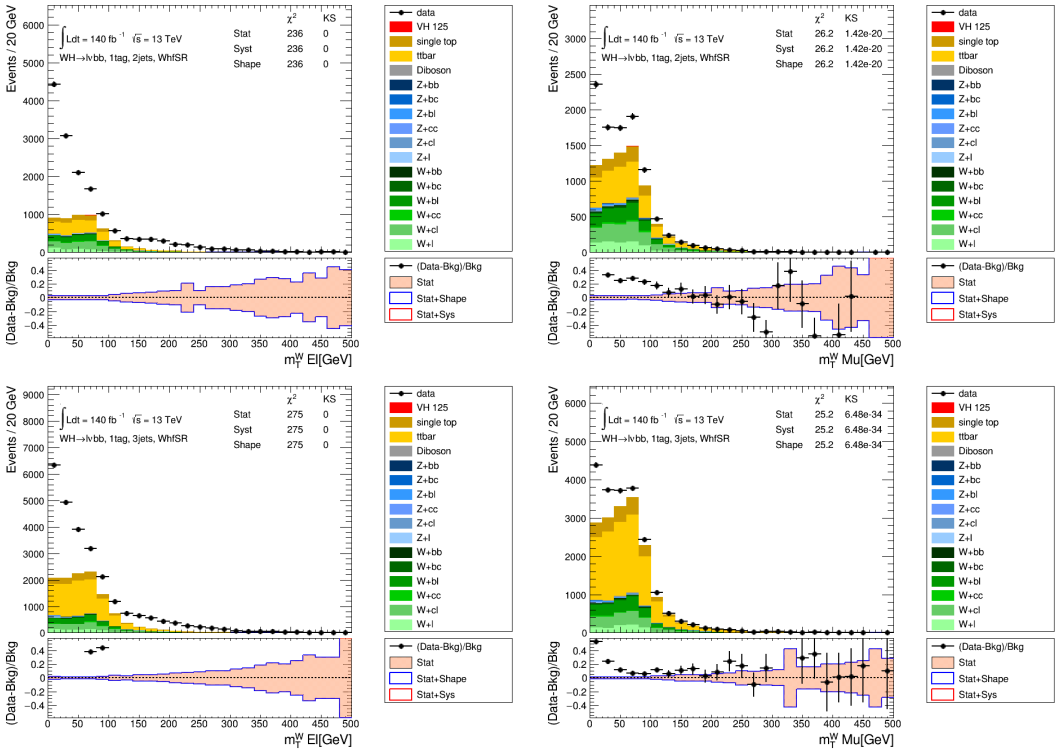

Figure 6.1 – The m_T^W distribution in the $p_T^V > 150$ GeV 1-tag inverted isolation region, requiring exactly 1 b-tag with 2 signal jets in the e sub-channel in the top left, in the μ sub-channel in the top right, and with 3 signal jets in the e sub-channel in the bottom left, in the μ sub-channel in the bottom right plots.

The multi-jet shape extracted in the 1-tag inverted isolation region and used as the multi-jet template in the 2-tag isolated region, considering that the template is the same in the two phase spaces, in each of the eight regions. The $t\bar{t}$ and single top samples are merged together in a single top template as the same is done for the flavors in the W+jets samples to create one W+jets template. The multi-jet, top and W+jets templates normalisations are floated in the fit, whereas the Z+jets, diboson and signal normalisations are fixed to their Monte Carlo prediction. The WhfCR yield is added as a single bin at the end of the m_T^W in the WhfSR to fit simultaneously the two regions and set the normalisation of W+jets. Prior to the template fit, the m_T^W distribution is rebinned to yield a constant Monte Carlo statistical uncertainty through all the bins. The electron and muon sub-channels are fitted separately to avoid any tension between them. The normalisation scale factors resulting from the fit are shown in Table 6.3. The fit results show that in some regions the top and W+jets scale factors are different from unity and have significant anti-correlations between them. Figures 6.5 and 6.6 show the m_T^W distributions with the same binning as the one used in the template fit after applying the normalisation factors from Table 6.3.

The multi-jet shape is estimated for all the kinematic variables by substracting the electroweak backgrounds from data and then apply the multi-jet normalisation factors obtained from the m_T^W template fit. Figures 6.7 to 6.14 show the $m_{b\bar{b}}$, E_T^{miss}, $\Delta\phi$(lepton, leading b-jet) and $\Delta\phi$(lepton, E_T^{miss}) distributions after setting the normalisation of all the backgrounds to the results of the fit.

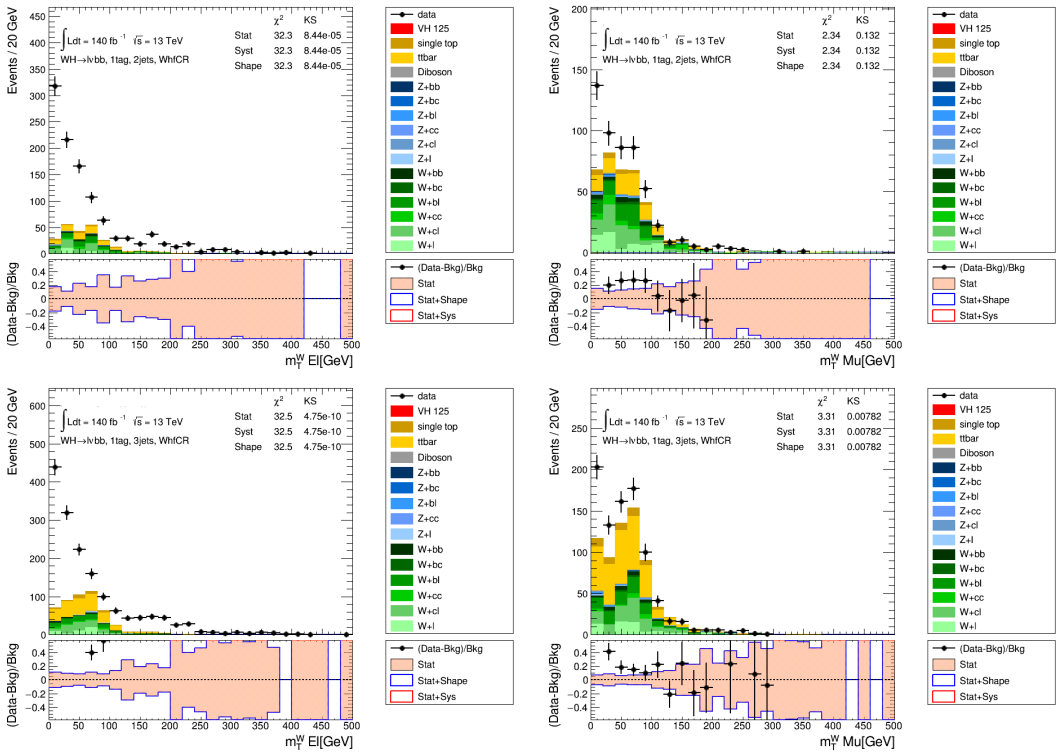

Figure 6.2 – The m_T^W distribution in the $p_T^V > 150$ GeV 1-tag inverted isolation region, W+heavy flavors control region, requiring exactly 1 b-tag with 2 signal jets in the e sub-channel in the top left, in the μ sub-channel in the top right, and with 3 signal jets in the e sub-channel in the bottom left, in the μ sub-channel in the bottom right plots.

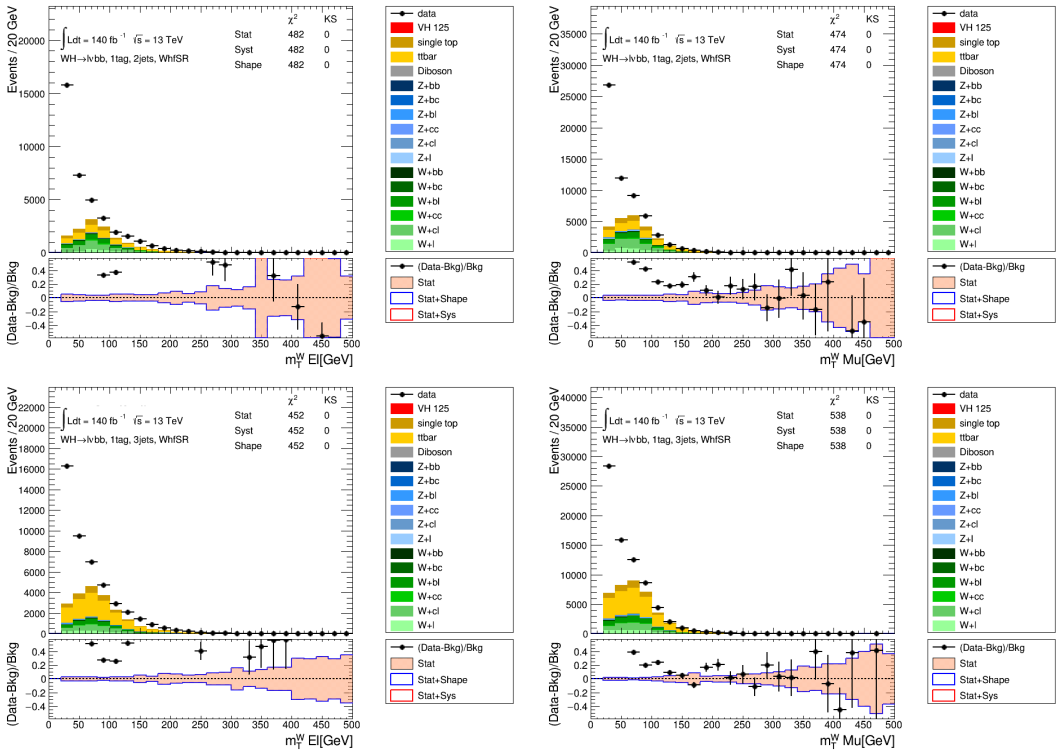

Figure 6.3 – The m_T^W distribution in the 75 GeV$< p_T^V <$150 GeV 1-tag inverted isolation region, with 2 signal jets in the e sub-channel in the top left, in the μ sub-channel in the top right, and with 3 signal jets in the e sub-channel in the bottom left, in the μ sub-channel in the bottom right plots.

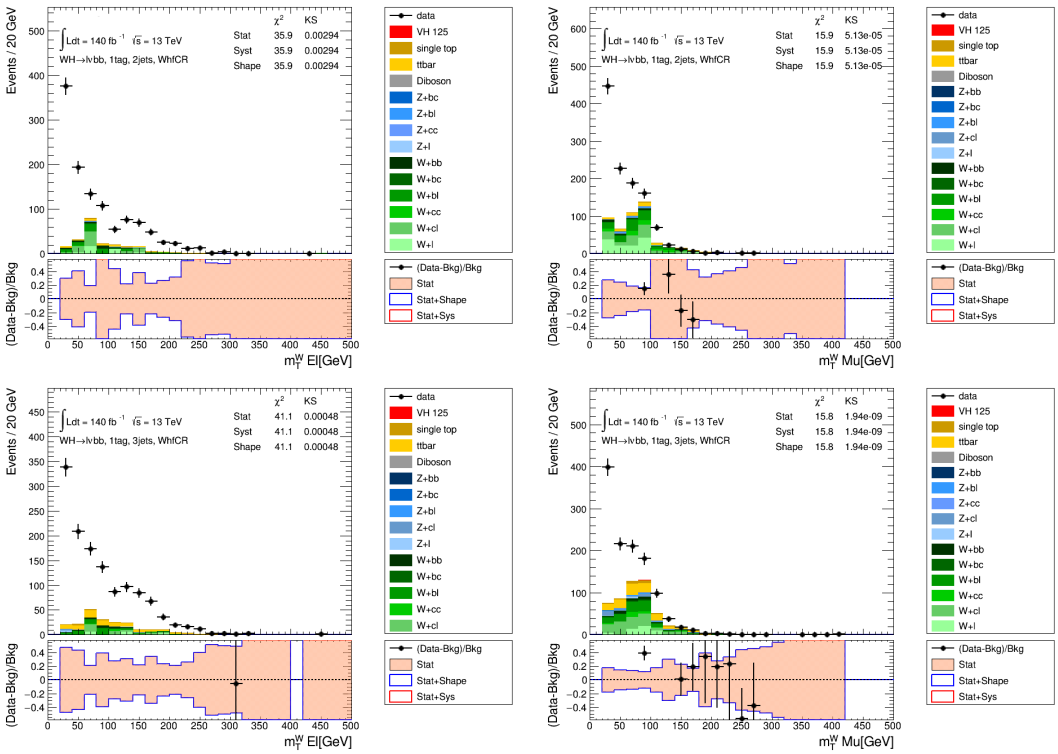

Figure 6.4 – The m_T^W distribution in the 75 GeV< p_T^V<150 GeV 1-tag inverted isolation region, W+heavy flavors control region, with 2 signal jets in the e sub-channel in the top left, in the μ sub-channel in the top right, and with 3 signal jets in the e sub-channel in the bottom left, in the μ sub-channel in the bottom right plots.

	Electron channel		Muon channel	
Region	Top	W+jets	Top	W+jets
$p_T^V > 150$ GeV, 2-jet	0.89 ±0.02	1.33 ±0.07	0.86 ±0.02	1.09 ±0.06
$p_T^V > 150$ GeV, 3-jet	0.904 ±0.006	1.22 ±0.05	0.899 ±0.006	1.13 ±0.04
75 GeV< $p_T^V < 150$ GeV, 2-jet	0.93 ±0.01	1.44 ±0.05	0.99 ±0.01	1.32 ±0.05
75 GeV< $p_T^V < 150$ GeV, 3-jet	0.991 ±0.004	1.10 ±0.05	0.977 ±0.004	1.10 ±0.04

Table 6.3 – Summary of normalisation scale factors for top and W+jets derived from the template fit to the 75 GeV< p_T^V < 150 GeV and p_T^V > 150 GeV regions in the electron and the muon sub-channels. The uncertainties shown are the statistical uncertainties from the template fit.

A good agreement between the data and the electroweak and multi-jet backgrounds is observed in all the distributions ensuring the good modelling of the multi-jet background.

The analysis categorisation detailed in Section 5.7 is different from the categorisation used in the multi-jet estimation. But since the template fit was performed in the full phase space, the results of the template fit are applied to all the events passing the analysis selection. This is done by applying the corresponding normalisation factors to all events before splitting the events into the analysis signal, low and high ΔR control regions using continuous $\Delta R(b,b)$-p_T^V cuts as described in Section 5.7. Following the same logic, the normalisation factors resulting from the template fit in the $p_T^V > 150$ GeV region are applied to the events in the 150 GeV< p_T^V <250 GeV and p_T^V >250 GeV regions. The multi-jet dedicated systematic uncertainties are obtained using the same approach as the nominal samples.

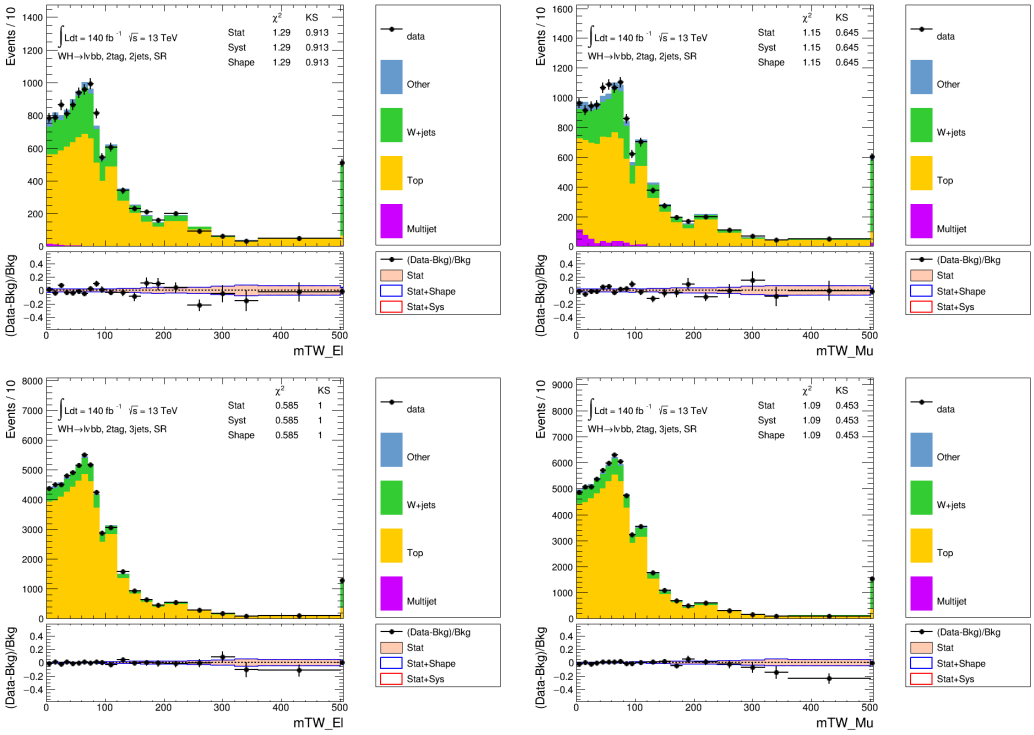

Figure 6.5 – The m_T^W distribution in the p_T^V >150 GeV 2-tag isolated region with 2-jets in the e sub-channel in the top right, in the μ sub-channel in the top right, with 3-jets in the e sub-channel in the bottom right and in the e sub-channel in the bottom left plots. The binning shown is as used in the template fit, with bins 1-20 corresponding to the WhfSR and bin 21 to the WhfCR. The errors in the bottom panel correspond to the statistical uncertainties only.

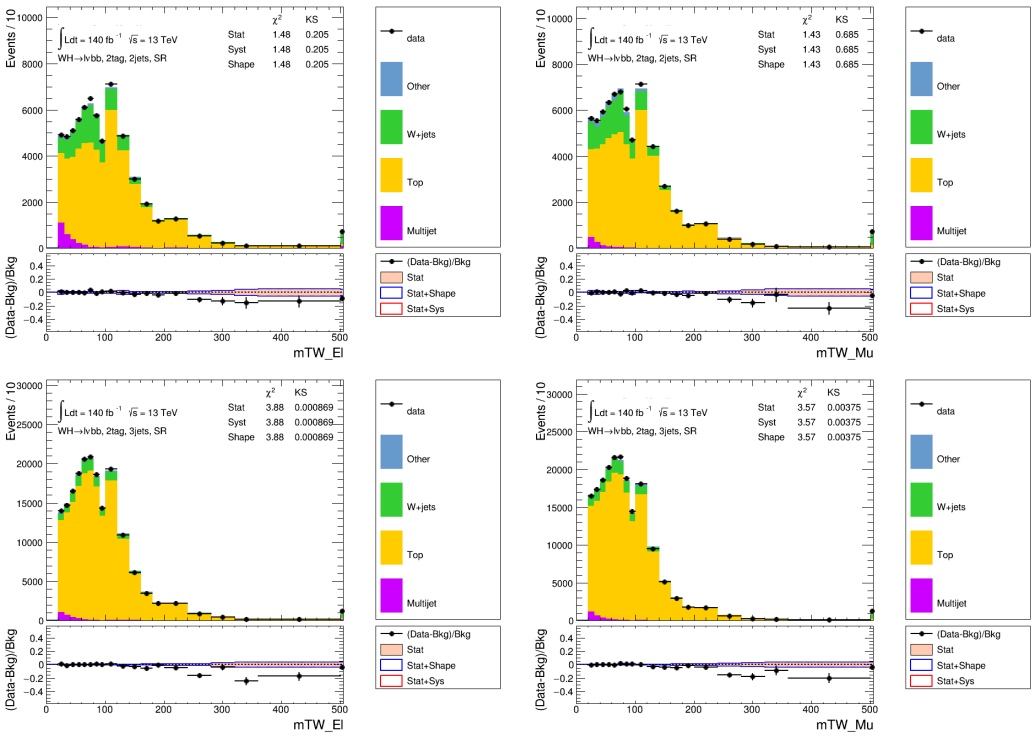

Figure 6.6 – The m_T^W distribution in the 75 GeV< p_T^V < 150 GeV 2-tag isolated region with 2-jets in the e sub-channel in the top right, in the μ sub-channel in the top right, with 3-jets in the e sub-channel in the bottom right and in the e sub-channel in the bottom left plots. The binning shown is as used in the template fit, with bins 1-20 corresponding to the WhfSR and bin 21 to the WhfCR. The errors in the bottom panel correspond to the statistical uncertainties only.

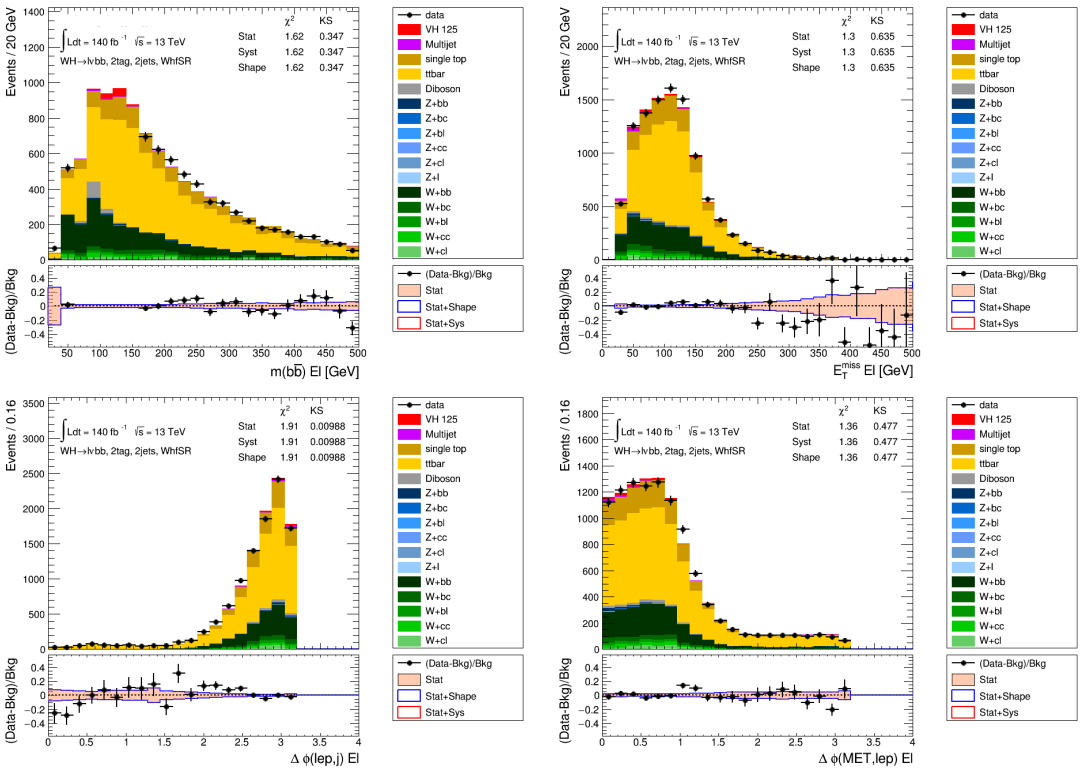

Figure 6.7 – The distributions, for the p_T^V >150 GeV 2-tag isolated region with 2-jets e sub-channel, of m_{bb}, E_T^{miss}, $\Delta\phi$(lepton, leading b-jet) and $\Delta\phi$(lepton, E_T^{miss}) are shown. The m_{bb} distribution is blinded around the Higgs boson mass at this stage of the analysis.

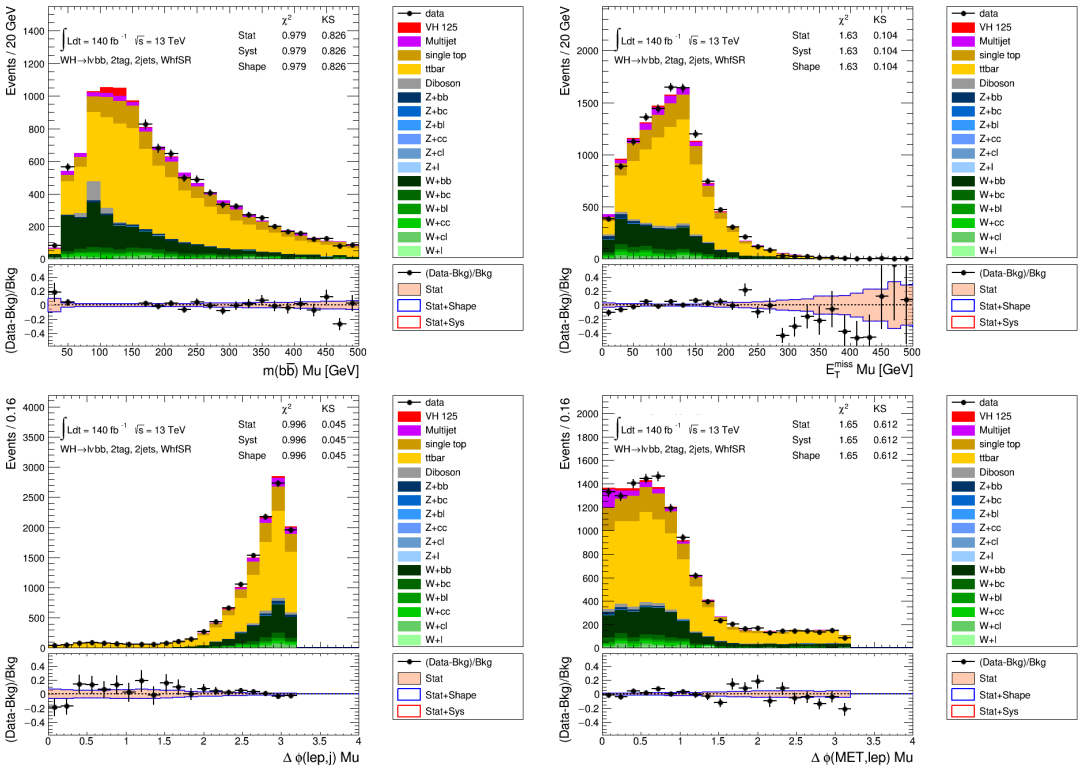

Figure 6.8 – The distributions, for the p_T^V >150 GeV 2-tag isolated region with 2-jets μ sub-channel, of m_{bb}, E_T^{miss}, $\Delta\phi$(lepton, leading b-jet) and $\Delta\phi$(lepton, E_T^{miss}) are shown. The m_{bb} distribution is blinded around the Higgs boson mass at this stage of the analysis.

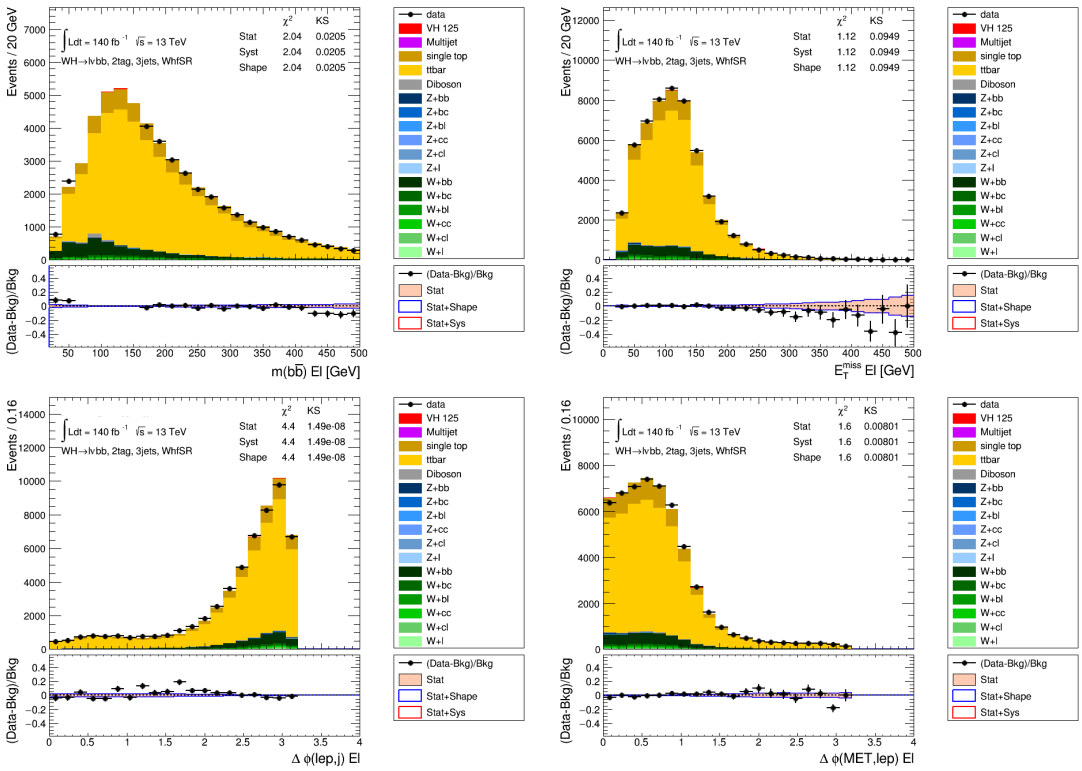

Figure 6.9 – The distributions, for the p_T^V >150 GeV 2-tag isolated region with 3-jets e sub-channel, of m_{bb}, E_T^{miss}, $\Delta\phi$(lepton, leading b-jet) and $\Delta\phi$(lepton, E_T^{miss}) are shown. The m_{bb} distribution is blinded around the Higgs boson mass at this stage of the analysis.

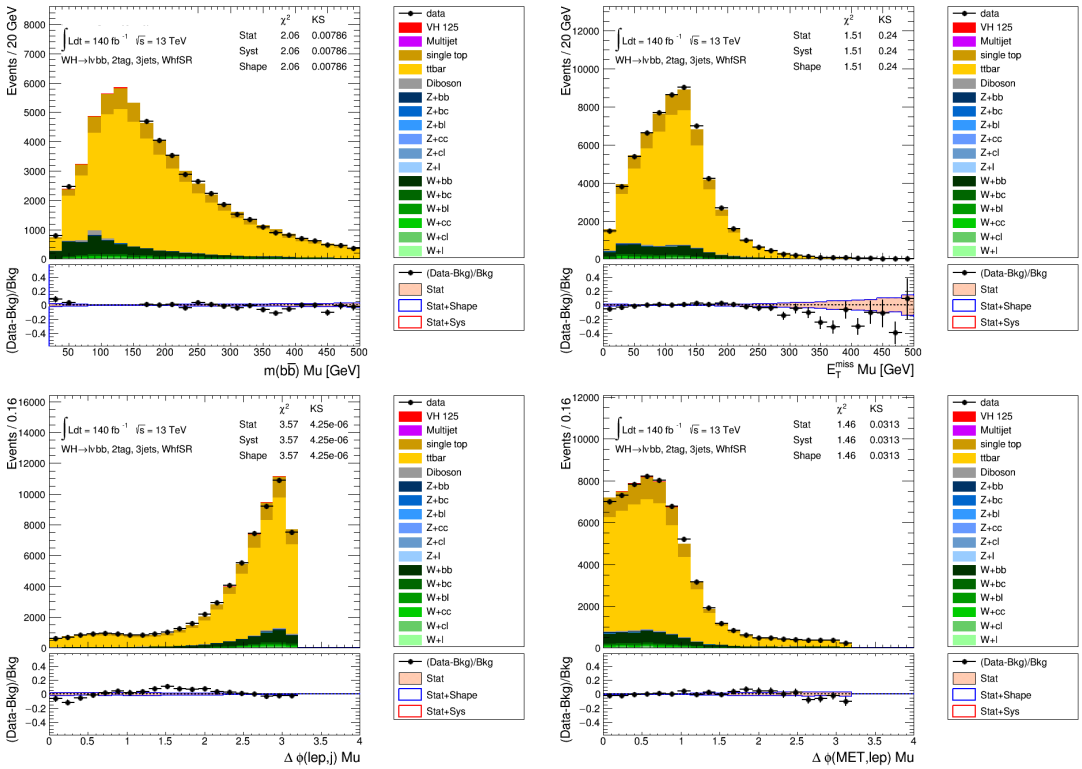

Figure 6.10 – The distributions, for the p_T^V >150 GeV 2-tag isolated region with 3-jets μ sub-channel, of m_{bb}, E_T^{miss}, $\Delta\phi$(lepton, leading b-jet) and $\Delta\phi$(lepton, E_T^{miss}) are shown. The m_{bb} distribution is blinded around the Higgs boson mass at this stage of the analysis.

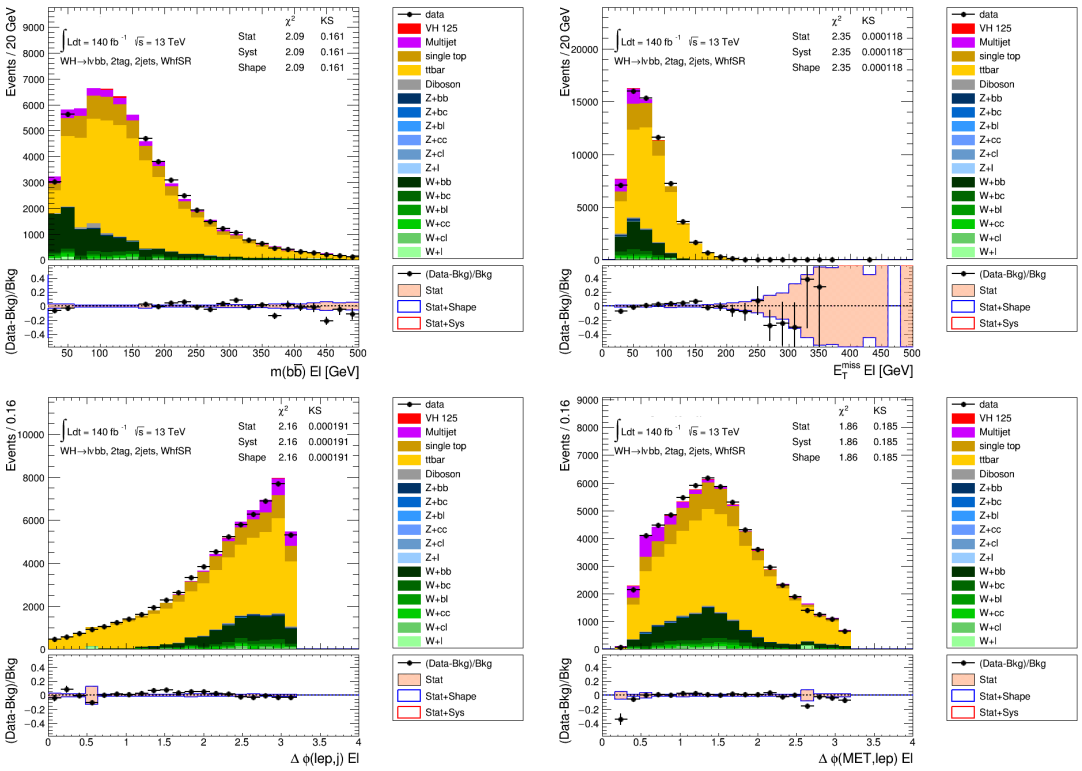

Figure 6.11 – The distributions, for the 75 GeV $< p_T^V <$150 GeV 2-tag isolated region with 2-jets e sub-channel, of m_{bb}, E_T^{miss}, $\Delta\phi$(lepton, leading b-jet) and $\Delta\phi$(lepton, E_T^{miss}) are shown. The m_{bb} distribution is blinded around the Higgs boson mass at this stage of the analysis.

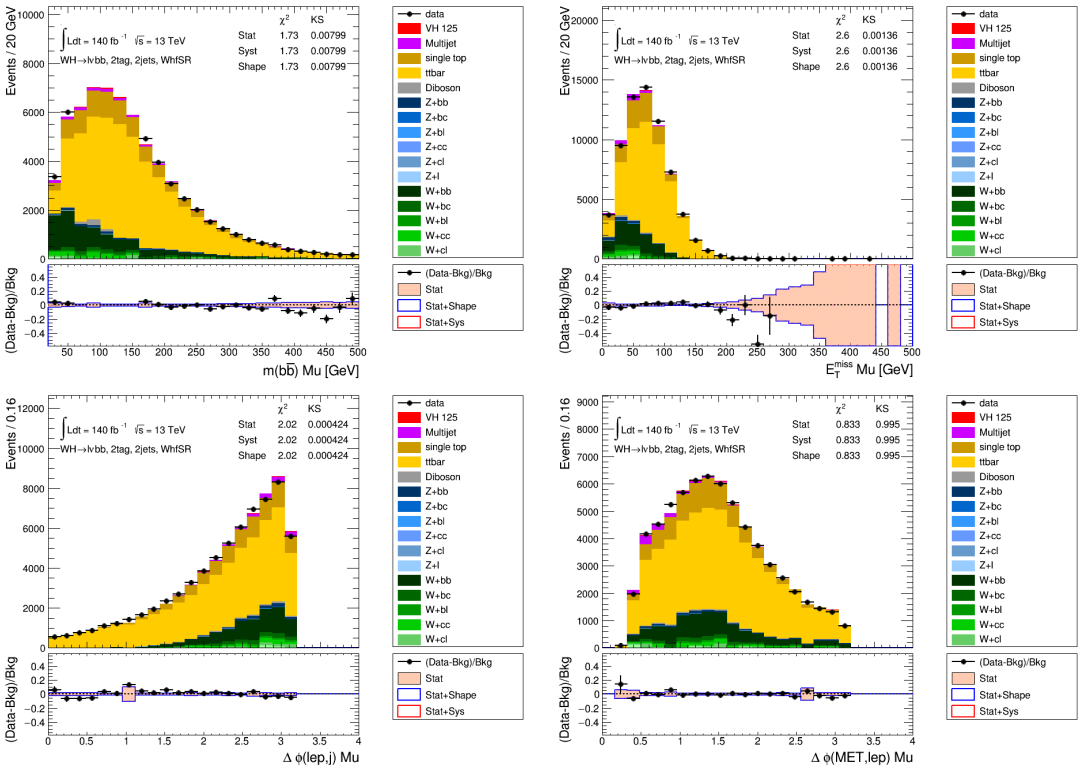

Figure 6.12 – The distributions, for the 75 GeV $< p_T^V <$150 GeV 2-tag isolated region with 2-jets μ sub-channel, of m_{bb}, E_T^{miss}, $\Delta\phi$(lepton, leading b-jet) and $\Delta\phi$(lepton, E_T^{miss}) are shown. The m_{bb} distribution is blinded around the Higgs boson mass at this stage of the analysis.

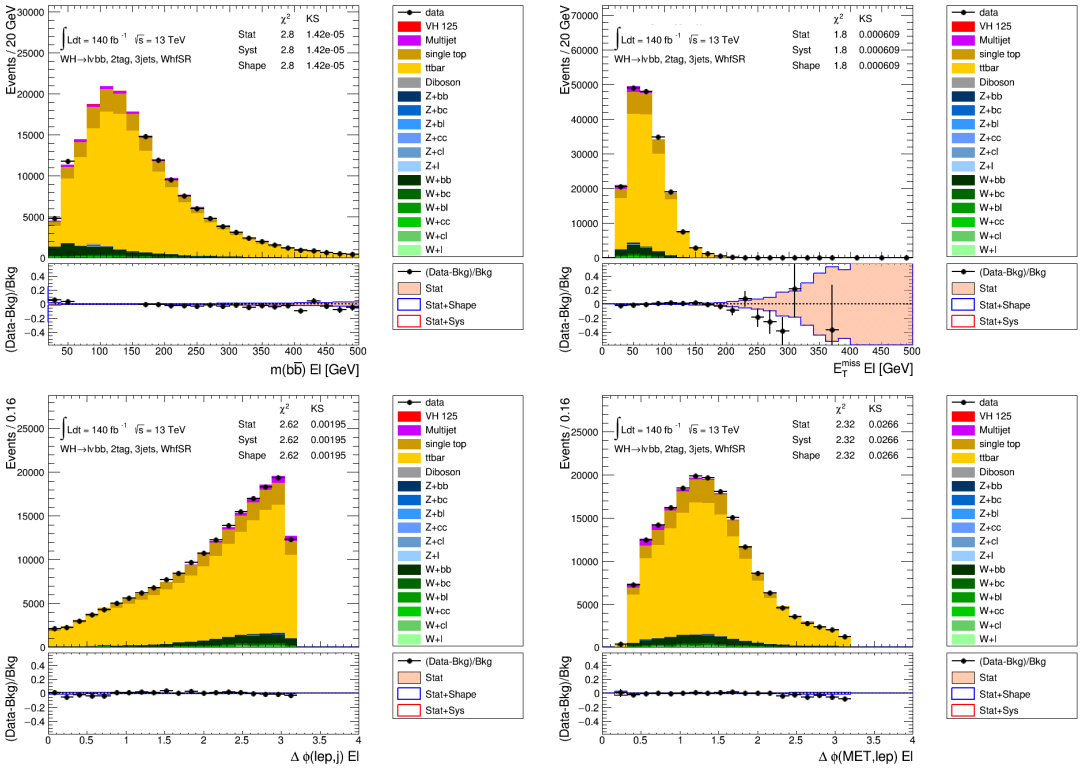

Figure 6.13 – The distributions, for the 75 GeV $< p_T^V <$150 GeV 2-tag isolated region with 3-jets e sub-channel, of m_{bb}, E_T^{miss}, $\Delta\phi$(lepton, leading b-jet) and $\Delta\phi$(lepton, E_T^{miss}) are shown. The m_{bb} distribution is blinded around the Higgs boson mass at this stage of the analysis.

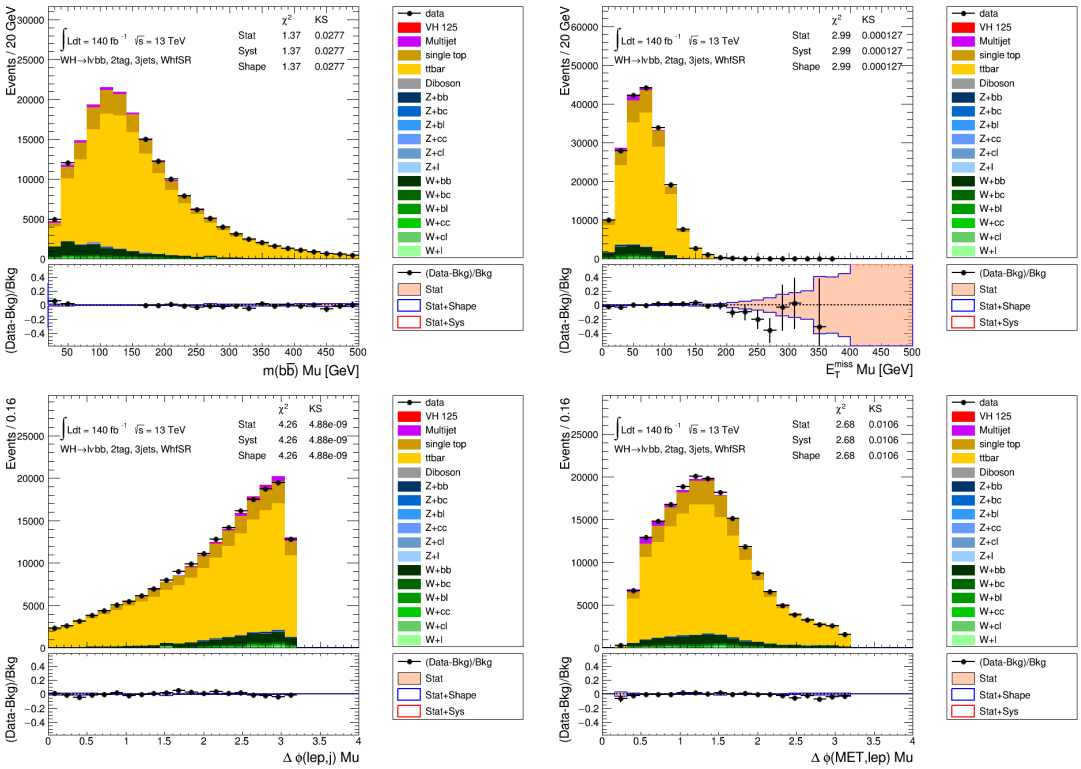

Figure 6.14 – The distributions, for the 75 GeV $< p_T^V <$150 GeV 2-tag isolated region with 2-jets μ sub-channel, of m_{bb}, E_T^{miss}, $\Delta\phi$(lepton, leading b-jet) and $\Delta\phi$(lepton, E_T^{miss}) are shown. The m_{bb} distribution is blinded around the Higgs boson mass at this stage of the analysis.

6.1.1.2 Assignment of the MV2c10 scores to multi-jet events

In the 1-lepton analysis, the MV2c10 scores of each of the 2 b-tagged jets are used as input variables for the analysis BDT. This causes a problem for the multi-jet estimation since the shape is obtained in the 1 b-tag region. This means that the MV2c10 values of the untagged jet will not pass the 70% working point requirement, and therefore the BDT evaluation might not yield a correct value. A solution is to emulate the MV2c10 values above 70% working point for the 1 b-tag events for both the data and the electroweak events to correctly obtain the multi-jet BDT distribution.

This is possible by using the 2 b-tag events and taking a 2 dimensional distribution with the MV2c10 values of the leading and sub-leading jets. The values in each of the direction will be split into two bins: 70-60% and 60-0%, following the description in Section 5.4.2. These distributions are required for both data and the electroweak backgrounds in the inverted isolation region. The electroweak 2 dimensional distributions are substracted from the data distribution after applying the template fit normalisation factors.

The resulting distributions are an estimation of the multi-jet MV2c10 distributions. They are then normalised to unity to show the fraction of events in each bin as presented in Figures 6.15 and 6.16. Using the probability of the event to land in each of the 4 MV2c10 configurations, the MV2c10 scores are assigned randomly to both the leading and the sub-leading jet for events in the 1-tag category to reproduce these distributions.

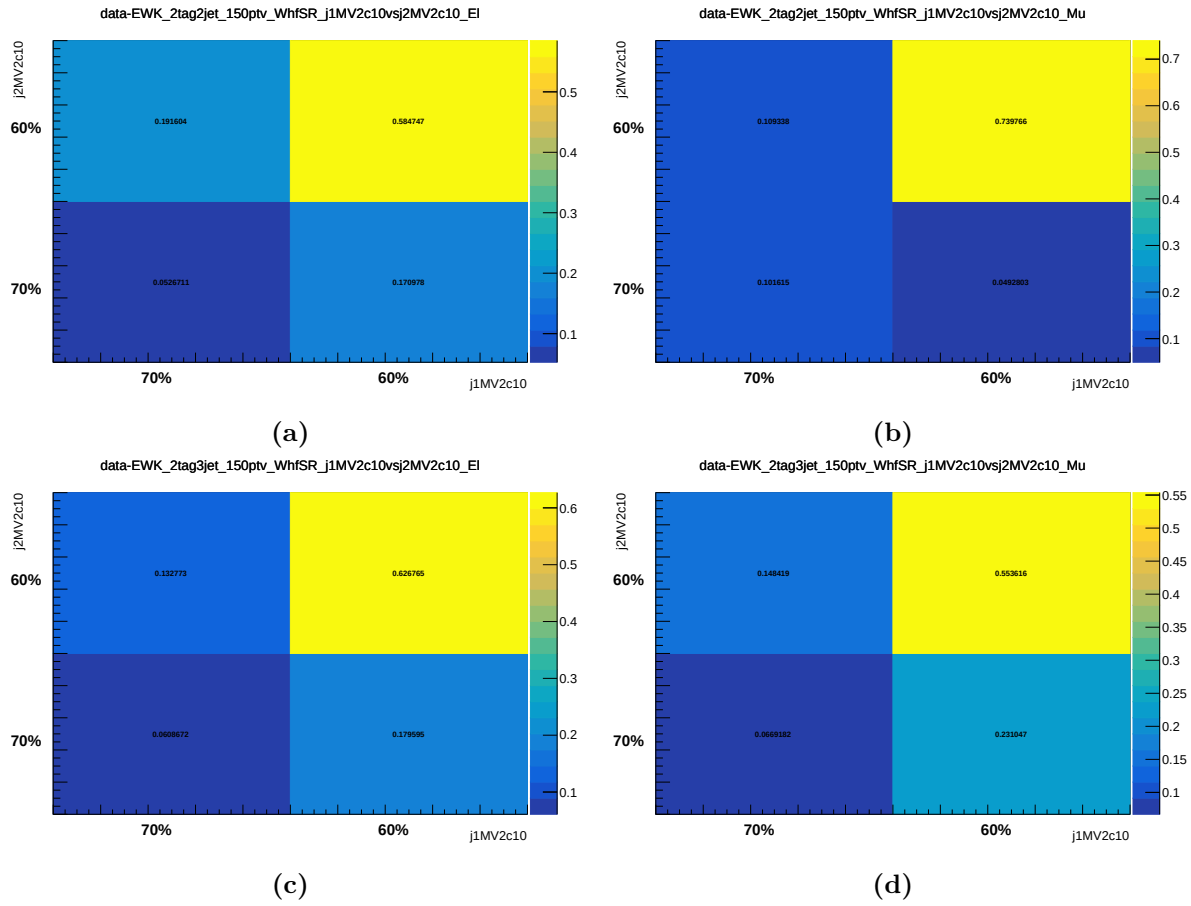

Figure 6.15 – Distribution of the MV2c10 values of the two b-tagged jets with the leading jet in the x-direction and the sub-leading jet in the y-direction, in the $p_T^V > 150\,\text{GeV}$ region in the (a) 2-jet e sub-channel, (b) 2-jet μ sub-channel, (c) 3-jet e sub-channel and (d) 3-jet μ sub-channel. The 70% bin corresponds to the [70,60]% b-tagging working point selection and the 60% to the [60,0]%.

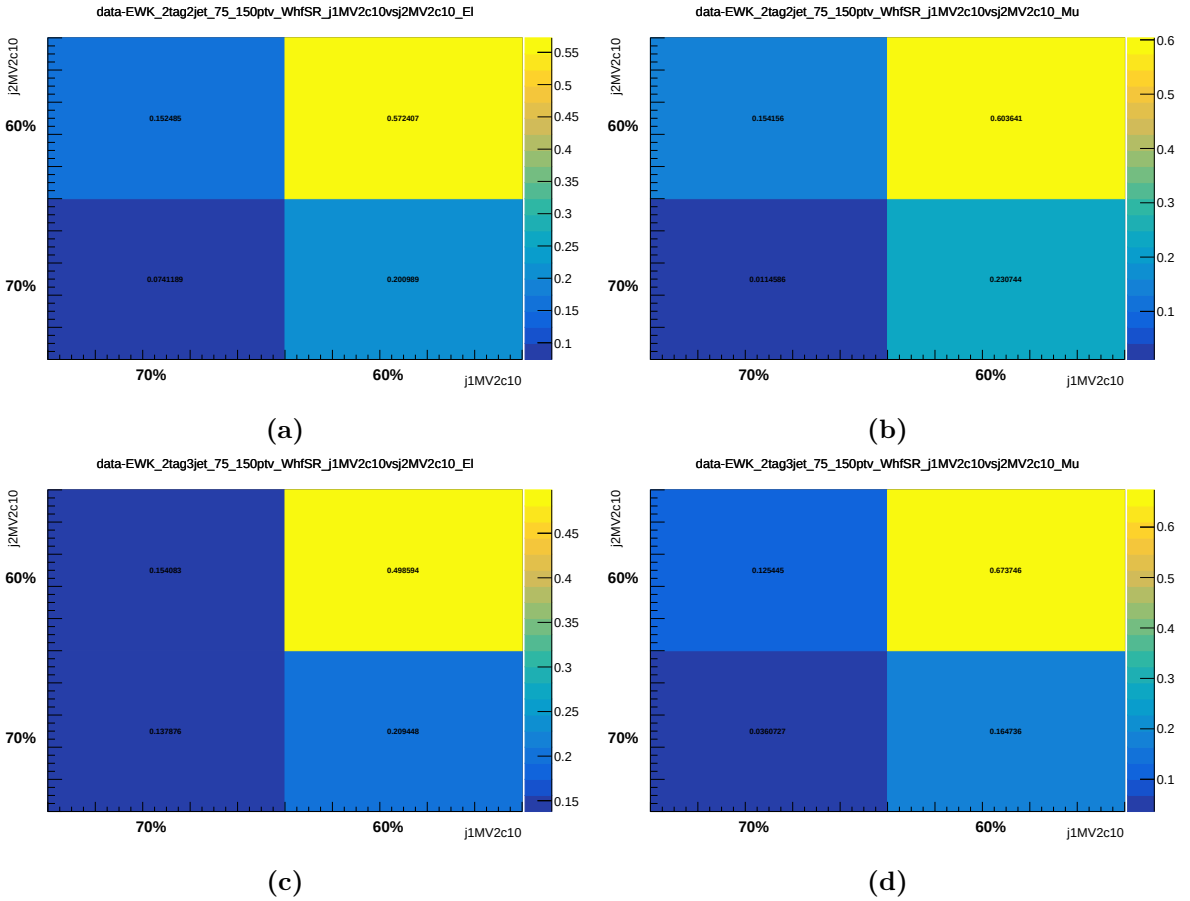

Figure 6.16 – Distribution of the MV2c10 values of the two b-tagged jets with the leading jet in the x-direction and the sub-leading jet in the y-direction, in the 75 GeV p_T^V < 150 GeV region in the (a) 2-jet e sub-channel, (b) 2-jet μ sub-channel, (c) 3-jet e sub-channel and (d) 3-jet μ sub-channel. The 70% bin corresponds to the [70,60]% b-tagging working point selection and the 60% to the [60,0]%.

6.1.1.3 Systematic uncertainties

Many sources of systematic uncertainty are assigned to the multi-jet background. These uncertainties are propagated to the BDT discriminant in the fit to cover both the normalisation and the shape of the multi-jet estimation. Similarly to the nominal template, these systematic uncertainties are obtained in each of the eight regions independently.

Shape Uncertainties

Two sources of shape uncertainty of the multi-jet background estimation are considered:

- One shape uncertainty is assigned to cover the assumption that the multi-jet shape is the same in the isolated region as in the inverted isolation region. To that aim, a reduced inverted isolation region with tighter cuts is defined in the electron and muon sub-channels to change the multi-jet distribution. In addition to the cuts in Table 6.1, the following cuts are applied: topoEtCone20< 12 GeV in the electron channel and PtCone20 < 2.9 GeV in the muon channel. Those cuts are chosen to keep about half of the data events in the reduced inverted isolation.
- The multi-jet shape is obtained from electroweak background subtraction from data events without applying any normalisation. However, the W+jets and top normalisation factors resulting from the template fit are different from unity. For that, the multi-jet template

shape is re-evaluated after applying the scale factors resulting from the template fit shown in Table 6.3.

Figure 6.17 shows an example of the m_T^W distributions resulting from the multi-jet template fit, after varying the multi-jet shape.

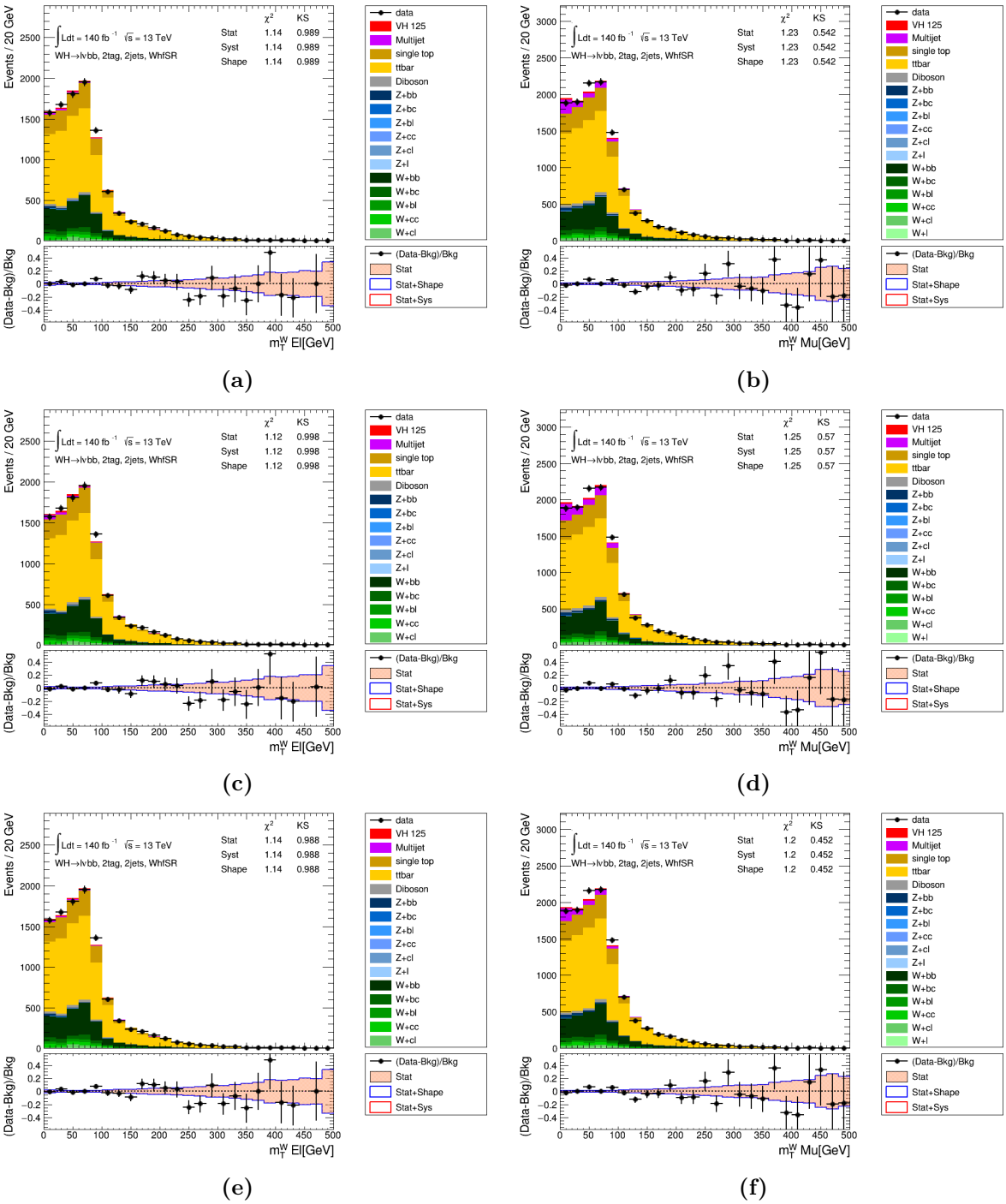

Figure 6.17 – The m_T^W distribution in the 2-tag, 2-jets, isolated p_T^V >150 GeV region. The nominal multi-jet estimation in the e sub-channel is shown in (a) and the μ sub-channel (b), the multi-jet derived in the tight inverted isolation region in the e sub-channel (c) and the μ sub-channel (d), while the multi-jet is derived in the inverted isolation region after applying the scale factors resulting from the template fit in the e sub-channel (e) and the μ sub-channel (f).

The two shape systematic uncertainties are added to the fit after normalising the yields to that of the nominal distribution. They are propagated to the final discriminant and implemented as independent nuisance parameters. The BDT distributions with the shape systematic uncertainties are presented in Figures 6.18 and 6.19 using the same binning as the main analysis BDT distribution. These shape uncertainties have a negligible impact in the $75\,\text{GeV} < p_T^V < 150\,\text{GeV}$ region and an impact of ~30$ in the $p_T^V > 150\,\text{GeV}$ regions with a significant statistical uncertainty.

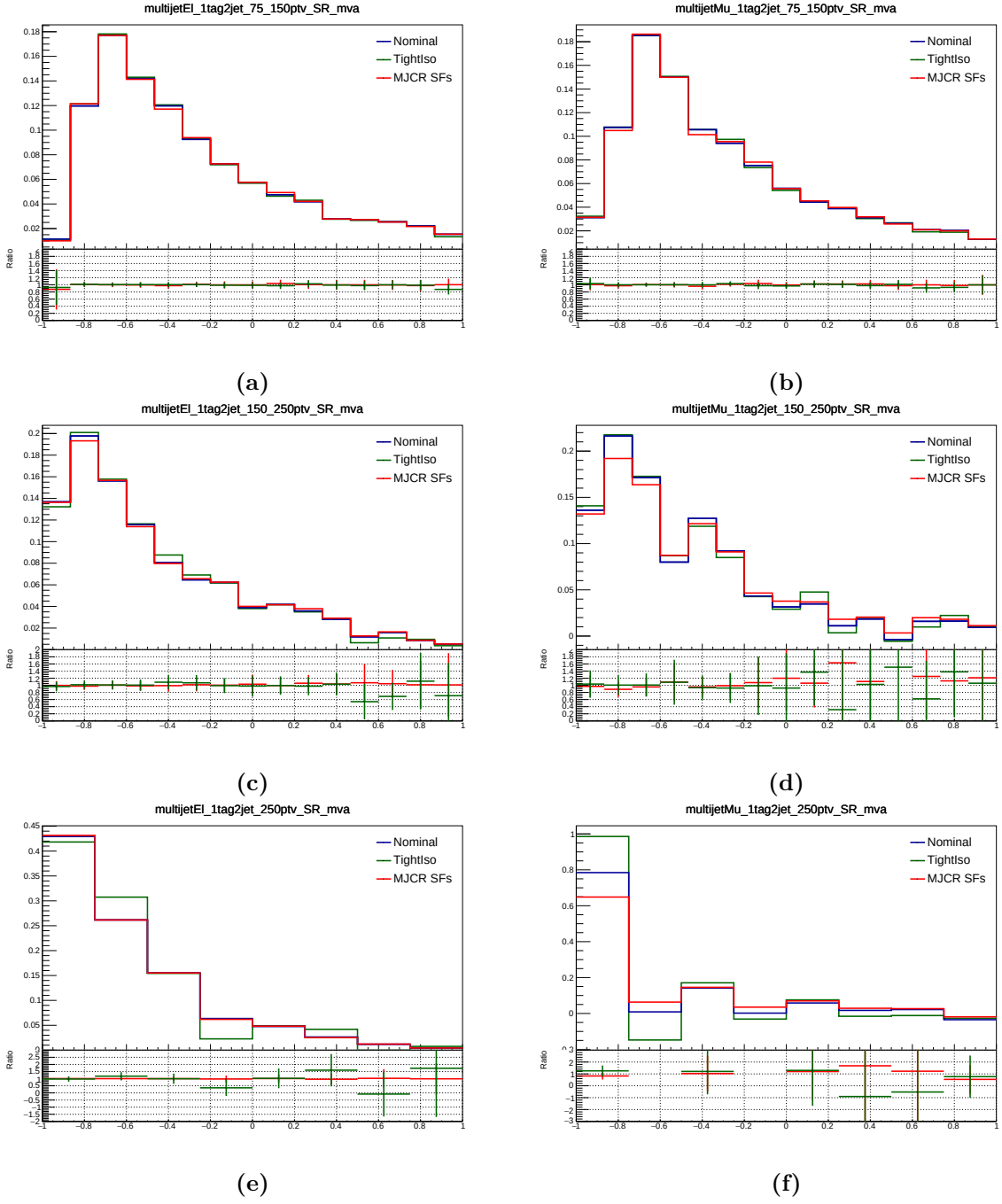

Figure 6.18 – The BDT distributions in the analysis signal region showing the multi-jet comparison for the nominal shape (in blue), the variation representing the multi-jet in the reduced inverted isolation region (in green) and the variation after applying the W+jets and top normalisation factors in the inverted isolation region (in blue). The distributions represent the 2-jet category in the $75\,\text{GeV} < p_T^V < 150\,\text{GeV}$ region for (a) e sub-channel and (b) μ sub-channel, the $150\,\text{GeV} < p_T^V < 250\,\text{GeV}$ region for (c) e sub-channel and (d) μ sub-channel and the $p_T^V > 250\,\text{GeV}$ region for (e) e sub-channel and (f) μ sub-channel.

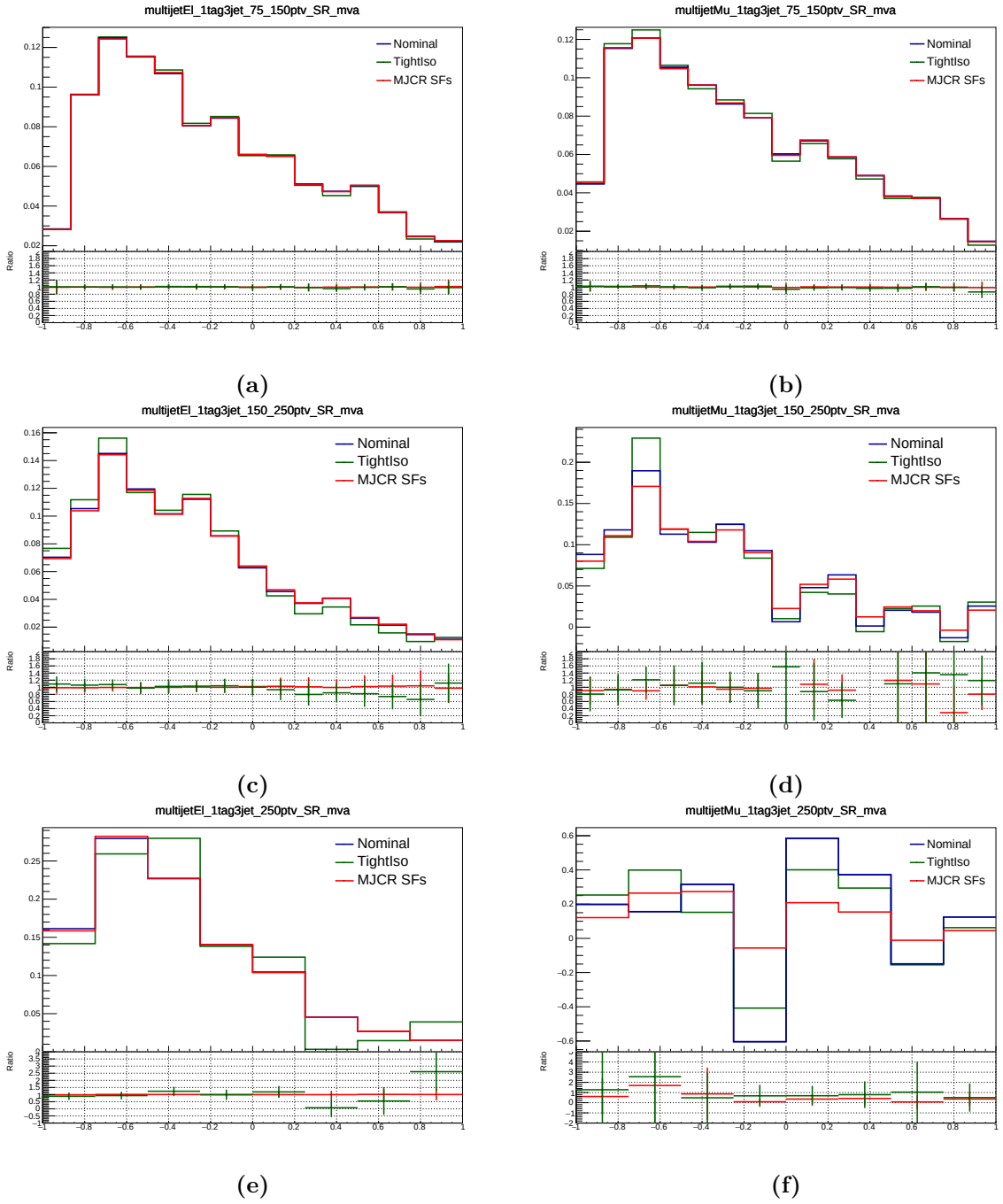

Figure 6.19 – The BDT distributions in the analysis signal region showing the multi-jet comparison for the nominal shape (in blue), the variation representing the multi-jet in the reduced inverted isolation region (in green) and the variation after applying the W+jets and top normalisation factors in the inverted isolation region (in blue). The distributions represent the 3-jet category in the 75 GeV $< p_T^V <$ 150 GeV region for (a) e sub-channel and (b) μ sub-channel, the 150 GeV $< p_T^V <$ 250 GeV region for (c) e sub-channel and (d) μ sub-channel and the $p_T^V >$ 250 GeV region for (e) e sub-channel and (f) μ sub-channel.

Normalisation Uncertainties

The choice of the m_T^W distribution to perform the fit in addition to the selection cuts required to reduce the multi-jet contribution in the 1-lepton channel have an impact on the multi-jet normalisation. The two shape systematic uncertainties described above are also considered as

sources of normalisation uncertainties and are taken into account in addition to the following sources:

- In the 75 GeV $< p_T^V <$ 150 GeV region, in order to increase the multi-jet contribution and to explore its impact on the normalisation, the $m_T^W > 20$ GeV cut is removed in both the inverted isolation and isolated regions. An example of the fit results is shown in Figure 6.20.
- The E_T^{miss} >30 GeV cut in the 75 GeV< p_T^V <150 GeV and p_T^V >150 GeV regions is removed in the electron channel to enhance the multi-jet contribution. An example of the fit results is shown in Figure 6.21.
- The $\Delta\phi$(lepton, E_T^{miss}) is a good discriminant variable between the multi-jet and the electroweak backgrounds. It was explored in the fit as an alternative to using the m_T^W distribution. An example of the fit results is shown in Figure 6.22

Each one of these systematic uncertainties changes the total multi-jet contribution. These positive and negative variations are added separately in quadrature to give the overall normalisation uncertainty in each of the eight regions independently. The fraction of nominal multi-jet events

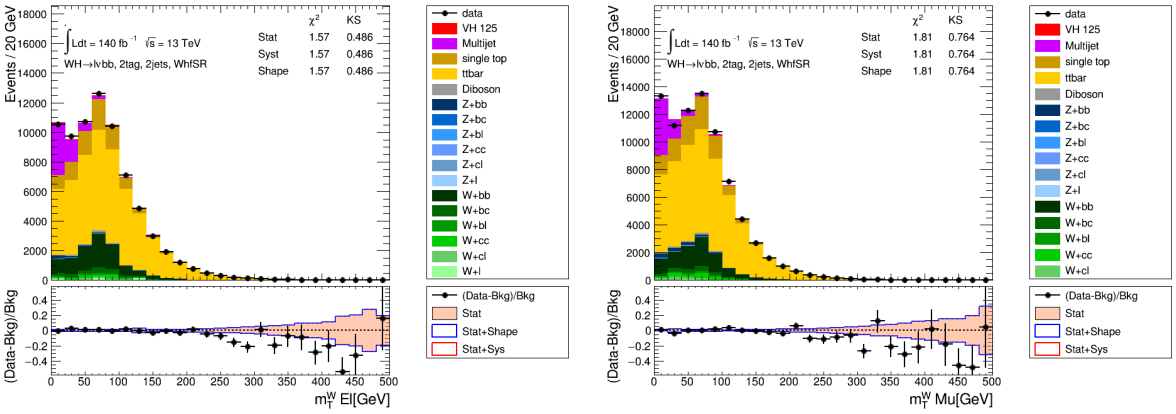

(a) **(b)**

Figure 6.20 – The m_T^W distributions in the 2-tag, 2-jets, isolated 75 GeV $< p_T^V <$150 GeV region after removing the m_T^W cut in the inverted isolation region in the e sub-channel (a) and the μ sub-channel (b).

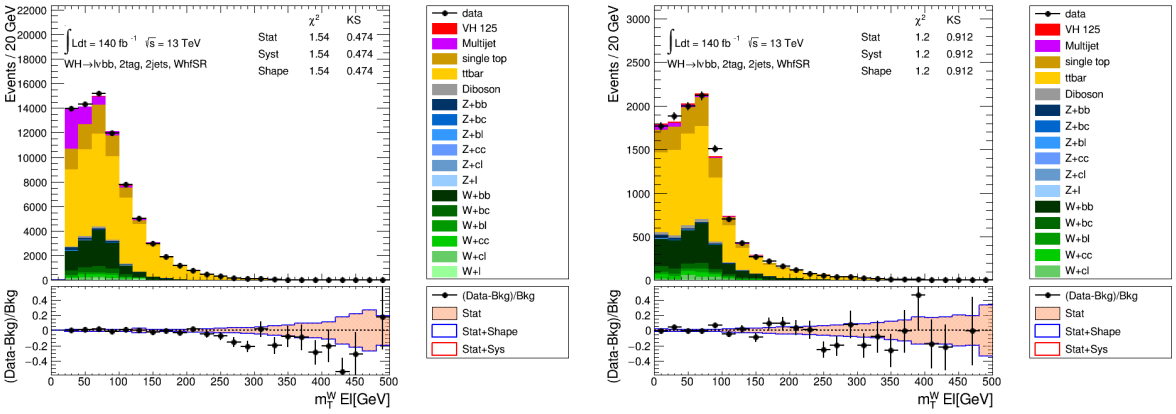

(a) **(b)**

Figure 6.21 – The m_T^W distributions in the 2-tag, 2-jets, isolated electron sub-channel, after removing the E_T^{miss} cut in the inverted isolation region in the 75 GeV $< p_T^V <$150 GeV region (a) and the p_T^V >150 GeV region (b).

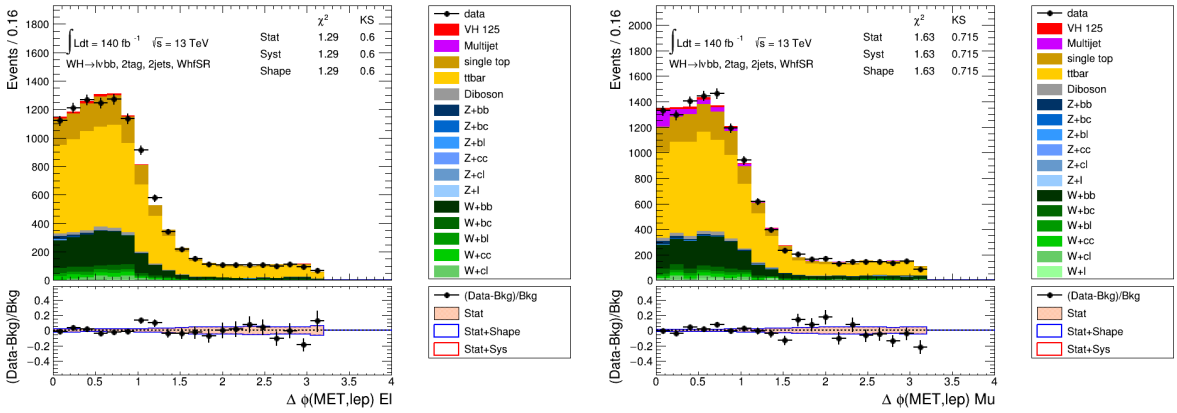

(a) **(b)**

Figure 6.22 – The $\Delta\phi$(lepton, E_T^{miss}) distributions in the 2-tag, 2-jets, isolated p_T^V >150 GeV region, after applying the scale factor resulting from the $\Delta\phi$(lepton, E_T^{miss}) fit, in the e sub-channel (a) and the μ sub-channel (b).

with their associated uncertainties are shown in Table 6.4. These uncertainties are introduced as constraints in the final fit. The multi-jet fraction is very small (up to ∼5% in the 2-jet 75 GeV $< p_T^V <$150 GeV muon sub-channel) with large uncertainties which sometimes reach the 200%.

Region	MJ Fractions (%)
p_T^V >150 GeV region	
2-tag, 2-jet, e	$0.7^{+1.4}_{-0.7}$
2-tag, 2-jet, μ	$3.8^{+1.8}_{-1.1}$
2-tag, 3-jet, e	$0.13^{+0.13}_{-0.13}$
2-tag, 3-jet, μ	$0.06^{+0.06}_{-0.06}$
75 GeV $< p_T^V <$150 GeV region	
2-tag, 2-jet, e	$4.8^{+0.4}_{-1.2}$
2-tag, 2-jet, μ	$1.8^{+1.5}_{-0.3}$
2-tag, 3-jet, e	$1.9^{+0.3}_{-0.6}$
2-tag, 3-jet, μ	$1.6^{+0.2}_{-0.2}$

Table 6.4 – Multi-jet relative contribution to the total background.

6.1.2 Top background modelling in the 2-lepton channel

A data-driven approach was chosen to model both $t\bar{t}$ and single top backgrounds in the 2-lepton channel intending to eliminate the top dedicated modelling systematic uncertainties to improve the signal measurement. The $e\mu$ control region is defined based on one property of the top background which is the flavor asymmetry. The top events are expected to have two leptons of the different flavor ($e\mu$) coming from the independent semi-leptonic top quarks decay, in half of the events. Whereas the signal and the other background have either a pair of e or μ in the final state coming for the Z boson decay, events in this control region are required to have a pair of leptons with two different flavor (one e and one μ).

From this control region highly pure in top background, data events are extrapolated into the signal region. A normalisation factor relative to the extrapolation between the $e\mu$ control and the analysis regions is applied using data to Monte Carlo comparisons, to be able to directly use

the data events as the top background template.

6.2 Modelling uncertainties of the Monte Carlo simulated events

The shape and the normalisation uncertainties cover the choice of the generator used in the analysis. These uncertainties are assigned to each process and are quantified by changing the generator description. They are taken from a Monte Carlo to Monte Carlo comparison or from a data to Monte Carlo comparison, which is the case for the Z+jets shape uncertainties derived in a highly pure control region.

6.2.1 Normalisation uncertainties

Normalisation uncertainties are assigned to the yields of each of the backgrounds. The normalisations of the main backgrounds (W+jets, Z+jets and $t\bar{t}$) are completely floated within the fit. These uncertainties are decorrelated between the 2- and 3-jets categories and between the $75\,\text{GeV} < p_T^V < 150\,\text{GeV}$ and the $p_T^V > 150\,\text{GeV}$ region in the 2-lepton channel. Since the W+cl, Z+cl, W+l and Z+l events are suppressed by the 2 $b-$tagged jets requirements (less than 1% of the total background), a loose constraint is applied to these events, calculated with respect to the Standard Model prediction.

For the single top background, a normalisation uncertainty is applied to each of the three subchannel independently, taken as the quadratic sum of the renormalisation and factorisation scale variations, the α_S uncertainty and the errors on the parton density functions.

The diboson background is composed of three different processes. Their normalisations are floated in the fit when measuring the diboson signal, and constrained with an overall normalisation when measuring the Higgs boson signal. The global normalisation uncertainty is set as the quadratic sum of variations obtained from the comparison of the nominal generator to scale variations (factorization, renormalization and resummation), comparison to parton shower and underlying event variations (Powheg+Pythia8 vs Powheg+Herwig++ [111]) and with both the parton shower and matrix element variations (Powheg+Pythia8 vs Sherpa 2.2.1).

All the signal samples are normalised to the best theoretical prediction of the cross section obtained by the LHC Higgs Cross Section working group. The QCD scale uncertainties on the overall VH cross section were obtained by varying the renormalisation and factorisation scales independently by factors of 1/3 and 3 of their original values. The electroweak higher order uncertainties are also added as function of p_T^V, as the maximum of the NLO EW correction factor, the size of the NNLO EW correction and the relative uncertainty of the photon induced contributions to the total VH cross section.

The signal scale uncertainties should be applied independently for the quark induced processes and the gluon induced processes. However, since the LHC Higgs working group recommendations are not given separately to the two processes, it was assumed that the global $qq \to ZH$ uncertainties are identical to that of $qq \to WH$. Therefore after calculating the $qq \to ZH$ uncertainties, the $gg \to ZH$ uncertainties are derived after considering that the overall ZH uncertainties are equal to the quadratic sum of both processes.

The $H \to b\bar{b}$ branching ratio uncertainty is also considered, taking into account the QCD and EW missing higher order terms, in addition to the uncertainty on the b-quark mass and α_s.

Additional uncertainties relative to the signal STXS bins cross-section are added, from the PDF+α_S variations using PDF4LHC15_30 PDF [78] set and from the comparison of the nominal Powheg+Pythia8 to an alternative sample with factorisation and renormalisation scale

variations.

6.2.2 Acceptance uncertainties

The acceptance uncertainties are needed to account for the change of the events distribution in the analysis regions. This is due to migration of the events across the regions, which will change the ratio of the events between regions. These uncertainties are calculated from yields comparison between Monte Carlo generators. The uncertainty on the ratio of acceptance between two categories (A and B) is based on the comparison of the nominal Monte Carlo generator used in the analysis and an alternative generator following the double ratio:

$$\frac{Acceptance[Category_A(nominalMC)}{Acceptance[Category_B(nominalMC)} \Big/ \frac{Acceptance[Category_A(alternativeMC)}{Acceptance[Category_B(alternativeMC)} \tag{6.1}$$

The following uncertainties are included in the analysis:

$t\bar{t}$ background

For the $t\bar{t}$ background, a 0- to 1-lepton $t\bar{t}$ extrapolation uncertainty is implemented. This correction in needed since the $t\bar{t}$ global normalisation is common between the two channels and is constrained in the 1-lepton channel. The uncertainty on the ratio of acceptances are taken as the quadratic sum from the comparison between the nominal generator Powheg+Pythia8 and the two alternative generators MadGraph5_aMCAtNLO+Pythia8 [112] (ME variation) and Powheg+Herwig7 [113] (PS variation).

For reconstruction of the Higgs boson candidate, the two b-jets are not always selected. Since the main contribution of this background comes from bb and bc events, the other flavors are merged together into one category denoted as "oth". These bb, bc and oth events are in different corners of the $t\bar{t}$ phase space, and therefore it is legitimate to cover this with a systematic. Two separate acceptances are derived to account for the oth/bb and bc/bb uncertainty on the ratio of acceptance from the comparison of the PS and ME variations to the nominal generator. These systematic uncertainties are correlated between 2- and 3-jets and between 0- and 1-lepton channels.

V+jets background

For V+jets, one of the sources of variation is the prediction given by the MadGraph [112] generator compared to the nominal Sherpa generator. Additional sources of uncertainty are taken into account, coming from scales variations of the nominal generator: the factorisation and renormalisation scales, the matrix element matching scale (CKKW) and the variation after reweighting the nominal to an alternative PDF.

First, a W+jets acceptance uncertainty is derived in the 0- and 1-lepton channels, corresponding to the events migration between the signal and control regions. This systematic is correlated between the 2- and 3-jets categories and between the 0- and 1-lepton channels. For Z+jets, the CR/SR migration is derived in the 0- and 2-lepton channels, separately for the high and low ΔR control regions and correlated between 2- and 3-jet category and between the two channels.

Since the W+jets phase space is similar in the 0- and 1-lepton, the normalisation is common in both channels (one parameter) and is floated in the fit. Acceptances are derived corresponding to the 1- to 0-lepton W+jets normalisation extrapolation, since the 1-lepton allows to better

control of this background. Similarly, a 0- to 2-lepton Z+jets extrapolation is implemented since the 2-lepton offers a better control for the Z+jets background.

Flavor uncertainties are also added since the bb, bc, bl and cc backgrounds are merged together to create the heavy flavor contribution in the final fit. For this reason the uncertainties on the bc/bb, bl/bb and cc/bb fractions are implemented in the 0- and 1- lepton channels for W+jets and in 0- and 2-lepton channels for the Z+jets background.

Single top background

This background mainly contributes in the 1-lepton channel with a negligible contribution of the s-channel production. Therefore separate acceptances are needed for the two sub-channels Wt and t. Several sources of variations are investigated: nominal generator with tuning to increase or decrease the QCD radiation, the parton shower variation using the Powheg+Herwig++ generator and last, both the matrix element and the parton shower from events generated with MadGraph 5_aMCAtNLO+Herwig ++ generator. An additional variation is only considered in the Wt channel, coming from the nominal generator with a matrix element calculation applying the diagram subtraction (DS) scheme instead of the diagram removal (DR) scheme.

For the t-channel, events with 2 b-jets in the final state are treated separately than the remaining categories (oth). The final constraints on the t-channel, the Wt $\rightarrow b\bar{b}$ and Wt $\rightarrow oth$ channel acceptances are calculated as the quadratic sum of the all possible variations.

Diboson background

For the diboson background, the acceptances are assigned only for the ZZ and WZ processes, since the WW has a very small contribution. They are derived as a quadratic sum of the parton-shower, hadronisation and underlying event variations, computed from the comparisons using Powheg+Pythia8 and Powheg+Herwig++ generators. Additional uncertainties are considered coming from the renormalisation, factorisation of the nominal Sherpa 2.2.1 generator.

Since the 1-lepton channel allows to better constrain the WZ background, and since the WZ normalisation is assigned simultaneously in both channels, a 0- to 1-lepton extrapolation uncertainty was introduced, derived separately for 2- and 3-jets events. Similarly, 0- to 2-lepton extrapolation uncertainties were implemented for the ZZ background.

Signal

For the signal processes only one acceptance uncertainty is considered from the PS/UE variations by computing the comparison between the Powheg+Pythia8 nominal generator to Powheg+Herwig7.

The analysis modelling normalisation and acceptance systematic uncertainties are summarised in Tables 6.5, 6.6 and 6.7.

6.2.3 Shape uncertainties

The evaluation of the shape uncertainties is independent from the acceptance uncertainties. It allows to quantify the effects that cause a shape modification to the Monte Carlo prediction. They are obtained by taking the difference between the nominal generator used in the analysis and an alternative generator after normalising them to the same yields. A bin by bin comparison

Z + jets	
Z + ll normalisation	18%
Z + cl normalisation	23%
Z + HF normalisation	Floating (2-jet, 3-jet) ($p_T^V < 150\,\text{GeV}$, $p_T^V > 150\,\text{GeV}$)
Z + bc-to-Z + bb ratio	30%–40%
Z + cc-to-Z + bb ratio	13%–16%
Z + bl-to-Z + bb ratio	20%–28%
SR-to-low ΔR CR ratio	3.8%–9.9% ($p_T^V < 150\,\text{GeV}$, $p_T^V > 150\,\text{GeV}$)
SR-to-high ΔR CR ratio	2.7%–4.1% ($p_T^V < 150\,\text{GeV}$, $p_T^V > 150\,\text{GeV}$)
0-to-2 lepton ratio	7%
W + jets	
W + ll normalisation	32%
W + cl normalisation	37%
W + HF normalisation	Floating (2-jet, 3-jet)
W + bc-to-W + bb ratio	15% (0-lepton) and 30% (1-lepton)
W + cc-to-W + bb ratio	10% (0-lepton) and 30% (1-lepton)
W + bl-to-W + bb ratio	26% (0-lepton) and 23% (1-lepton)
SR-to-CR ratio	3.6%–15%
0-to-1 lepton ratio	5%
$t\bar{t}$ (only 0- and 1-lepton channel)	
tt normalisation	Floating (2-jet, 3-jet)
0-to-1 lepton ratio	8%
$t\bar{t}$ bc-to-bb ratio (ME)	7.6%–8.2% (0-lepton), 1.3%–3.8% (1-lepton)
$t\bar{t}$ bc-to-bb ratio (PS)	2.1%–3.2% (0-lepton), 1.5%–7.1% (1-lepton)
$t\bar{t}$ oth-to-bb ratio (ME)	2.8%–6.4% (0-lepton), 3.3%–5.7% (1-lepton)
$t\bar{t}$ oth-to-bb ratio (PS)	5.6%–13% (0-lepton), 0.3%–2.1% (1-lepton)
Single top quark	
Cross-section	4.6% (s-channel), 4.4% (t-channel), 6.2% (Wt)
Acceptance 2-jet	17% (t-channel), 55% ($Wt(bb)$), 24% (Wt(other))
Acceptance 3-jet	20% (t-channel), 51% ($Wt(bb)$), 21% (Wt(other))

Table 6.5 – Summary of the normalisation and acceptance uncertainties for the V+jets and top background modelling.

to all the possible variations is then performed on the final fit discriminant. These bin by bin comparisons, in most of the cases, are impacted by the statistical fluctuations of the distributions, which prompts to seek a method to smooth these fluctuations. For this reason a simple reweighting approach is used to map all the nominal generator to be identical to the alternative generator. The weights are calculated using the ratio of the alternative to nominal distributions after using a parametric fit to smooth the distributions. These weights are obtained from the most discriminant variables between the two generators. Different sources of variation must be studied and derived independently to each of the nominal samples.

6.2.3.1 One dimensional reweighting

These uncertainties must be computed from discriminant variables allowing to underline and correctly compute the shape variations. They should also cover the shape variation of the BDT distribution and the variables used in training of the BDT. Therefore, the m_{bb} and p_T^V distributions are used in the analysis to derive the shape systematic uncertainties. These two variables were chosen because they are uncorrelated, which allows to map different kinematic

ZZ	
Normalisation	20%
0-to-2 lepton ratio	6%
Acceptance from scale variations	10%–18%
Acceptance from PS/UE variations for 2 or more jets	6%
Acceptance from PS/UE variations for 3 jets	7% (0-lepton), 3% (2-lepton)
WZ	
Normalisation	26%
0-to-1 lepton ratio	11%
Acceptance from scale variations	13%–21%
Acceptance from PS/UE variations for 2 or more jets	4%
Acceptance from PS/UE variations for 3 jets	11%
WW	
Normalisation	25%

Table 6.6 – Summary of the normalisation and acceptance uncertainties for the diboson background modelling.

Signal	
Cross-section (scale)	0.7% (qq), 25% (gg)
$H \to bb$ branching fraction	1.7%
Scale variations in STXS bins	3.0%–3.9% ($qq \to WH$), 6.7%–12% ($qq \to ZH$), 37%–100% ($gg \to ZH$)
PS/UE variations in STXS bins	1%–5% for $qq \to VH$, 5%–20% for $gg \to ZH$
PDF+α_S variations in STXS bins	1.8%–2.2% ($qq \to WH$), 1.4%–1.7% ($qq \to ZH$), 2.9%–3.3% ($gg \to ZH$)

Table 6.7 – Summary of the normalisation and acceptance uncertainties for the signal modelling.

effects. In addition, they are the most important variables in the BDT training and will therefore model the most important contribution to the shape uncertainty of the BDT distribution. Using only these two variables to derive the shape uncertainties was deemed sufficient when the closure tests show that the two distributions are enough to correctly model the shape uncertainties on the BDT input variables. These systematic uncertainties are derived by taking the ratio of the alternative generator showing the largest variation (in the bin-by-bin comparison) with respect to the nominal generator. The ratio is then fitted to derive a reweighting function which will be used to apply weights to all the events. These weights are then applied to all events to change the shape of the distributions of the variables used the BDT training and of BDT output itself. The p_T^V systematic covers the acceptance uncertainty between the different p_T^V regions of the analysis, and is therefore used as an uncertainty for all the background processes. An example of the p_T^V systematic uncertainties is shown in Figure 6.23 for the $t\bar{t}$ background where the ratio showing the largest variation is the ratio MadGraph5_aMCAtNLO+Pythia8 over Powheg+Pythia8. The m_{bb} systematic implemented in addition to the p_T^V systematic is only used for the signal, single top, Z+jets and diboson modelling. For $t\bar{t}$ and W+jets backgrounds a BDT-based reweighting method (BDTr) was adopted as presented in the next section, since the m_{bb} reweighting was found to be insufficient to cover variation on all the input variables. Table 6.8 shows the shape systematic uncertainties for each process.

shape	Description	category
	VH signal	
p_T^V	from NLO EW correction	0- , 1- and 2-lepton
m_{bb}	from PS/UE variation	0- , 1- and 2-lepton
m_{bb}	from scale variations	0- , 1- and 2-lepton
	W+jets	
p_T^V	from ME variation (Sherpa vs MadGraph)	0- and 1-lepton
BDTr	from ME variation (Sherpa vs MadGraph)	0- and 1-lepton
	Z+jets	
p_T^V	data-driven	0- and 2-lepton
m_{bb}	data-driven	0- and 2-lepton
	$t\bar{t}$	
p_T^V	from ME variation	0- and 1-lepton
BDTr	from ME variation	0- and 1-lepton
BDTr	from PS variation	0- and 1-lepton
	single top	
p_T^V	from DS variation for $Wt \to bb$ and $Wt \to oth$	0- and 1-lepton
m_{bb}	from DS vs DR variation for $Wt \to bb$	0- and 1-lepton
m_{bb}	from PS vs DR variation for $Wt \to oth$	0- and 1-lepton
p_T^V	from PS variation for t-channel	0- and 1-lepton
m_{bb}	increased and decreased radiation tuning for t-channel	0- and 1-lepton
	diboson	
p_T^V	from PS/UE variation	0- , 1- and 2-lepton
m_{bb}	from PS/UE variation	0- , 1- and 2-lepton
p_T^V	from ME variation	0- , 1- and 2-lepton
m_{bb}	from ME variation	0- , 1- and 2-lepton

Table 6.8 – Summary of the shape uncertainties in the VHbb analysis. The correlation between categories of these uncertainties have been studied to decide on the final scheme.

6.2.3.2 BDT reweighting technique

The p_T^V and m_{bb} reweightings do not estimate correctly the shape variation of all variables, as illustrated in the example in Figure 6.24 showing the $p_T^{jet_2}$ and m_{bbJ} distributions in the 0-lepton channel. There is a clear shape systematic in the $p_T^{jet_2}$ and the m_{bbJ} distributions, but neither of the two systematic uncertainties is able to correctly reproduce it. Therefore, a hybrid approach has been developed for both $t\bar{t}$ and W+jets backgrounds to use the p_T^V-derived systematic uncertainty and replace the m_{bb} systematic by a multi-dimensional reweighting uncertainty. This additional uncertainty uses correlation between all the analysis BDT inputs to represent the whole phase space with a single parameter instead of focusing only on the m_{bb} distribution.

This technique consists of training a BDT using the nominal generator as signal and the alternative generator as background and using the same input variables for the training as the main analysis BDT. When training one generator against another, the BDT will probe pieces of the phase space where the two generators do not have the same acceptance, and group them by an S/B which will reflect their differences in acceptance.

To avoid the double counting of the p_T^V variation, the events are first reweighted using the p_T^V systematic weights to factorise this effects before using them in the training. The BDT score ratio of the nominal and alternative generator is fitted to smooth the variation. Similarly to the p_T^V and m_{bb} systematic uncertainties, this ratio gives an event weight which is applied to the nominal generator to obtain the systematic shape. For the W+jets background, the BDT reweighting method is used to parametrise the difference between Sherpa and MadGraph, while for $t\bar{t}$ two different BDTs are implemented to separate Powheg+Pythia8 from

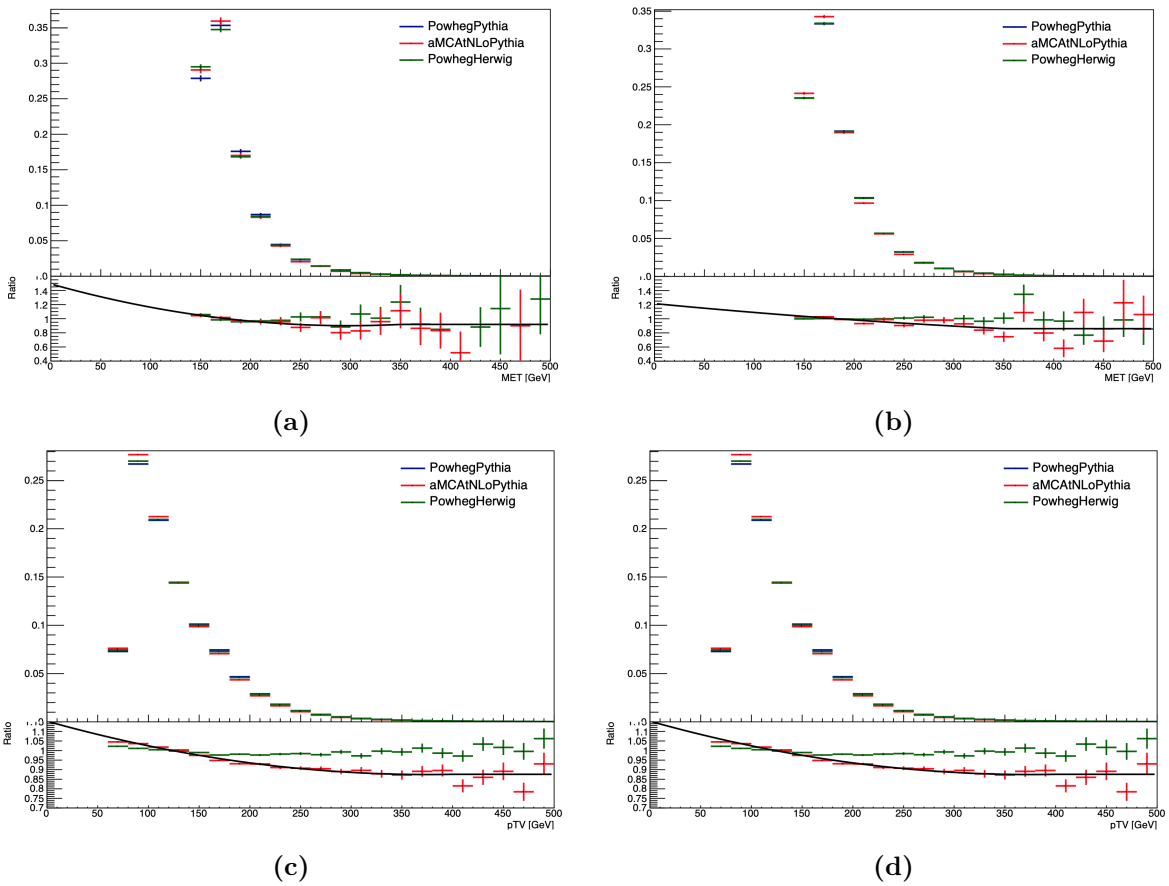

Figure 6.23 – The p_T^V/E_T^{miss} shape uncertainties on the $t\bar{t}$ prediction in the 0-lepton channel (a) 2-jet and (b) 3-jet categories and in the 1-lepton (c) 2-jet and (d) 3-jet categories. the black curve in the lower pad corresponds to the fit of the largest variation and is used as a shape systematic. These uncertainties are symmetrised in the fit.

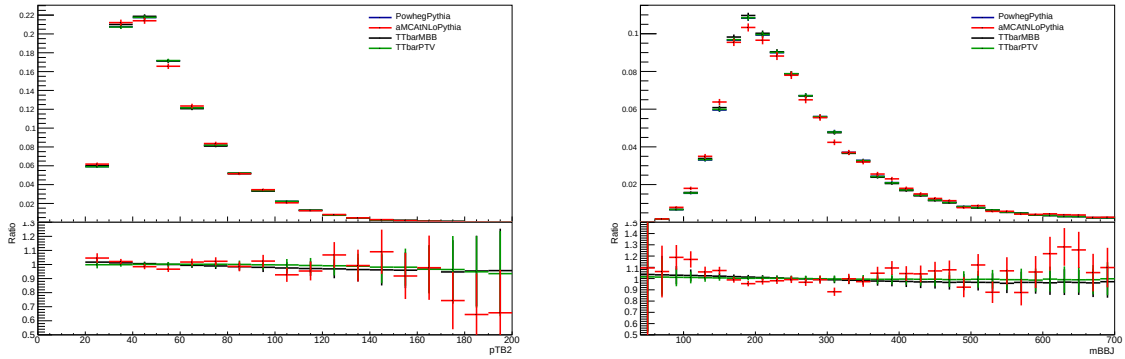

Figure 6.24 – Impact of the p_T^V and m_{bb} reweighting on the sub-leading jet p_T (a) and 3-jet mass (b) in the 0-lepton 3-jet channel on the $t\bar{t}$ background. The bottom panels show the ratios to the nominal prediction.

MadGraph5_aMCAtNLO+Pythia8 and Powheg+Pythia8 from Powheg+Herwig7. This Section details the procedure to derive the $t\bar{t}$ dedicated BDT based systematic uncertainties in the 0- and 1-lepton channels.

BDT training

Two BDT classifiers are trained to separate between the p_T^V-reweighted nominal generator and each of the two variations using the inputs variables in Table 5.12. The training was done after separating the events depending on the jet multiplicity and separating them into three categories depending on the truth-flavor label: bb, bc and oth. Separating the events depending on their flavors is necessary since the flavor fractions are different between the nominal and alternative generators. The different flavor contributions are taken into account when computing the systematic event weights. The training was performed in the whole phase space after including the $75\,\text{GeV} < p_T^V < 150\,\text{GeV}$ region in the 1-lepton channel. To avoid over-training, the statistics in the training inputs are increased by using truth tagging. Table 6.9 shows the number of events and Table 6.10 the flavor acceptance in each of the samples. BDT hyperparameters tuning was also necessary, such as the number of trees and the numbers of nodes, especially in the bc category because of the lower statistics. The same k-folding strategy as the main analysis BDT is applied, by using two folds to increase the performance of the BDT. However, the training in the 0-lepton channel showed difficulties due to low statistics after splitting the events into 2 folds even after tuning. Therefore it was decided to use a single fold, to train and evaluate using all the events to improve the statistics in the training folds. However this method makes the BDT very sensitive to over-training. Using this method is acceptable when the statistics are limited, as long as the BDT-based reweighting yields good closure on all the input variables.

Categories	Powheg+Pythia8	aMCAtNLO+Pythia8	Powheg+Herwig7
0-lepton, 2jet, bb	13964	16270	19961
0-lepton, 2jet, bc	15561	14986	15625
0-lepton, 2jet, oth	74193	80422	87930
0-lepton, 3jet, bb	88891	100135	108237
0-lepton, 3jet, bc	70809	74802	71288
0-lepton, 3jet, oth	171508	205734	203768
1-lepton, 2jet, bb	695369	766178	950091
1-lepton, 2jet, bc	233317	210543	209985
1-lepton, 2jet, oth	1055216	1141360	1231020
1-lepton, 3jet, bb	2718639	2832510	3077782
1-lepton, 3jet, bc	951417	908613	843155
1-lepton, 3jet, oth	2216041	2504223	2474512

Table 6.9 – Number of events in each training sample.

BDT evaluation and closure

The classifier response is evaluated for each event in the two Monte Carlo generators, and the BDT output distribution is computed. The ratio of the alternative distribution over the nominal is then fitted using a second order polynomial function in all the training categories. The distributions are normalised to the same integral to illustrate the difference in shape between the two generators. The BDT score distributions are shown in Figures 6.25, and 6.26 for the ME variation in the 0- and 1-lepton channel respectively.

The closure of the BDT-based reweighting and the p_T^V shape systematic uncertainties can be evaluated when comparing the shape of the nominal generator to both the alternative generator and the nominal generator after reweighting. The reweighting is expected to morph the nominal into the alternative generator but still keeping a smooth ratio to the nominal. The reweighting

Categories	Powheg+Pythia8	aMCAtNLO+Pythia8	Powheg+Herwig7
0-lepton, 2jet, bb	81.7%	80.7%	82.2%
0-lepton, 2jet, bc	15.6%	16.8%	15.4%
0-lepton, 2jet, oth	2.7%	2.5%	2.4%
0-lepton, 3jet, bb	84.1%	83.3%	84.6%
0-lepton, 3jet, bc	13.6%	14.6%	13.3%
0-lepton, 3jet, oth	2.2%	2.1%	2.1%
1-lepton, 2jet, bb	93.6%	93.5%	93.2%
1-lepton, 2jet, bc	5.3%	5.4%	5.9%
1-lepton, 2jet, oth	1.0%	1.1%	0.9%
1-lepton, 3jet, bb	91.8%	91.7%	91.8%
1-lepton, 3jet, bc	7.0%	7.1%	7.2%
1-lepton, 3jet, oth	1.2%	1.2%	1.1%

Table 6.10 – Flavor acceptance in each training sample.

closure of the parton shower variation in the 3-jet bb category is presented in Figures 6.27 and 6.28 for the 0-lepton and in Figures 6.29 and 6.30 for the 1-lepton channels for some of the BDT inputs variables. As shown, the reweighting allows to transform the nominal into the alternative and thus provide a good closure for many of the distributions. The p_T^V and BDT-based shapes systematic uncertainties are un-correlated and complementary, since the BDT-based reweighting is shown to have an effect on the distributions where the p_T^V reweighting does not act.

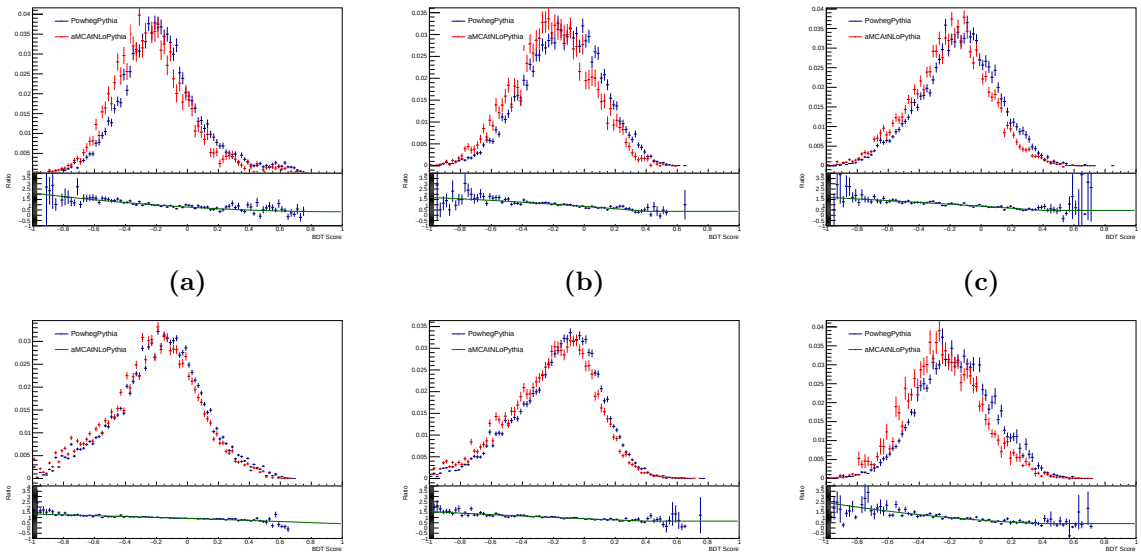

Figure 6.25 – The BDT score distributions for the $t\bar{t}$ prediction showing the nominal Powheg+Pythia8 and the alternative aMCAtNLO+Pythia8 distributions in the 0-lepton, 2-jet bb (a), bc (b), and oth (c) events and 3-jet bb (d), bc (e), and oth (f) events. The bottom pad shows the ratio alternative/nominal distributions and the fitting function is shown in green. The fit of the ratio will be used as the uncertainty.

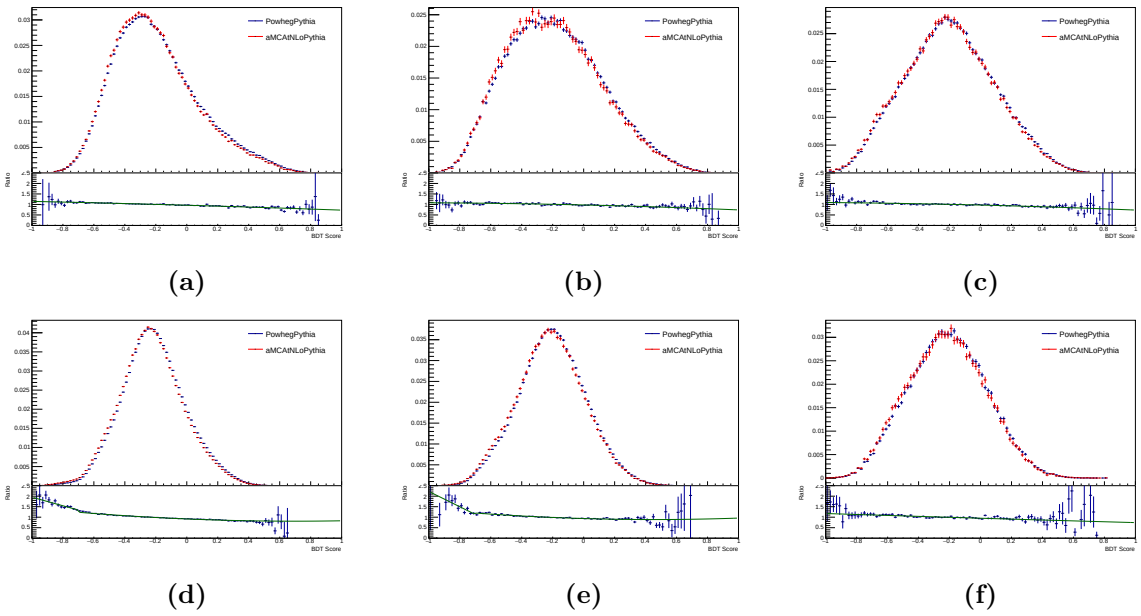

Figure 6.26 – The BDT score distributions for the $t\bar{t}$ prediction showing the nominal Powheg+Pythia8 and the alternative aMCAtNLO+Pythia8 distributions in the 1-lepton, 2-jet bb (a), bc (b), and oth (c) events and 3-jet bb (d), bc (e), and oth (f) events. The bottom pad shows the ratio alternative/nominal distributions and the fitting function is shown in green. The fit of the ratio will be used as the uncertainty.

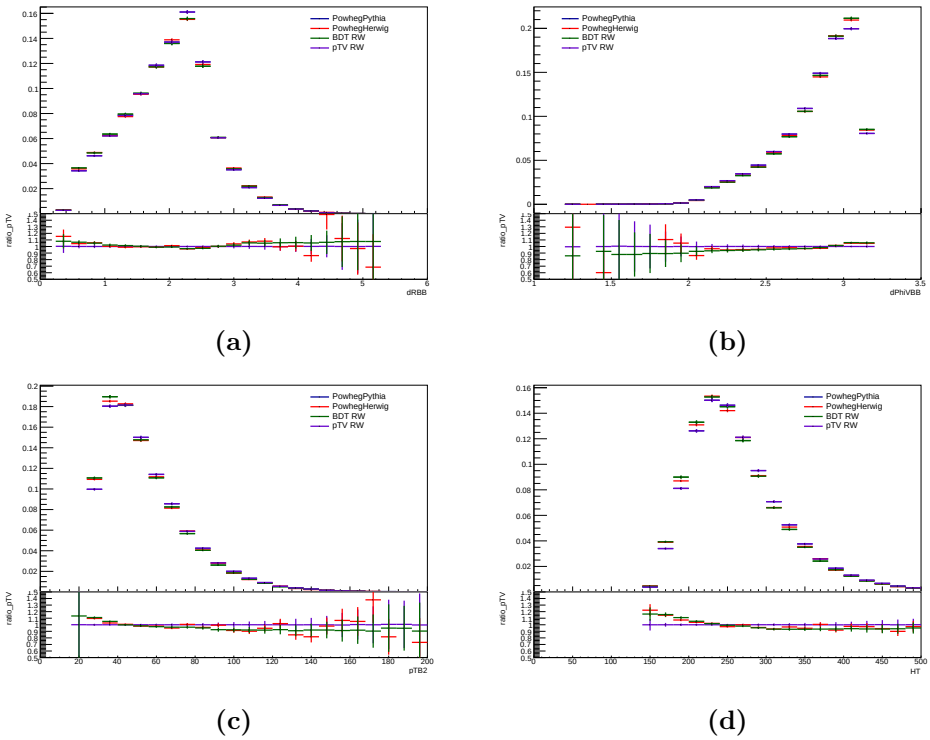

Figure 6.27 – Comparison of the 0-lepton 3-jet *bb* channel BDT training inputs variables, nominal (blue), the alternative (red), the nominal after BDT-reweighting (green) and the nominal after p_T^V-reweighting (Violet) distributions. The bottom pad shows the ratio with respect to the nominal distribution.

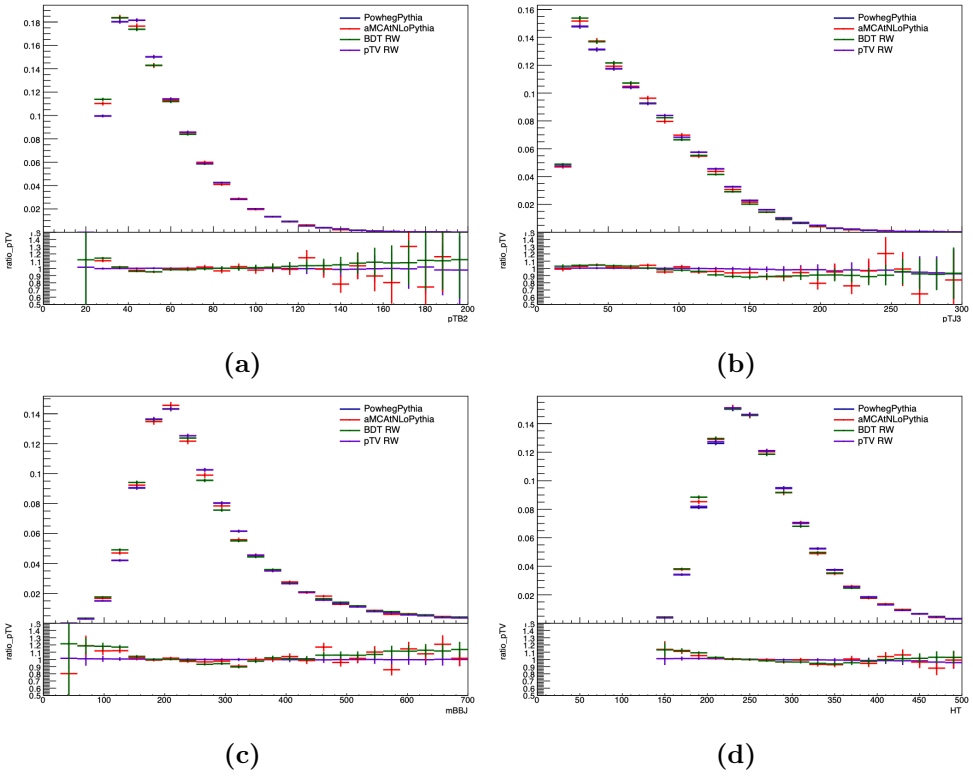

Figure 6.28 – Comparison of the 0-lepton 3-jet *bb* channel BDT training inputs variables, nominal (blue), the alternative (red), the nominal after BDT-reweighting (green) and the nominal after p_T^V-reweighting (Violet) distributions. The bottom pad shows the ratio with respect to the nominal distribution.

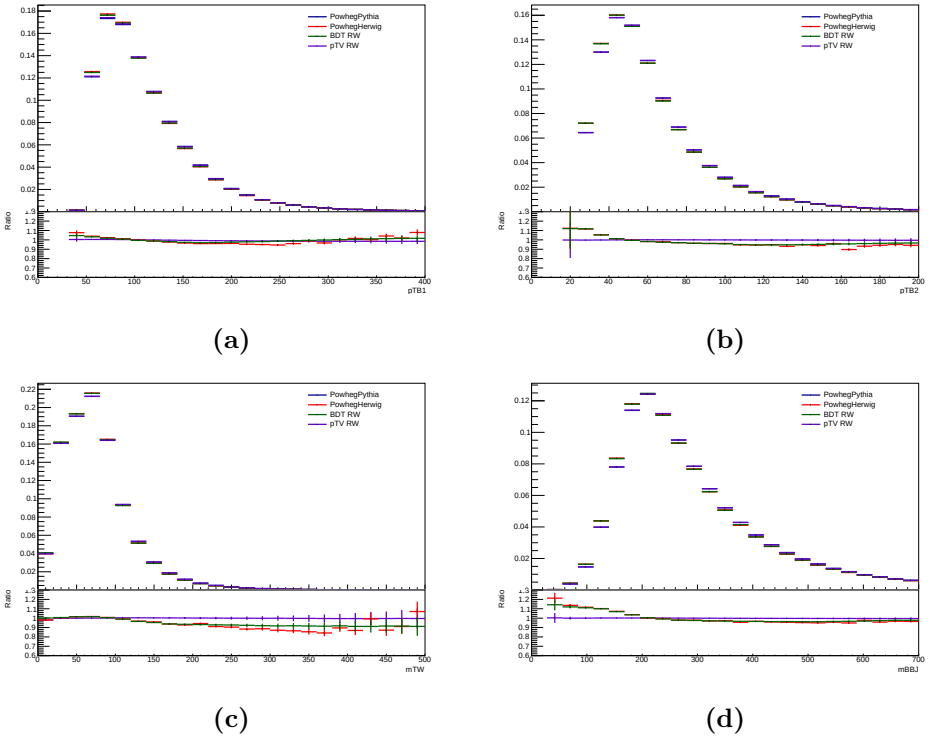

Figure 6.29 – Comparison of the 1-lepton 3-jet *bb* channel BDT training inputs variables, nominal (blue), the alternative (red), the nominal after BDT-reweighting (green) and the nominal after p_T^V-reweighting (Violet) distributions. The bottom pad shows the ratio with respect to the nominal distribution.

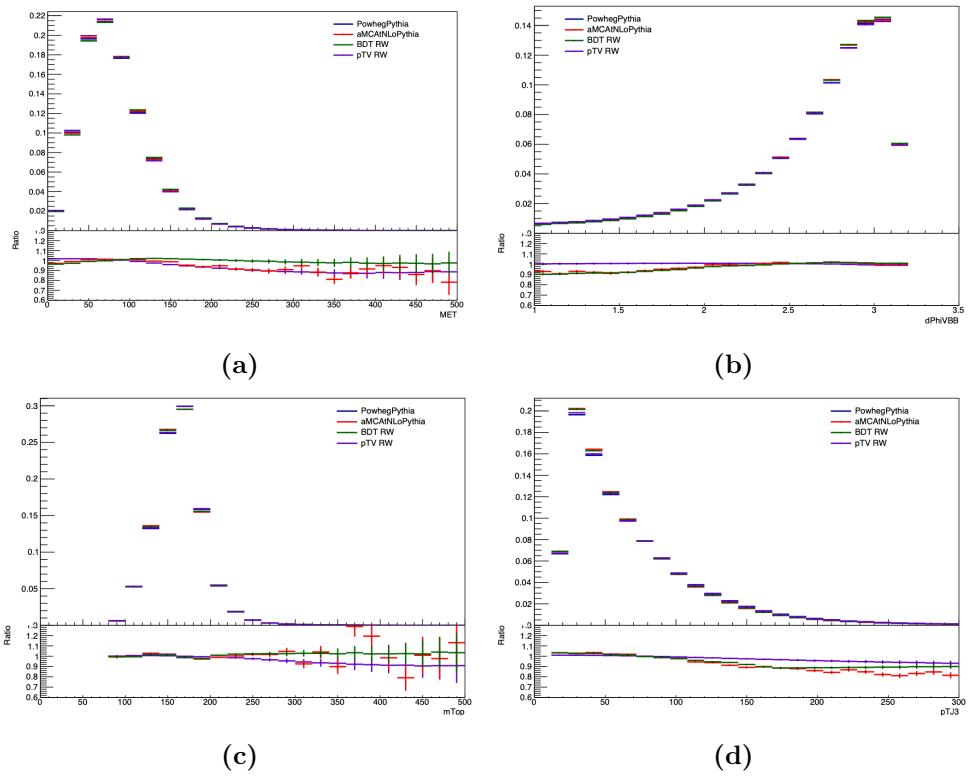

Figure 6.30 – Comparison of the 1-lepton 3-jet *bb* channel BDT training inputs variables, nominal (blue), the alternative (red), the nominal after BDT-reweighting (green) and the nominal after p_T^V-reweighting (Violet) distributions. The bottom pad shows the ratio with respect to the nominal distribution.

BDT-based uncertainties on the final discriminant

The BDT-based weights are applied to the events entering the BDT discriminant depending on the flavor of the jets. The additional flavor composition acceptances are added to reflect the difference in bb, bc and oth fractions in the training between the nominal and alternative generators. The p_T^V and BDT-based shape systematic uncertainties, defined as the difference of the nominal before and after reweighting, are symmetrised to cover the variations in all the BDT bins as shown in Figures 6.31, 6.32, 6.33 and 6.34.

Even though the BDT-reweighting shows a good closure on most of the input variables, the closure on the BDT distributions is not perfect in all the bins of the distribution. Since there are two $t\bar{t}$ systematic uncertainties coming from different sources, they should be enough to cover the BDT distribution when combined together and when combined with the p_T^V systematic uncertainties. Although the BDT performance can still be improved by re-tuning the hyperparameters, the BDT-based systematic uncertainties are still a large improvement in the accuracy of estimating of the modelling systematics with respect to what was used before.

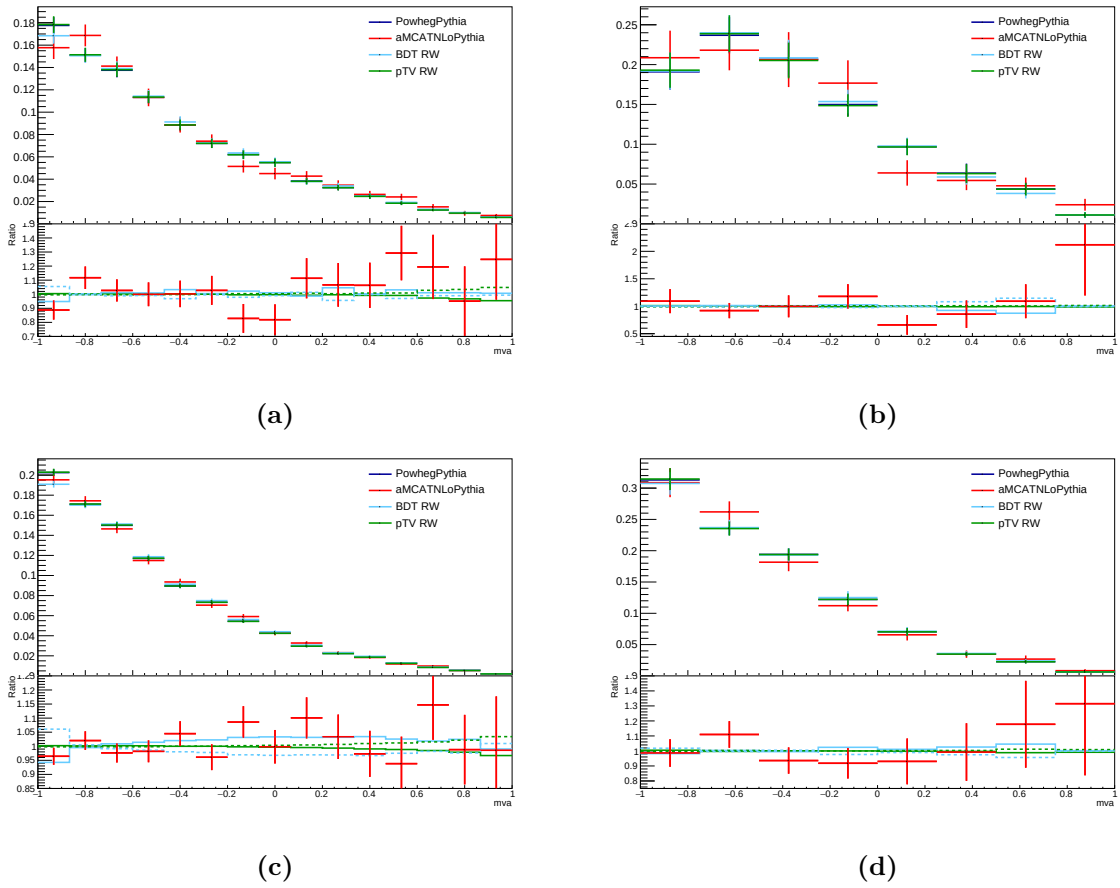

Figure 6.31 – Comparison of the 0-lepton BDT discriminant after transformation in the 2-jet 150 GeV $< p_T^V <$ 250 GeV (a) and $p_T^V >$ 250 GeV (b), 3-jet 150 GeV $< p_T^V <$ 250 GeV (c) and $p_T^V >$ 250 GeV (d) regions showing the nominal distribution in blue, the ME variation in blue, the BDT-based systematic uncertainties in cyan and the p_T^V based systematic in green. The bottom pad shows the ratio of the variation with respect to the nominal. The dashed lines correspond to the symmetrised variation.

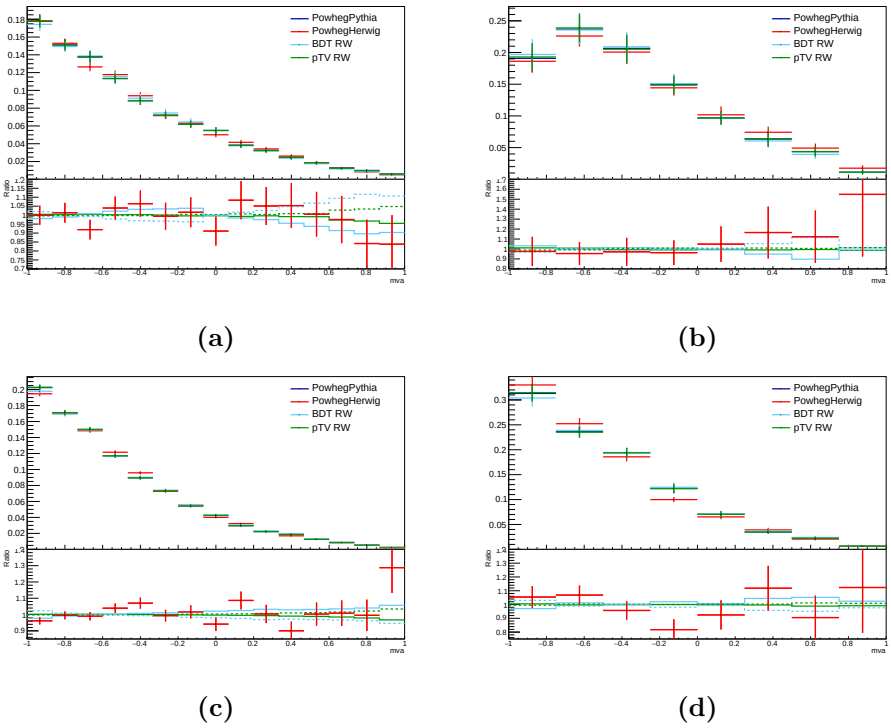

Figure 6.32 – Comparison of the 0-lepton BDT discriminant after transformation in the 2-jet 150 GeV $< p_T^V <$ 250 GeV (a) and $p_T^V >$ 250 GeV (b), 3-jet 150 GeV $< p_T^V <$ 250 GeV (c) and $p_T^V >$ 250 GeV (d) regions showing the nominal distribution in blue, the PS variation in blue, the BDT-based systematic uncertainties in cyan and the p_T^V based systematic in green. The bottom pad shows the ratio of the variation with respect to the nominal. The dashed lines correspond to the symmetrised variation.

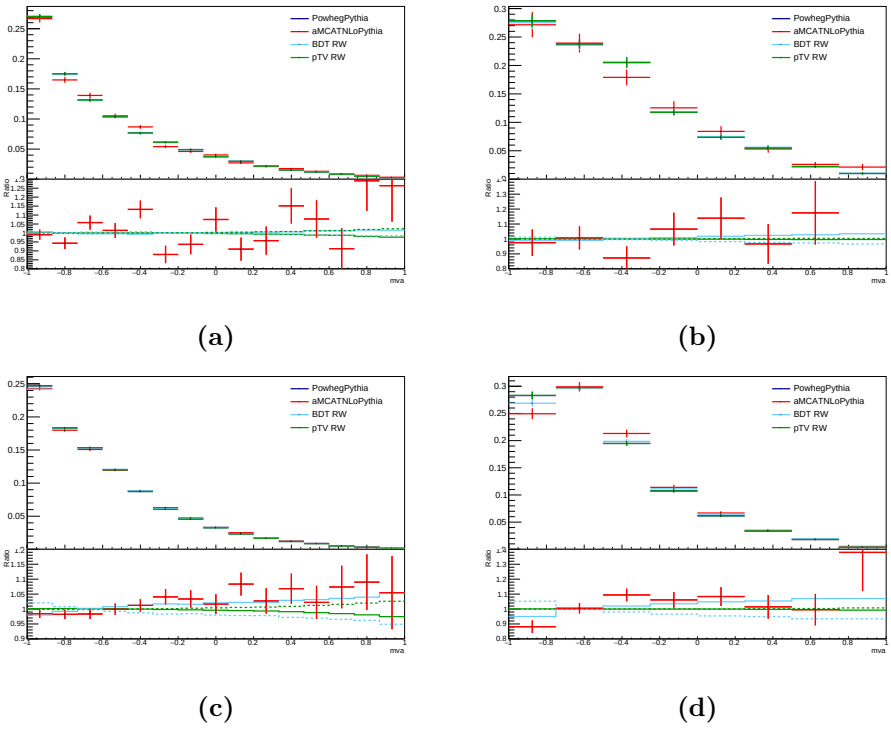

Figure 6.33 – Comparison of the 1-lepton BDT discriminant after transformation in the 2-jet 150 GeV $< p_T^V <$ 250 GeV (a) and $p_T^V >$ 250 GeV (b), 3-jet 150 GeV $< p_T^V <$ 250 GeV (c) and $p_T^V >$ 250 GeV (d) regions showing the nominal distribution in blue, the ME variation in blue, the BDT-based systematic uncertainties in cyan and the p_T^V based systematic in green. The bottom pad shows the ratio of the variation with respect to the nominal. The dashed lines correspond to the symmetrised variation.

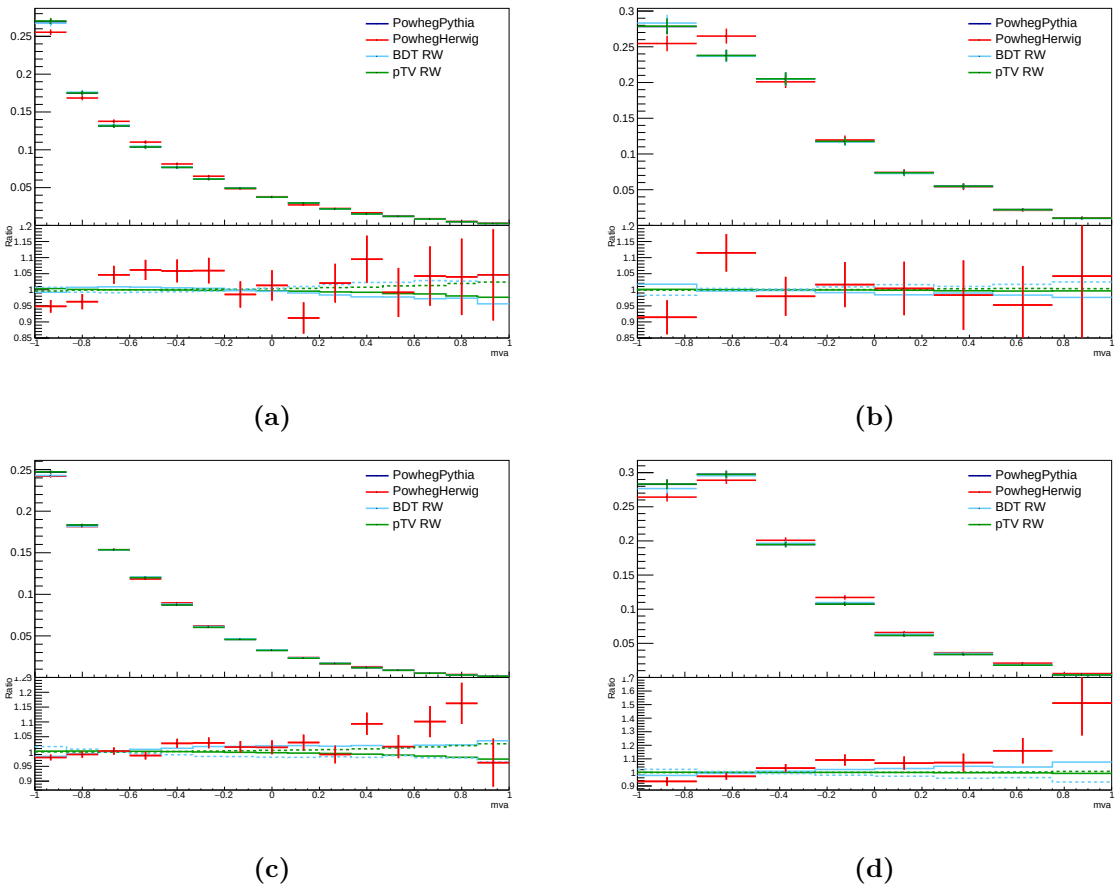

Figure 6.34 – Comparison of the 1-lepton BDT discriminant after transformation in the 2-jet 150 GeV $< p_T^V <$ 250 GeV (a) and $p_T^V >$ 250 GeV (b), 3-jet 150 GeV $< p_T^V <$ 250 GeV (c) and $p_T^V >$ 250 GeV (d) regions showing the nominal distribution in blue, the PS variation in blue, the BDT-based systematic uncertainties in cyan and the p_T^V based systematic in green. The bottom pad shows the ratio of the variation with respect to the nominal. The dashed lines correspond to the symmetrised variation.

Chapter 7

Statistical Analysis

This Chapter is dedicated to the global likelihood fit procedure, used to obtain the $VH, H \to b\bar{b}$ results using 139 fb^{-1} data. First, the profile likelihood function is presented in Section 7.1, which includes a detailed description of the binned maximum likelihood fit used to extract the signal yield, significance and signal strength. In Section 7.2 the VHbb nuisance parameters scheme is presented followed by an introduction of the Asimov dataset in Section 7.3, the analysis fit strategy in Section 7.4 and finally the MVA, di-jet mass and diboson analyses fit results in Section 7.5.

7.1 The profile likelihood function

The signal strength μ is the quantity measured to compare the observed signal yield to the expected yield given by a certain theory. In the VHbb analysis, this parameter of interest is used to compare the signal rate from the data collected by the experiment to the Standard Model prediction. It is the ratio of the observed signal corresponding to the cross-section of the VH production mode multiplied by the branching ratio of the $H \to b\bar{b}$ decay to the Standard Model values:

$$\mu = \frac{\sigma \times BR}{\sigma_{\text{SM}} \times BR_{\text{SM}}} \tag{7.1}$$

The signal strength is a parameter of the model, corresponding respectively to μ =1 which indicates that the observation matches the prediction and μ =0 which indicates that there is no observed signal. The μ value is estimated from a binned likelihood fit simultaneously across the three analysis channels and across the analysis regions as described in Section 5.7.4. The binned likelihood fit function is described as the product of Poisson probabilities over all the histogram bins:

$$\mathcal{L}(\mu) = \prod_{i=1}^{N_{bins}} \frac{(\mu s_i + b_i)^{n_i}}{n_i!} e^{-(\mu s_i + b_i)} \tag{7.2}$$

where s_i is the amount of signal and b_i is the amount of background within the bin i and n_i is the number of observed data events. The binned likelihood function must contain all aspects of the analysis. Therefore it should also include all sources of systematic uncertainties to be accounted for in the statistical test. The systematic uncertainties are incorporated in the

likelihood function to make the modelling more accurate. The complete likelihood function is then modified to include a set of nuisance parameters θ to be written as:

$$\mathcal{L}(\mu,\theta) = \prod_{i=1}^{N_{bins}} \frac{(\mu s_i(\theta) + b_i(\theta))^{n_i}}{n_i!} e^{-(\mu s_i(\theta)+b_i(\theta))} \times \mathcal{L}_{aux}(\theta) \tag{7.3}$$

The θ correspond to all the modelling and experimental uncertainties described in the previous Chapters that have an impact on the signal and background yields. They also include the so-called floated normalisations of the $t\bar{t}$ and V+jets backgrounds, which are set only from the likelihood fit to data. The profile likelihood function contains an additional $\mathcal{L}_{aux}(\theta)$ auxiliary term which is is the product of Gaussian distributions:

$$\mathcal{L}_{aux}(\theta) = \prod_{j=1}^{N_{syst}} \frac{1}{\sigma_j\sqrt{2\pi}} \times e^{\frac{-(\bar{\theta}_j-\theta_j)^2}{2\sigma_j^2}} \tag{7.4}$$

The auxiliary likelihood function represents the uncertainty assigned on the parameters coming from auxiliary measurements (constraints) from fitting the model to data. No auxiliary likelihood function is attributed to the floated background normalisations. The Gaussian probability density functions constrain the nuisance parameters around their central values $\bar{\theta}_j$ in the up and down direction. The $\bar{\theta}_j$ is set to 0 for all nuisance parameters.

The result of the fit is obtained by maximising the likelihood function with respect to all the parameters. The profile likelihood ratio is computed to test a hypothesis and is defined as the ratio between the likelihood function maximised for a set of θ parameters for a given μ value and the likelihood fit maximised to both the θ and μ:

$$\lambda(\mu) = \frac{\mathcal{L}(\mu,\hat{\hat{\theta}}(\mu))}{\mathcal{L}(\hat{\mu},\hat{\theta}(\hat{\mu}))} \tag{7.5}$$

where $\hat{\mu}$ and $\hat{\theta}$ are the maximum likelihood estimators and $\hat{\hat{\theta}}$ is the best fit value that maximises the likelihood for a certain μ value. Furthermore $\lambda(\mu)$ should satisfy the requirement of $0 \leq \lambda(\mu) \leq 1$ where $\lambda(\mu) = 0$ corresponds to the poorest agreement between the data and the hypothesised value of μ. The level of compatibility between the data and the test hypothesis can therefore be computed from:

$$t_\mu = -2\ \ln\lambda(\mu) \tag{7.6}$$

Where a higher value of t_μ implies a higher incompatibility between the data and the tested hypothesis. The q_0 test statistic is built to test the compatibility between the background-only hypothesis ($\mu = 0$) and the data using the following:

$$q_0 = \begin{cases} -2\,ln\,\lambda(0) & \hat{\mu} \geq 0 \\ 0 & \hat{\mu} < 0 \end{cases} = \begin{cases} -2\,ln\frac{\mathcal{L}(0,\hat{\hat{\theta}}(0))}{\mathcal{L}(\hat{\mu},\hat{\theta}(\hat{\mu}))} & \hat{\mu} \geq 0 \\ 0 & \hat{\mu} < 0 \end{cases} \tag{7.7}$$

The requirement of having $\hat{\mu} \geq 0$, for which the test statistics is non zero, is a physics motivated assumption and indicates that the disagreement between the data and the background-only

hypothesis is only considered for a non negative signal strength fluctuation. The incompatibility between the two hypotheses can be expressed in terms of a p-value following:

$$p_0 = \int_{q_{0,obs}}^{\infty} f(q_0|0, \hat{\hat{\theta}}(0))dq_0 \tag{7.8}$$

where $f(q_0|0, \hat{\hat{\theta}}(0))$ is the expected distribution of the test statistics under the assumption of the background-only hypothesis and $q_{0,obs}$ is the value of the test statistics from the observed data. The p_0 can be expressed in terms of the significance Z [114] in units of the number of Gaussian distribution standard deviations (σ) and corresponding to the integral of the tail distribution above the measured p-value as shown in Figure 7.1 and following:

$$Z = \Phi^{-1}(1 - p_0) = \sqrt{q_{0,obs}} \tag{7.9}$$

with Φ being the cumulative distribution of the Gaussian distribution. Depending on the value of p_0, the $\mu = 0$ hypothesis is rejected in favor of the $\mu \neq 0$ hypothesis. Conventionally, the $Z = 3\sigma$ fixed threshold (corresponding to $p_0 = 1.35 \times 10^{-4}$) was chosen so that the analysis can claim an evidence of the signal and the $Z = 5\sigma$ threshold [115] (corresponding to $p_0 = 2.87 \times 10^{-7}$) for the analysis to claim an observation of the signal.

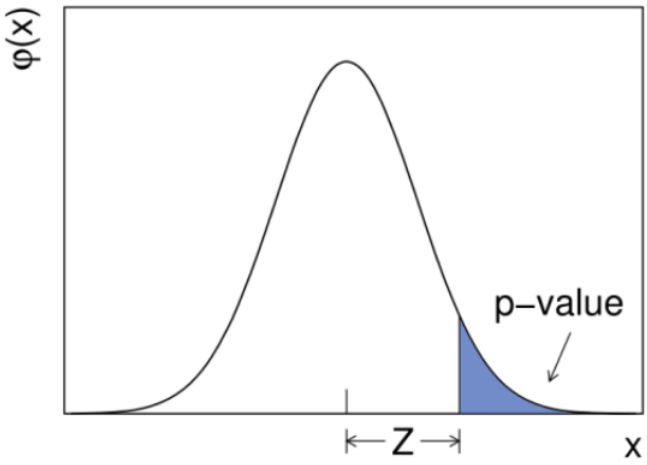

Figure 7.1 – Distribution showing the relation between the significance Z and the one tailed p-value. It corresponds to a Gaussian distribution of $\mu = 0$ and $\sigma = 1$.

7.2 The nuisance parameters

The systematic uncertainties are stored as additional histograms to the nominal distributions to be included in the likelihood fit. The advantage of using a profile likelihood fit, is that the fit to data could provide additional information on these systematic uncertainties. It is a response model that consists of finding the best model of systematic uncertainties that describes the data. In the fit, the nuisance parameters can be displaced ("pulled") in the upward or the downward direction to maximise the agreement between the data and the predictions. In addition, the uncertainties on these nuisance parameters can be reduced from their initial value. This reduction is referred to as constraining the systematic uncertainties. The constraining of a certain nuisance parameter happens when the fitted data is sufficiently precise to provide additional information to the prior knowledge on the nuisance parameter. Even though this reduction in the effect of systematic uncertainties effect improves the analysis sensitivity, it

is crucial to check that the observed constraints are legitimate and do not come from a bad modelling of the systematic uncertainty, or from an incomplete fit model that lacks additional degreed of freedom. Such constraints coming from issues in the fit model are referred to as over-constraints. The line between legitimate constraints and over-constraints is ofter blurry, and detailed study comparing different but similar models are done to be convinced that the constraints are genuine.

The nuisance parameters describing different systematic effects should be treated as separate parameters and this is referred to as uncorrelating the nuisance parameters. In addition, correlations between two (or more) nuisance parameters might arise in the fit. These correlations introduced in the fit to data and occur when the behavior of a certain nuisance parameter is affected by the behavior of the others when describing the same data. This leads to a large uncertainty caused by these parameters. Thus, one should decide whether to decorrelate these nuisance parameters across the channels or the analysis regions or to leave them correlated in the fit model. Therefore, it is crucial to lead dedicated studies to understand all these correlations and to decide on the fit model. This is necessary so as not to create a bias in the fit coming from the pulls and constraints of one nuisance parameter affecting the others. At the same time, de-correlating all the nuisance parameters across categories is a very conservative approach in the case of the $VH(H \to b\bar{b})$ analysis, as the correlations are between the signal and the control regions which allows to create large constraints and to control the systematic uncertainties. The final fit model is decided on after evaluating all the correlations of the nuisance parameters and ensuring that the fit model is correct.

In the final fit model, a pruning approach is used to remove all nuisance parameters with insignificant impact on the fit results. In addition, two smoothing algorithms are implemented to smooth the variations across the distributions entering the fit. The results of the fit are checked at every iteration to refine the model to be sure that the results of pruning and smoothing are correct and that the nuisance parameters are behaving reasonably.

7.2.1 Smoothing of uncertainties

The uncertainties associated with the reconstruction of objects such as: E_T^{miss}, muons, taus, jets, pile-up, e-γ, JVT in addition to the multi-jet systematic uncertainties are propagated with two different ways: by shifting event weights to compute the acceptance uncertainties or by modifying the kinematic properties of the objects and re-running the analysis chain. The first approach is used for uncertainties such as the b-tagging uncertainties where a scale factor is applied to correct the simulation efficiency to match that of data. These weights correspond to a scale factor shift in the upward and downward direction and are propagated to the final discriminant as a $+1\sigma$ and -1σ variation. The second approach is applied for uncertainties such as the jet energy scale (JES), since the changes of the energy scale cannot be estimated using efficiency scale factors. When the JES is shifted, the events can migrate in and out of the analysis acceptance or between analysis bins. These uncertainties are also propagated to the final discriminant as $\pm 1\sigma$ variations. The Monte Carlo statistics can have a considerable impact on the precision of these variations in case of limited Monte Carlo statistics and/or small systematic variations. For this reason, it is necessary to smooth out these statistical effects to not create spurious effects in the likelihood fit.

Two smoothing algorithms are used, in sequence, to reduce these effects by merging consecutive bins of the Monte Carlo templates. The first algorithm consists of merging bins iteratively, between two extrema of the distributions, until there is no local extremum or at most one extremum when treating the jet energy resolution systematic uncertainties or when using the m_{bb} template in the di-jet mass analysis. At each step of the iterative procedure, the merging is done to have the smallest difference between the merged and the unmerged templates.

The second algorithm consists of taking the binned template resulting from the first algorithm and merging the bins together to reduce the statistical uncertainties to less than 5% in each bin, starting from the left of the distribution and moving towards the right bins. The nominal and the shifted distributions are compared in each merged bins to give a variation of $\pm 1\sigma$. The resulting variation is associated to all the bins in the distribution.

7.2.2 Pruning of uncertainties

A large number of uncertainties are considered on the discriminant distributions used in the fit. Many of these uncertainties have a negligible impact on the final result such that removing them from the model allows to save time. The analysis follows a pruning procedure to discard a systematic uncertainty if it satisfies one of the requirements in one of the analysis categories:

- Normalisation uncertainties are ignored if they give a relative variation smaller than 0.5% or if the up and down variations have the same sign.
- Shape uncertainties are neglected if they do not provide a variation of more than 0.5% in all of the bins of the distribution or if the variation is only in one direction (either the up or the down variation is null).
- Uncertainties are pruned in regions where at least one bin has a signal yield more than 2% of the total backgrounds if the normalisation and the shape variations have an effect of less than 2% of the signal contribution in these bins.

7.2.3 Quantifying the impact of systematic uncertainties on the measurement

When building a response model to describe the data, the nuisance parameters are not fixed but rather move according to the fit. In the profile likelihood fit, these nuisance parameters have an impact on the signal measurement and their effect is propagated to the total uncertainty on the best fit value $\hat{\mu}$.

Given the correlations between the nuisance parameters that appear during the fit, the quantification of the impact of individual systematic uncertainties on the result can be considered in several ways. In the analysis, this impact is presented in two complementary ways: the ranking of systematic uncertainties which allows to illustrate which of the systematic uncertainties are the most important in the fit, and the breakdown of systematic uncertainties to illustrate the influence of a certain set of systematic uncertainties to the total uncertainty.

The ranking of systematic uncertainties shows the impact of individual nuisance parameters. It is done by fixing the value of all nuisance parameters to their values from the fit and then changing the value of individual nuisance parameters to both their up and down uncertainty before performing the fit again to assess the individual impact on $\hat{\mu}$. The difference between the new value of μ and the value of $\hat{\mu}$ is taken as the impact of the individual nuisance parameter on the measurement.

In the breakdown method, the impact of a single nuisance parameter is evaluated by repeating the fit and measuring the new μ value after removing this nuisance parameter. The fit gives a new total uncertainty, which is then subtracted quadratically from the total uncertainty of the measured $\hat{\mu}$ to get the impact of the nuisance parameter.

7.3 The Asimov dataset

The Asimov fit is used to understand the systematic model independently from the data. The Asimov dataset [114] suppresses all statistical fluctuations and allows to represent the expectations from the model. It is obtained from replacing the real data with a dataset built from Monte Carlo simulations. The Asimov dataset is used to evaluate the Asimov likelihood and the corresponding profile likelihood ratio to compute the expected (median) p-value and expected significance. By definition, the data statistical fluctuations are suppressed in the Asimov fit and the evaluation of all the parameters gives their input value. Therefore all the nuisance parameters pulls should be null. However in the data fit, some pulls are expected and they can be significant. When the nuisance parameters are significantly pulled, or when the constraints or the correlations are significantly different from the Asimov fit, the nuisance parameters scheme and the individual parameters are carefully studied.

7.4 The analysis fit strategy

The analysis strategy towards measuring the signal is based on three steps to validate the results.

- The first step, consists on blinding the data in the right-most bins in the BDT distribution and the bins in the m_{bb} distribution in the 80-150 GeV mass window, which does not bias the tests conducted to understand the fit. A conditional fit to data is then performed by fixing the value of μ to 1, to study the fit model. The discriminant variables deployed in each of the categories for the fit are shown in Table 7.1. During this step, the MVA, the di-jet mass and the diboson fits are studied in parallel and the nuisance parameters behavior is compared between these three fits. Thereby the model can change, by adding or removing nuisance parameters from the fit model or changing their correlations. The details of the $t\bar{t}$ background modeling presented in the Chapter 6 were thus finalised by studying the behavior of this model in the different analysis regions.
- Once the model is decided upon, it is allowed to proceed to the second step where the remaining bins are unblinded in the diboson fit and a fit (μ floating) is performed to check the compatibility of the background modelling with the data.
- Finally, when the results of the diboson fit are trustworthy, the BDT_{VH} and the m_{bb} distributions are fully unblinded to measure the signal strength and the significance.

Channel	Region	Categories					
		75 GeV $< p_{\mathrm{T}}^{V} <$ 150 GeV		150 GeV $< p_{\mathrm{T}}^{V} <$ 250 GeV		$p_{\mathrm{T}}^{V} >$ 250 GeV	
		2-jet	3-jet	2-jet	3-jet	2-jet	3-jet
0-lepton	low ΔR CR	–	–	yields	yields	yields	yields
	SR	–	–	BDT or m_{bb}	BDT or m_{bb}	BDT or m_{bb}	BDT or m_{bb}
	high ΔR CR	–	–	yields	yields	yields	yields
1-lepton	low ΔR CR	–	–	yields	yields	yields	yields
	SR	–	–	BDT or m_{bb}	BDT or m_{bb}	BDT or m_{bb}	BDT or m_{bb}
	high ΔR CR	–	–	yields	yields	yields	yields
2-lepton	low ΔR CR	yields	yields	yields	yields	yields	yields
	SR	BDT or m_{bb}	BDT or m_{bb}	BDT or m_{bb}	BDT or m_{bb}	BDT or m_{bb}	BDT or m_{bb}
	high ΔR CR	yields	yields	yields	yields	yields	yields

Table 7.1 – Discriminant variables fitted in each of the event categories in the 0-, 1- and 2-lepton channels.

7.5 VH, $H \to b\bar{b}$ results

In this Section are presented the results of the main multivariate analysis using full Run-2 data corresponding to 139 fb^{-1} [116]. In addition, the results of the diboson analysis and the di-jet mass analyses are discussed.

7.5.1 Diboson analysis

The diboson analysis provides a technical validation for the Higgs boson MVA results, where the diboson signal strength is measured in a fit very similar to that of the MVA, but using the BDT$_{VZ}$ output instead of the BDT$_{VH}$. The measured signal strength in the combined fit is in good agreement with the Standard Model predication with a value of:

$$\mu_{VZ}^{bb} = 0.93^{+0.15}_{-0.14} = 0.93^{+0.07}_{-0.06}(\text{Stat})^{+0.14}_{-0.12}(\text{Syst})$$

The post-fit BDT$_{VZ}$ distributions used in the fit are shown in Figures 7.3, 7.4 and 7.5. The corresponding observed and expected significances are above 10σ. A combined fit with WZ and ZZ processes measured independently was also performed and the results are shown in Figure 7.2.

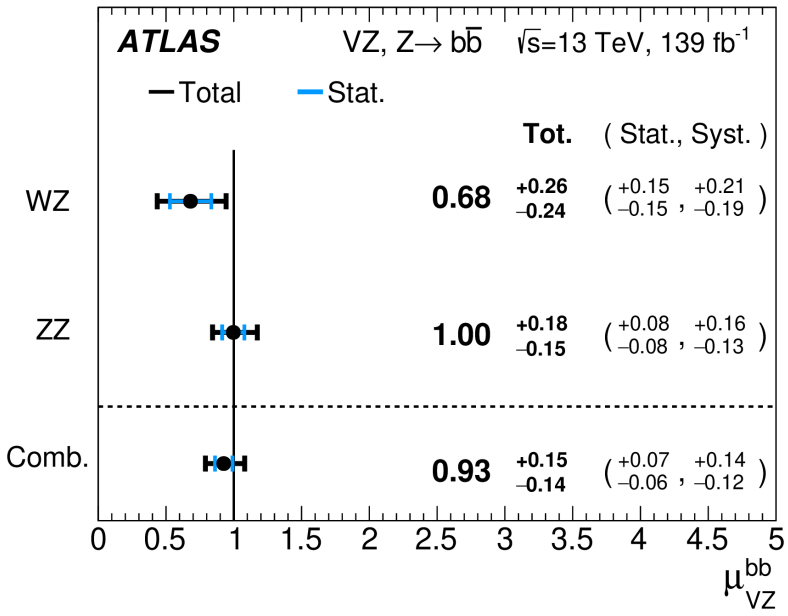

Figure 7.2 – The signal strength values for the WZ and ZZ processes and their combination.

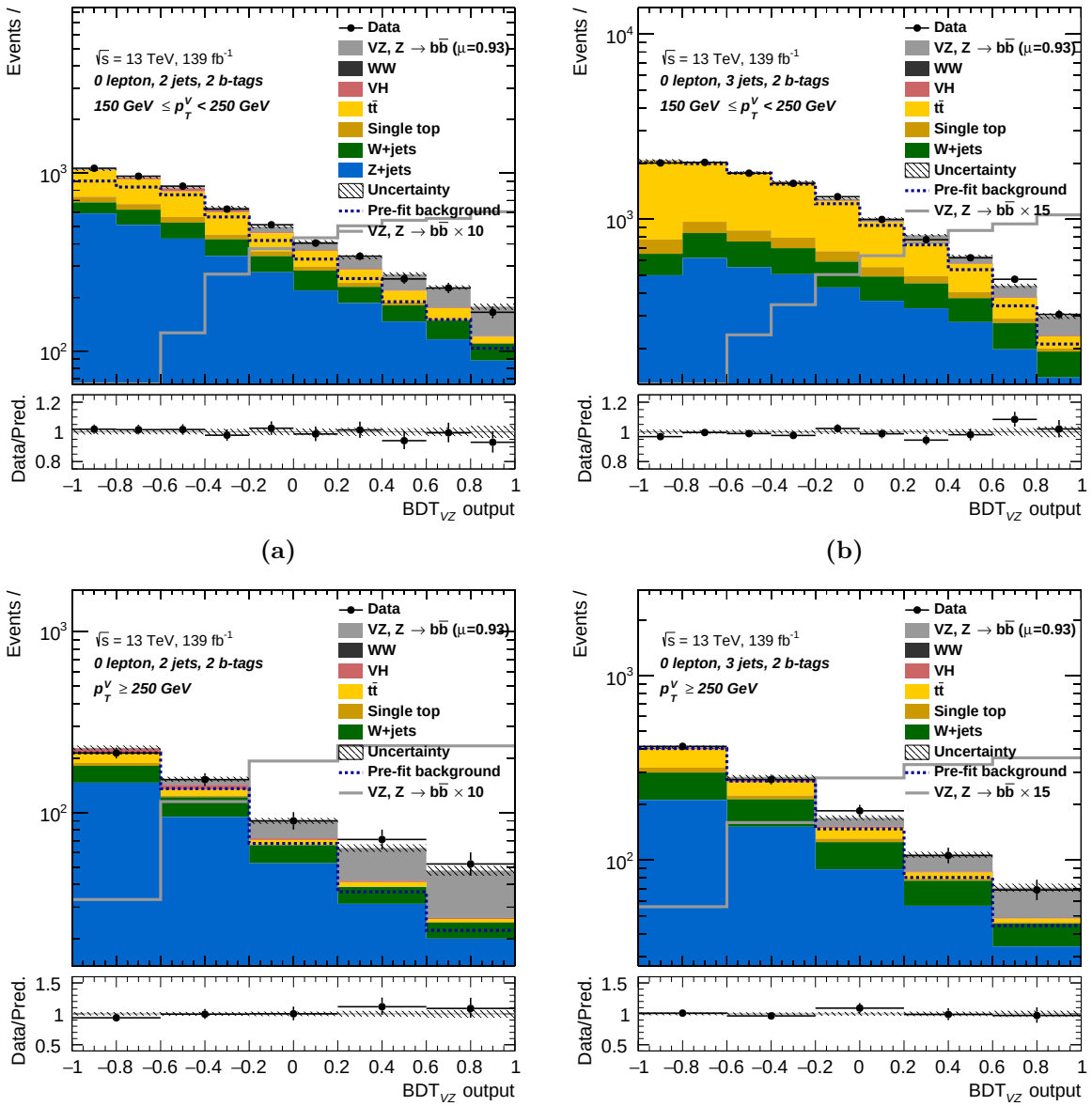

Figure 7.3 – The BDT_{VZ} post-fit distributions in the 0-lepton channel resulting from the global fit in the signal region 2-jet $150 < p_T^V < 250\,\mathrm{GeV}$ (a), 3-jet $150 < p_T^V < 250\,\mathrm{GeV}$ (b), 2-jet $p_T^V > 250\,\mathrm{GeV}$ (c), 3-jet $p_T^V > 250\,\mathrm{GeV}$ (d) regions. The background contributions after the global likelihood fit are shown as filled histograms. The diboson signal is shown as a filled histogram on top of the fitted backgrounds normalised to the signal yield extracted from data ($\hat{\mu} = 0.93$), and unstacked as an unfilled histogram, scaled by the factor indicated in the legend. The dashed histogram shows the total pre-fit background. The size of the combined statistical and systematic uncertainty for the sum of the fitted signal and background is indicated by the hatched band. The ratio of the data to the sum of the fitted signal ($\hat{\mu} = 0.93$) and background is shown in the lower panel.

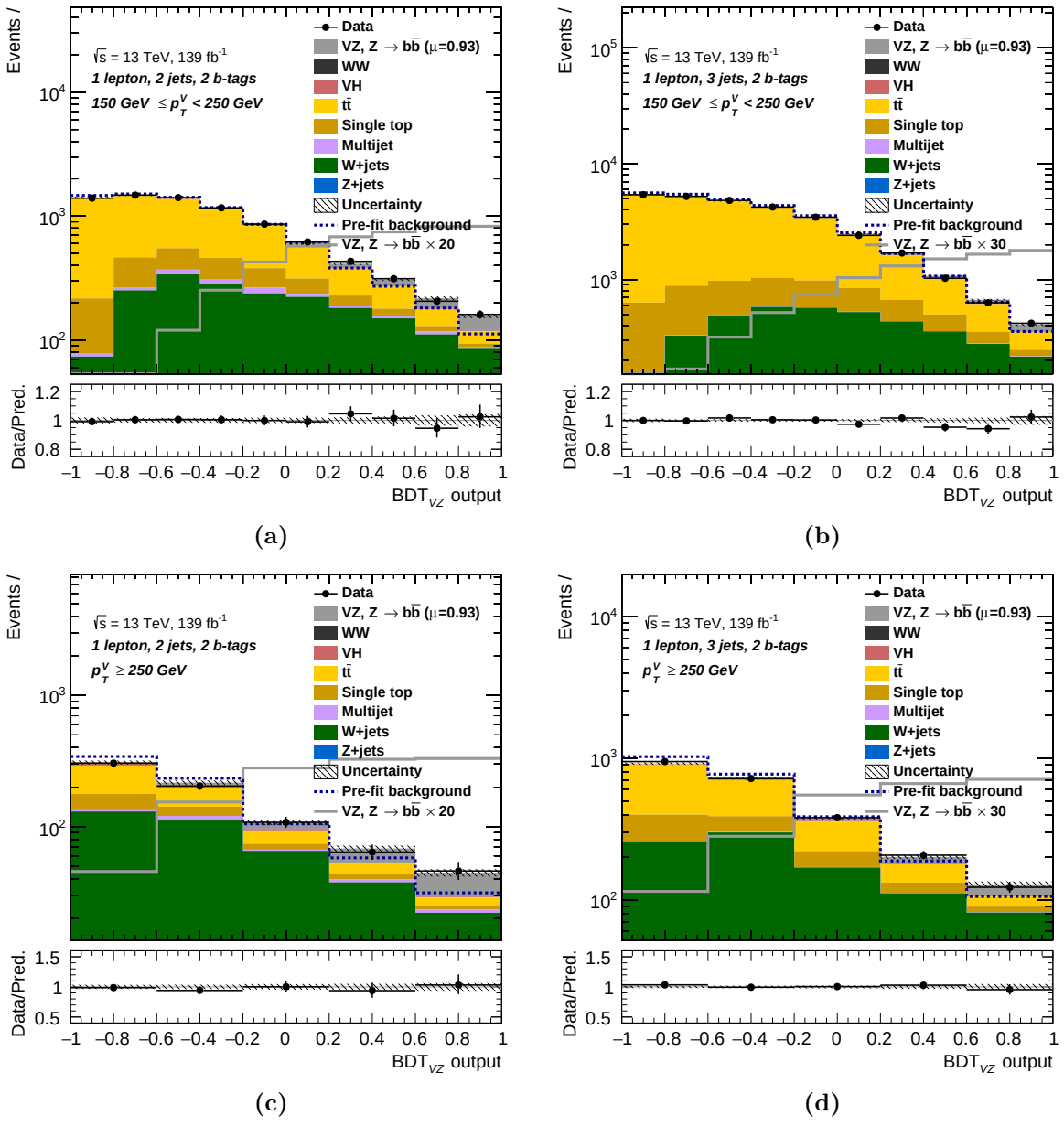

Figure 7.4 – The BDT_{VZ} post-fit distributions in the 1-lepton channel resulting from the global fit in the signal region 2-jet $150 < p_T^V < 250\,\mathrm{GeV}$ (a), 3-jet $150 < p_T^V < 250\,\mathrm{GeV}$ (b), 2-jet $p_T^V > 250\,\mathrm{GeV}$ (c), 3-jet $p_T^V > 250\,\mathrm{GeV}$ (d) regions. The background contributions after the global likelihood fit are shown as filled histograms. The diboson signal is shown as a filled histogram on top of the fitted backgrounds normalised to the signal yield extracted from data ($\hat{\mu} = 0.93$), and unstacked as an unfilled histogram, scaled by the factor indicated in the legend. The dashed histogram shows the total pre-fit background. The size of the combined statistical and systematic uncertainty for the sum of the fitted signal and background is indicated by the hatched band. The ratio of the data to the sum of the fitted signal ($\hat{\mu} = 0.93$) and background is shown in the lower panel.

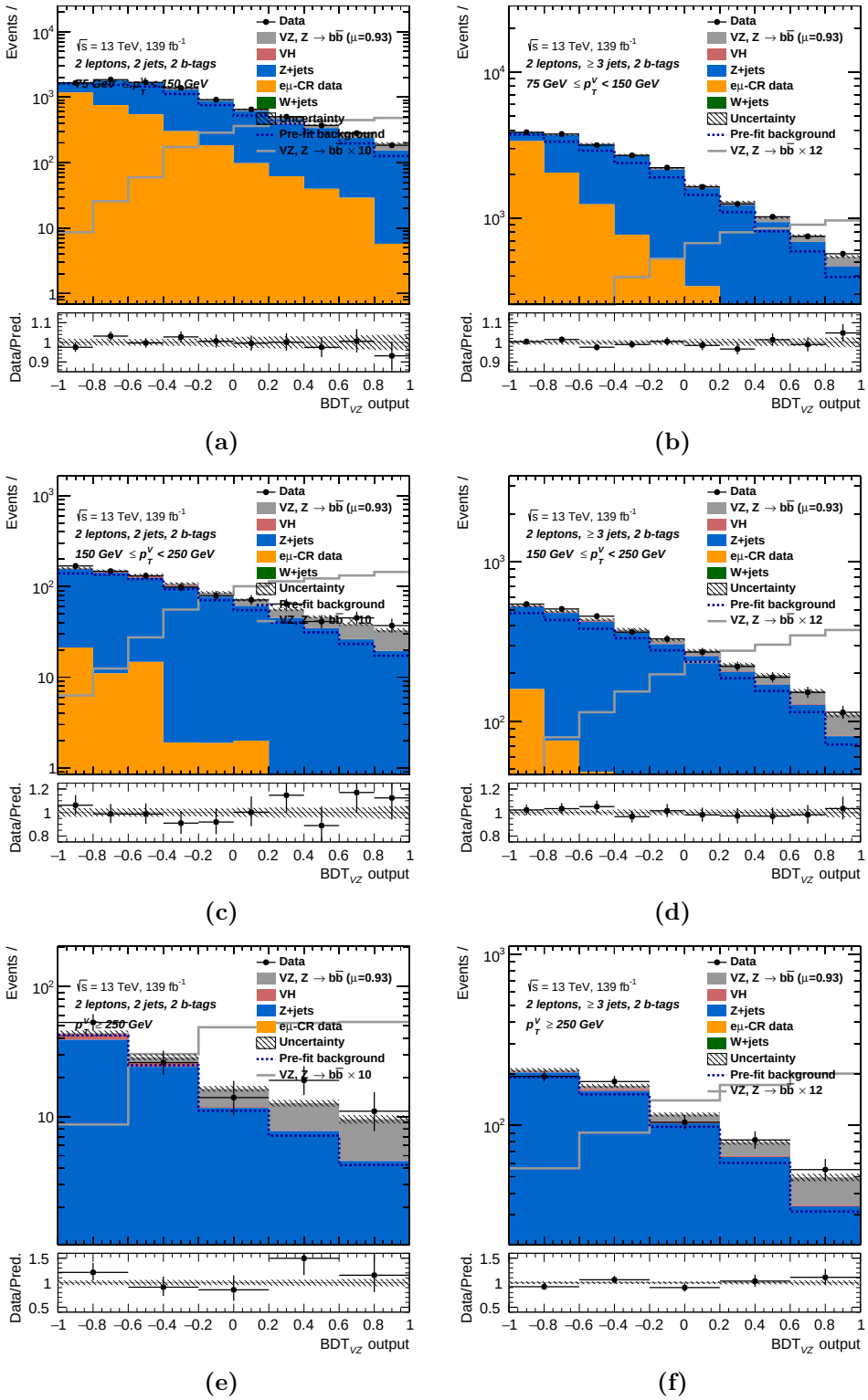

Figure 7.5 – The BDT$_{VZ}$ post-fit distributions in the 2-lepton channel resulting from the global fit in the signal region 2-jet $75 < p_T^V < 150$ GeV (a), 2-jet $75 < p_T^V < 150$ GeV (b), 2-jet $150 < p_T^V < 250$ GeV (c), 3-jet $150 < p_T^V < 250$ GeV (d), 2-jet $p_T^V > 250$ GeV (e), 3-jet $p_T^V > 250$ GeV (f) regions. The background contributions after the global likelihood fit are shown as filled histograms. The diboson signal is shown as a filled histogram on top of the fitted backgrounds normalised to the signal yield extracted from data ($\hat{\mu} = 0.93$), and unstacked as an unfilled histogram, scaled by the factor indicated in the legend. The dashed histogram shows the total pre-fit background. The size of the combined statistical and systematic uncertainty for the sum of the fitted signal and background is indicated by the hatched band. The ratio of the data to the sum of the fitted signal ($\hat{\mu} = 0.93$) and background is shown in the lower panel.

7.5.2 Multivariate analysis

Post-fit yields and distributions

The analysis results are obtained from a global fit to the data collected by the ATLAS detector, for a Higgs boson mass of 125 GeV. The fit, called the combined fit, is performed simultaneously in the three lepton channels and in all the analysis regions to the BDT_{VH} distribution in the signal region and the yields in the control regions. The post-fit normalisation factors of the floated background normalisations, obtained for the best fit values of μ and θ are presented in Table 7.2. The data yields and the signal and background post-fit yields in each analysis regions are presented in Tables 7.3 to 7.9.

The post-fit distributions consist of applying these normalisation factors to the Monte Carlo templates, as well as the impact of the pulls of the uncertainties to compare their agreement with the data. The BDT_{VH} output post-fit distributions with the binning used in the global likelihood fit are shown in Figures 7.6, 7.7 and 7.8. The BDT_{VH} discriminant is combined in the signal regions across all the categories, as presented in Figure 7.10, to show the data yields, the signal (S) and background (B) yields resulting from the combined fit, in bins of $\log_{10}(\mathrm{S/B})$.

The agreement between the data and the post-fit model resulting from the combined fit can be evaluated from other kinematic distributions. Figure 7.9 shows the post-fit distributions of some of the kinematic variables used in the BDT_{VH} training. The data is in excellent agreement with the post-fit Monte Carlo predictions and no mis-modelling was observed in any of the distributions inspected.

Process and Category	Normalisation factor
$t\bar{t}$ 2-jet	0.98 ± 0.09
$t\bar{t}$ 3-jet	0.93 ± 0.06
$W+$ heavy flavors 2-jet	1.06 ± 0.11
$W+$ heavy flavors 3-jet	1.15 ± 0.09
$Z+$ heavy flavors 2-jet, $75 < p_T^V < 150$ GeV	1.28 ± 0.08
$Z+$ heavy flavors 3-jet, $75 < p_T^V < 150$ GeV	1.17 ± 0.05
$Z+$ heavy flavors 2-jet, $p_T^V > 150$ GeV	1.16 ± 0.07
$Z+$ heavy flavors 3-jet, $p_T^V > 150$ GeV	1.09 ± 0.04

Table 7.2 – The normalisation factors obtained from the global likelihood fit. The uncertainties correspond to the combined statistical and systematic uncertainties. The Z+jets simulation predicts less events then what is observed, similarly to what is observed in Standard Model analysis measurements of Z+bb [117].

	2-jet			3-jet		
	Low ΔR CR	SR	High ΔR CR	Low ΔR CR	SR	High ΔR CR
Zl	2 ± 1.4	4 ± 2.7	5.2 ± 3.5	2.1 ± 1.5	5.4 ± 3.7	8.5 ± 5.8
Zcl	6.7 ± 3	17.1 ± 7.6	20.1 ± 8.7	7.9 ± 3.5	25 ± 11	37 ± 16
Zhf	1083 ± 37	2825 ± 81	3364 ± 85	1405 ± 60	3800 ± 160	4840 ± 190
Wl	1.9 ± 1.4	4.7 ± 3.1	8.5 ± 5.2	2.4 ± 1.7	7 ± 4.8	13.6 ± 8.6
Wcl	6.1 ± 3.1	17.4 ± 8.5	25 ± 11	7.9 ± 4.1	28 ± 14	48 ± 22
Whf	478 ± 33	612 ± 63	275 ± 57	895 ± 57	1460 ± 110	775 ± 81
single top	33.8 ± 5.8	237 ± 35	288 ± 44	95 ± 18	770 ± 130	1140 ± 200
ttbar	154 ± 13	1157 ± 76	1193 ± 81	566 ± 36	5470 ± 220	8600 ± 300
diboson	39.8 ± 8.5	360 ± 55	9.05 ± 0.53	42 ± 11	333 ± 79	50.2 ± 2.1
Total Bkg	1806 ± 34	5234 ± 63	5188 ± 63	3024 ± 46	11907 ± 97	15510 ± 120
Signal	3.2 ± 1.2	147 ± 24	7.1 ± 1.3	4.6 ± 2.2	130 ± 22	20 ± 4.2
S/B	1.76e-03	2.81e-02	1.38e-03	1.52e-03	1.09e-02	1.29e-03
$S/\sqrt{S+B}$	7.49e-02	2.00	9.91e-02	8.34e-02	1.19	1.61e-01
data	1802	5397	5273	3034	11875	15663

Table 7.3 – The post-fit yields, S/B and $S/\sqrt{S+B}$ for the 0-lepton channel analysis categories in the 150 GeV< p_T^V <250 GeV region. The uncertainty shown in this table is of statistical nature only.

	2-jet			3-jet		
	Low ΔR CR	SR	High ΔR CR	Low ΔR CR	SR	High ΔR CR
Zl	0.099 ± 0.067	0.77 ± 0.52	1.5 ± 1	0.22 ± 0.15	1.11 ± 0.75	2.9 ± 2
Zcl	0.28 ± 0.12	2.5 ± 1.1	4.7 ± 2	0.71 ± 0.31	4.1 ± 1.8	10.7 ± 4.7
Zhf	55.2 ± 3.4	335 ± 13	575 ± 18	116.7 ± 5.8	528 ± 24	1038 ± 41
Wl	0.064 ± 0.046	0.48 ± 0.35	1.21 ± 0.81	0.15 ± 0.11	0.75 ± 0.54	2.5 ± 1.7
Wcl	0.178 ± 0.092	1.61 ± 0.83	3.7 ± 1.8	0.52 ± 0.27	2.9 ± 1.5	8.2 ± 4
Whf	17 ± 2	81 ± 9.4	47.5 ± 9.8	61.6 ± 5.7	217 ± 20	188 ± 21
single top	0.652 ± 0.033	9.1 ± 2.1	28.2 ± 6.1	3.08 ± 0.82	36.3 ± 8	134 ± 33
ttbar	1.8 ± 0.31	38.6 ± 4.8	62.3 ± 8.2	9.8 ± 1.1	151 ± 16	625 ± 45
diboson	7.8 ± 1.6	86 ± 13	2.88 ± 0.19	11.1 ± 2.8	70 ± 17	18.3 ± 4.5
Total Bkg	83.1 ± 4.2	554 ± 15	727 ± 18	203.8 ± 6.7	1011 ± 21	2028 ± 32
Signal	0.5 ± 0.12	39.9 ± 6.3	1.89 ± 0.4	1.38 ± 0.39	33 ± 5.5	6.3 ± 1.4
S/B	5.99e-03	7.20e-02	2.60e-03	6.76e-03	3.27e-02	3.10e-03
$S/\sqrt{S+B}$	5.44e-02	1.64	7.01e-02	9.61e-02	1.02	1.39e-01
data	72	578	730	210	1046	2011

Table 7.4 – The post-fit yields, S/B and $S/\sqrt{S+B}$ for the 0-lepton channel analysis categories in the p_T^V >250 GeV region. The uncertainty shown in this table is of statistical nature only.

	2-jet			3-jet		
	Low ΔR CR	SR	High ΔR CR	Low ΔR CR	SR	High ΔR CR
Zl	0.122 ± 0.08	0.32 ± 0.19	0.86 ± 0.46	0.19 ± 0.12	0.59 ± 0.36	1.78 ± 0.98
Zcl	0.34 ± 0.14	1.02 ± 0.39	2.25 ± 0.74	0.61 ± 0.26	2.1 ± 0.82	5.6 ± 1.9
Zhf	40.6 ± 2.5	100.8 ± 5.4	150.8 ± 7.6	77 ± 4.9	204 ± 11	349 ± 14
Wl	3.3 ± 2.5	6.4 ± 4.8	11.6 ± 8.5	4.3 ± 3.2	10.5 ± 7.8	24 ± 18
Wcl	16.5 ± 8.7	46 ± 24	75 ± 39	22 ± 11	72 ± 38	153 ± 80
Whf	1302 ± 63	1800 ± 160	1100 ± 220	2370 ± 120	4000 ± 270	3120 ± 370
single top	128 ± 26	990 ± 160	1750 ± 290	444 ± 86	3570 ± 600	8500 ± 1500
ttbar	624 ± 35	4600 ± 210	7180 ± 350	2460 ± 100	21030 ± 620	56200 ± 1500
diboson	24.2 ± 6.8	229 ± 57	10.05 ± 0.74	42 ± 13	264 ± 83	84.4 ± 3.5
multijetEl	8 ± 13	15 ± 24	27 ± 42	6.63 ± 0.028	15 ± 14	30.222 ± 0.031
multijetMu	50 ± 18	114 ± 41	247 ± 88	4.011 ± 0.017	8.789 ± 0.016	24.042 ± 0.025
Total Bkg	2197 ± 44	7899 ± 82	10550 ± 97	5430 ± 68	29170 ± 170	68430 ± 260
Signal	2.2 ± 1.2	148 ± 24	8 ± 1.7	4.4 ± 2.3	125 ± 21	22.3 ± 4.2
S/B	9.98e-04	1.87e-02	7.56e-04	8.14e-04	4.30e-03	3.26e-04
$S/\sqrt{S+B}$	4.67e-02	1.64	7.76e-02	6.00e-02	7.33e-01	8.53e-02
data	2218	8044	10507	5456	29316	68450

Table 7.5 – The post-fit yields, S/B and $S/\sqrt{S+B}$ for the 1-lepton channel analysis categories in the 150 GeV< p_T^V <250 GeV region. The uncertainty shown in this table is of statistical nature only.

	2-jet			3-jet		
	Low ΔR CR	SR	High ΔR CR	Low ΔR CR	SR	High ΔR CR
Zl	0.0045 ± 0.0031	0.036 ± 0.023	0.2 ± 0.1	0.0143 ± 0.0093	0.071 ± 0.046	0.43 ± 0.24
Zcl	0.01 ± 0.0041	0.102 ± 0.042	0.39 ± 0.13	0.044 ± 0.017	0.225 ± 0.093	1.08 ± 0.37
Zhf	1.75 ± 0.22	10.2 ± 0.88	21.8 ± 1.5	6.04 ± 0.57	24.2 ± 1.6	57.7 ± 2.3
Wl	0.19 ± 0.14	1.5 ± 1.1	3.8 ± 2.8	0.48 ± 0.35	2.5 ± 1.8	9 ± 6.6
Wcl	0.73 ± 0.38	6.7 ± 3.5	15.5 ± 8.2	2 ± 1	11.7 ± 6.1	44 ± 22
Whf	71.1 ± 5.4	344 ± 34	268 ± 53	232 ± 14	921 ± 70	1070 ± 120
single top	2.57 ± 0.82	70 ± 15	326 ± 65	21.8 ± 5.3	313 ± 66	1780 ± 390
ttbar	6.34 ± 0.73	188 ± 19	974 ± 72	60.1 ± 4.1	970 ± 58	9060 ± 400
diboson	6.6 ± 1.9	57 ± 15	3.9 ± 0.33	13.6 ± 4.5	68 ± 22	42.5 ± 1.7
multijetEl	0.8 ± 1.2	5.9 ± 9	14 ± 21	1.246 ± 0.02	7.4 ± 8.3	18.5 ± 0.04
multijetMu	0	10.3 ± 4.7	32 ± 12	0.1826 ± 0.003	0	1.8539 ± 0.004
Total Bkg	90 ± 5.1	694 ± 23	1659 ± 35	338 ± 12	2318 ± 42	12080 ± 110
Signal	0.41 ± 0.14	52.2 ± 8.6	2.5 ± 0.5	1.8 ± 0.52	44.1 ± 7.4	7.7 ± 1.5
S/B	4.59e-03	7.52e-02	1.51e-03	5.32e-03	1.90e-02	6.38e-04
$S/\sqrt{S+B}$	4.34e-02	1.91	6.14e-02	9.76e-02	9.07e-01	7.01e-02
data	94	727	1686	339	2378	12059

Table 7.6 – The post-fit yields, S/B and $S/\sqrt{S+B}$ for the 1-lepton channel analysis categories in the p_T^V >250 GeV region. The uncertainty shown in this table is of statistical nature only.

	2-jet			≥3-jet		
	Low ΔR CR	SR	High ΔR CR	Low ΔR CR	SR	High ΔR CR
Zl	2.3 ± 1.6	4.1 ± 2.8	3.9 ± 2.7	4.6 ± 3.2	13.2 ± 9.2	18 ± 12
Zcl	10.1 ± 4.5	23 ± 10	18 ± 8	20.3 ± 9.1	75 ± 33	90 ± 40
Zhf	2086 ± 57	5870 ± 100	4284 ± 73	3777 ± 66	11550 ± 170	11040 ± 150
Whf	0.192 ± 0.02	1.27 ± 0.13	0.073 ± 0.019	3.05 ± 0.24	5.91 ± 0.45	3.18 ± 0.25
emuCRData	822 ± 29	3193 ± 57	1617 ± 41	1367 ± 36	8796 ± 87	6114 ± 77
diboson	16.17 ± 0.39	283 ± 47	8.33 ± 0.31	73 ± 13	443 ± 78	104.2 ± 3.6
Total Bkg	2937 ± 51	9378 ± 86	5931 ± 66	5245 ± 59	20880 ± 130	17370 ± 130
Signal	1.02 ± 0.69	78 ± 14	5.34 ± 0.97	6.1 ± 2.5	106 ± 21	22 ± 4.4
S/B	3.47e-04	8.37e-03	9.01e-04	1.16e-03	5.07e-03	1.27e-03
$S/\sqrt{S+B}$	1.88e-02	8.07e-01	6.93e-02	8.39e-02	7.31e-01	1.67e-01
data	2940	9463	5919	5275	20927	17443

Table 7.7 – The post-fit yields, S/B and $S/\sqrt{S+B}$ for the 2-lepton channel analysis categories in the 75 GeV< p_T^V <150 GeV region. The uncertainty shown in this table is of statistical nature only.

	2-jet			≥3-jet		
	Low ΔR CR	SR	High ΔR CR	Low ΔR CR	SR	High ΔR CR
Zl	0.35 ± 0.24	0.72 ± 0.49	1.33 ± 0.9	1.24 ± 0.86	3.4 ± 2.4	9.5 ± 6.5
Zcl	1.38 ± 0.61	3.6 ± 1.6	5.6 ± 2.5	5.1 ± 2.2	17.5 ± 7.8	48 ± 21
Zhf	252 ± 11	711 ± 19	1083 ± 26	919 ± 22	2478 ± 53	4456 ± 75
Whf	0.315 ± 0.032	0.316 ± 0.032	0.179 ± 0.018	0.751 ± 0.059	1.96 ± 0.15	1.6 ± 0.12
emuCRData	8.1 ± 2.8	51.9 ± 7.1	107 ± 10	53.5 ± 7.2	389 ± 19	934 ± 30
diboson	3.48 ± 0.73	83 ± 14	2.54 ± 0.12	28.3 ± 5	169 ± 30	63 ± 12
Total Bkg	265 ± 11	851 ± 19	1199 ± 25	1008 ± 20	3058 ± 44	5513 ± 66
Signal	0.34 ± 0.24	34.1 ± 6.4	2.26 ± 0.45	2.5 ± 1.3	59 ± 12	18.8 ± 4.7
S/B	1.27e-03	4.01e-02	1.88e-03	2.49e-03	1.94e-02	3.41e-03
$S/\sqrt{S+B}$	2.07e-02	1.15	6.52e-02	7.89e-02	1.06	2.53e-01
data	271	881	1174	1010	3148	5493

Table 7.8 – The post-fit yields, S/B and $S/\sqrt{S+B}$ for the 2-lepton channel analysis categories in the 150 GeV< p_T^V <250 GeV region. The uncertainty shown in this table is of statistical nature only.

	2-jet			≥3-jet		
	Low ΔR CR	SR	High ΔR CR	Low ΔR CR	SR	High ΔR CR
Zl	0.021 ± 0.014	0.17 ± 0.11	0.44 ± 0.29	0.17 ± 0.12	0.99 ± 0.67	4.6 ± 3.1
Zcl	0.065 ± 0.028	0.57 ± 0.25	1.39 ± 0.6	0.61 ± 0.26	4.1 ± 1.8	19.8 ± 8.6
Zhf	11.79 ± 0.93	83.3 ± 3.2	182.5 ± 6.1	111.3 ± 3.7	532 ± 16	1330 ± 31
emuCRData	0.001 ± 0.022	1 ± 1	1.8 ± 1.3	0.001 ± 0.017	15.3 ± 3.9	85.4 ± 9.2
diboson	1.12 ± 0.22	20.4 ± 3.5	0.763 ± 0.043	8.5 ± 1.6	51.8 ± 9.7	36.6 ± 7.4
Total Bkg	13 ± 0.99	105.5 ± 4.1	187 ± 6.1	120.6 ± 3.5	605 ± 14	1477 ± 28
Signal	0.039 ± 0.021	10.2 ± 1.8	0.56 ± 0.1	0.64 ± 0.21	17.6 ± 3.3	8 ± 2.1
S/B	3.03e-03	9.67e-02	3.00e-03	5.33e-03	2.91e-02	5.38e-03
$S/\sqrt{S+B}$	1.09e-02	9.48e-01	4.09e-02	5.84e-02	7.06e-01	2.06e-01
data	16	123	168	126	614	1511

Table 7.9 – The post-fit yields, S/B and $S/\sqrt{S+B}$ for the 2-lepton channel analysis categories in the p_T^V >250 GeV region. The uncertainty shown in this table is of statistical nature only.

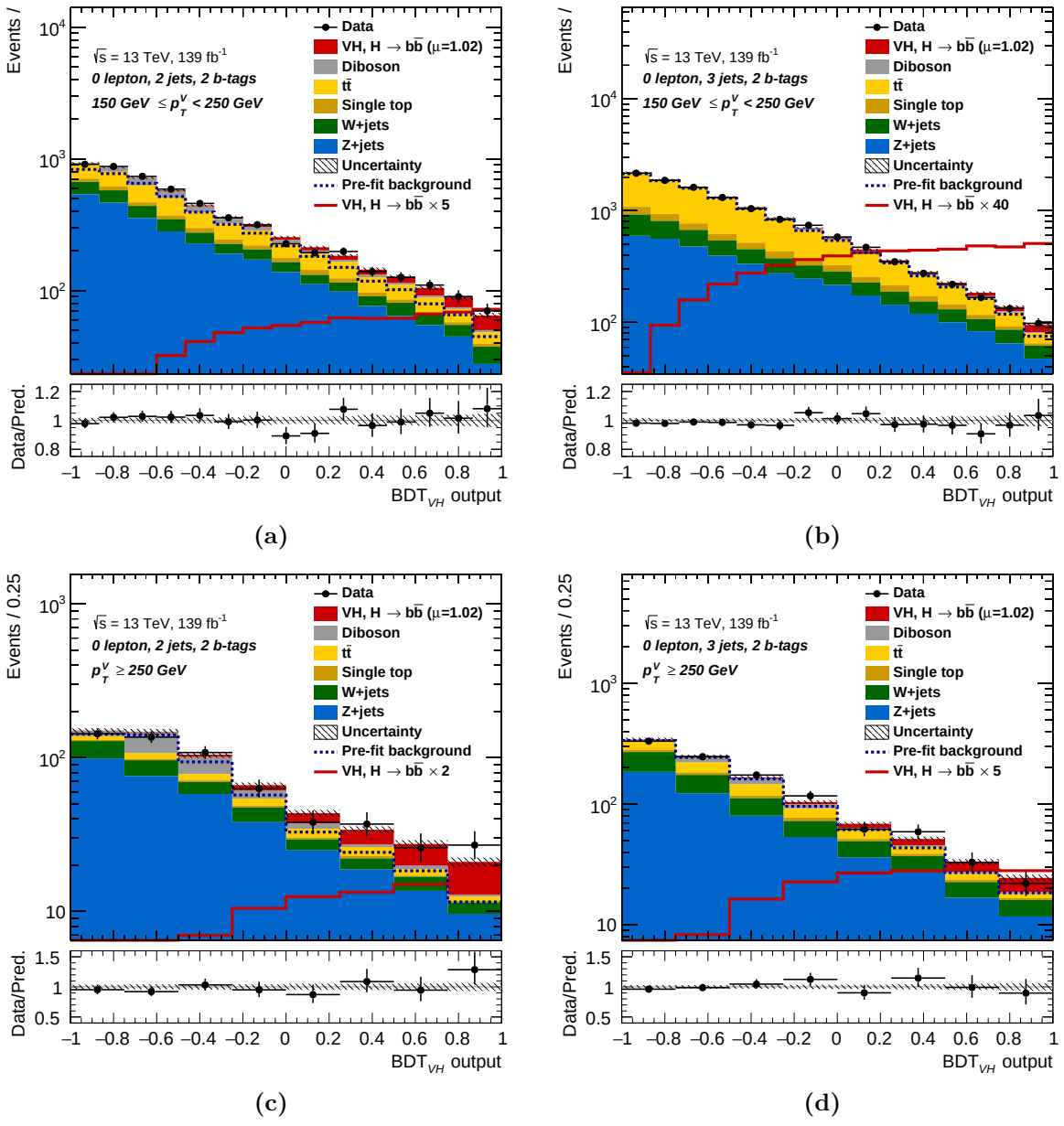

Figure 7.6 – The BDT_{VH} post-fit distributions in the 0-lepton channel resulting from the global fit in the signal region 2-jet $150 < p_T^V < 250\,\mathrm{GeV}$ (a), 3-jet $150 < p_T^V < 250\,\mathrm{GeV}$ (b), 2-jet $p_T^V > 250\,\mathrm{GeV}$ (c), 3-jet $p_T^V > 250\,\mathrm{GeV}$ (d) regions. The background contributions after the global likelihood fit are shown as filled histograms. The Higgs boson signal ($m_H = 125\,\mathrm{GeV}$) is shown as a filled histogram on top of the fitted backgrounds normalised to the signal yield extracted from data ($\hat{\mu} = 1.02$), and unstacked as an unfilled histogram, scaled by the factor indicated in the legend. The dashed histogram shows the total pre-fit background. The size of the combined statistical and systematic uncertainty for the sum of the fitted signal and background is indicated by the hatched band. The ratio of the data to the sum of the fitted signal ($\hat{\mu} = 1.02$) and background is shown in the lower panel.

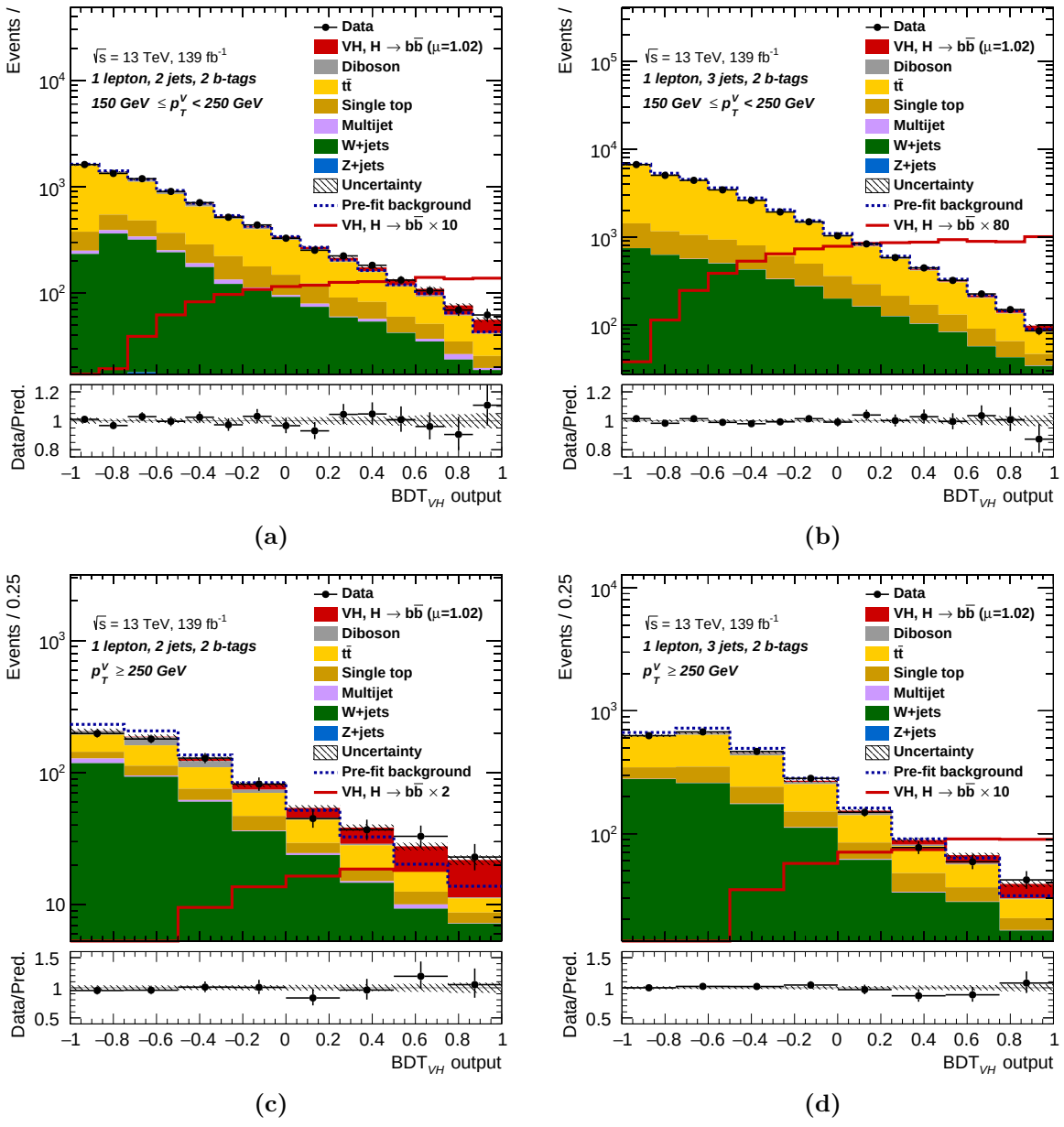

Figure 7.7 – The BDT_{VH} post-fit distributions in the 1-lepton channel resulting from the global fit in the signal region 2-jet $150 < p_T^V < 250\,\mathrm{GeV}$ (a), 3-jet $150 < p_T^V < 250\,\mathrm{GeV}$ (b), 2-jet $p_T^V > 250\,\mathrm{GeV}$ (c), 3-jet $p_T^V > 250\,\mathrm{GeV}$ (d) regions. The background contributions after the global likelihood fit are shown as filled histograms. The Higgs boson signal ($m_H = 125\,\mathrm{GeV}$) is shown as a filled histogram on top of the fitted backgrounds normalised to the signal yield extracted from data ($\hat{\mu} = 1.02$), and unstacked as an unfilled histogram, scaled by the factor indicated in the legend. The dashed histogram shows the total pre-fit background. The size of the combined statistical and systematic uncertainty for the sum of the fitted signal and background is indicated by the hatched band. The ratio of the data to the sum of the fitted signal ($\hat{\mu} = 1.02$) and background is shown in the lower panel.

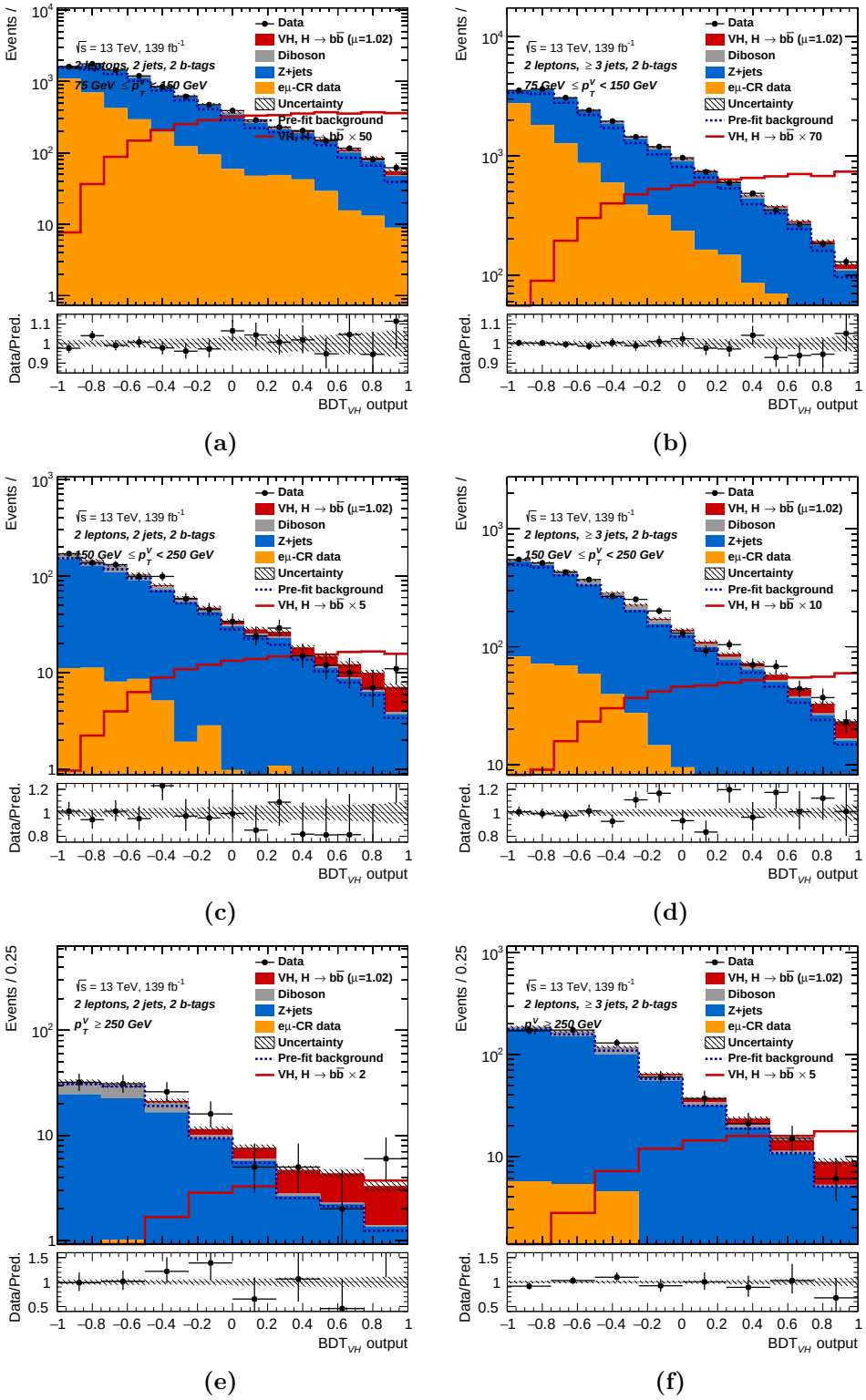

Figure 7.8 – The BDT_{VH} post-fit distributions in the 2-lepton channel resulting from the global fit in the signal region 2-jet $75 < p_T^V < 150\,\mathrm{GeV}$ (a), 2-jet $75 < p_T^V < 150\,\mathrm{GeV}$ (b), 2-jet $150 < p_T^V < 250\,\mathrm{GeV}$ (c), 3-jet $150 < p_T^V < 250\,\mathrm{GeV}$ (d), 2-jet $p_T^V > 250\,\mathrm{GeV}$ (e), 3-jet $p_T^V > 250\,\mathrm{GeV}$ (f) regions. The background contributions after the global likelihood fit are shown as filled histograms. The Higgs boson signal (m_H = 125 GeV) is shown as a filled histogram on top of the fitted backgrounds normalised to the signal yield extracted from data ($\hat{\mu} = 1.02$), and unstacked as an unfilled histogram, scaled by the factor indicated in the legend. The dashed histogram shows the total pre-fit background. The size of the combined statistical and systematic uncertainty for the sum of the fitted signal and background is indicated by the hatched band. The ratio of the data to the sum of the fitted signal ($\hat{\mu} = 1.02$) and background is shown in the lower panel.

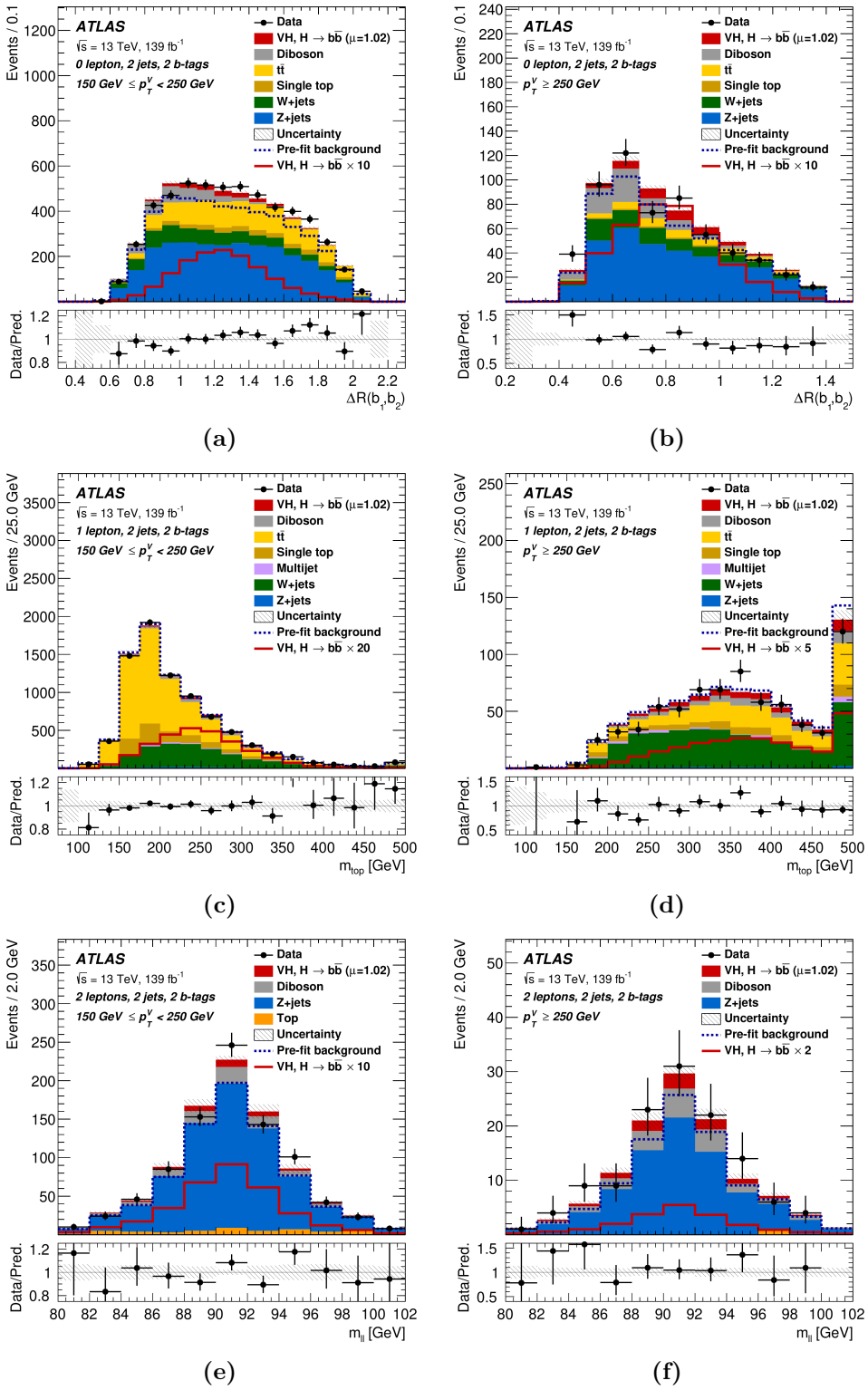

Figure 7.9 – The post-fit distribution in the signal regions for $\Delta R(b_1, b_2)$ in the 0-lepton channel 2-jet $150 < p_T^V < 250\,\text{GeV}$ (a) and $p_T^V > 250\,\text{GeV}$ (b) regions, for m_{top} in the 1-lepton channel 2-jet $150 < p_T^V < 250\,\text{GeV}$ (c) and $p_T^V > 250\,\text{GeV}$ (d) regions and the m_{ll} in the 2-lepton channel 2-jet $150 < p_T^V < 250\,\text{GeV}$ (e) and $p_T^V > 250\,\text{GeV}$ (f) regions. The background contributions after the global likelihood fit are shown as filled histograms. The Higgs boson signal ($m_H = 125\,\text{GeV}$) is shown as a filled histogram on top of the fitted backgrounds normalised to the signal yield extracted from data ($\hat{\mu} = 1.02$), and unstacked as an unfilled histogram, scaled by the factor indicated in the legend. The dashed histogram shows the total pre-fit background. The size of the combined statistical and systematic uncertainty for the sum of the fitted signal and background is indicated by the hatched band. The ratio of the data to the sum of the fitted signal ($\hat{\mu} = 1.02$) and background is shown in the lower panel.

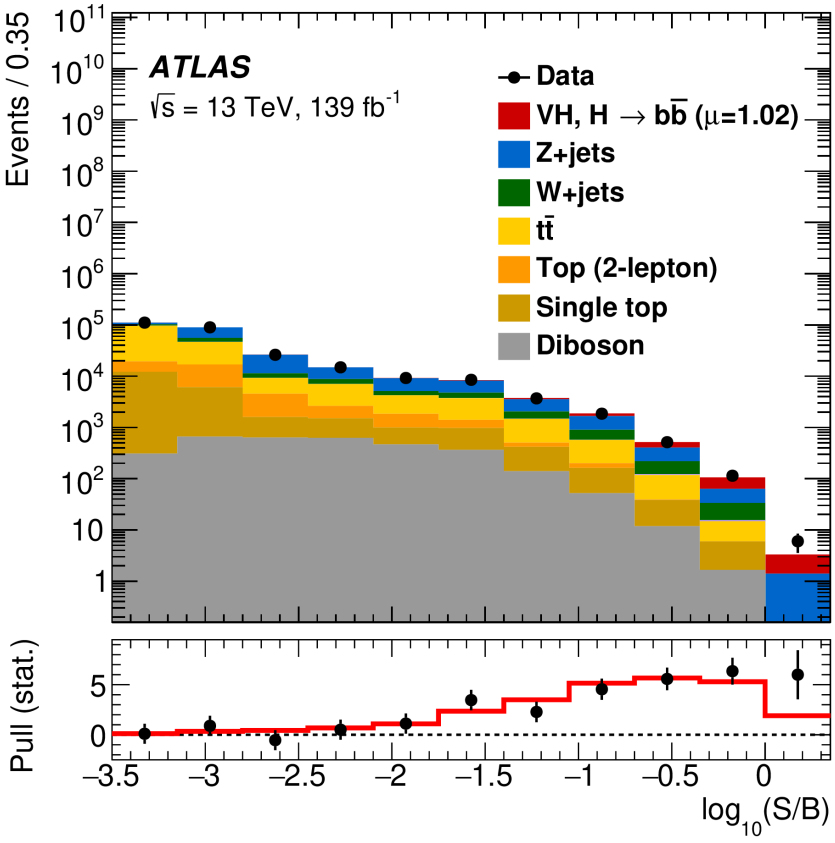

Figure 7.10 – Event yields as a function of the observed $\log_{10}$(S/B) for data, background and a Higgs boson signal with m_H =125 GeV for the nominal VH fit. Final-discriminant bins in all regions are combined into bins of $\log_{10}$(S/B), with S being the fitted signal and B the fitted background yields. The Higgs boson signal contribution is shown after rescaling the SM cross-section according to the value of the signal strength extracted from data ($\hat{\mu} = 1.02$). In the lower panel, the pull of the data with respect to the background (the statistical significance of the difference between data and fitted background) is shown with statistical uncertainties only. The full line indicates the pull shape expected from the sum of fitted signal and background relative to the fitted background.

Significance and signal strength

In the combined fit, for a Higgs boson mass of 125 GeV, one parameter of interest (1POI) is estimated. This corresponds to the VH normalisation that is floated allowing to measure a single value of μ_{VH}^{bb}. The global fit gives a signal strength value of:

$$\mu_{VH}^{bb} = 1.02^{+0.18}_{-0.17} = 1.02^{+0.12}_{-0.11}(\text{Stat})^{+0.14}_{-0.13}(\text{Syst})$$

The result corresponds to an observed significance of 6.7 σ. The expected significance for the same measurement is 6.7 σ, obtained from the Asimov dataset constructed with $\mu = 1$ and setting the nuisance parameters to those obtained from the fit to data (post-fit expectation).

The signal sensitivity comes mainly from the 2-jet category because of the better S/B ratio than that of the 3-jet category. Moreover, the 150 GeV $< p_T^V <$ 250 GeV region is as sensitive as the $p_T^V >$ 250 GeV region.

A two POI fit is also performed to measure independently the WH and the ZH signals. Two signal strengths are measured simultaneously in the same fit and their values are:

$$\mu^{bb}_{WH} = 0.95^{+0.27}_{-0.25} = 0.95^{+0.18}_{-0.18}(\text{Stat})^{+0.19}_{-0.18}(\text{Syst})$$

$$\mu^{bb}_{ZH} = 1.08^{+0.25}_{-0.23} = 1.08^{+0.17}_{-0.17}(\text{Stat})^{+0.18}_{-0.15}(\text{Syst})$$

The comparison of these values to the inclusive VH measurement is shown in Figure 7.11. The values of the observed (expected) significance are equal to 4.0σ (4.1σ) and 5.3σ (5.1σ) for WH and ZH respectively. These values are summarised in Table 7.10, and indicate an observation of the ZH signal and a strong evidence of the WH signal in the $H \to b\bar{b}$ decay channel.

The ZH sensitivity comes in equal parts from 0- and 2-lepton channels. The WH signal sensitivity is lower than ZH despite a larger cross-section since the 1-lepton channel has an overall lower S/B ratio, in particular because of the $t\bar{t}$ background contribution in 3-jet region.

The compatibility between the measurement of the inclusive VH signal and the separate WH and ZH signals is evaluated from the maximum likelihood values. When computing the compatibility between these two fit results for the same likelihood fit, their difference is supposed to follow a χ^2 distribution, since it is a Gaussian regime, with 1 degree of freedom. The compatibility between the two results (or their difference with 0) was measured to be 71% proving a good agreement between the two measurements. The compatibility between the combined fit and the individual channels was also checked, by performing a three POI fit where the VH in the 3 channels is measured independently in the same fit. The compatibility between the inclusive measurement and the 3 channels measurement was measured to be 92%. Another three POI fit was also conducted by measuring separately the signal in the 3 p_T^V regimes, and the compatibility with the inclusive VH fit was found to be 98%.

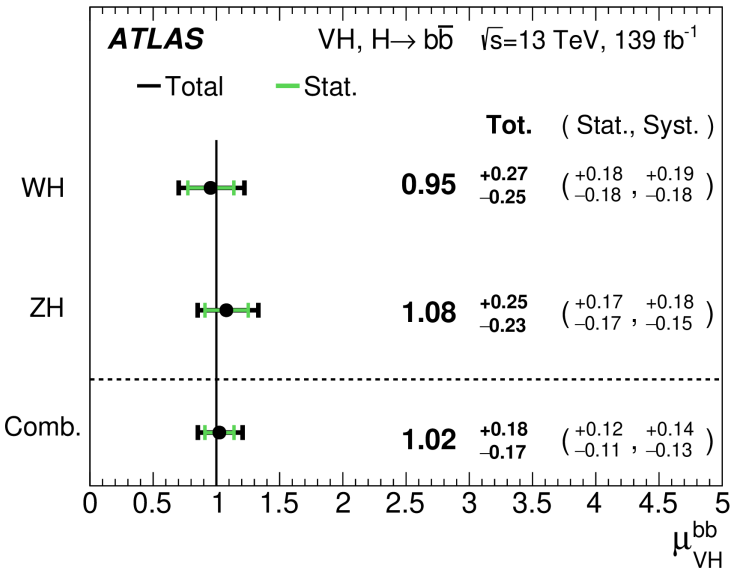

Figure 7.11 – The fitted values of the Higgs boson signal strength μ^{bb}_{VH} for m_H =125 GeV for the WH and ZH processes and their combination. The individual μ^{bb}_{VH} values for the $(W/Z)H$ processes are obtained from a simultaneous fit with the signal strength for each of the WH and ZH processes floating independently.

	Exp.	Obs.
WH	4.1	4.0
ZH	5.1	5.3
VH	6.7	6.7

Table 7.10 – The observed and the expected significance for the WH and ZH signal processes from the 2POI fit and the VH signal from the 1POI fit.

Ranking and breakdown of systematic uncertainties

The total uncertainty and the contribution of individual uncertainties are computed following the description of Section 7.2.3. The breakdown of systematic uncertainties showing the impact of the different sets of systematic uncertainties on the measured VH, WH and ZH signal strengths are presented in Figure 7.12. As shown, the VH signal measurement is dominated by systematic uncertainties where the uncertainties with the highest impact are the signal and background modelling uncertainties, followed by the b-tagging and the JET uncertainties, in addition to the Monte Carlo statistical uncertainties and the data statistics. The data statistics have an impact comparable to that of the systematic uncertainties. When the statistic will be increased in the future, the challenge of the analysis is to keep the systematic uncertainties at the same level as that statistical uncertainties.

The rankings of the impact on the signal strengths of the 15 leading systematic uncertainties are shown in Figure 7.13 where the pulls and constraints of systematic uncertainties were studied one by one and modifications of the fit model were done (decorrelations of nuisance parameters) to be sure that the results are robust. The pulls and constraints were considered reasonable given the good agreement between data and Monte Carlo in the post-fit plots (Figure 7.3 to 7.5). The rankings are compatible with the breakdown of systematic uncertainties, and they include six theoretical uncertainties on the signal, background modelling uncertainties (W+jets and diboson shape uncertainties and Z+jets extrapolation uncertainty), b-tagging, jet and Z+heavy flavor floating uncertainties.

STXS measurement

The STXS measurement is performed in the reduced 1.2 stage binning, after merging the 2- and the 3-jet categories together to reduce the statistical uncertainties and after removing the split in p_T^V at 400 GeV since the analysis does not have a specific category for it. There is a boosted VHbb analysis [118] dedicated to this study at a high p_T^V regime which includes this p_T^V split at 400 GeV. This results in 5 measured STXS bins, split depending only on the p_T^V regime. The measured cross-sections times the branching ratio are presented in Table 7.11 and Figure 7.14. The ratio of the results to the Standard Model predictions are computed and are presented in Figure 7.15. The STXS measurements and the Standard Model are found to be in excellent agreement.

The correlation between the measurements in the 5 p_T^V bins are presented in Figure 7.16, where very little correlation between the STXS bins was observed. This is an improvement compared to the previous 80 fb^{-1} analysis, and it is due to the split in p_T^V at 250 GeV introduced after the previous 80 fb^{-1} [119] analysis to synchronise the analysis categories with the STXS binning.

Source of uncertainty		σ_μ VH	WH	ZH
Total		0.177	0.260	0.240
Statistical		0.115	0.182	0.171
Systematic		0.134	0.186	0.168
Statistical uncertainties				
Data statistical		0.108	0.171	0.157
$t\bar{t}$ $e\mu$ control region		0.014	0.003	0.026
Floating normalisations		0.034	0.061	0.045
Experimental uncertainties				
Jets		0.043	0.050	0.057
$E_{\mathrm{T}}^{\mathrm{miss}}$		0.015	0.045	0.013
Leptons		0.004	0.015	0.005
b-tagging	b-jets	0.045	0.025	0.064
	c-jets	0.035	0.068	0.010
	light-flavour jets	0.009	0.004	0.014
Pile-up		0.003	0.002	0.007
Luminosity		0.016	0.016	0.016
Theoretical and modelling uncertainties				
Signal		0.052	0.048	0.072
Z + jets		0.032	0.013	0.059
W + jets		0.040	0.079	0.009
$t\bar{t}$		0.021	0.046	0.029
Single top quark		0.019	0.048	0.015
Diboson		0.033	0.033	0.039
Multi-jet		0.005	0.017	0.005
MC statistical		0.031	0.055	0.038

Figure 7.12 – The breakdown of the contributions of individual uncertainties to the total uncertainty on μ_{VH}^{bb}, μ_{WH}^{bb} and μ_{ZH}^{bb} measurements. The sum in quadrature of the systematic uncertainties attached to the categories differs from the total systematic uncertainty due to correlations.

STXS bin	$\sigma \times BR$ [fb]
WH, 150 GeV $p_T^V < 250$ GeV	$19.0^{+12.2}_{-12.0}$
WH, $p_T^V > 250$ GeV	$7.2^{+2.3}_{-2.1}$
ZH, 75 GeV $p_T^V < 150$ GeV	$42.5^{+36.4}_{-35.4}$
ZH, 150 GeV $p_T^V < 250$ GeV	$20.5^{+6.4}_{-6.0}$
ZH, $p_T^V > 250$ GeV	$5.4^{+1.6}_{-1.6}$

Table 7.11 – The measured cross-sections times the branching ratio in the 5 STXS bins.

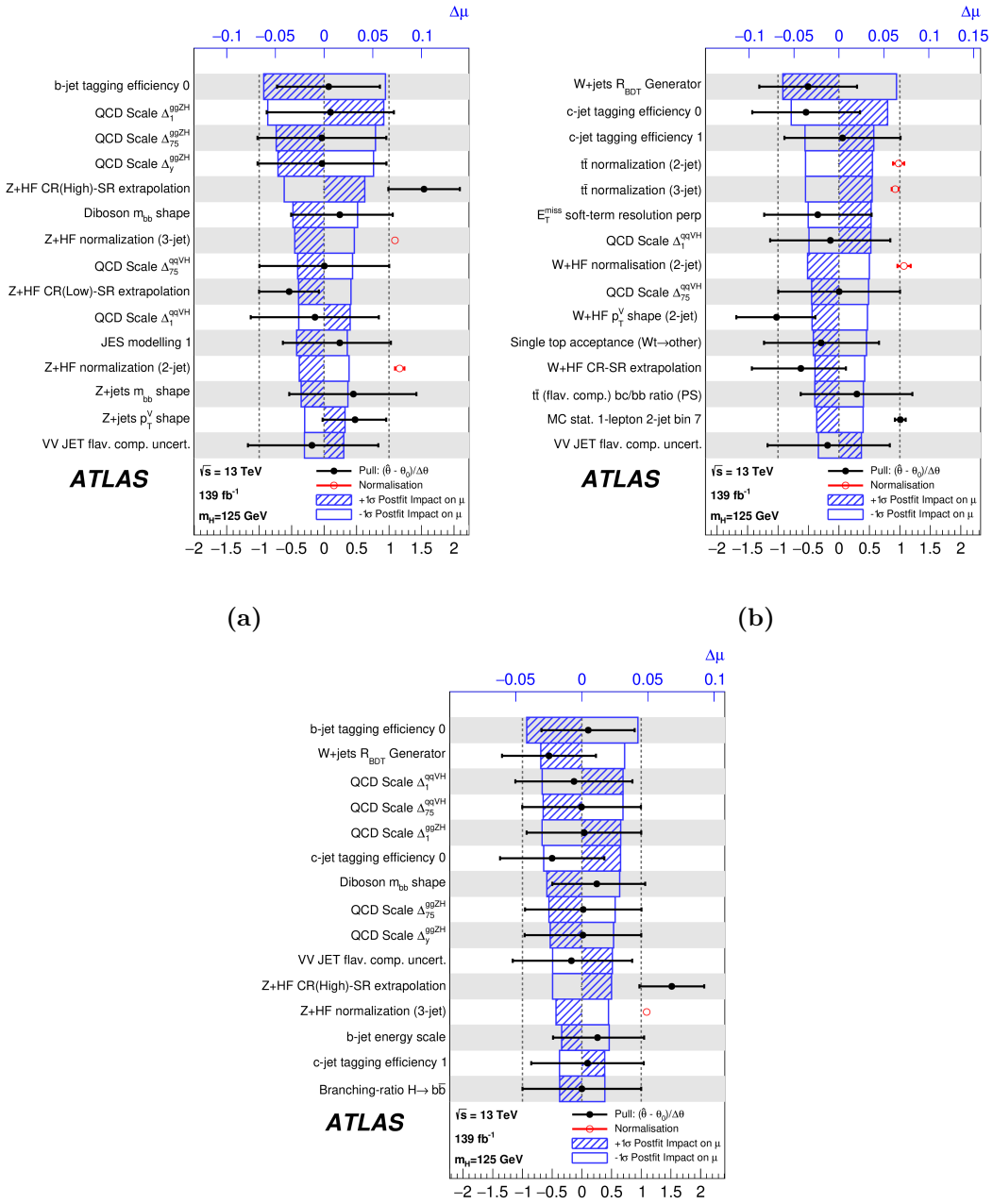

Figure 7.13 – Ranking of the impact of systematic uncertainties on the signal strength $\hat{\mu}$ for the ZH (a), WH (b) and the combined VH (c) signals. The systematic uncertainties are listed in decreasing order of their impact. The blue boxes show the changes in $\hat{\mu}$, referring to the top x-axis, when fixing the corresponding individual nuisance parameter θ to its fitted value $\hat{\theta}$ modified upwards or downwards by its fitted uncertainty, and performing the fit again, with all the other parameters allowed to vary, so as to take correlations between systematic uncertainties properly into account. The hatched and open areas correspond to the upwards and downwards variations, respectively, and the yellow boxes show the same variations but calculated for the pre-fit uncertainty values. The filled circles, referring to the bottom x-axis, show the deviations of the fitted nuisance parameters $\hat{\theta}$ from their nominal values θ_0, expressed in terms of standard deviations with respect to their nominal uncertainties $\Delta\theta$. The associated error bars show the fitted uncertainties of the nuisance parameters, relative to their nominal uncertainties.

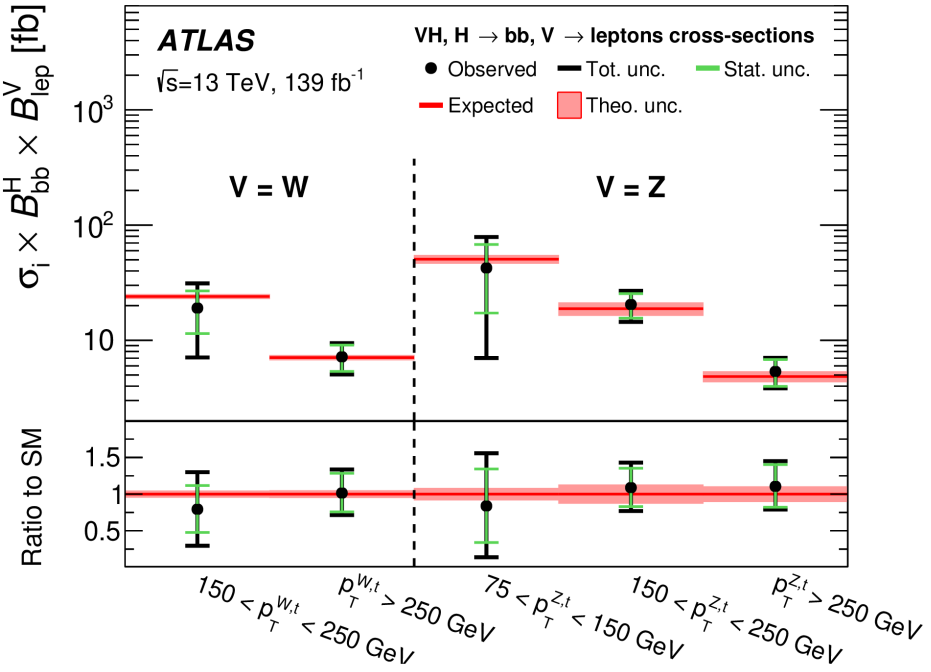

Figure 7.14 – The measured cross-sections times the branching ratio in the 5 STXS bins. The ratios with respect to the Standard Model prediction are presented in the lower pad.

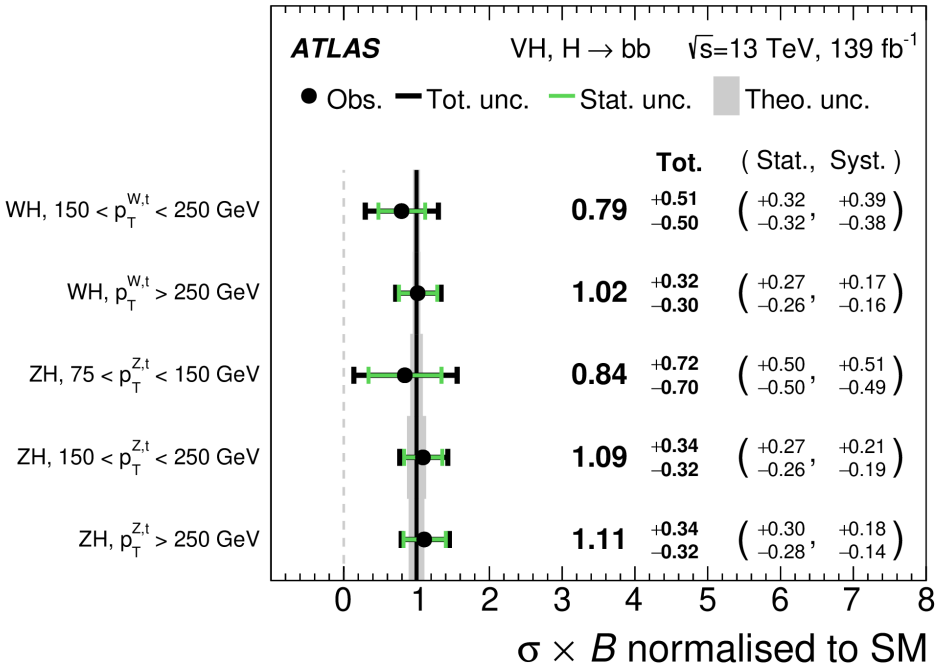

Figure 7.15 – The measured VH cross-section times the $H \to b\bar{b}$ branching ratio normalised to the SM prediction in the reduced STXS scheme. The theoretical uncertainties on the SM prediction are represented by the gray shaded area and are calculated following the description in Ref [120].

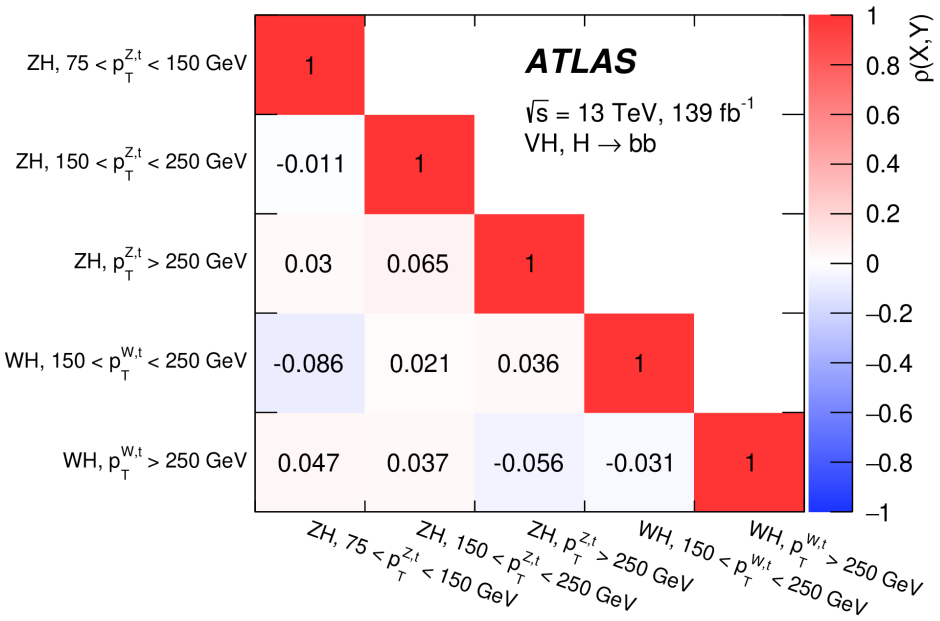

Figure 7.16 – The observed correlations between the measured VH, $H \to b\bar{b}$ reduced STXS in the 5POI scheme, including both the statistical and systematic uncertainties.

7.5.3 Di-jet mass analysis

The di-jet mass analysis consists on performing the same fit as the MVA, but replacing the BDT_{VH} with the m_{bb} distribution in the signal region to cross-check the MVA results. The combined fit gives a value for the signal strength of:

$$\mu_{VH}^{bb} = 1.17^{+0.25}_{-0.23} = 1.17^{+0.16}_{-0.16}(\mathrm{Stat})^{+0.19}_{-0.16}(\mathrm{Syst})$$

The corresponding observed significance is 5.5σ compared to an expected significance of 4.9σ, which indicates an observation of the VH signal in the di-jet mass analysis. The difference in sensitivity between the MVA and the di-jet mass fit is due to the greater sensitivity reached with the BDT method. The comparison of the signal strengths measured in the MVA and di-jet mass fits for the combined fit and the individual channel fits are presented in Figure 7.17.

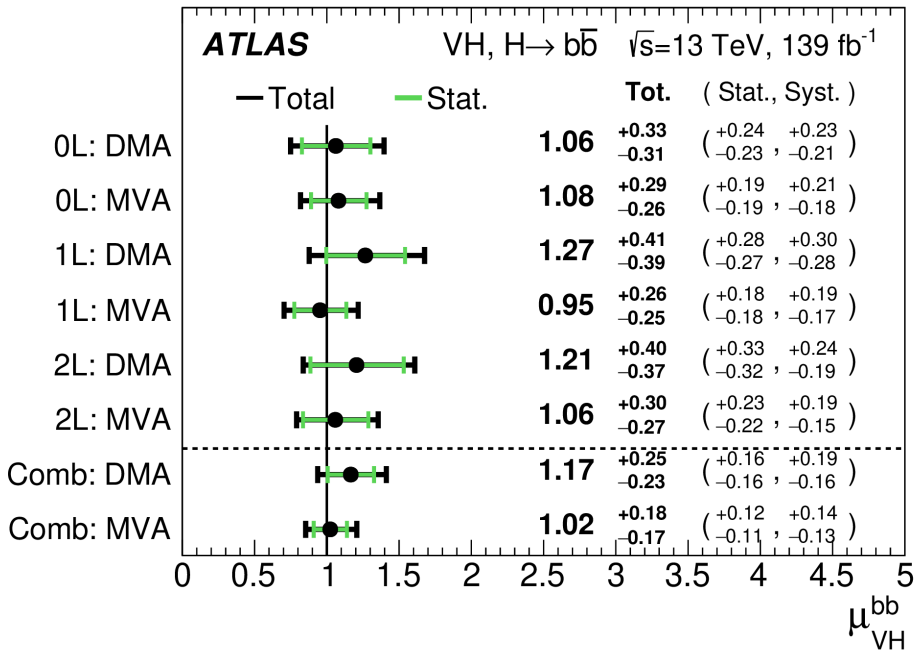

Figure 7.17 – The VH signal strength values for $m_H = 125\,\mathrm{GeV}$ for the 0-, 1- and 2-lepton channels and their combination, for both the MVA and the di-jet mass analyses (DMA). The individual channels $\hat{\mu}$ values are obtained from a simultaneous fit where the signal strength for each channel is independently floated.

The post-fit m_{bb} distributions used in the fit are shown in Figures 7.18, 7.19 and 7.20. The m_{bb} distribution summed over all the channels and the analysis categories, weighted by their respective values of the ratio of the fitted Higgs boson signal to the background yields, and after subtraction of all backgrounds except for the diboson processes is presented in Figure 7.21 and shows a good agreement with data.

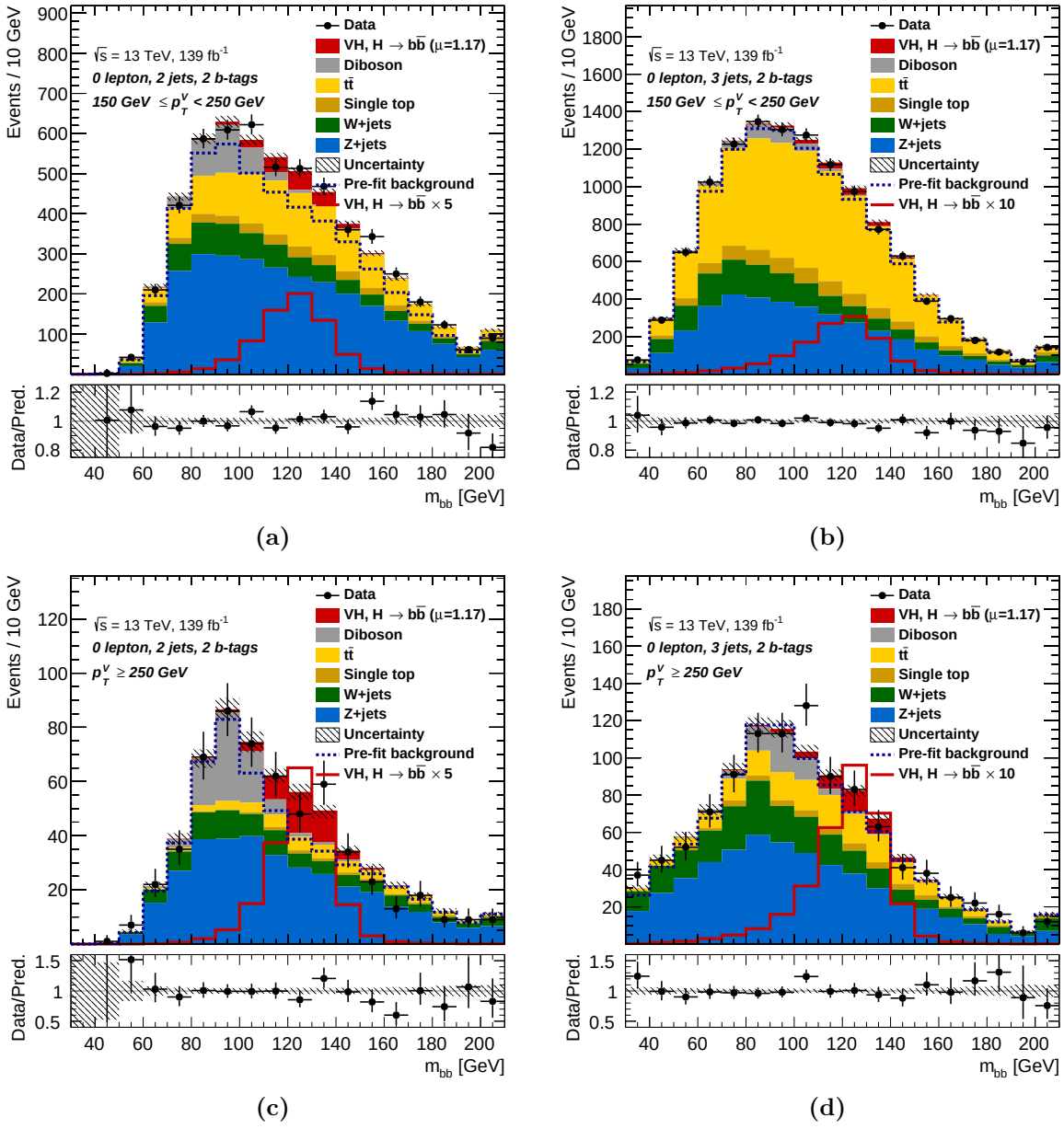

Figure 7.18 – The m_{bb} post-fit distributions in the 0-lepton channel used in the global fit in the signal region 2-jet $150 < p_T^V < 250\,\text{GeV}$ (a), 3-jet $150 < p_T^V < 250\,\text{GeV}$ (b), 2-jet $p_T^V > 250\,\text{GeV}$ (c), 3-jet $p_T^V > 250\,\text{GeV}$ (d) regions. The background contributions after the global likelihood fit are shown as filled histograms. The Higgs boson signal ($m_H = 125\,\text{GeV}$) is shown as a filled histogram on top of the fitted backgrounds normalised to the signal yield extracted from data ($\hat{\mu} = 1.17$), and unstacked as an unfilled histogram, scaled by the factor indicated in the legend. The last bin in each distribution include the overflow events. The dashed histogram shows the total pre-fit background. The size of the combined statistical and systematic uncertainty for the sum of the fitted signal and background is indicated by the hatched band. The ratio of the data to the sum of the fitted signal ($\hat{\mu} = 1.17$) and background is shown in the lower panel.

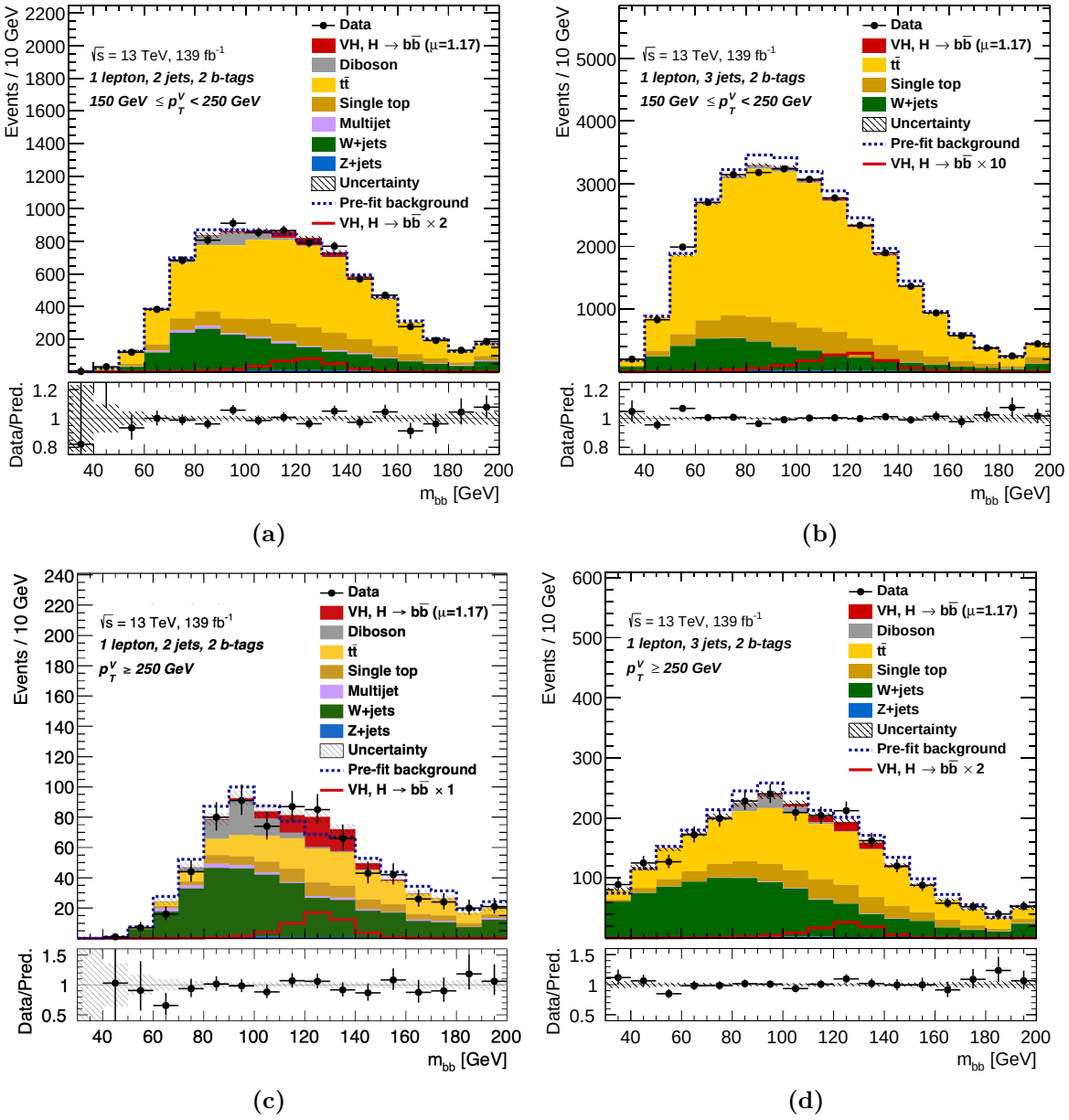

Figure 7.19 – The m_{bb} post-fit distributions in the 1-lepton channel used in the global unconditionnal fit in the signal region 2-jet $150 < p_T^V < 250$ GeV (a), 3-jet $150 < p_T^V < 250$ GeV (b), 2-jet $p_T^V > 250$ GeV (c), 3-jet $p_T^V > 250$ GeV (d) regions. The background contributions after the global likelihood fit are shown as filled histograms. The Higgs boson signal ($m_H = 125$ GeV) is shown as a filled histogram on top of the fitted backgrounds normalised to the signal yield extracted from data ($\hat{\mu} = 1.17$), and unstacked as an unfilled histogram, scaled by the factor indicated in the legend. The last bin in each distribution include the overflow events. The dashed histogram shows the total pre-fit background. The size of the combined statistical and systematic uncertainty for the sum of the fitted signal and background is indicated by the hatched band. The ratio of the data to the sum of the fitted signal ($\hat{\mu} = 1.17$) and background is shown in the lower panel.

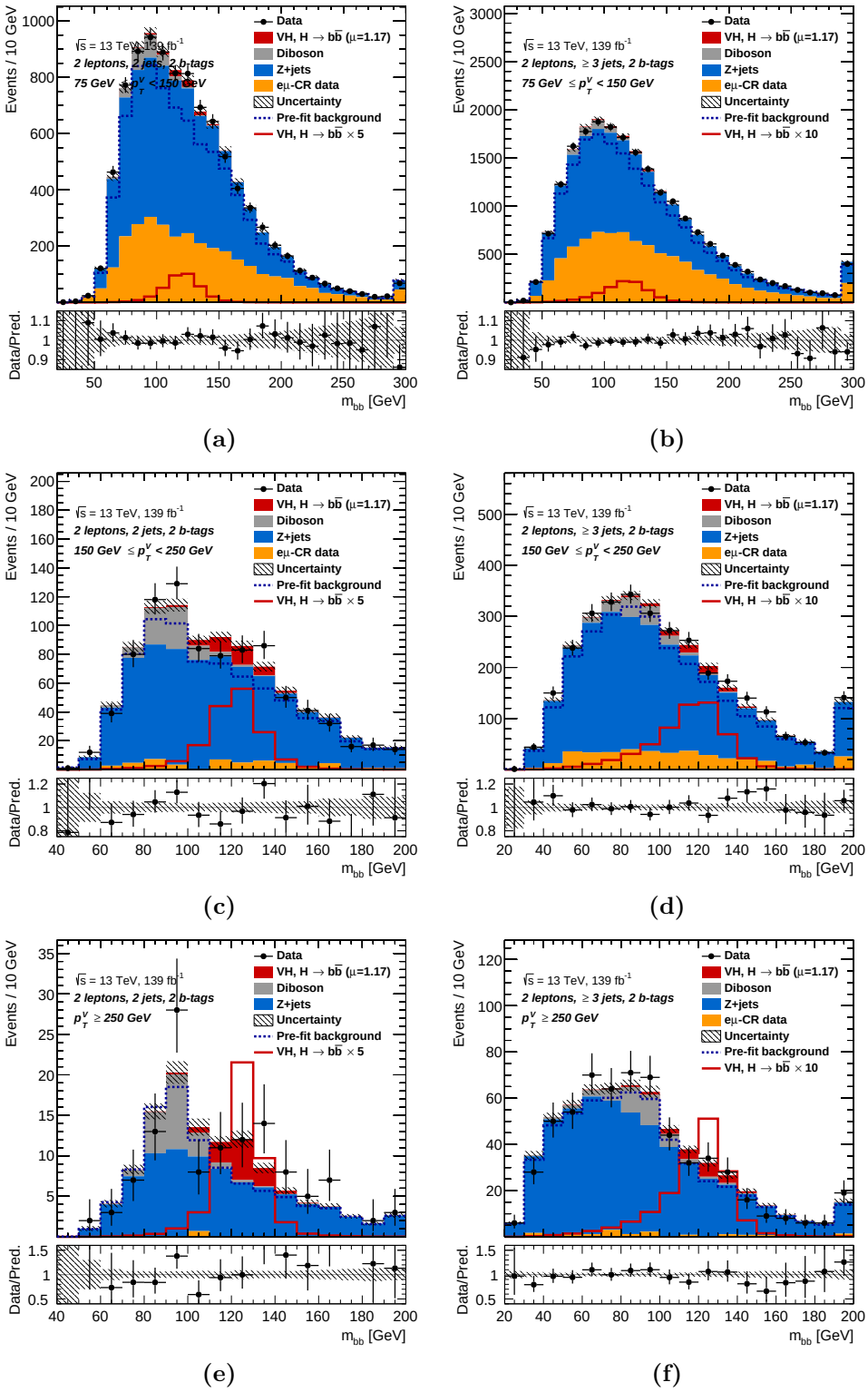

Figure 7.20 – The m_{bb} post-fit distributions in the 2-lepton channel used in the global fit in the signal region 2-jet $75 < p_T^V < 150\,\text{GeV}$ (a), 2-jet $75 < p_T^V < 150\,\text{GeV}$ (b), 2-jet $150 < p_T^V < 250\,\text{GeV}$ (c), 3-jet $150 < p_T^V < 250\,\text{GeV}$ (d), 2-jet $p_T^V > 250\,\text{GeV}$ (e), 3-jet $p_T^V > 250\,\text{GeV}$ (f) regions. The background contributions after the global likelihood fit are shown as filled histograms. The Higgs boson signal ($m_H = 125\,\text{GeV}$) is shown as a filled histogram on top of the fitted backgrounds normalised to the signal yield extracted from data ($\hat{\mu} = 1.17$), and unstacked as an unfilled histogram, scaled by the factor indicated in the legend. The last bin in each distribution include the overflow events. The dashed histogram shows the total pre-fit background. The size of the combined statistical and systematic uncertainty for the sum of the fitted signal and background is indicated by the hatched band. The ratio of the data to the sum of the fitted signal ($\hat{\mu} = 1.17$) and background is shown in the lower panel.

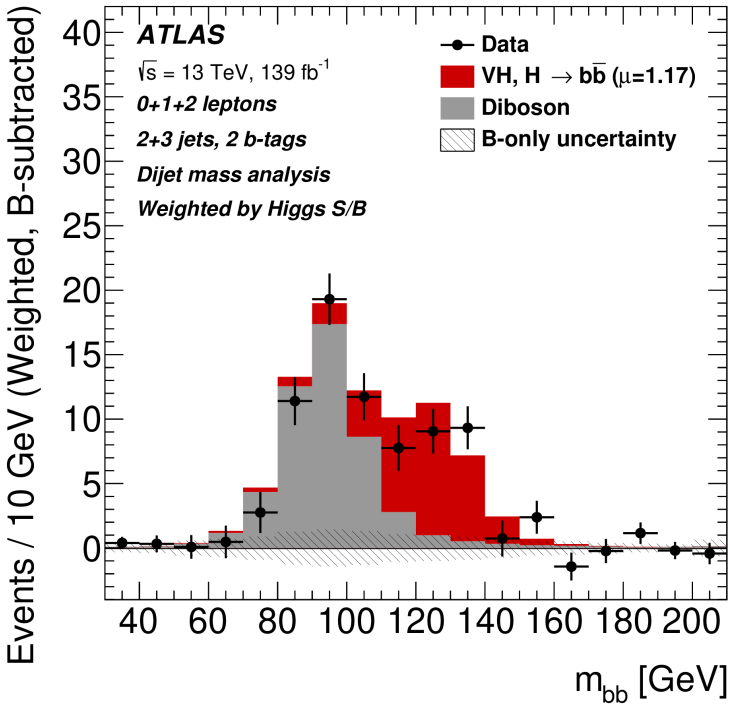

Figure 7.21 – The m_{bb} distribution from the di-jet mass fit showing the data after substraction of all the backgrounds except the diboson process. All the analysis regions are summed and weighted by the corresponding S/B ratio for each region. The expected contribution of the associated WH and ZH production of a SM Higgs boson with $m_H = 125\,\text{GeV}$ is shown scaled by the measured signal strength ($\hat{\mu} = 1.17$). The size of the combined statistical and systematic uncertainty for the fitted background is indicated by the hatched band.

7.5.4 Compatibility between the multivariate analysis and the di-jet mass analysis

For the MVA and the di-jet mass analysis, the same events are used in the fit to measure the Higgs boson signal but using a different observable. Since their measured μ values differ, it is interesting to estimate the compatibility between the two measured signal strengths. The compatibility between the results of the two fits is evaluated using the bootstrap method [121], based only on the statistical fluctuations of data. This method requires generating a set of replicas of the BDT_{VH} and m_{bb} data distributions used in the fit, by reweighting all the events in the same manner in both distributions.

The data replicas of the BDT_{VH} and m_{bb} distributions are produced by calculating a random weight for each event around the nominal value, from a Poisson distribution with the mean value of 1. This implies that depending on the value of the selected weight, the events can migrate out of the analysis or can be included several times.

Around 450 fits of MVA and m_{bb} are then performed, where the data histogram corresponds to one of the data replicas. The best fit values of the two analyses are then compared for the same pseudo-data. The difference between the two $\hat{\mu}$ values is then computed to quantify their compatibility. A total of 445 combined fits are performed using the pseudo-data histograms and the results are shown in Figure 7.23. A Gaussian fit is performed to the $\hat{\mu}$ distributions to smooth all the statistical fluctuations and to get the mean of these distributions. The $\hat{\mu}$ values of the MVA and m_{bb} fits are centered around the nominal fit values (1.02 for MVA and 1.17 for m_{bb}).

The compatibility between the two measurements is evaluated by computing the compatibility of their difference with 0 from the mean and the standard deviation of the Gaussian fit to the difference between the best fit values of the two fits. The MVA and the di-jet mass results were found to be compatible within $\sim 1\sigma$. The correlation between the two measurements was found to be of 60% as shown in Figure 7.22. The compatibility is assessed by taking into account only the data fluctuations, but the auxiliary measurements should also be fluctuated in the likelihood fit. The results here are enough to be prove that the MVA and the m_{bb} fit results are well compatible.

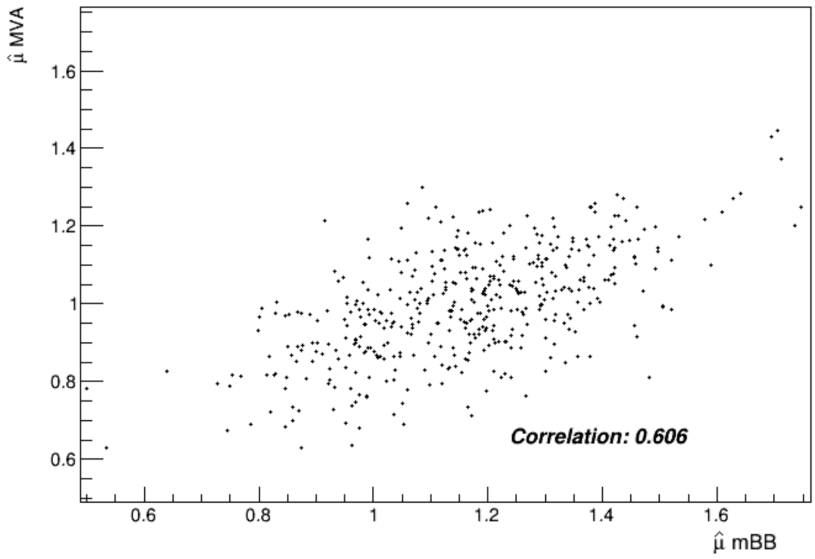

(a)

Figure 7.22 – The correlation between the measured $\hat{\mu}_{MVA}$ and $\hat{\mu}_{m_{bb}}$ from the bootstrap fits.

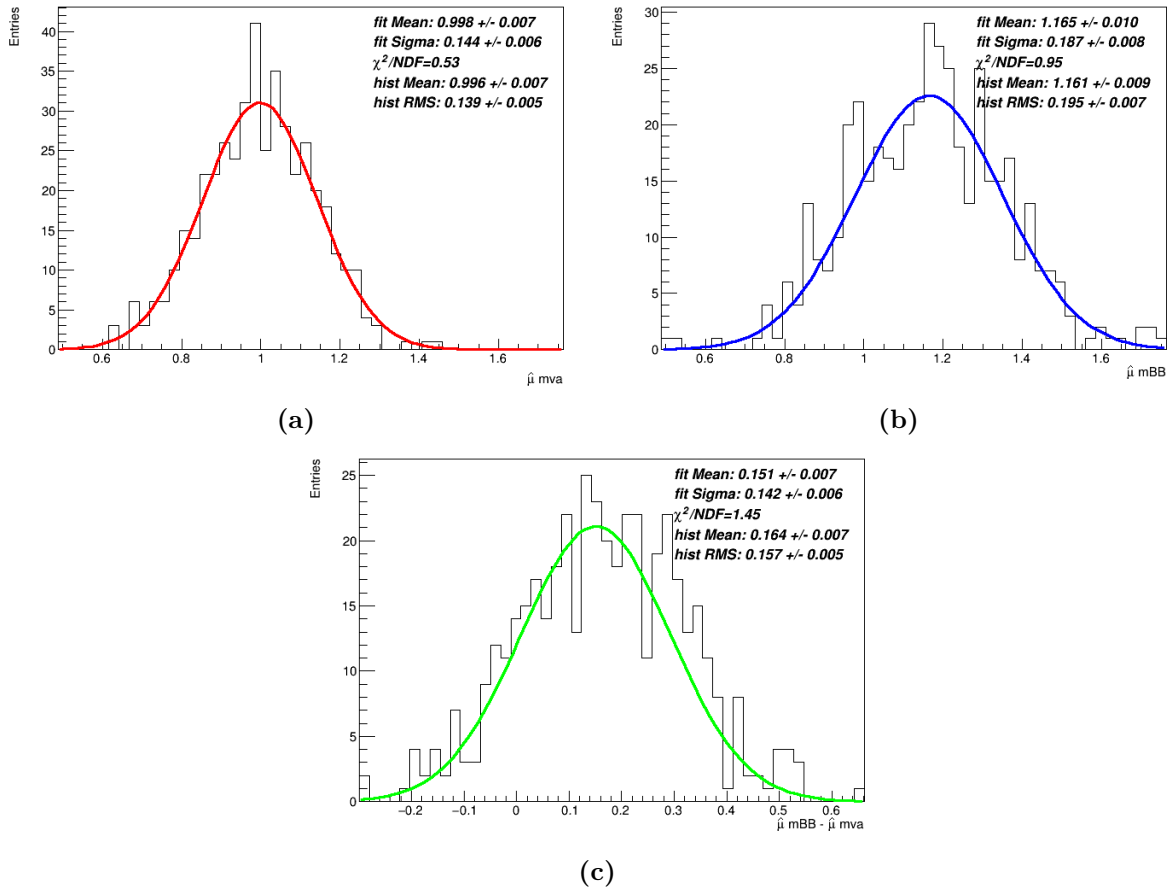

Figure 7.23 – The $\hat{\mu}_{mva}$ (a), $\hat{\mu}_{m_{bb}}$ (b) and $\hat{\mu}_{mva} - \hat{\mu}_{m_{bb}}$ (c) distributions obtained from the combined fits using 445 data replicas. The red, blue and green lines are the Gaussian functions used to fit the $\hat{\mu}$ distributions.

7.6 Measurements using the VH, $H \to b\bar{b}$ results

7.6.1 Constrains on the EFT coefficients

The $VH(H \to b\bar{b})$ analysis STXS measurements are interpreted in the effective field theory (EFT) approach. In this approach, the production cross-section and branching ratio of the Higgs boson are parametrised in terms of the SMEFT coefficients and operators as described in Section 1.6.3. The analysis is most sensitive to 6 EFT operators affecting the VH production and one operator affecting the $H \to b\bar{b}$ decay. This interpretation does not take into account the operators to which the $ggZH$ is sensitive, which means that these are fixed to the Standard Model prediction.

The constrains on the Wilson coefficients are obtained from the binned likelihood fit across the 5 STXS regions. The measurement of the coefficients are done one by one by removing the other coefficients and deriving a confidence level (CL) interval to the coefficient. The EFT parametrisation includes either a linear coefficient contribution to account for the interference between the Standard Model and physics beyond this model or a sum of a linear and quadratic contribution to account in addition for the beyond the Standard Model interactions as presented in Equation 1.21. The resulting 68% and 95% CL intervals for the Wilson coefficients, with both the linear and the sum of the linear and quadratic contributions, are presented in Figure 7.24.

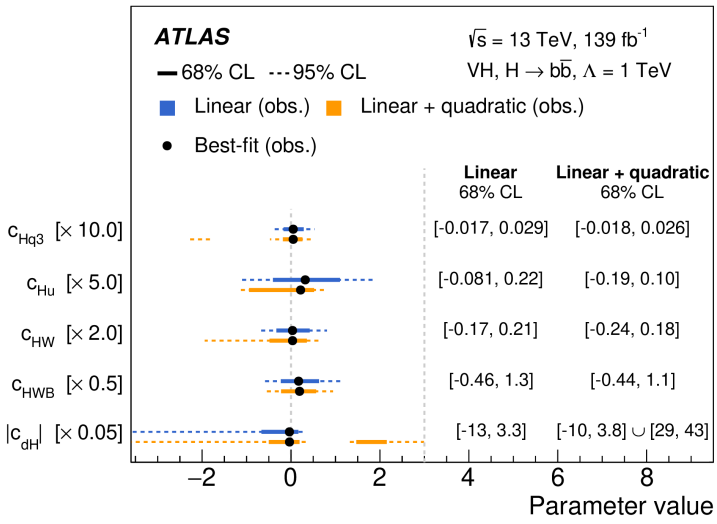

(a)

Figure 7.24 – The observed best fit values for each of the Wilson coefficients and their 68% and 95% CL intervals. The limits on the coefficients were set when the linear contribution (blue) and the sum of the linear and quadratic (orange) contributions are considered. The constrains on the c_{Hd} and c_{Hq1} coefficients are not shown since they have similar impact on the measurements as that of the c_{Hu} coefficient.

The constraints on the Wilson coefficients are measured individually due to the difficulty of managing all the correlations which are induced when constraining simultaneously all the coefficients. In order to solve this problem and remove all assumptions that only one operator acts at a time, a linear combination of the coefficient can be measured instead of measuring the coefficients individually. The chosen coefficient combinations (eigenvectors) are presented in Table 7.12. The impact of the eigenvectors on the cross-section measurements when varying their values by $\pm 1\sigma$ around their best fit values are shown in Figure 7.25 in each of the STXS bins.

Eigenvector	Wilson coefficient
$0.98 \times c_{Hq3}$	c_{E0}
$0.85 \times c_{Hu}$ - $0.39 \times c_{Hq1}$ - $0.27 \times c_{Hd}$	c_{E1}
$0.70 \times \Delta\mathrm{BR}/\mathrm{BR}_{SM}$ + $0.62 \times c_{HW}$	c_{E2}
$0.74 \times c_{HWB}$ + $0.53 \times c_{Hq1}$ - $0.32 \times c_{HW}$	c_{E3}

Table 7.12 – The eigenvectors composition from the linear combination of Wilson coefficients. A $\Delta\mathrm{BR}/\mathrm{BR}_{SM}$ term is added to take into account modifications that can affect the branching ratio. Only four eigenvectors are considered as they are only ones with significant impact on the measurements.

7.6.2 Higgs combination

The results of the $VH(H \to b\bar{b})$ analysis were combined with other measurements of the Higgs boson in different production and decays channels for a Higgs boson mass value of 125.09 GeV. The Higgs combination [122] benefits from the full Run-2 dataset in several channels which allows to have more precision on the Higgs boson cross-section measurements to improve the measurements on the Higgs boson couplings. The $VH(H \to b\bar{b})$ plays a very important role in this combination, since it allows to have more STXS bins and thus more precision on the measurements, as well as it allows to benefit from the improvements adopted by the analysis to increase the signal sensitivity to improve the combination results.

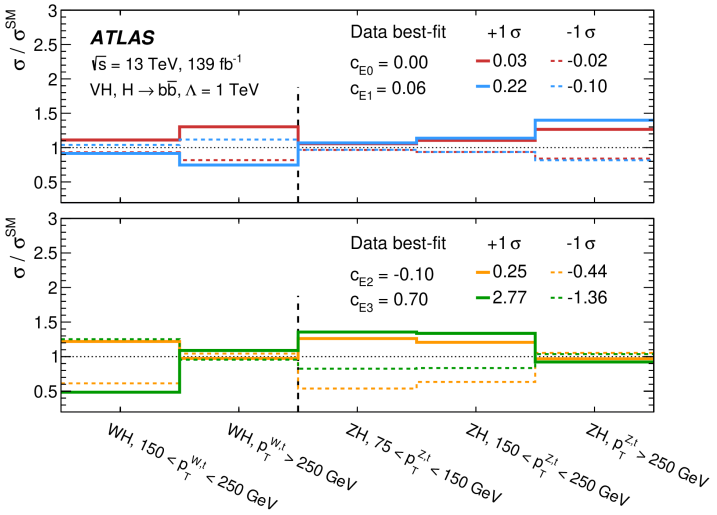

(a)

Figure 7.25 – The impact of the eigenvectors on the cross-section measurements with the best fit values for each of the eigenvalues. The changes to the cross-section are shown in the solid line for $+1\sigma$ variation of the eigenvectors and in the dashes line for the -1σ variation.

The measured signal strength from the combination of all the channels was measured to $\hat{\mu} = 1.06 \pm 0.07$ and to be in good agreement with the predictions. The results from the Higgs boson combination are shown in Figure 7.27 and were found to be close to unity within uncertainties.

Figure 7.26 shows the fermions and weak boson coupling modifiers obtained from the Higgs combination, which were found to be consistent with the Standard Model predictions.

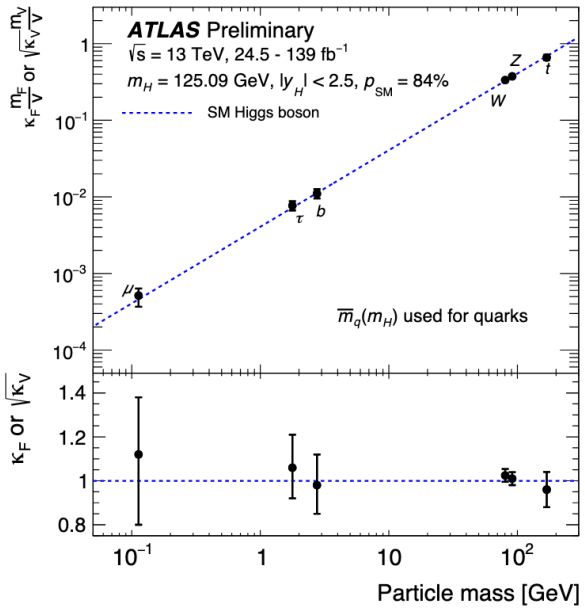

(a)

Figure 7.26 – The upper pad shows the reduced coupling modifiers for fermions and bosons as function of their masses. The dotted line corresponds to the SM prediction and the black error bars correspond to the 68% CL measurement from Higgs combination. The lower pad corresponds to the ratio to the SM prediction [122].

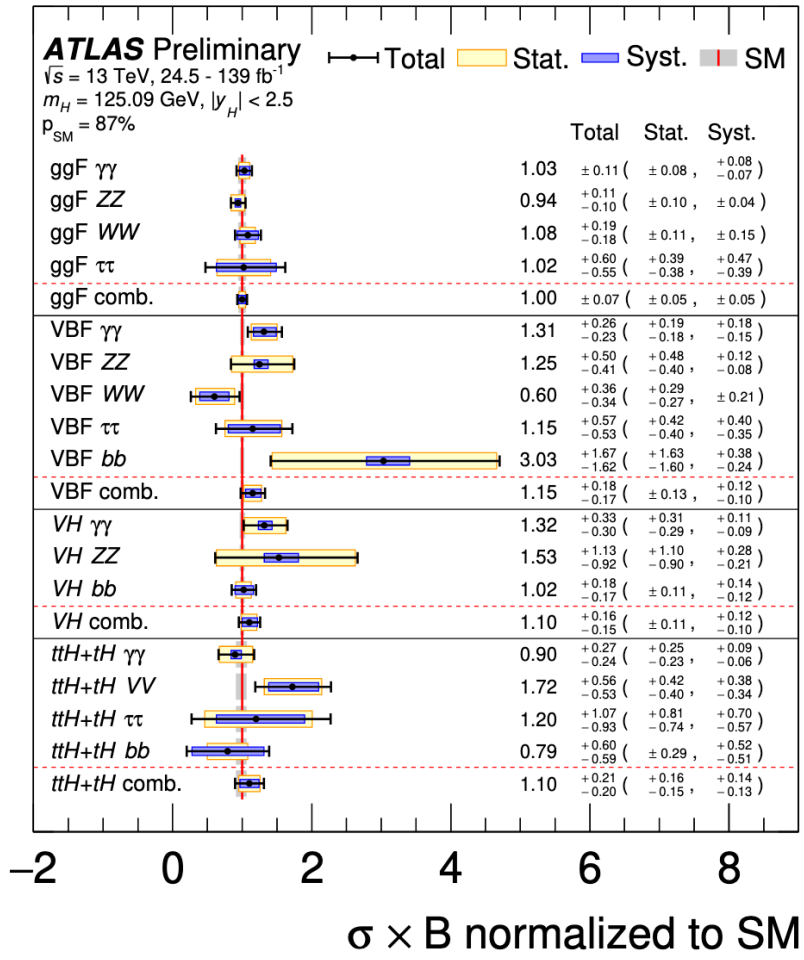

(a)

Figure 7.27 – Cross sections times branching fraction for four production modes (ggF, VBF, VH and ttH+th) in each relevant decay mode, normalized to their SM predictions. The results of these measurements are obtained from a combined fit to all the channels. Modes which are not shown in this Figure are fixed to the SM prediction [122].

Conclusion

During the ATLAS detector Phase-II upgrade which is planned to take place between 2024 and 2026, the liquid argon calorimeter readout electronics will be replaced to handle the increase in the LHC delivered luminosity. Two early pre-amplifier prototypes for the upgrade were tested to examine their behavior and to check if they match the physics requirements. The results of the tests that I conducted are presented in this thesis and show that the proposed designs have a large enough dynamic range with excellent linearity. The tests also revealed that the electronics noise is not yet at the desired level. Finally, I have performed a simulation study to choose the optimal gain ratio of the pre-amplifiers for the new proposed gain scheme, which is important to reduce intercalibration uncertainties in analyses measuring the mass of the Higgs boson. The results of the characterisation allowed to highlight the features to improve in the design of the next iteration of electronics. Because of my work, the performance of the current iterations (two generations later) is expected to comply with all the specifications, so that a final design for the upgrade will be selected in 2020 after comparing their performance using the same criteria as for LAUROC0 and HLC1.

The measurements of the Higgs boson produced alongside a vector boson and decaying to a pair of b-quarks allow to carry out precision measurements of the Standard Model predictions and constrain new physics. The measurements were performed using the full dataset collected by the ATLAS detector during Run-2 corresponding to $139\,\text{fb}^{-1}$ of data, using p-p collisions at a center-of-mass energy of 13 TeV. My contributions to the analysis are presented in this thesis and include many techniques developed to improve the analysis sensitivity and studies performed to assess the robustness of the fit model.

My initial involvement in the analysis was to focus on the analysis of the 1-lepton channel, starting with defining the signal and control region in this channel and then generalise the categorisation to all of the analysis channels. These regions are designed in a way to have control regions enriched in dedicated backgrounds and low signal acceptance. The fit model was studied to choose the discriminant variable to fit in the control regions and to make sure that with the new categorisation background modelling uncertainties are well controlled.

The multi-jet background estimation is also presented in this thesis. This background has a small contribution (less than 5%) in the 1-lepton channel and a negligible contribution in the other channels, and cannot be reliably modelled using Monte Carlo generators. Thereby, a data-driven method is implemented to obtain the shape and fix the normalisation of this background using the template fit method. Multiple sources of shape and normalisation uncertainties are assigned to this estimation to accurately model this background process.

In addition, I have developed a new method to estimate modelling shape uncertainties of the $t\bar{t}$ background using boosted decision trees (BDTs). It consists on training a BDT to separate between the nominal generator used in the analysis for the background template and alternative

generators. This method allows to parametrise the difference between the two generators in the relevant different corners of the phase space using kinematic variables. In the future this method can be used for the estimation of the shape uncertainties of all main backgrounds.

The $VH(H \to b\bar{b})$ MVA fit yielded the observation of the VH signal where the signal strength, which is the ratio of the observed signal yield to the expected yield, was measured to be $\mu_{VH}^{bb} = 1.02^{+0.12}_{-0.11}(\text{Stat})^{+0.14}_{-0.13}(\text{Syst})$ and in agreement with the Standard Model expectations. The ZH and WH signals were measured simultaneously, yielding an observation of the ZH signal with 5.3σ (expected 5.1σ) and strong evidence for the WH signal with 4.0σ (expected 4.1σ). These measurements were performed in the context of the simplified template cross-section (STXS) in 5 bins defined depending on the p_T of the vector boson. All the measurements were found to be in excellent agreement with the Standard Model predictions. The MVA results were cross-checked with the di-jet mass analysis that focused on m_{bb} instead of the BDT_{VH} discriminant. The cross-check analysis also lead to the observation of the VH signal with 5.5σ (expected 4.9σ). I have compared the results of the MVA and the di-jet mass analyses using the bootstrap method based only on the statistical fluctuations of data and the two measurements were found to be in agreement within 1σ. Finally, the results of the diboson fit focusing on the BDT_{VZ} discriminant are in good agreement with the Standard Model with $\mu_{VZ}^{bb} = 0.93^{+0.07}_{-0.06}(\text{Stat})^{+0.14}_{-0.12}(\text{Syst})$, thus allowing to validate the MVA fit results.

The results of the $VH(H \to b\bar{b})$ analysis presented in this manuscript were also interpreted using the effective field theory (EFT) approach where constraints on the EFT operators affecting the $VH(H \to b\bar{b})$ channel were set [116] and were used in the Higgs combination [122].

In the analysis, the uncertainties are not limited to a single source, so to further improve the results in the next iteration of the analysis it will be difficult to go and improve all the methods used in the analysis. However, it is possible to improve the following aspects that currently have the largest impact in the analysis: use generators for the background modelling with more filters to increase the Monte Carlo statistic and thus to decrease the uncertainty, use better alternative generator to have a better estimation of the modeling systematics, extend the BDT-based systematic uncertainties to all background processes to have a better estimation of the shape uncertainties and finally improve the b-tagging algorithms and therefore reduce their uncertainties.

Currently ATLAS has produced a specific $VH(H \to b\bar{b})$ analysis in the boosted regime, looking for the Higgs boson produced at a higher vector boson transverse momentum (p_T^V), which is not orthogonal to the analysis presented in this manuscript [123]. On the longer time scale, the combination of the two analyses will benefit from novel technologies to improve the overall sensitivity and will allow to have better precision at high p_T^V, in particular for $p_T^V > 400\,\text{GeV}$. Therefore for the combination of the two analyses, the STXS measurements will include an additional category for events with $p_T^V > 400\,\text{GeV}$ and be closer to the recommended STXS binning scheme. Another motivation for the combination is that the Higgs boson is sensitive to new physics at a high energy scale, therefore making differential measurements with bins at higher p_T^V is very beneficial.

Acknowledgments

First I would like to thank Marie-Hélène Schune for accepting to be the president of the jury, the referees André David and Marco Delmastro and the examiners Tim Scanlon and William Murray for taking part in my jury and for reading my manuscript.

I would like to thank the director of the lab Achille Stocchi for welcoming me to the lab for the first time for my master's internship and then for my thesis.

I would like to express my gratitude to my supervisor Nicolas Morange. I have really enjoyed working with you for the last three years. Thank you for your guidance, support and for giving me the opportunity to work on very interesting and challenging topics. Your advice and encouragement allowed me to push my curiosity, strengthen my knowledge and always want to go further in my studies. I have learned a lot from you these past three years and I will always appreciate it.

A big thank you goes to the members of the Hbb group at IJCLab, especially Jean-François Grivaz for all our discussions, for transmitting to me all your knowledge about the estimation of the multi-jet background and benefiting from your expertise to understand a lot of the analysis aspects. I received tremendous help and support from the previous members: Charles, Tasneem, Arthur and Yanhui, who taught me a lot about the analysis and gave me the needed kick start when I arrived in the group. I also wish to thank the members of the group at LPHNE, especially Louis and Ilaria, as well as the hard working VHbb group at CERN. I really enjoyed working with you and I am very grateful for the opportunity to share the wonderful results of this analysis with you.

I also would like to thank Jean-Baptiste De Vivie and Laurent Duflot for reviewing my manuscript and for their comments which helped me improve it.

I would like to thank all the members of the ATLAS group at IJCLab for their support.

I enjoyed the time I spent with other students and postdocs in the group: Christina, Anastasia, Tobias, Laurent and Erwann for the long discussions about anything and everything during the lunch break and which most of the time extended to the coffee breaks; Aishik for answering all my questions about machine learning, for your company during the breaks we took while our codes were running and the hang outs in Paris; Antoine for always leaving your office door open for my questions and most important for teaching me French expressions that I still use to this day; Finally Corentin for all your stories about Brittany, for coming with me to discover new corners of Paris, for the Louvre visits on Saturdays and the sushi dinners on Thursday.

I also thank all my friends, Elie, Linea, Marleine, Mykola, Jad and Elise, as I am really grateful for all the memories and for your support during the last three years.

Je remercie mes parents et mes soeurs qui ont toujours été présents à mes cotés malgré la

distance, ainsi que ma famille à Paris. Vous m'avez toujours soutenu et c'est en partie grace à votre soutient que j'ai réussi ma thèse.

Abschließend möchte ich mich bei jemandem bedanken, der mir sehr wichtig ist, Manuel. Danke, dass du immer für mich da bist, durch die Höhen und Tiefen. Vielen Dank für deine Unterstützung und Liebe in den letzten drei Jahren.

Bibliography

[1] The ATLAS Collaboration. *Observation of a new particle in the search for the Standard Model Higgs boson with the ATLAS detector at the LHC*. 2012. DOI: 10.1016/j.physletb.2012.08.020. arXiv: 1207.7214 [hep-ex]. URL: http://dx.doi.org/10.1016/j.physletb.2012.08.020 (Cited on pages 13, 22, 24)

[2] The CMS Collaboration. *Observation of a new boson at a mass of 125 GeV with the CMS experiment at the LHC*. 2012. DOI: 10.1016/j.physletb.2012.08.021. arXiv: 1207.7235 [hep-ex]. URL: http://dx.doi.org/10.1016/j.physletb.2012.08.021 (Cited on pages 13, 22–24)

[3] M. Tanabashi et al. "Review of Particle Physics". *Phys. Rev. D* 98 (3 2018), p. 030001. DOI: 10.1103/PhysRevD.98.030001. URL: https://link.aps.org/doi/10.1103/PhysRevD.98.030001 (Cited on pages 14, 15)

[4] S.M. Bilenky, C. Giunti, and W. Grimus. "Phenomenology of neutrino oscillations". *Progress in Particle and Nuclear Physics* 43 (1999), 1–86. ISSN: 0146-6410. DOI: 10.1016/s0146-6410(99)00092-7. URL: http://dx.doi.org/10.1016/S0146-6410(99)00092-7 (Cited on page 14)

[5] Abdus Salam. "Weak and Electromagnetic Interactions". *Conf. Proc.* C680519 (1968), pp. 367–377. DOI: 10.1142/9789812795915_0034 (Cited on page 15)

[6] M. Gell-Mann. "The interpretation of the new particles as displaced charge multiplets". *Nuovo Cim.* 4.S2 (1956), pp. 848–866. DOI: 10.1007/BF02748000 (Cited on page 15)

[7] Tadao Nakano and Kazuhiko Nishijima. "Charge Independence for V-particles*". *Progress of Theoretical Physics* 10.5 (Nov. 1953), pp. 581–582. ISSN: 0033-068X. DOI: 10.1143/PTP.10.581. eprint: https://academic.oup.com/ptp/article-pdf/10/5/581/5364926/10-5-581.pdf. URL: https://doi.org/10.1143/PTP.10.581 (Cited on page 15)

[8] Andrey Grozin. *Quantum Chromodynamics*. 2012. arXiv: 1205.1815 [hep-ph] (Cited on page 17)

[9] ATLAS Collaboration. *Measurement of the W-boson mass in pp collisions at $\sqrt{s} = 7$ TeV with the ATLAS detector*. 2017. arXiv: 1701.07240 [hep-ex] (Cited on page 17)

[10] The ALEPH Collaboration, the DELPHI Collaboration, the L3 Collaboration, the OPAL Collaboration, the SLD Collaboration, the LEP Electroweak Working Group, the SLD electroweak, and heavy flavour groups. *Precision Electroweak Measurements on the Z Resonance*. 2005. DOI: 10.1016/j.physrep.2005.12.006. arXiv: hep-ex/0509008 [hep-ex]. URL: http://dx.doi.org/10.1016/j.physrep.2005.12.006 (Cited on page 17)

[11] F Englert and R Brout. "Broken symmetry and the masses of gauge vector mesons". *Phys. Rev. Lett.* 13 (1964), pp. 321–323. DOI: 10.1103/PhysRevLett.13.321. URL: http://cds.cern.ch/record/641592 (Cited on page 17)

[12] Peter W. Higgs. "Broken Symmetries and the Masses of Gauge Bosons". *Phys. Rev. Lett.* 13 (16 1964), pp. 508–509. DOI: 10.1103/PhysRevLett.13.508. URL: https://link.aps.org/doi/10.1103/PhysRevLett.13.508 (Cited on page 17)

[13] M. Tanabashi et al. "Review of Particle Physics". *Phys. Rev. D* 98 (3 2018), p. 030001. DOI: 10.1103/PhysRevD.98.030001. URL: https://link.aps.org/doi/10.1103/PhysRevD.98.030001 (Cited on page 19)

[14] URL: https://twiki.cern.ch/twiki/bin/view/LHCPhysics/HiggsEuropeanStrategy (Cited on page 21)

[15] LHC Higgs Cross Section Working Group. "Handbook of LHC Higgs Cross Sections: 4. Deciphering the Nature of the Higgs Sector" (2016). DOI: 10.2172/1345634,10.23731/CYRM-2017-002. arXiv: 1610.07922 [hep-ph] (Cited on pages 21, 25, 87)

[16] A. Lopez-Fernandez, J. C. Romão, F. de Campos, and J. W. F. Valle. *Model Independent Higgs Boson Mass Limits at LEP*. 1993. DOI: 10.1016/0370-2693(93)90518-m. arXiv: hep-ph/9304255 [hep-ph]. URL: http://dx.doi.org/10.1016/0370-2693(93)90518-M (Cited on page 22)

[17] Yuri Oksuzian. *Searches for the Higgs boson at the Tevatron*. 2012. DOI: 10.1063/1.4826714. arXiv: 1209.1586 [hep-ex]. URL: http://dx.doi.org/10.1063/1.4826714 (Cited on page 22)

[18] CDF Collaboration and D0 Collaboration. *Evidence for a particle produced in association with weak bosons and decaying to a bottom-antibottom quark pair in Higgs boson searches at the Tevatron*. 2012. DOI: 10.1103/physrevlett.109.071804. arXiv: 1207.6436 [hep-ex]. URL: http://dx.doi.org/10.1103/PhysRevLett.109.071804 (Cited on page 22)

[19] CDF and D0 Collaborations. *Higgs Boson Studies at the Tevatron*. 2013. DOI: 10.1103/physrevd.88.052014. arXiv: 1303.6346 [hep-ex]. URL: http://dx.doi.org/10.1103/PhysRevD.88.052014 (Cited on pages 22, 23)

[20] the L3 Collaboration the ALEPH Collaboration The DELPHI Collaboration and The LEP Working Group for Higgs Boson Searches the OPAL Collaboration. *Search for the Standard Model Higgs Boson at LEP*. 2003. DOI: 10.1016/s0370-2693(03)00614-2. arXiv: hep-ex/0306033 [hep-ex]. URL: http://dx.doi.org/10.1016/S0370-2693(03)00614-2 (Cited on page 23)

[21] ATLAS Collaboration. *Combined search for the Standard Model Higgs boson in pp collisions at sqrt(s) = 7 TeV with the ATLAS detector*. 2012. DOI: 10.1103/physrevd.86.032003. arXiv: 1207.0319 [hep-ex]. URL: http://dx.doi.org/10.1103/PhysRevD.86.032003 (Cited on page 22)

[22] CMS Collaboration. *Combined results of searches for the standard model Higgs boson in pp collisions at sqrt(s) = 7 TeV*. 2012. arXiv: 1202.1488 [hep-ex] (Cited on page 22)

[23] ATLAS and CMS Collaborations. *Combined Measurement of the Higgs Boson Mass in pp Collisions at $\sqrt{s} = 7$ and 8 TeV with the ATLAS and CMS Experiments*. 2015. arXiv: 1503.07589 [hep-ex] (Cited on page 24)

[24] CMS Collaboration. *Inclusive search for a highly boosted Higgs boson decaying to a bottom quark-antiquark pair*. 2017. arXiv: 1709.05543 [hep-ex] (Cited on page 25)

[25] *Search for boosted resonances decaying to two b-quarks and produced in association with a jet at $\sqrt{s} = 13$ TeV with the ATLAS detector*. Tech. rep. ATLAS-CONF-2018-052. Geneva: CERN, 2018. URL: http://cds.cern.ch/record/2649081 (Cited on page 25)

[26] *Search for the standard model Higgs boson produced through vector boson fusion and decaying to bb with proton-proton collisions at sqrt(s) = 13 TeV*. Tech. rep. CMS-PAS-HIG-16-003. Geneva: CERN, 2016. URL: https://cds.cern.ch/record/2160154 (Cited on page 25)

[27] ATLAS Collaboration. *Search for Higgs bosons produced via vector-boson fusion and decaying into bottom quark pairs in* $\sqrt{s} = 13$ TeV *pp collisions with the ATLAS detector*. 2018. arXiv: 1807.08639 [hep-ex] (Cited on page 25)

[28] Emidio Gabrielli, Fabio Maltoni, Barbara Mele, Mauro Moretti, Fulvio Piccinini, and Roberto Pittau. "Higgs boson production in association with a photon in vector boson fusion at the LHC". *Nuclear Physics B* 781.1-3 (2007), 64–84. ISSN: 0550-3213. DOI: 10.1016/j.nuclphysb.2007.05.010. URL: http://dx.doi.org/10.1016/j.nuclphysb.2007.05.010 (Cited on page 25)

[29] *Search for Higgs boson production via weak boson fusion and decaying to* $b\bar{b}$ *in association with a high-energy photon in the ATLAS detector*. Tech. rep. ATLAS-CONF-2016-063. Geneva: CERN, 2016. URL: http://cds.cern.ch/record/2206201 (Cited on page 25)

[30] ATLAS Collaboration. *Search for the Standard Model Higgs boson produced in association with top quarks and decaying into a* $b\bar{b}$ *pair in pp collisions at* $\sqrt{s} = 13$ *TeV with the ATLAS detector*. 2017. arXiv: 1712.08895 [hep-ex] (Cited on page 25)

[31] CMS Collaboration. *Search for* $t\bar{t}H$ *production in the* $H \to b\bar{b}$ *decay channel with leptonic* $t\bar{t}$ *decays in proton-proton collisions at* $\sqrt{s} = 13$ *TeV*. 2018. arXiv: 1804.03682 [hep-ex] (Cited on page 25)

[32] ATLAS Collaboration. *Evidence for the* $H \to b\bar{b}$ *decay with the ATLAS detector*. 2017. arXiv: 1708.03299 [hep-ex] (Cited on page 25)

[33] CMS Collaboration. *Evidence for the Higgs boson decay to a bottom quark-antiquark pair*. 2017. DOI: 10.1016/j.physletb.2018.02.050. arXiv: 1709.07497 [hep-ex]. URL: http://dx.doi.org/10.1016/j.physletb.2018.02.050 (Cited on page 25)

[34] ATLAS Collaboration. *Observation of* $H \to b\bar{b}$ *decays and VH production with the ATLAS detector*. 2018. DOI: 10.1016/j.physletb.2018.09.013. arXiv: 1808.08238 [hep-ex]. URL: http://dx.doi.org/10.1016/j.physletb.2018.09.013 (Cited on pages 25–27, 110)

[35] CMS Collaboration. *Observation of Higgs boson decay to bottom quarks*. 2018. DOI: 10.1103/physrevlett.121.121801. arXiv: 1808.08242 [hep-ex]. URL: http://dx.doi.org/10.1103/PhysRevLett.121.121801 (Cited on pages 25, 26)

[36] ATLAS and CMS Collaborations. *Measurements of the Higgs boson production and decay rates and constraints on its couplings from a combined ATLAS and CMS analysis of the LHC pp collision data at* $\sqrt{s} = 7$ *and 8 TeV*. 2016. arXiv: 1606.02266 [hep-ex] (Cited on page 27)

[37] CMS Collaboration. *Observation of* $t\bar{t}H$ *production*. 2018. arXiv: 1804.02610 [hep-ex] (Cited on page 27)

[38] ATLAS Collaboration. *Observation of Higgs boson production in association with a top quark pair at the LHC with the ATLAS detector*. 2018. arXiv: 1806.00425 [hep-ex] (Cited on page 27)

[39] A. M. Sirunyan, A. Tumasyan, W. Adam, F. Ambrogi, T. Bergauer, M. Dragicevic, J. Erö, A. Escalante Del Valle, M. Flechl, and et al. "A search for the standard model Higgs boson decaying to charm quarks". *Journal of High Energy Physics* 2020.3 (2020). ISSN: 1029-8479. DOI: 10.1007/jhep03(2020)131. URL: http://dx.doi.org/10.1007/JHEP03(2020)131 (Cited on page 27)

[40] ATLAS Collaboration. *A search for the dimuon decay of the Standard Model Higgs boson with the ATLAS detector*. 2020. arXiv: 2007.07830 [hep-ex] (Cited on page 27)

[41] CMS Collaboration. *Evidence for Higgs boson decay to a pair of muons*. 2020. arXiv: 2009.04363 [hep-ex] (Cited on page 27)

[42] CMS Collaboration. *Combined measurements of Higgs boson couplings in proton-proton collisions at $\sqrt{s} = 13$ TeV*. 2018. DOI: 10.1140/epjc/s10052-019-6909-y. arXiv: 1809.10733 [hep-ex]. URL: http://dx.doi.org/10.1140/epjc/s10052-019-6909-y (Cited on pages 27, 28)

[43] ATLAS Collaboration. *Combined measurements of Higgs boson production and decay using up to 80 fb^{-1} of proton-proton collision data at $\sqrt{s} = 13$ TeV collected with the ATLAS experiment*. 2019. DOI: 10.1103/physrevd.101.012002. arXiv: 1909.02845 [hep-ex]. URL: http://dx.doi.org/10.1103/PhysRevD.101.012002 (Cited on pages 27, 29)

[44] Planck Collaboration et al. *Planck 2015 results. XIV. Dark energy and modified gravity*. 2015. arXiv: 1502.01590 [astro-ph.CO] (Cited on page 28)

[45] LHC Higgs Cross Section Working Group, A. David, A. Denner, M. Duehrssen, M. Grazzini, C. Grojean, G. Passarino, M. Schumacher, M. Spira, G. Weiglein, and M. Zanetti. *LHC HXSWG interim recommendations to explore the coupling structure of a Higgs-like particle*. 2012. arXiv: 1209.0040 [hep-ph] (Cited on page 30)

[46] Andre Sopczak. *Precision Measurements in the Higgs Sector at ATLAS and CMS*. 2020. arXiv: 2001.05927 [hep-ex] (Cited on page 30)

[47] *LHC HIGGS CROSS SECTION WORKING GROUP, Nicolas Berger and Claudia Bertella and Thomas P. Calvet and Milene Calvetti and Valerio Dao and Marco Delmastro and Michael Duehrssen-Debling and Paolo Francavilla and Yacine Haddad and Oleh Kivernyk and Jonathon M. Langford and Changqiao Li and Giovanni Marchiori and Predrag Milenovic and Carlo E. Pandini and Edward Scott and Frank J. Tackmann and Kerstin Tackmann and Lorenzo Viliani and Meng Xiao*. 2019. arXiv: 1906.02754 [hep-ph] (Cited on page 30)

[48] URL: https://twiki.cern.ch/twiki/bin/view/LHCPhysics/LHCHXSWGFiducialAndSTXS (Cited on page 31)

[49] B. Grzadkowski, M. Iskrzynski, M. Misiak, and J. Rosiek. *Dimension-Six Terms in the Standard Model Lagrangian*. 2010. arXiv: 1008.4884 [hep-ph] (Cited on pages 31, 32)

[50] Chris Hays, Veronica Sanz Gonzalez, and Gabija Zemaityte. *Constraining EFT parameters using simplified template cross sections*. Tech. rep. LHCHXSWG-2019-004. Geneva: CERN, 2019. URL: https://cds.cern.ch/record/2673969 (Cited on page 32)

[51] The ATLAS Collaboration. "The ATLAS Experiment at the CERN Large Hadron Collider". *Journal of Instrumentation* 3.08 (2008), S08003–S08003. DOI: 10.1088/1748-0221/3/08/s08003. URL: https://doi.org/10.1088%2F1748-0221%2F3%2F08%2Fs08003 (Cited on pages 33, 35)

[52] Apollinari G., Béjar Alonso I., Brüning O., Fessia P., Lamont M., Rossi L., and Tavian L. *High-Luminosity Large Hadron Collider (HL-LHC): Technical Design Report V. 0.1*. CERN Yellow Reports: Monographs. Geneva: CERN, 2017. DOI: 10.23731/CYRM-2017-004. URL: https://cds.cern.ch/record/2284929 (Cited on pages 33, 49, 51)

[53] Esma Mobs. "The CERN accelerator complex - August 2018. Complexe des accélérateurs du CERN - Août 2018" (2018). General Photo. URL: http://cds.cern.ch/record/2636343 (Cited on page 34)

[54] Oliver Sim Brüning, Paul Collier, P Lebrun, Stephen Myers, Ranko Ostojic, John Poole, and Paul Proudlock. *LHC Design Report*. CERN Yellow Reports: Monographs. Geneva: CERN, 2004. DOI: 10.5170/CERN-2004-003-V-1. URL: https://cds.cern.ch/record/782076 (Cited on page 36)

[55] CMS Collaboration. "The CMS Experiment at the CERN LHC". *JINST* 3 (2008), S08004. DOI: 10.1088/1748-0221/3/08/S08004 (Cited on page 36)

[56] LHCb Collaboration. *JINST* 3.LHCb-DP-2008-001. CERN-LHCb-DP-2008-001 (2008). Also published by CERN Geneva in 2010, S08005. DOI: 10.1088/1748-0221/3/08/S08005. URL: https://cds.cern.ch/record/1129809 (Cited on page 36)

[57] ALICE Collaboration. "The ALICE experiment at the CERN LHC. A Large Ion Collider Experiment". *JINST* 3 (2008). Also published by CERN Geneva in 2010, S08002. 259 p. DOI: 10.1088/1748-0221/3/08/S08002. URL: http://cds.cern.ch/record/1129812 (Cited on page 37)

[58] *ATLAS inner detector: Technical Design Report, 1*. Technical Design Report ATLAS. Geneva: CERN, 1997. URL: https://cds.cern.ch/record/331063 (Cited on page 39)

[59] *ATLAS liquid-argon calorimeter: Technical Design Report*. Technical Design Report ATLAS. Geneva: CERN, 1996. URL: https://cds.cern.ch/record/331061 (Cited on page 41)

[60] *ATLAS tile calorimeter: Technical Design Report*. Technical Design Report ATLAS. Geneva: CERN, 1996. URL: https://cds.cern.ch/record/331062 (Cited on page 43)

[61] Dag Gillberg and the ATLAS Liquid Argon Calorimeter Group. "Performance of the ATLAS Forward Calorimeters in First LHC Data". *Journal of Physics: Conference Series* 293 (2011), p. 012041. DOI: 10.1088/1742-6596/293/1/012041. URL: https://doi.org/10.1088%2F1742-6596%2F293%2F1%2F012041 (Cited on page 44)

[62] *ATLAS muon spectrometer: Technical Design Report*. Technical Design Report ATLAS. Geneva: CERN, 1997. URL: https://cds.cern.ch/record/331068 (Cited on page 45)

[63] *ATLAS magnet system: Technical Design Report, 1*. Technical Design Report ATLAS. Geneva: CERN, 1997. URL: https://cds.cern.ch/record/338080 (Cited on page 45)

[64] Rhys Edward Owen. "The ATLAS Trigger System" (2018). URL: https://cds.cern.ch/record/2302730 (Cited on page 46)

[65] G. Avoni et al. "The new LUCID-2 detector for luminosity measurement and monitoring in ATLAS". *JINST* 13.07 (2018), P07017. DOI: 10.1088/1748-0221/13/07/P07017 (Cited on page 46)

[66] T Gleisberg, S Höche, F Krauss, M Schönherr, S Schumann, F Siegert, and J Winter. "Event generation with SHERPA 1.1". *Journal of High Energy Physics* 2009.02 (2009), 007–007. ISSN: 1029-8479. DOI: 10.1088/1126-6708/2009/02/007. URL: http://dx.doi.org/10.1088/1126-6708/2009/02/007 (Cited on pages 48, 88)

[67] *Preconfinement as a property of perturbative QCD* (Cited on page 49)

[68] S. Agostinelli et al. "GEANT4: A Simulation toolkit". *Nucl. Instrum. Meth. A* 506 (2003), pp. 250–303. DOI: 10.1016/S0168-9002(03)01368-8 (Cited on page 49)

[69] Wolfgang Lukas. "Fast Simulation for ATLAS: Atlfast-II and ISF". *Journal of Physics: Conference Series* 396.2 (2012), p. 022031. DOI: 10.1088/1742-6596/396/2/022031. URL: https://doi.org/10.1088%2F1742-6596%2F396%2F2%2F022031 (Cited on page 49)

[70] G. Barrand et al. "GAUDI - A software architecture and framework for building HEP data processing applications". *Comput. Phys. Commun.* 140 (2001), pp. 45–55. DOI: 10.1016/S0010-4655(01)00254-5 (Cited on page 49)

[71] ATLAS Collaboration. *New Small Wheel Technical Design Report*. Tech. rep. CERN-LHCC-2013-006. ATLAS-TDR-020. ATLAS New Small Wheel Technical Design Report. 2013. URL: https://cds.cern.ch/record/1552862 (Cited on page 50)

[72] ATLAS Collaboration. *Technical Design Report for the ATLAS Inner Tracker Pixel Detector*. Tech. rep. CERN-LHCC-2017-021. ATLAS-TDR-030. Geneva: CERN, 2017. URL: http://cds.cern.ch/record/2285585 (Cited on page 50)

[73] ATLAS Collaboration. *Technical Design Report for the ATLAS Inner Tracker Strip Detector*. Tech. rep. CERN-LHCC-2017-005. ATLAS-TDR-025. Geneva: CERN, 2017. URL: http://cds.cern.ch/record/2257755 (Cited on page 50)

[74] ATLAS Collaboration. *Technical Design Report for the Phase-II Upgrade of the ATLAS LAr Calorimeter*. Tech. rep. CERN-LHCC-2017-018. ATLAS-TDR-027. Geneva: CERN, 2017. URL: http://cds.cern.ch/record/2285582 (Cited on pages 56, 62, 63)

[75] ATLAS Collaboration. *Measurement of Higgs boson production in the diphoton decay channel in pp collisions at center-of-mass energies of 7 and 8 TeV with the ATLAS detector*. 2014. arXiv: 1408.7084 [hep-ex] (Cited on page 58)

[76] ATLAS Collaboration. *Measurement of the Higgs boson mass in the $H \to ZZ^* \to 4\ell$ and $H \to \gamma\gamma$ channels with $\sqrt{s} = 13$ TeV pp collisions using the ATLAS detector*. 2018. arXiv: 1806.00242 [hep-ex] (Cited on page 58)

[77] Simone Alioli, Paolo Nason, Carlo Oleari, and Emanuele Re. "A general framework for implementing NLO calculations in shower Monte Carlo programs: the POWHEG BOX". *Journal of High Energy Physics* 2010.6 (2010). ISSN: 1029-8479. DOI: 10.1007/jhep06(2010)043. URL: http://dx.doi.org/10.1007/JHEP06(2010)043 (Cited on page 58)

[78] Jon Butterworth, Stefano Carrazza, Amanda Cooper-Sarkar, Albert De Roeck, Joël Feltesse, Stefano Forte, Jun Gao, Sasha Glazov, Joey Huston, Zahari Kassabov, and et al. "PDF4LHC recommendations for LHC Run II". *Journal of Physics G: Nuclear and Particle Physics* 43.2 (2016), p. 023001. ISSN: 1361-6471. DOI: 10.1088/0954-3899/43/2/023001. URL: http://dx.doi.org/10.1088/0954-3899/43/2/023001 (Cited on pages 58, 134)

[79] Torbjörn Sjöstrand, Stephen Mrenna, and Peter Skands. "A brief introduction to PYTHIA 8.1". *Computer Physics Communications* 178.11 (2008), 852–867. ISSN: 0010-4655. DOI: 10.1016/j.cpc.2008.01.036. URL: http://dx.doi.org/10.1016/j.cpc.2008.01.036 (Cited on pages 58, 86)

[80] W.E. Cleland and E.G. Stern. "Signal processing considerations for liquid ionization calorimeters in a high rate environment". *Nucl. Instrum. Meth. A* 338.2-3 (1994), pp. 467–497. DOI: 10.1016/0168-9002(94)91332-3 (Cited on page 68)

[81] ATLAS Liquid Argon group. *Internal communications*. (Cited on pages 70, 71)

[82] ATLAS Collaboration. *Reconstruction of primary vertices at the ATLAS experiment in Run 1 proton-proton collisions at the LHC*. 2016. DOI: 10.1140/epjc/s10052-017-4887-5. arXiv: 1611.10235 [physics.ins-det]. URL: http://dx.doi.org/10.1140/epjc/s10052-017-4887-5 (Cited on page 73)

[83] R Frühwirth. "Application of Kalman filtering to track and vertex fitting". *Nucl. Instrum. Methods Phys. Res., A* 262.HEPHY-PUB-503 (1987), 444. 19 p. URL: https://cds.cern.ch/record/178627 (Cited on pages 73, 74)

[84] ATLAS Collaboration. *Performance of the ATLAS Track Reconstruction Algorithms in Dense Environments in LHC Run 2*. 2017. arXiv: 1704.07983 [hep-ex] (Cited on page 73)

[85] ATLAS Collaboration. *Electron and photon performance measurements with the ATLAS detector using the 2015-2017 LHC proton-proton collision data*. 2019. DOI: 10.1088/1748-0221/14/12/p12006. arXiv: 1908.00005 [hep-ex]. URL: http://dx.doi.org/10.1088/1748-0221/14/12/P12006 (Cited on pages 74–77)

[86] T Cornelissen, M Elsing, S Fleischmann, W Liebig, E Moyse, and A for the ATLAS Inner Detector Software Group Salzburger. *Concepts, Design and Implementation of the ATLAS New Tracking (NEWT)*. Tech. rep. ATL-SOFT-PUB-2007-007. ATL-COM-SOFT-2007-002. Geneva: CERN, 2007. URL: https://cds.cern.ch/record/1020106 (Cited on page 74)

[87] T G Cornelissen, M Elsing, I Gavrilenko, J-F Laporte, W Liebig, M Limper, K Nikolopoulos, A Poppleton, and A Salzburger. "The global χ^2track fitter in ATLAS". *Journal of Physics: Conference Series* 119.3 (2008), p. 032013. DOI: 10.1088/1742-6596/119/3/032013. URL: https://doi.org/10.1088%2F1742-6596%2F119%2F3%2F032013 (Cited on page 74)

[88] *Electron and photon reconstruction and performance in ATLAS using a dynamical, topological cell clustering-based approach*. Tech. rep. ATL-PHYS-PUB-2017-022. Geneva: CERN, 2017. URL: https://cds.cern.ch/record/2298955 (Cited on page 74)

[89] ATLAS Collaboration. *Electron and photon energy calibration with the ATLAS detector using 2015-2016 LHC proton-proton collision data*. 2018. arXiv: 1812.03848 [hep-ex] (Cited on page 75)

[90] ATLAS Collaboration. *Muon reconstruction performance of the ATLAS detector in proton–proton collision data at $\sqrt{s}$=13 TeV*. 2016. arXiv: 1603.05598 [hep-ex] (Cited on pages 78, 79)

[91] Matteo Cacciari, Gavin P Salam, and Gregory Soyez. "The anti-ktjet clustering algorithm". *Journal of High Energy Physics* 2008.04 (2008), 063–063. ISSN: 1029-8479. DOI: 10.1088/1126-6708/2008/04/063. URL: http://dx.doi.org/10.1088/1126-6708/2008/04/063 (Cited on page 79)

[92] ATLAS Collaboration. *Determination of jet calibration and energy resolution in proton-proton collisions at $\sqrt{s}$ = 8 TeV using the ATLAS detector*. 2019. arXiv: 1910.04482 [hep-ex] (Cited on page 80)

[93] *Tagging and suppression of pileup jets with the ATLAS detector*. Tech. rep. ATLAS-CONF-2014-018. Geneva: CERN, 2014. URL: https://cds.cern.ch/record/1700870 (Cited on pages 80, 81, 91)

[94] *Optimisation and performance studies of the ATLAS b-tagging algorithms for the 2017-18 LHC run*. Tech. rep. ATL-PHYS-PUB-2017-013. Geneva: CERN, 2017. URL: https://cds.cern.ch/record/2273281 (Cited on page 81)

[95] *Calibration of light-flavour b-jet mistagging rates using ATLAS proton-proton collision data at $\sqrt{s}$ = 13 TeV*. Tech. rep. ATLAS-CONF-2018-006. Geneva: CERN, 2018. URL: https://cds.cern.ch/record/2314418 (Cited on page 81)

[96] ATLAS Collaboration. *ATLAS b-jet identification performance and efficiency measurement with $t\bar{t}$ events in pp collisions at $\sqrt{s}$ = 13 TeV*. 2019. arXiv: 1907.05120 [hep-ex] (Cited on pages 81, 82)

[97] ATLAS Collaboration. "Measurements of b-jet tagging efficiency with the ATLAS detector using $t\bar{t}$ events at $\sqrt{s}$ = 13 TeV". *Journal of High Energy Physics* 2018.8 (2018). ISSN: 1029-8479. DOI: 10.1007/jhep08(2018)089. URL: http://dx.doi.org/10.1007/JHEP08(2018)089 (Cited on page 81)

[98] *Measurement of the tau lepton reconstruction and identification performance in the ATLAS experiment using pp collisions at $\sqrt{s}$ = 13 TeV*. Tech. rep. ATLAS-CONF-2017-029. Geneva: CERN, 2017. URL: https://cds.cern.ch/record/2261772 (Cited on page 83)

[99] ATLAS Collaboration. *Performance of missing transverse momentum reconstruction with the ATLAS detector using proton-proton collisions at $\sqrt{s}$ = 13 TeV*. 2018. arXiv: 1802.08168 [hep-ex] (Cited on page 83)

[100] *Luminosity determination in pp collisions at $\sqrt{s}$ = 13 TeV using the ATLAS detector at the LHC*. Tech. rep. ATLAS-CONF-2019-021. Geneva: CERN, 2019. URL: https://cds.cern.ch/record/2677054 (Cited on pages 85, 115)

[101] ATLAS Collaboration. *ATLAS data quality operations and performance for 2015-2018 data-taking*. 2019. arXiv: 1911.04632 [physics.ins-det] (Cited on page 86)

[102] S. Agostinelli et al. "GEANT4: A Simulation toolkit". *Nucl. Instrum. Meth.* A506 (2003), pp. 250–303. DOI: 10.1016/S0168-9002(03)01368-8 (Cited on page 86)

[103] Keith Hamilton, Paolo Nason, and Giulia Zanderighi. "MINLO: multi-scale improved NLO". *Journal of High Energy Physics* 2012.10 (2012). ISSN: 1029-8479. DOI: 10.1007/jhep10(2012)155. URL: http://dx.doi.org/10.1007/JHEP10(2012)155 (Cited on page 86)

[104] Gionata Luisoni, Paolo Nason, Carlo Oleari, and Francesco Tramontano. "HW ±/HZ + 0 and 1 jet at NLO with the POWHEG BOX interfaced to GoSam and their merging within MiNLO". *Journal of High Energy Physics* 2013.10 (2013). ISSN: 1029-8479. DOI: 10.1007/jhep10(2013)083. URL: http://dx.doi.org/10.1007/JHEP10(2013)083 (Cited on page 86)

[105] ATLAS Collaboration. *Measurement of the Z/γ^* boson transverse momentum distribution in pp collisions at $\sqrt{s}$ = 7 TeV with the ATLAS detector*. 2014. arXiv: 1406.3660 [hep-ex] (Cited on page 86)

[106] Richard D. Ball, Valerio Bertone, Stefano Carrazza, Christopher S. Deans, Luigi Del Debbio, Stefano Forte, Alberto Guffanti, Nathan P. Hartland, José I. Latorre, and et al. "Parton distributions for the LHC run II". *Journal of High Energy Physics* 2015.4 (2015). ISSN: 1029-8479. DOI: 10.1007/jhep04(2015)040. URL: http://dx.doi.org/10.1007/JHEP04(2015)040 (Cited on page 86)

[107] Gionata Luisoni, Paolo Nason, Carlo Oleari, and Francesco Tramontano. "HW ±/HZ + 0 and 1 jet at NLO with the POWHEG BOX interfaced to GoSam and their merging within MiNLO". *Journal of High Energy Physics* 2013.10 (2013). ISSN: 1029-8479. DOI: 10.1007/jhep10(2013)083. URL: http://dx.doi.org/10.1007/JHEP10(2013)083 (Cited on page 88)

[108] *ATLAS Pythia 8 tunes to 7 TeV datas*. Tech. rep. ATL-PHYS-PUB-2014-021. Geneva: CERN, 2014. URL: https://cds.cern.ch/record/1966419 (Cited on page 88)

[109] ATLAS Collaboration. *Search for the $b\bar{b}$ decay of the Standard Model Higgs boson in associated $(W/Z)H$ production with the ATLAS detector*. 2014. arXiv: 1409.6212 [hep-ex] (Cited on page 98)

[110] Glen Cowan, Kyle Cranmer, Eilam Gross, and Ofer Vitells. "Asymptotic formulae for likelihood-based tests of new physics". *The European Physical Journal C* 71.2 (2011). ISSN: 1434-6052. DOI: 10.1140/epjc/s10052-011-1554-0. URL: http://dx.doi.org/10.1140/epjc/s10052-011-1554-0 (Cited on page 104)

[111] Manuel Bähr, Stefan Gieseke, Martyn A. Gigg, David Grellscheid, Keith Hamilton, Oluseyi Latunde-Dada, Simon Plätzer, Peter Richardson, Michael H. Seymour, Alexander Sherstnev, and et al. "Herwig++ physics and manual". *The European Physical Journal C* 58.4 (2008), 639–707. ISSN: 1434-6052. DOI: 10.1140/epjc/s10052-008-0798-9. URL: http://dx.doi.org/10.1140/epjc/s10052-008-0798-9 (Cited on page 134)

[112] J. Alwall, R. Frederix, S. Frixione, V. Hirschi, F. Maltoni, O. Mattelaer, H.-S. Shao, T. Stelzer, P. Torrielli, and M. Zaro. "The automated computation of tree-level and next-to-leading order differential cross sections, and their matching to parton shower simulations". *Journal of High Energy Physics* 2014.7 (2014). ISSN: 1029-8479. DOI: 10.1007/jhep07(2014)079. URL: http://dx.doi.org/10.1007/JHEP07(2014)079 (Cited on page 135)

[113] Johannes Bellm, Stefan Gieseke, David Grellscheid, Simon Plätzer, Michael Rauch, Christian Reuschle, Peter Richardson, Peter Schichtel, Michael H. Seymour, Andrzej Siódmok, and et al. "Herwig 7.0/Herwig++ 3.0 release note". *The European Physical Journal C* 76.4 (2016). ISSN: 1434-6052. DOI: 10.1140/epjc/s10052-016-4018-8. URL: http://dx.doi.org/10.1140/epjc/s10052-016-4018-8 (Cited on page 135)

[114] Glen Cowan, Kyle Cranmer, Eilam Gross, and Ofer Vitells. "Asymptotic formulae for likelihood-based tests of new physics". *The European Physical Journal C* 71.2 (2011). ISSN: 1434-6052. DOI: 10.1140/epjc/s10052-011-1554-0. URL: http://dx.doi.org/10.1140/epjc/s10052-011-1554-0 (Cited on pages 151, 154)

[115] Tommaso Dorigo. "Extraordinary claims: the 0.000029% solution". *EPJ Web Conf.* 95 (2015). Ed. by L. Bravina, Y. Foka, and S. Kabana, p. 02003. DOI: 10.1051/epjconf/20149502003 (Cited on page 151)

[116] ATLAS Collaboration. *Measurements of WH and ZH production in the $H \to b\bar{b}$ decay channel in pp collisions at 13 TeV with the ATLAS detector*. 2020. arXiv: 2007.02873 [hep-ex] (Cited on pages 155, 186)

[117] ATLAS Collaboration. "Measurements of the production cross-section for a Z boson in association with b-jets in proton-proton collisions at

$$\sqrt{s}$$

= 13 TeV with the ATLAS detector". *Journal of High Energy Physics* 2020.7 (2020). ISSN: 1029-8479. DOI: 10.1007/jhep07(2020)044. URL: http://dx.doi.org/10.1007/JHEP07(2020)044 (Cited on page 159)

[118] *Measurement of the associated production of a Higgs boson decaying to b quarks with a vector boson at high transverse momentum in pp collisions at $\sqrt{s}$ = 13 TeV with the ATLAS detector*. Tech. rep. ATLAS-CONF-2020-007. Geneva: CERN, 2020. URL: http://cds.cern.ch/record/2715063 (Cited on page 169)

[119] ATLAS Collaboration. *Measurement of VH, $H \to b\bar{b}$ production as a function of the vector-boson transverse momentum in 13 TeV pp collisions with the ATLAS detector*. 2019. arXiv: 1903.04618 [hep-ex] (Cited on page 169)

[120] *Evaluation of theoretical uncertainties for simplified template cross section measurements of V-associated production of the Higgs boson*. Tech. rep. ATL-PHYS-PUB-2018-035. Geneva: CERN, 2018. URL: https://cds.cern.ch/record/2649241 (Cited on page 172)

[121] Gerhard Bohm and Günter Zech. *Introduction to Statistics and Data Analysis for Physicists; 3rd revised*. Hamburg: Verlag Deutsches Elektronen-Synchrotron, 2017, p. 488. ISBN: 978-3-945931-13-4. DOI: 10.3204/PUBDB-2017-08987. URL: https://bib-pubdb1.desy.de/record/389738 (Cited on page 179)

[122] *A combination of measurements of Higgs boson production and decay using up to 139 fb^{-1} of proton–proton collision data at $\sqrt{s}$ = 13 TeV collected with the ATLAS experiment*. Tech. rep. ATLAS-CONF-2020-027. Geneva: CERN, 2020. URL: https://cds.cern.ch/record/2725733 (Cited on pages 181–183, 186)

[123] ATLAS Collaboration. *Measurement of the associated production of a Higgs boson decaying into b-quarks with a vector boson at high transverse momentum in pp collisions at* $\sqrt{s} = 13$ *TeV with the ATLAS detector*. 2020. arXiv: 2008.02508 [hep-ex] (Cited on page 186)

Chapter A

Synthèse en français

A.1 Introduction

A.1.1 Le Modèle Standard des particules

Le Modèle Standard de la physique des particules est un modèle développé dans les années 1960 pour expliquer la structure de la matière. Cette théorie décrit les particules élémentaires et 3 des 4 interactions fondamentales correspondant aux interactions électromagnétique, faible et forte. Dans cette théorie, les particules sont divisées en deux types. Le premier type correspond aux fermions qui sont les éléments qui constituent la matière et qui peut être des leptons ou des quarks. Le second type est constitué des bosons qui sont les vecteurs d'interactions: le photon pour l'interaction électromagnétique, les bosons W et Z pour l'interaction faible et le gluon pour la forte. Ces particules sont présentées dans la Figure A.1.

Le mécanisme de Brout-Englert-Higgs (BEH) implique une brisure spontanée de la symétrie électrofaible pour expliquer l'origine des masses de ces particules et prédit l'existence d'une nouvelle particule: le boson de Higgs. Cette particule a été observée pour la première fois en 2012 indépendamment par les détecteurs ATLAS et CMS confirmant cette prédiction, et complétant ainsi le contenu du Modèle Standard. Les mesures des propriétés de cette particule permettent de tester le Modèle Standard avec une grande précision et de rechercher la physique au-delà du Modèle Standard. Cette particule peut être créée par quatre principaux modes de production et peut se désintègrer dans de nombreux canaux. Par conséquent, mesurer cette particule dans tous ces canaux permet de tester très puissamment la théorie.

A.1.2 Le Grand Collisionneur de Hadrons (LHC) et l'expérience ATLAS

Le Grand Collisionneur de Hadrons est le plus grand et le plus puissant accélérateur de particules au monde. Ce collisionneur est constitué d'un système d'accélération en plusieurs étapes pour accélérer les faisceaux de protons. Les faisceaux de protons circulent sous vide, dans deux directions opposées et dans deux tuyaux différents. Les protons sont organisés en 2808 paquets contenant chacun 1.15×10^{11} particules et séparées par 25 ns. Ces protons sont guidés le long de leur trajectoire à l'intérieur du tuyau à l'aide d'aimants supraconducteurs de 8.3 T, et leur énergie est augmentée jusqu'à la valeur souhaitée à l'aide de cavités radio-fréquence.

Le détecteur ATLAS est l'une des quatre expériences placées le long de l'anneau du LHC à quatre points d'interaction différents. Le détecteur ATLAS est l'un des deux détecteurs polyvalents du LHC, de même que le détecteur CMS. Ce détecteur est composé de trois sous-détecteurs

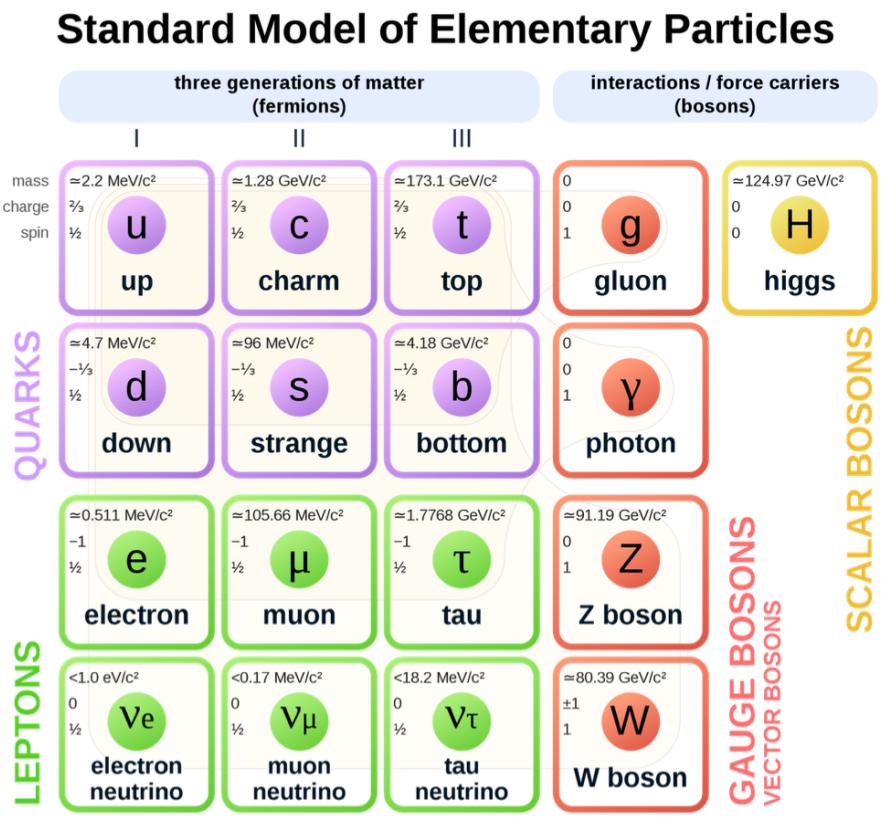

Figure A.1 – Le tableau récapitulatif des particules du Modèle Standard.

différents concentriques, construits autour du point d'interaction comme présenté dans la Figure A.2. Ces différents sous-détecteurs sont: le détecteur interne (ID) pour reconstruire les traces des particules chargées, les calorimètres électromagnétiques et hadroniques pour reconstruire l'énergie des électrons, des photons et des jets et finalement le détecteur de muons (MS) pour identifier et reconstruire l'impulsion des muons.

Le programme de physique de l'experience ATLAS est un vaste programme de physique qui comprend: les mesures de précision du Modèle Standard, la recherche d'une nouvelle physique au-delà du Modèle Standard et les mesures des propriétés du boson de Higgs. Les analyses utilisent actuellement $139\,\mathrm{fb}^{-1}$ de données accumulées lors des prises de données du Run-2 entre 2015 et 2018.

A.2 Caractérisation des préamplificateurs LAr pour le HL-LHC

A.2.1 L'électronique du calorimètre à agron liquide

La technologie à argon liquide est utlisée dans le tonneau et les bouchons du calorimètre electromagnétique ainsi que dans les bouchons du calorimètre hadronique et le calorimètre vers l'avant (*Forward calorimeter ou FCal*). C'est un calorimètre à échantillonnage utilisant de l'argon liquide pour le materiel actif et utilisant du plomb dans le calorimètre electromagnétique et du cuivre dans de calorimètre hadronique et le FCal comme absorbeur (le tungstène est utilisé comme absorbeur dans quelques modules du FCal). Le mode de fonctionnement de ce détecteur est le suivant: les particules incidentes dans le détecteur créent des gerbes électromagnétiques de particules, qui ensuite ionisent l'argon liquide pour créer des électrons. Ces électrons sont ensuite collectés par des électrodes sous l'effet d'un champ électrique. Ces électrodes sont com-

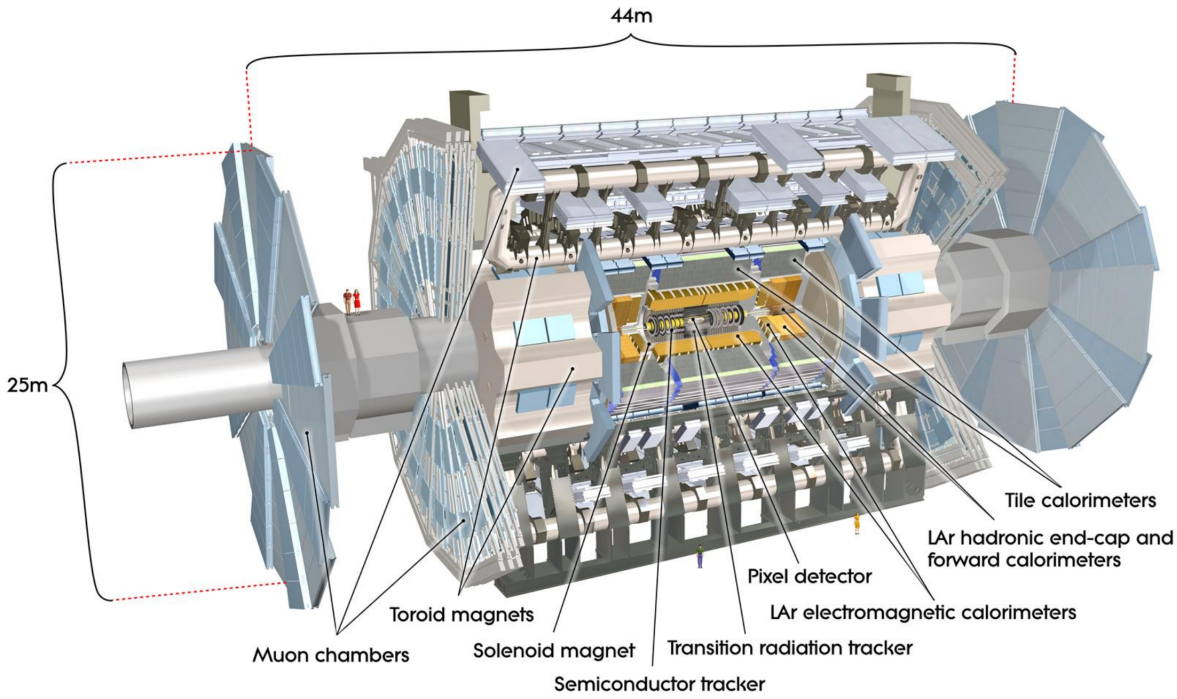

Figure A.2 – Vue du détecteur ATLAS.

posées de cuivre et de Kapton, et reçoivent le courant sous forme d'une impulsion triangulaire. Le courant provenant du détecteur est ensuite traité par l'électronique du calorimètre à argon liquide.

La chaîne électronique de traitement des signaux se compose de cartes électroniques frontales (*front-end board* ou FEB) qui sont responsables de l'amplification du signal au-dessus du bruit électronique en passant par des préamplificateur, la mise en forme du signal en une forme bipolaire à l'aide du shaper CR-$(RC)^2$ sur trois gains différents (*low, middle et high* avec un rapport de gain de 10 entre les gains) et finalement la numérisation des événements acceptés par le trigger L1 par des ADCs de 10-bits à 40 MHz.

Le HL-HLC (*high-luminosity LHC*) est un programme continuellement mis à jour, et le projet LHC à haute luminosité (HL-LHC) devrait avoir lieu après la troisième séquence de prise de données (Run-3). Ce nouveau projet vise à augmenter l'énergie jusqu'à 14 TeV et à fournir une luminosité intégrée de 3000 fb^{-1}. Afin de travailler de manière fiable sous les conditions du HL-LHC, l'électronique de lecture du calorimètre à argon liquide sera remplacée lors de la deuxième mise à jour du détecteur ATLAS (entre 2024 et 2026). La nouvelle électronique doit être conforme aux exigences physiques suivantes: avoir une gamme dynamique large pour atteindre des énergies jusqu'à 3 TeV avec une linéarité au niveau du pour mille, ansi qu'un faible bruit électronique. Finalement, le système de trois gains sera replacé par un système à deux gains avec un rapport autour de 23 entre les gains.

A.2.2 Les nouveaux designs de préamplificateurs

Deux différents modèles de préamplificateur et shaper intégrés dans un ASIC sont proposés pour la mise à jour: LAUROC0 et HLC1. Les deux modèles ont deux types différents de préamplificateurs adaptés à la ligne de sortie correspondant aux canaux 25Ω et 50Ω qui seront utilisés dans différentes parties du détecteur. Ils amplifient également le signal en deux gains de sortie: bas gain (*low*) et haut gain (*high*). La différence entre les deux modèles est que LAUROC0 est réalisé avec la technologie CMOS 130 nm tandis que HLC1 est réalisée avec

65 nm. L'autre différence principale réside dans l'architecture, où dans LAUROC0 les haut et bas gains sont tous deux fabriqués sur le même préamplificateur tandis que dans le modèle du HLC1 le préamplificateur fournit une sortie bas gain qui sera ensuite amplifié pour obtenir la sortie haut gain. Les deux modèles LAUROC0 et HLC1 sont présentés dans les Figures A.3 et A.4. Des tests ont été menés pour vérifier si les deux modèles sont conformes aux exigences et pour mettre en évidence les améliorations à effectuer dans les prochaines itérations.

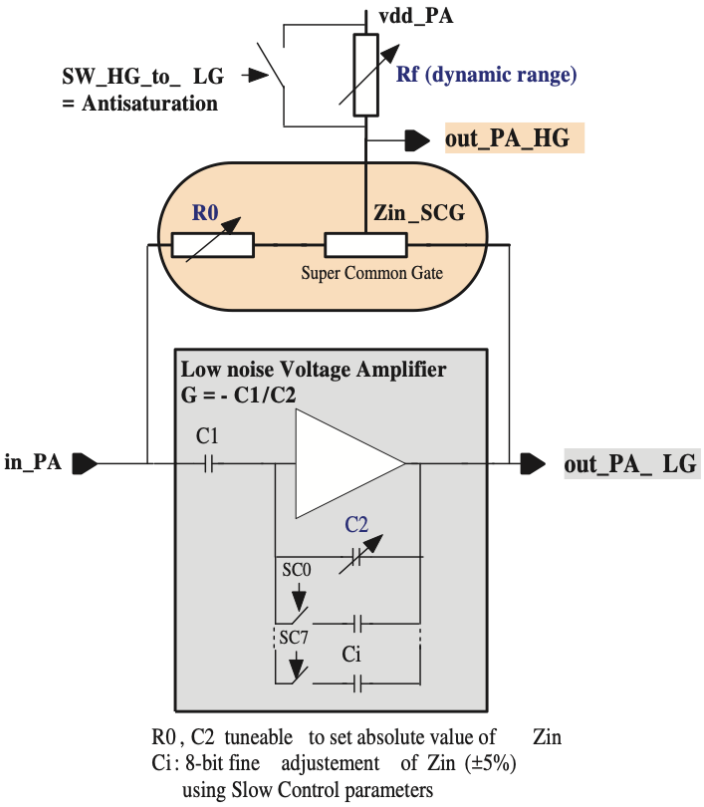

Figure A.3 – Dessin du préamplificateur implémenté dans LAUROC0.

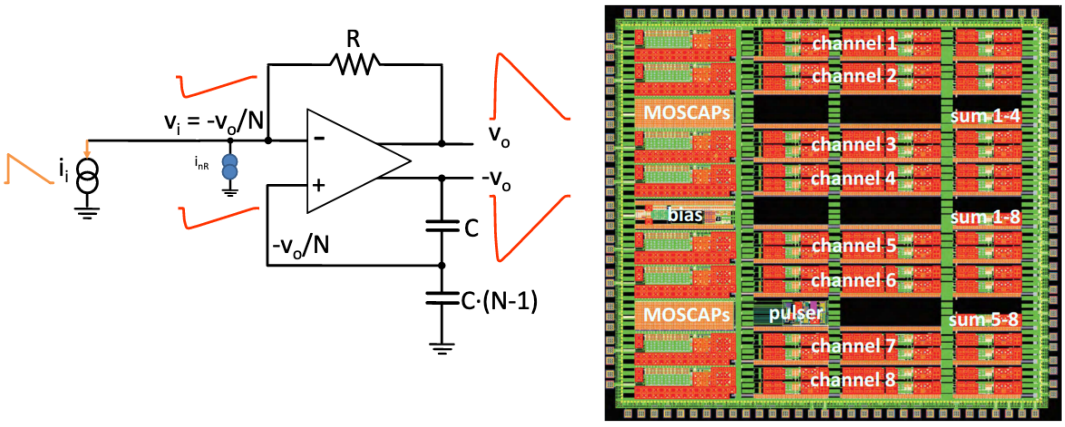

(a) **(b)**

Figure A.4 – Dessin du préamplificateur entièrement différentiel implémenté dans HLC1 en (a) et de la disposition de l'ASIC HLC1 en (b)

A.2.3 Résultats des mesures

Le premier test consistait à mesurer le niveau de bruit des préamplificateurs, qui est mesuré en tant que courant d'entrée équivalent. Les exigences physiques demandent d'avoir un bruit électronique inférieur à l'énergie minimale déposée par les muons (300 nA et 120 nA dans les canaux 25Ω et 50Ω) et idéalement équivalent à l'électronique actuelle (150 nA et 45 nA dans les canaux 25Ω et 50Ω). Le bruit mesuré s'est avéré être deux fois plus grand que le niveau attendu de la simulation des deux modèles LAUROC0 et HLC1: ∼300 nA dans le canal 25Ω et et jusqu'à ∼100 nA dans le canal 50Ω. Le bruit étant plus élevé que prévu, a été reduit dans les itérations suivantes des préamplificateurs.

Le deuxième test consiste à mesurer la linéarité et la gamme dynamique des deux modèles proposés. Les conditions requises sont une gamme dynamique allant jusqu'à 10 mA pour le canal 25Ω et 2 mA pour le canal 50Ω avec une non-linéarité inférieur à 0,2% à travers 80% de la gamme et de 2% au delà. Les résultats des tests ont montré que tous les canaux sont conformes aux exigences sauf le canal 50Ω dans LAUROC0 où la non-linéarité est au dessus du poucent jusqu'à 1 mA et augmente pour atteindre une non-linéarité de 8% à 2 mA. Un exemple des résultats de linéarité du modèle LAUROC0 et de la sortie haut gain des canaux 25Ω et 50Ω sont montrés dans la Figure A.5. La linéarité du canal 50Ω de LAUROC0 a été corrigé dans l'itération suivante pour atteindre 2 mA avec une bonne linéarité.

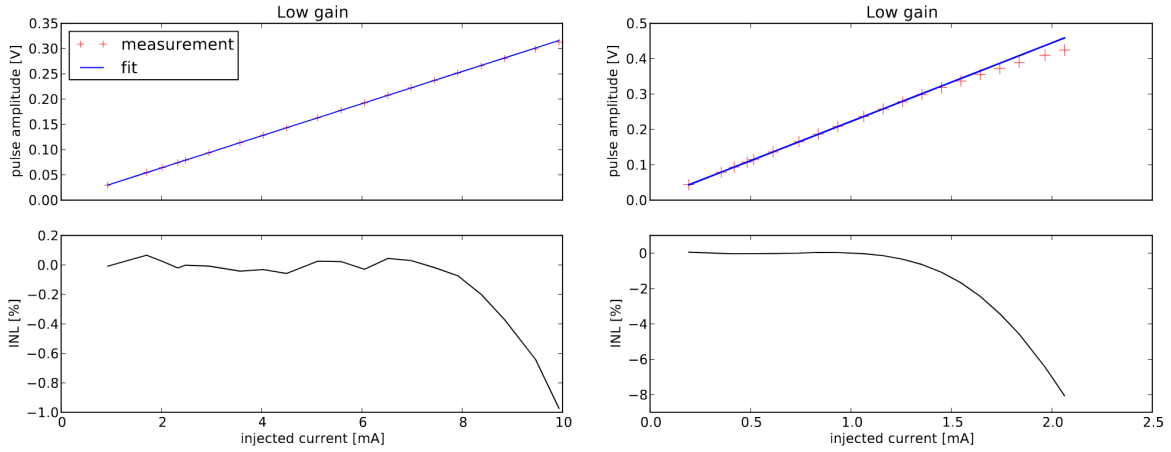

(a) **(b)**

Figure A.5 – Les résultats des mesures de la linéarité de LAUROC0 des sorties haut gain du canal 25Ω (a) et 50Ω (b). Le panneau supérieur montre l'amplitude de l'impulsion en fonction du courant d'entrée et le panneau inférieur montre la non-linéarité intégrale.

A.2.4 Validation du système à deux gains

Trois ADC sont implémentés dans l'électronique actuelle pour numériser les sorties des préamplificateurs. Les signaux numérisés en sortie seront ensuite traités pour déterminer l'énergie et la position du pic pour calculer le temps, ainsi que la qualité du signal. Le nouveau système à deux gains qui remplacera le système actuel à trois gains, est considéré pour améliorer les performances de lecture: l'implémentation du système à deux gains permet d'éviter le transfert de gain (*gain switching*) à des énergies pertinentes pour la calibration des photons provenant de la désintégration du boson de Higgs dans le canal diphoton ($H \rightarrow \gamma\gamma$). Ce système à deux gains est possible à réaliser grâce à l'utilisation d'ADC à 14-bits de gamme dynamique pour numériser chaque gain.

La première exigence est d'avoir le bruit de quantification inférieur au bruit intrinsèque du

calorimètre à argon liquide à l'énergie de transfert de gain, pour éviter la dégradation de la résolution totale du détecteur. Le transfert d'énergie se produit à la fin de la gamme dynamique et correspond à l'énergie maximale qui peut être mesurée par le bas gain, et à partir de laquelle seul le haut gain peut être mesuré. Les résultats de la simulation montrent qu'à cette énergie le bruit de quantisation est d'un ordre de grandeur inférieur à la résolution du calorimètre comme le montre la Figure A.6.

Une autre exigence que la majorité des photons provenant de la désintégration $H \to \gamma\gamma$ aient toutes leurs cellules measurées dans le haut gain. Cette exigence permet de réduire les incertitudes de calibration de gain dans les analyses mesurant la masse du boson de Higgs puisque la calibration est effectuée à l'aide d'électrons provenant de la désintégration $Z \to ee$ avec le système actuel à trois gains où les électrons ont leurs cellules dans le haut gain. Les résultats de l'étude ont montré que le système à deux gains proposé avec un rapport de gains entre 20 et 30 répond aux spécifications où seulement 1,8% des photons ont leurs énergies dans les cellules à bas gain de la couche avant et 1,1% dans le couche médiane, ce qui permet de valider ce nouveau système.

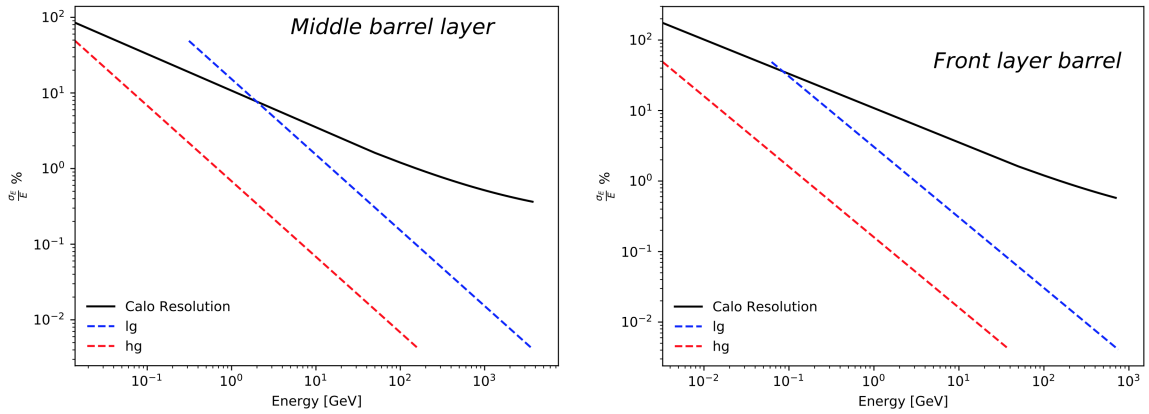

Figure A.6 – Le bruit de quantification estimé des sorties haut (en rouge) et bas (en bleu) gains et la résolution intrinsèque du calorimètre (en noir) en fonction de l'énergie dans les couches médiane (a) et avant (b) du tonneau.

A.3 Analyse du canal $VH(H \to b\bar{b})$

A.3.1 Introduction et stratégie de l'analyse

La mesure du boson de Higgs se désintégrant en quarks b est intéressante car c'est la désintégration dominante (avec un rapport de branchement de 58%) en plus de permettre de mesurer directement le couplage du boson de Higgs aux quarks b. Cependant, cette désintégration ne peut pas être détectée inclusivement et sera donc mesurée dans le mode de production associé à un boson vecteur (W ou Z). Ce mode de production a été étudié lorsque le boson vecteur se désintègre en leptons, ce qui permet de supprimer les bruits de fond QCD. Ce mode de production donne la sensibilité la plus élevée et permet de mesurer le couplage du boson de Higgs aux bosons vecteurs à des énergies élevées.

Trois canaux d'analyse sont définis en fonction du nombre de leptons chargés dans l'état final venant de la désintégration du boson vecteur: les canaux 0-lepton pour $Z(\to \nu\nu)H(\to bb)$, 1-lepton pour $W(\to l\nu)H(\to bb)$ et 2-lepton pour $Z(\to ll)H(\to bb)$ comme présenté dans la Figure A.7 où le lepton peut être un électron ou un muon. Puisque l'analyse recherche des

candidats $H \to b\bar{b}$, les événements avec exactement 2 b-jets sont sélectionnés en utilisant une méthode appelée b-tagging. Des coupures de sélection sont implémentées et optimisées dans les trois canaux d'analyse pour réduire la contamination des bruits de fond.

Des générateurs Monte Carlo sont utilisés pour la modélisation des bruits de fond dominants: le boson vecteur produit en association avec des jets (V+jets), top ($t\bar{t}$ et single-top) et le diboson (VZ). Des méthodes de modélisation basées sur les données ont été développées et utilisées pour estimer le fond top dans le canal 2-lepton et le multi-jet dans le canal 1-lepton.

Pour maximiser la sensibilité, l'analyse utilise une approche multivariée (MVA) basée sur des arbres de décision boostés (BDT). Les BDT utilisent des coupures simples sur des variables cinématiques pour classer un événement comme étant plus semblable à un signal ou semblable à un bruit de fond. Cette approche consiste à construire un discriminant (BDT_{VH}) à partir des variables cinématiques pour mieux distinguer le signal VH des bruits de fond.

Pour mesurer le signal VH, un ajustement de la fonction de vraisemblance profilée est effectué sur la variable discriminante BDT_{VH} dans les régions de signal. Deux autres analyses permettent de vérifier et valider les résultats: l'analyse qui se concentre sur la masse des deux jets b (m_{bb}) au lieu de BDT_{VH} et l'analyse diboson pour mesurer le signal VZ au lieu de VH à partir de la distribution BDT_{VZ}.

Les événements sont répartis en fonction de leur cinématique en catégories 2- et 3-jets ($\geq$ 3-jets dans le canal 2-lepton). Puisque la sensibilité est plus élevée à grand p_T^V, l'impulsion reconstruite du boson vecteur, les événements sont répartis en catégories de p_T^V: $75\,\text{GeV} < p_T^V < 150\,\text{GeV}$ seulement dans le canal 2-lepton, $150\,\text{GeV} < p_T^V < 250\,\text{GeV}$ et $p_T^V > 250\,\text{GeV}$ dans tous les cannaux.

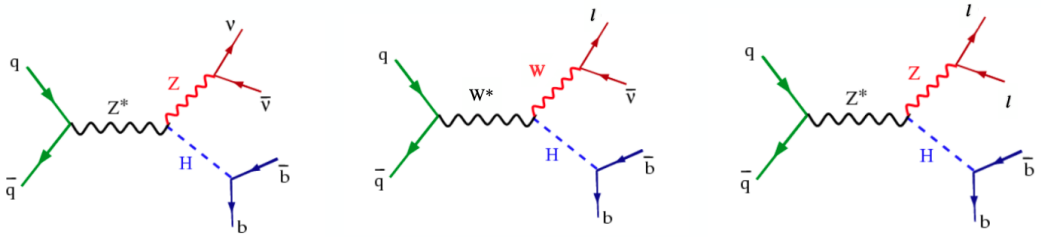

Figure A.7 – Les trois diagrammes de Feynman principaux des canaux $VH, H \to b\bar{b}$.

A.3.2 Catégorisation des évènements

La création des régions de signal et de contrôle est motivée par la faible pureté du signal dans l'espace des phases qui est dûe aux coupures de sélection. Par conséquent, des régions de signal sont créées pour augmenter la sensibilité et des régions de contrôle pour être très riches en bruits de fond. Ainsi des regions de contrôle sont conçues pour contrôler les bruits de fond W+jets et $t\bar{t}$. Ces deux bruits de fond sont dominants dans le canal 1-lepton, donc les coupures sont optimisées dans ce canal puis généralisées aux canaux 0- et 2-lepton. La variable qui permet de mieux distinguer entre W+jets et $t\bar{t}$ est la distance angulaire entre les deux jets b (ΔR_{bb}) puisque W+jets est dominant à petit ΔR_{bb} et $t\bar{t}$ à grand ΔR_{bb} comme le montre la Figure A.8.

Les régions de signal et de contrôle sont définies en utilisant deux coupures dans le plan ΔR_{bb}-p_T^V à partir de la distribution de signal comme présenté dans la Figure A.9. La coupure inférieur définit la région de contrôle dédiée à W+jets et appelée région de contrôle à bas ΔR, et la coupure supérieure définit la région de contrôle dédiée à $t\bar{t}$ et appelée région de contrôle à grand ΔR. Ces coupures sont optimisées non seulement pour avoir des régions de contrôle riches en bruits de fond, mais aussi pour avoir une faible acceptance du signal pour ne pas diminuer la

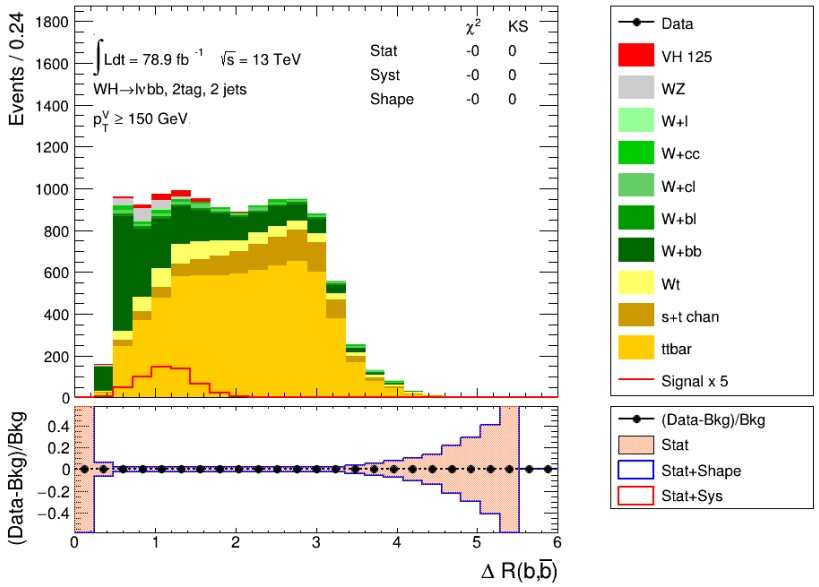

Figure A.8 – Distribution ΔR_{bb} dans le canal 1-lepton et la catégorie 2-jets.

sensibilité.

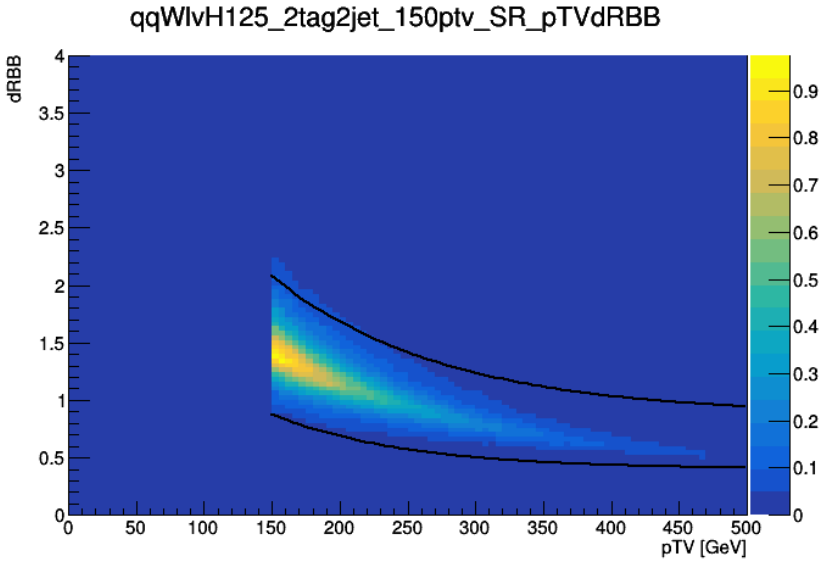

(a)

Figure A.9 – Les distributions ΔR_{bb} en fonction de p_T^V et les deux coupures utilisées pour définir les régions de signal et de contrôle dans la catégorie 2-jet.

Quand les coupures sont utilisées dans le canal 0-lepton, celle-ci permettent aussi d'avoir deux régions de contrôle dédiées à W+jets et $t\bar{t}$, de la même manière que le canal 1-lepton. La figure A.10 montre la compatibilité entre les deux coupures définies dans le canal 1-lepton et celles redéfinies dans le canal 0-lepton. Cependant, lorsque les coupures sont utilisées dans le canal 2-lepton, les deux régions de contrôles sont pures en Z+jets seulement car c'est le seul bruit de fond dominant dans ce canal. Quand les coupures sont comparées à celles redéfinies à partir de la distribution du signal dans le 2-lepton (Figure A.11), les coupures paraissent plus agressives dans la catégorie 3p-jet mais n'ont pas d'impact important sur la sensibilité.

L'analyse comprend un total de 14 régions de signal et 28 régions de contrôle, où les distributions

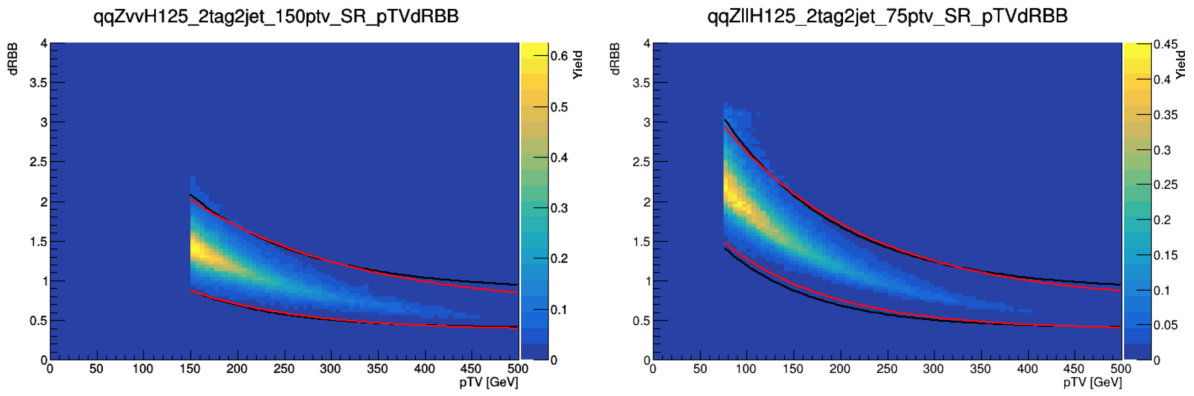

(a) **(b)**

Figure A.10 – Les distributions ΔR_{bb} en fonction de p_T^V et les deux coupures utilisées pour définir les régions de signal et de contrôle dans la catégorie 2-jet dans le canal 0-lepton (a) et 2-lepton (b). Les lignes rouges correspondent aux coupures redéfinies dans les deux canaux.

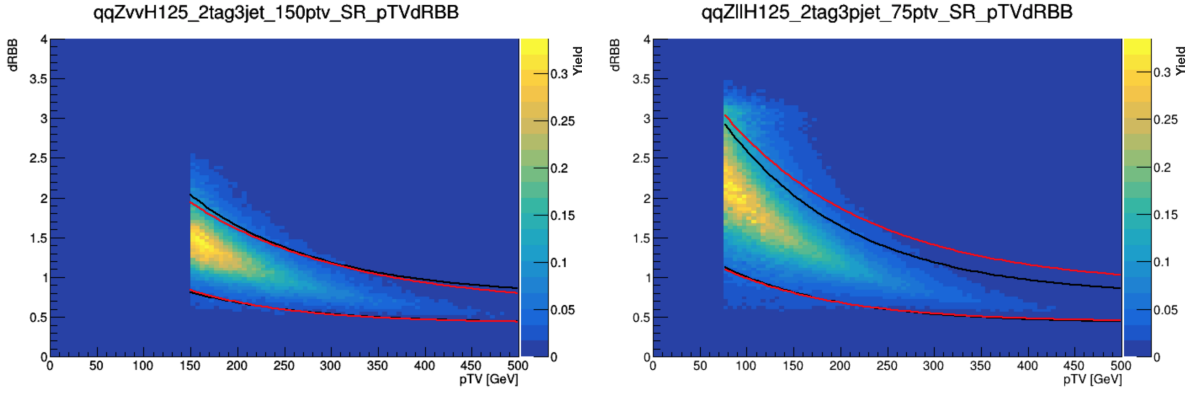

(a) **(b)**

Figure A.11 – Les distributions ΔR_{bb} en fonction de p_T^V et les deux coupures utilisées pour définir les régions de signal et de contrôle dans la catégorie 3-jet dans le canal 0-lepton (a) et 2-lepton (b). Les lignes rouges correspondent aux coupures redéfinies dans les deux canaux.

BDT_{VH}, m_{bb} ou BDT_{VZ} sont utilisées dans les régions de signal en fonction de la mesure souhaitée. Dans les régions de contrôle, les distributions sont combiné en un seul bin (*yield*) et utilisé dans ces régions pour mieux contrôler la normalisation des bruits de fond.

A.3.3 Estimation du bruit de fond multi-jet

Le bruit de fond multi-jets (MJ) provient des désintégrations semi-leptoniques des hadrons à l'intérieur du détecteur, des photons convertis ($\gamma \to ee$) et des jets mal indentifiés. La contamination du MJ est négligeable dans les canaux 0-lepton et dans le 2-lepton à cause des coupures de sélection d'événements appliquées dans les canaux. Cependant, il y a encore une petite fraction de multi-jets dans le canal 1-lepton même avec les coupures d'isolation des leptons qui visent à réduire la contamination de ce bruit de fond. Ainsi il faut trouver une méthode pour estimer correctement ce bruit de fond vu que les générateurs Monte Carlo ne peuvent pas être utilisés pour la modélisation en raison des faibles statistiques.

L'estimation de ce bruit de fond est faite est utilisant une méthode d'ajustement de modèle basée sur les données. Cette méthode se compose de deux étapes: premièrement obtenir la forme du MJ et ensuite obtenir la bonne normalisation. La forme MJ est obtenue à partir d'une

région de contrôle bien riche en MJ qui est la région avec des coupures d'isolation inversées avec exactement un seul jet-b. La forme est obtenue par soustraction des bruits de fond électrofaibles des événements de données. La figure A.12 montre la distribution de l'impulsion du boson W dans le plan transverse (m_T^W) dans la région de contrôle MJ.

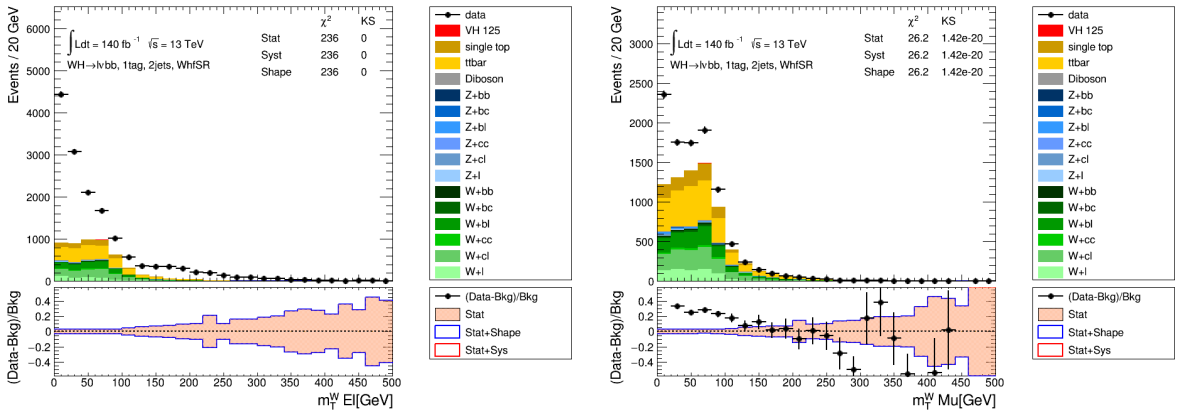

(a) **(b)**

Figure A.12 – La distribution m_T^W dans la région 1 b-tag avec les coupures d'isolation inversées pour $p_T^V > 150\,\text{GeV}$ dans le canal électron (a) et muon (b). Le MJ est obtenu à partir de la soutraction des bruits de fond électrofaibles des événements de données.

La forme du MJ est ensuite extrapolée à la région 2 b-tag avec les coupures d'isolation des leptons (qui est l'espace des phases de l'analyse), où un ajustement est effectué pour fixer la normalisation du bruit de fond MJ. La distribution m_T^W est choisi comme la distribution discriminante car elle fournit une bonne discrimination entre le bruit MJ et les autres bruits de fond électrofaibles. Les résultats sont montrés dans la Figure A.13.

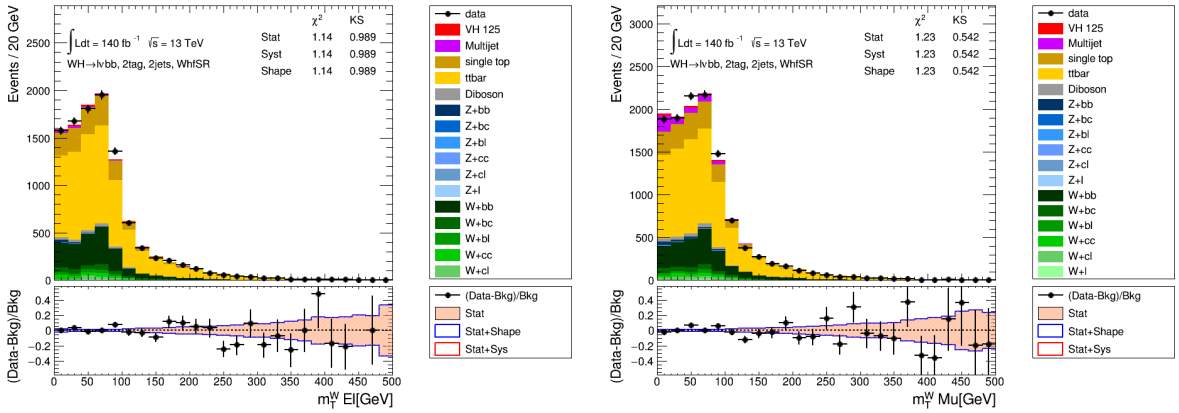

(a) **(b)**

Figure A.13 – La distribution m_T^W résultante dans la région 2 b-tag avec des coupures d'isolation des leptons pour $p_T^V > 150\,\text{GeV}$ dans le canal électron (a) et muon (b).

De nombreuses sources d'incertitudes ont été étudiées pour l'estimation du bruit de fond MJ. Le premier type d'incertitudes couvre le changement de la forme de distribution BDT_{VH} du MJ dans l'ajustement final pour mesurer le signal. Cette incertitude a été estimée en changeant les coupures d'isolation des leptons ainsi que la normalisation des bruits électrofaibles. Le deuxième type d'incertitudes concerne le changement de la normalisation du MJ obtenue à partir de la distribution m_T^W. Celles-ci sont évaluées en remplacant la distribution m_T^W dans l'ajustement par la distribution $\Delta\phi$ entre le lepton et l'énergie transverse manquant ($\Delta\phi$(lep,MET)) qui est une variable sensible au MJ, ainsi qu'en supprimant les coupures dédiées à réduire la contamination

du MJ. La table A.1 montre la contribution du MJ au bruits de fond total et les incertitudes de normalisation et statistiques correspondantes.

Régions	Fractions de MJ (%)
p_T^V >150 GeV region	
2-tag, 2-jet, e	$0.7^{+1.4}_{-0.7}$
2-tag, 2-jet, μ	$3.8^{+1.8}_{-1.1}$
2-tag, 3-jet, e	$0.13^{+0.13}_{-0.13}$
2-tag, 3-jet, μ	$0.06^{+0.06}_{-0.06}$

Table A.1 – La contribution du bruit de fond multi-jet et les incertitudes correpondantes.

A.3.4 Estimation des incertitudes par repondération multidimensionnelle

Dans cette partie sera présentée l'estimation des incertitudes associées à la forme des bruits de fond électrofaibles. La méthode habituelle pour l'estimation consiste à comparer différentes implémentations Monte Carlo sur le discriminant final de l'analyse. Cependant, cette technique manque de précision lorsqu'il y a un manque de statistiques dans les générateurs Monte Carlo alternatifs. Une alternative est de repondérer la distribution nominale pour la transformer en variation. La repondération est paramétrée à partir de la différence entre le générateur nominal et le générateur alternatif. Cette différence est estimée à partir de distributions discriminantes en prenant le rapport entre les générateurs nominal et alternatif après les avoir normalisées à la même surface. Ce rapport sera ensuite utilisée comme fonction pour repondérer la distribution nominale. Deux distributions sont choisies pour estimer ces incertitudes, p_T^V et m_{bb}, car ces deux variables sont importantes dans l'analyse et ne sont pas corrélées. La distribution de p_T^V pour le bruit de fond $t\bar{t}$ montrant le générateur nominal (PowhegPhyia8) ainsi que les génerateurs aMCAtNLoPythia8 (variation d'élément de matrice) et PowhegHerwig7 (variation des gerbes de partons) est présentée dans la Figure A.14.

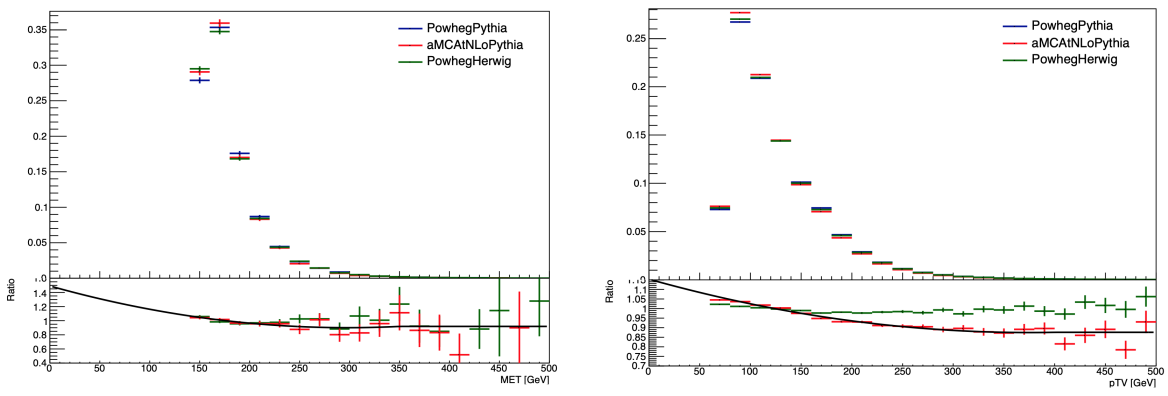

(a) **(b)**

Figure A.14 – la distribution p_T^V dans le cannal 0-lepton (a) et 1-lepton (b) dans la région 2-jets pour le bruit de fond $t\bar{t}$. Le plus grand rapport des distributions est considéré comme étant la variation.

Une nouvelle méthode de repondération multidimensionnelle a été développée à l'aide de BDT. Cette nouvelle méthode ne se concentre pas sur une seule variable, mais utilise toutes les variables et leurs corrélations pour explorer l'ensemble de l'espace des phases. Elle permet de couvrir la variation sur toutes les variables cinématiques. Dans cette méthode, un BDT est entraîné pour séparer entre le génerateur nominal et le génerateur alternatif représentant une variation. De la

même manière que les systématiques calculées à partir de p_T^V et m_{bb}, le rapport entre le nominal et le générateur altérnatif est calculé mais cette fois en utilisant la distribution de BDT résultante. La Figure A.15 monte les distributions de BDT dans le canal 1-lepton pour le bruit de fond $t\bar{t}$, utilisés pour l'estimation des systématiques liées à sa forme. Un exemple des distributions cinématiques dans le canal à 1-lepton est présenté dans la Figure A.15 et montre les générateurs nominal et alternatif en plus des deux variations estimées à partir de la distribution de p_T^V et de la méthode de repondération multidimensionnelle. Cette nouvelle méthode de repondération permet de transformer la distribution nominale en variation, et de sonder les variations dans les coins de l'espace des phases où la pondération unidimensionnelle n'a pas pu capter.

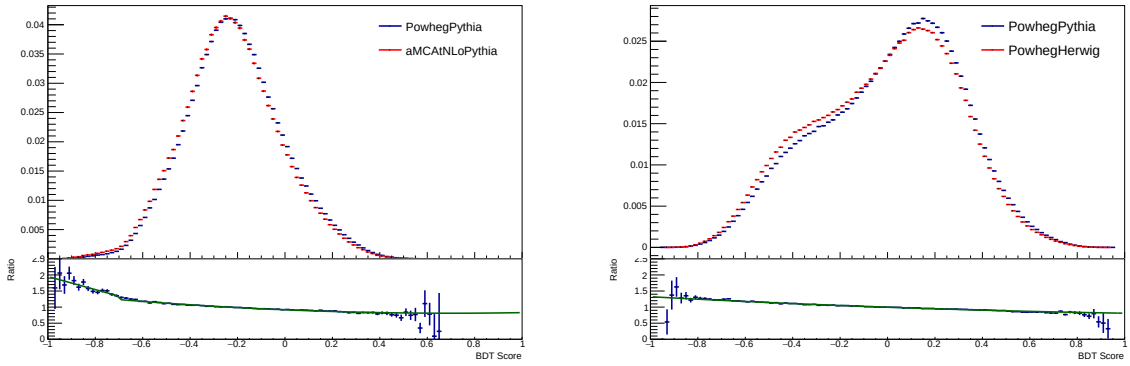

(a) **(b)**

Figure A.15 – la distribution de BDT résultante dans le canal 1-lepton pour le bruit de fond $t\bar{t}$ pour la variation d'élément de matrice (a) et la variation des gerbes de partons (b).

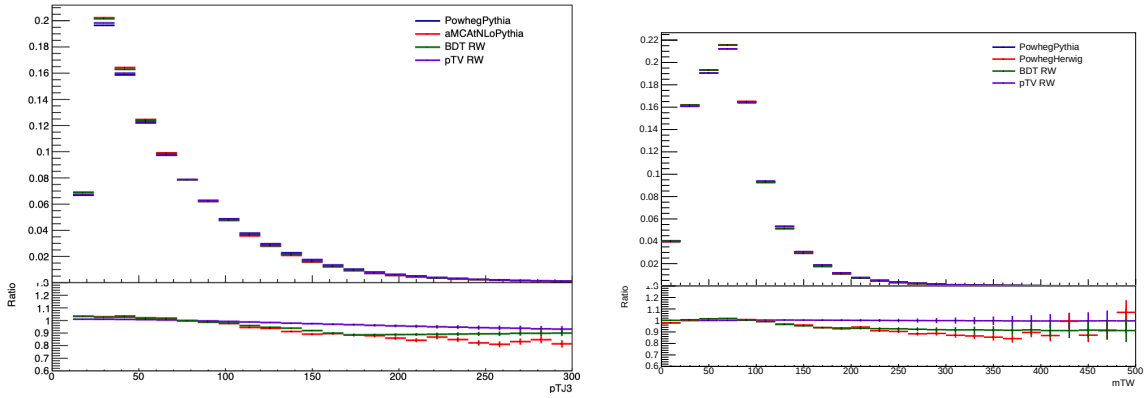

(a) **(b)**

Figure A.16 – Les distributions de l'impulsion du troisième jet dans le plan transverse pour la variation d'élément de matrice (a) et de la masse transverse du boson W pour la variation des gerbes de partons (b) dans le canal 1-lepton pour le bruit de fond $t\bar{t}$.

A.3.5 Résultats de l'analyse

L'analyse diboson est une validation robuste de l'analyse et du modèle de bruits de fond puisque le processus $VZ, Z \to b\bar{b}$ est très similaire au processus $VH, H \to b\bar{b}$. La stratégie de l'analyse consiste à mesurer le signal VZ en premier. Ainsi lorsque les résultats des mesures sont validés, le signal VH sera mesuré. Cette analyse se focalise sur le discriminant BDT_{VZ} où le BDT est réentraîné pour séparer le signal VZ des bruits de fond. Les valeurs de la force du signal (*signal*

strength) de l'analyse du diboson se sont avérées être en bon accord avec la prédiction du Modèle Standard comme le montre la Figure A.17.

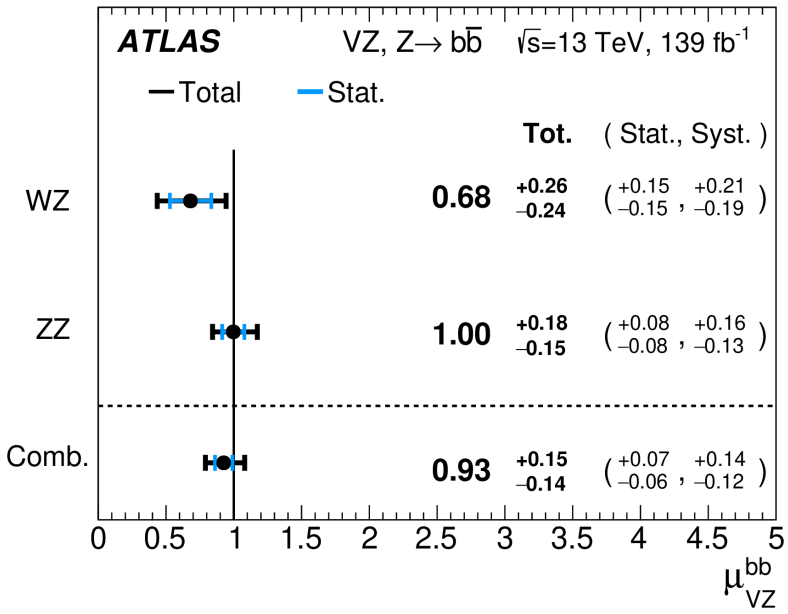

Figure A.17 – Les valeurs extraites pour la force du signal de l'analyse du diboson correspondant au rapport du signal mesuré sur le signal attendu par le Modèle Standard.

Les résultats de l'analyse multivariée pour mesurer le signal VH ont été réalisées en utilisant $139\,\text{fb}^{-1}$ de données collectées par le détecteur ATLAS à partir de collisions de protons à une énergie du centre de masse de 13 TeV. Celà consiste à ajuster les distributions BDT_{VH} dans les régions de signal simultanément aux normalisations dans les régions de contrôle. La Figure A.18 montre la combinaison de toutes les distibutions BDT_{VH} dans les trois canaux. Les mesures ont mené à l'observation du signal VH avec une significance de 6.7σ (écart-type) où 6.7σ ont été attendus. Les mesures ont aussi mené à l'observation du signal ZH avec 5.3σ (5.2σ attendu) et une preuve solide du signal WH avec 4.0σ (4.1σ attendu).

En plus d'effectuer des mesures inclusives, des mesures de section efficaces différentielle (STXS) ont été effectuées. Les catégories de l'analyse ont été harmonisées avec les catégories de STXS qui ont été définies en concertation entre les expériences ATLAS et CMS et les théoriciens. Par conséquent, l'analyse a effectué ces mesures en 5 bins STXS qui ont été définis en se basant uniquement sur les catégories de p_T^V. Les sections efficaces multipliées par les rapports de branchement mesurés dans les bins STXS sont présentées dans la Figure A.19 et se sont avérées être en bon accord avec les prédictions du Modèle Standard.

Les résultats de l'analyse multivariée ont été vérifiée en mesurant le signal VH à partir de la distribution m_{bb} au lieu de BDT_{VH}. Ces mesures ont permis également l'observation du signal VH avec une significance de 5.5σ (4.9σ attendu). La distribution m_{bb} résultante et combinant toutes les catégories est présentée dans la Figure A.20 pour montrer l'accord entre les données et les prédictions Monte Carlo.

Puisque l'analyse multivariée et l'analayse m_{bb} mesurent le même signal à partir de deux discriminants différents, la compatibilité entre les deux mesures a été mesurée à l'aide de la méthode bootstrap. La méthode est effectuée uniquement sur la base de fluctuations statistiques des données en générant des réplications multiples des données (*toy data*). Les résultats des mesures MVA et m_{bb} se sont avérés en accord à 1σ.

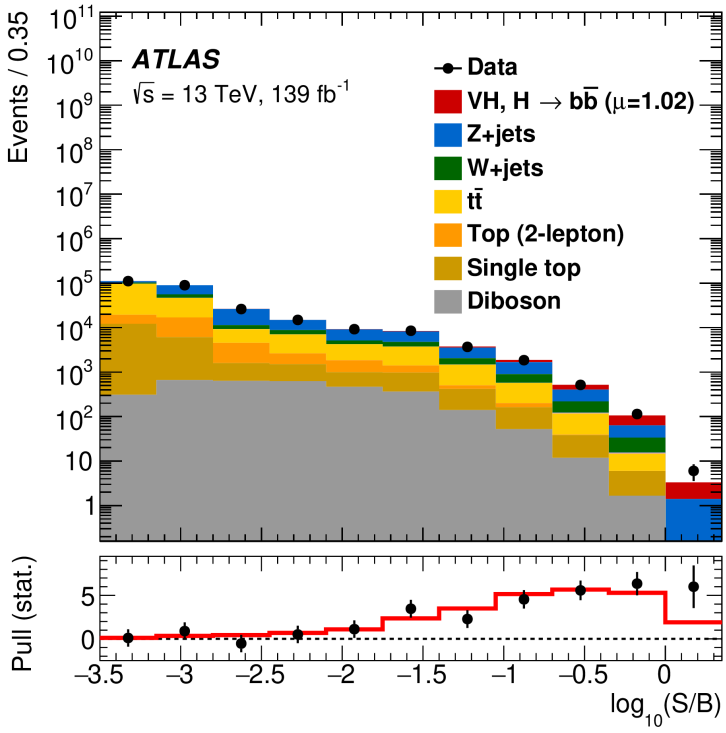

Figure A.18 – Les distributions BDT_{VH} de toutes les régions regroupées en bins de log de signal/bruits.

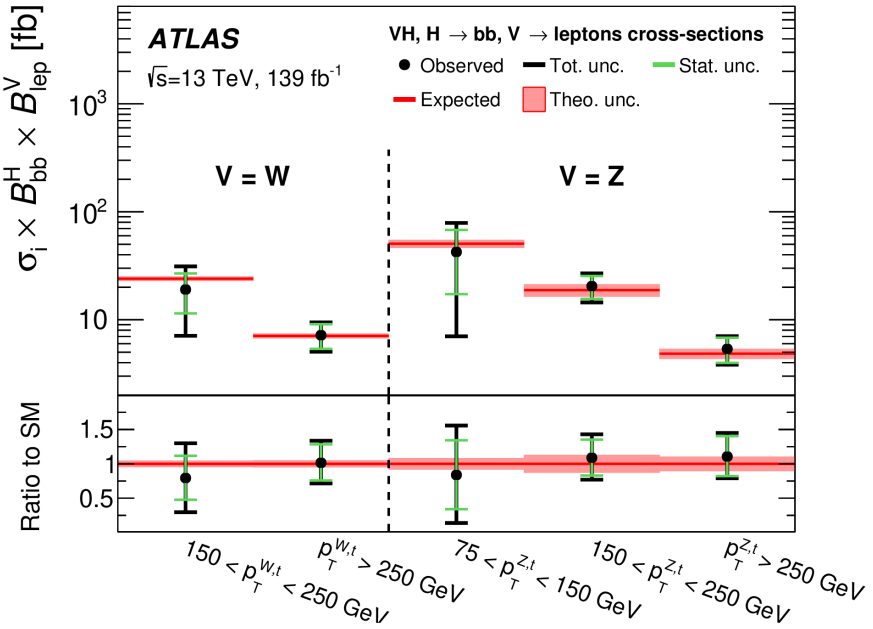

Figure A.19 – Les résultats des sections efficaces de $VH, V \to$ leptons mesurées multipliée par les rapport de branchement $H \to b\bar{b}$.

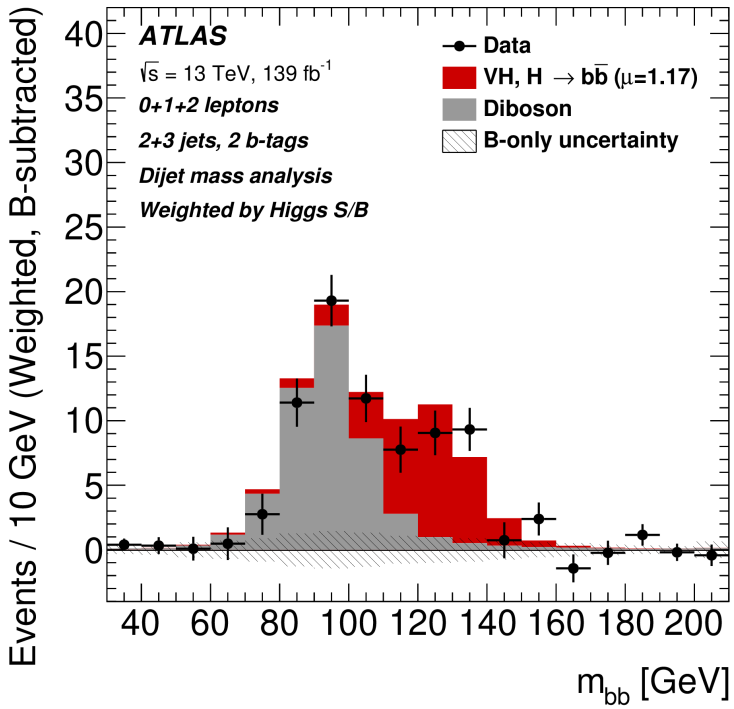

Figure A.20 – La distribution m_{bb} combinant toutes les catégories après soustraction des bruits de fond.

université PARIS-SACLAY

ÉCOLE DOCTORALE
Particules, hadrons, énergie et noyau : instrumentation, imagerie, cosmos et simulation (PHENIICS)

Titre: Mesures du boson de Higgs produit en association avec un boson vecteur et se désintégrant en une paire de quarks-b avec le détecteur ATLAS

Mots clés: Higgs, particules élémentaires, VHbb, ATLAS, LHC, théorie électrofaible

Résumé: La découverte du boson de Higgs en 2012 par les expériences ATLAS et CMS a ouvert tout un nouveau domaine de recherche au LHC: la mesure des propriétés de cette particule permet d'affiner notre compréhension du Modèle Standard et de contraindre la physique au-delà de ce Modèle.
Cette thèse présente les mesures du boson de Higgs se désintégrant en une paire de quarks-b et produit avec un boson W ou Z, réalisées en utilisant 139 fb^{-1} de données de collisions proton-proton à une énergie de 13 TeV dans le centre de masse collectées par le détecteur ATLAS. Trois canaux sont définis, nommés 0-, 1- et 2-leptons, selon le nombre de leptons chargés provenant de la désintégration du boson vecteur. L'analyse bénéficie de la grande statistique des données Run-2 et de l'amélioration de nombreuses techniques d'analyse, ce qui accroît sa sensibilité et permet l'observation du signal ZH et une preuve solide du signal WH dans la désintégration du boson de Higgs en paires de quarks-b. Des mesures de sections efficaces différentielles sont également menées, et sont en bon accord avec la théorie.
Le détecteur ATLAS fera l'objet de nombreuses mises à jour en vue de l'exploitation du HL-LHC afin de pouvoir tolérer l'augmentation de la luminosité et du niveau d'empilement. L'électronique de lecture du calorimètre à argon liquide sera ainsi remplacée. Une partie de cette thèse est consacrée à vérifier si les prototypes de préamplificateurs Front-End proposés pour la mise à jour sont conformes aux éxigences physiques.

Title: Measurements of the Higgs boson produced in association with a vector boson and decaying to a pair of b-quarks with the ATLAS detector

Keywords: Higgs, elementary particles, VHbb, ATLAS, LHC, electroweak theory

Abstract: The discovery of the Higgs boson in 2012 by the ATLAS and CMS experiments has opened a new research domain at the LHC, with the measurement of the properties of this particle to refine our understanding of the Standard Model and constrain physics beyond this model.
The measurements of the Higgs boson decaying to a pair of b-quarks and produced alongside a W or Z boson, performed with the ATLAS detector using 139 fb^{-1} of data collected in proton-proton collisions at a center-of-mass energy of 13 TeV are presented in this thesis. Three channels are defined, the 0-, 1- and 2-lepton channels, depending on the number of charged leptons coming from the decay of the vector boson. The analysis takes advantage of the full Run-2 data statistics and of the improvement of many analysis techniques, which increase its sensitivity and yields the observation of the ZH signal and a strong evidence of the WH signal in this decay channel of the Higgs boson into pairs of b-quarks. Differential cross-section measurements are also performed and are found to be in good agreement with the Standard Model.
The ATLAS detector will undergo many upgrades in preparation for the HL-LHC operation to be able to cope with the increase in luminosity and pile-up level. Therefore the liquid argon calorimeter readout electronics will be replaced. A part of this thesis is dedicated to check if the Front-End pre-amplifier prototypes proposed for the upgrade comply with the physics requirements.

Université Paris-Saclay
Espace Technologique / Immeuble Discovery
Route de l'Orme aux Merisiers RD 128 / 91190 Saint-Aubin, France